Methods and applications in vascular physiology: 2021

Edited by
Ali Dabiri, Julien Vincent Brugniaux, Alexey Goltsov, Kıvılcım Kılıç,
Antonio Colantuoni, Rosalia Rodriguez-Rodriguez and
Calum Wilson

About Frontiers

Frontiers is more than just an open access publisher of scholarly articles: it is a pioneering approach to the world of academia, radically improving the way scholarly research is managed. The grand vision of Frontiers is a world where all people have an equal opportunity to seek, share and generate knowledge. Frontiers provides immediate and permanent online open access to all its publications, but this alone is not enough to realize our grand goals.

Frontiers journal series

The Frontiers journal series is a multi-tier and interdisciplinary set of open-access, online journals, promising a paradigm shift from the current review, selection and dissemination processes in academic publishing. All Frontiers journals are driven by researchers for researchers; therefore, they constitute a service to the scholarly community. At the same time, the *Frontiers journal series* operates on a revolutionary invention, the tiered publishing system, initially addressing specific communities of scholars, and gradually climbing up to broader public understanding, thus serving the interests of the lay society, too.

Dedication to quality

Each Frontiers article is a landmark of the highest quality, thanks to genuinely collaborative interactions between authors and review editors, who include some of the world's best academicians. Research must be certified by peers before entering a stream of knowledge that may eventually reach the public - and shape society; therefore, Frontiers only applies the most rigorous and unbiased reviews. Frontiers revolutionizes research publishing by freely delivering the most outstanding research, evaluated with no bias from both the academic and social point of view. By applying the most advanced information technologies, Frontiers is catapulting scholarly publishing into a new generation.

What are Frontiers Research Topics?

Frontiers Research Topics are very popular trademarks of the *Frontiers journals series*: they are collections of at least ten articles, all centered on a particular subject. With their unique mix of varied contributions from Original Research to Review Articles, Frontiers Research Topics unify the most influential researchers, the latest key findings and historical advances in a hot research area.

Find out more on how to host your own Frontiers Research Topic or contribute to one as an author by contacting the Frontiers editorial office: frontiersin.org/about/contact

Methods and applications in vascular physiology: 2021

Topic editors

Ali Dabiri — California Medical Innovations Institute, United States

Julien Vincent Brugniaux — Université Grenoble Alpes, France

Alexey Goltsov — Moscow State Institute of Radio Engineering, Electronics and Automation, Russia

Kıvılcım Kılıç — Boston University, United States

Antonio Colantuoni — University of Naples Federico II, Italy

Rosalia Rodriguez-Rodriguez — International University of Catalonia, Spain

Calum Wilson — University of Strathclyde, United Kingdom

Table of contents

frontiers | Frontiers in Physiology

Check for updates

Editorial: Methods and applications in vascular physiology: 2021

Julien V. Brugniaux[1], Rosalia Rodriguez-Rodriguez[2], Ali Dabiri[3], Kıvılcım Kılıç[4], Calum Wilson[5], Alexey Goltsov[6]* and Antonio Colantuoni[7]

[1]HP2 laboratory (INSERM 1300), Université Grenoble Alpes, Saint Martin d'Hères, France, [2]Basic Sciences Department, Faculty of Medicine and Health Sciences, Universitat Internacional de Catalunya, Sant Cugat del Valles, Spain, [3]California Medical Innovations Institute, San Diego, CA, United States, [4]Biomedical Engineering Department, Boston University, Boston, MA, United States, [5]Strathclyde Institute of Pharmacy and Biomedical Sciences, University of Strathclyde, Glasgow, United Kingdom, [6]Institute for Artificial Intelligence, Russian Technological University (MIREA), Moscow, Russia, [7]University of Naples Federico II, Naples, Italy

---

Editorial on the Research Topic
Methods and applications in vascular physiology: 2021

This Research Topic is a part of the Methods and Applications in Physiology series and aims at highlighting the latest experimental and computational methods in vascular physiology and their pharmacological, clinical and healthcare applications. The Research Topic includes methodological articles, describing either novel technical approaches or new applications of the conventional methods for measurement of vascular functions and parameters in health and pathological conditions. Since the vascular system is the main diagnostic and therapeutic target in much pathology, the most selected works directly relate to the clinical research and translation of the research methods to clinical practice. We hope that detailed discussion of methods and their applications in the separate Research Topic will be fruitful in relation to meeting one of the key challenges in experimental physiology, i.e., the development of reliable and rigorous methods, which ensure reproducibility of scientific results as well as unbiased and robust data analysis. Below, we briefly reviewed articles included in this Research Topic and presented main findings of the contributors.

Coagulation relies on the complex interaction of procoagulation and anticoagulation factors, as well as the fibrinolytic system. The normal clotting process goes through four phases among which, primary hemostasis and secondary hemostasis relate to clot formation. During the former, an unstable platelets plug forms at the site of injury. Indeed, within seconds to minutes after the injury, the blood vessels vasoconstriction and attract circulating platelets, which are activated, aggregate to one another and adhere to the subendothelium, eventually forming the platelet plug. During the first step of this

process, the circulating platelets need to deposit to the exposed injured surface. The article from Wang et al. published herein, explores a novel mechanism that could regulate the deposition of platelets on the surface of the blood vessels. Due to the presence of sialic acid, the surface of platelets has an electronegatively charged and it has, therefore, been postulated by the authors that imposing an electric field (EF) could stimulate electrotaxis, i.e., the migration of the living cell towards cathode or anode. In this particular case, platelet deposition was reduced when the cathode of the EF was placed at the injured site, while it was increased should the anode be placed at the site. Most importantly, the authors found that to ensure only (or mostly) platelets would be deposited, the current needed to be less than 20 mV. Taken together, the present results suggest that manipulating the electric signal is an advantageous method to regulate the deposition of platelet onto the vessel wall.

Rajanathan et al. devoted their Methods paper to the development of an *in vivo* murine model for integrated assessment of the cardiovascular system in a pharmacological study of drug intervention. The *in vivo* model was used for the development of the protocol to investigate cardiac and vascular responses to the α_1-agonist phenylephrine. Assessment of multiple intrinsic cardiac and vascular parameters allowed authors to validate the experimental protocol and distinguish phenylephrine-induced subsequent changes in peripheral vascular and cardiac systems. The developed method may contribute to the further progress in the integrated investigation of cardiovascular system responses to pharmacological intervention and testing new therapeutic targets.

Gu et al. described a developed protocol for a randomized clinical trial to study effectiveness of a mobile stroke unit (MSU) to manage acute stroke. This work focused on the comparison of clinical and economic outcomes of the innovative MSU based on 5G technology with a conventional emergency medical system. Authors see the advantages of the 5G-based MSU in combination of integrating neurological symptom examination, CT diagnosis, intravenous thrombolytic therapy, and remote consultation with the stroke centre through telemedicine system during patient transportation. Effective reducing the door-to-needle time and ensuring treatment within the golden time of stroke management are expected as the results of 5G-based MSU introduction in hospitals. This work extended the clinical trials on therapy to the trials on the effectiveness of the whole clinical unit to prove its benefits.

Nartsissov developed a computational method in vascular physiology to investigate dynamics of glucose supply to brain tissue. Author constructed a multi-scale computational model of glucose diffusion, transport and consumption in a neurovascular unit. In model construction, a multiphysical approach was utilised to combine different biophysical models to jointly describe hemodynamic in capillary, metabolite diffusion in heterogeneous tissue media and kinetics of biochemical

reactions. The developed multi-scale computational approach may be extended to estimate distribution of different metabolites and drugs in brain tissue and used as a perspective computational tool in quantitative systems pharmacology (QSP) and PK/PD preclinical investigation.

The elegant review published by Masood et al. highlighted the importance of understanding lymphatic vessel regression in both physiological and pathological contexts, and explored the therapeutic potential of this knowledge. Considering the higher number of publications on the formation and regression of blood vessels compared to lymphatics, the authors proposed to extend insights from the fruitful field of blood vessels regression to shed light on the mechanisms underlying lymphatic vessel regression. Following these lessons, the potential mechanisms in lymphatic vessel regression may involve pro-survival and homeostatic signals, inflammation, anti-angiogenic switch and negative feedback, and apoptosis of regressing vessels. The authors also discussed the implications of newly identified roles of lymphatics in several pathologies, such as cardiovascular and neurodegenerative diseases, but importantly the potential avenues for therapeutic use of targeting lymphatic vessel regression. In particular, the use of appropriate models for the study of this process (e.g., mouse cornea, tail, bone or lung) has revealed the promising anti-lymphangiogenic effect of several drugs in pre-clinical and clinical studies in several pathologies such as lymphedema or Inflammatory Bowel Disease, but also in the prevention of tumour metastasis.

Palombo et al. have studied in ten young healthy volunteers, before and after a 5-week head-down tilt bed rest, the arterial pressure waveforms, which reflect the interaction between the heart and the arterial system with potentially relevant information about circulation conditions. According to the commonly accepted "wave transmission model," the net blood pressure waveform results from the superposition of discrete forward and backward pressure waves, with the forward wave in systole determined mainly by the left ventricular ejection function and the backward by the wave reflection from the periphery, the timing and amplitude of which depend on arterial stiffness. However, this approach obscures the "windkessel function" (WF) of the elastic arteries. A "reservoir-excess pressure" (REP) model has been proposed, which interprets the arterial blood pressure waveform as a composite of a volume-related "reservoir" pressure and a wave-related "excess" pressure. The results in young people confirmed the hypothesis that REP analysis complements the wave-model adding a volume component related to the aorta WF, which may have variable impact and relevance according to age and health/disease status of the subjects.

Van der Laan et al. have improved their analysis method to automatically characterize vascular smooth muscle cells (VSMC) orientation and transmural distribution in murine carotid arteries under well-controlled biomechanical conditions. In the present study, they added a "nucleus splitting" procedure

to split coinciding nuclei to increase the accuracy of their method. They tested this analysis technique in a mouse model of VSMC apoptosis. Carotid arteries from SM22a-hDTR Apoe−/− and control Apoe 37 −/− mice were dissected, excised, mounted in a biaxial biomechanical tester. Nuclei and elastin fibres were stained and imaged using 3D two-photon laser scanning microscopy. Nuclei were segmented from images and coincident nuclei were split. The nucleus splitting procedure increased the accuracy of the methods, in comparison with manual nucleus count. This improvement of the method may contribute to accurately determine the VSMC in the investigated vessels.

In a comparative study, Hersant et al. have found that in patients with suspected thoracic outlet syndrome (TOS) during the Candlestick-Prayer (Ca+Pra) maneuver, forearm pulse plethysmography, with red (R) or infrared (IR) light wavelength, was more accurate than fingertip pulse pletismography. They tested the effect of probe position (fingertip *versus* forearm) and compared the pattern classifications to the results of ultrasound. They recruited 20 patients for a Ca+Pra maneuver with simultaneous fingertip and forearm pulse pletismography (V-PPG) recording. V-PPG suggested the presence of venous outflow impairment in 27 and 20 limbs with forearm V-PPG-IR and forearm V-PPG-R, respectively. Fingertip V-PPG-R provided no patterns suggesting outflow impairment. The authors pointed out that probe position is essential if aiming to perform upper-limb V-PPG during the Ca+Pra maneuver in patients with suspected TOS. Moreover, V-PPG during the Ca+Pra maneuver is of low cost, easy and provides reliable and objective evidence of forearm swelling.

In a well-planned study, Zócalo and Bia have utilized ultrasound-derived blood flow velocity (BFV) levels (i.e., peak systolic velocity, PSV), intra-beat indexes (i.e., resistive) and inter-segment ratios (i.e., internal/common carotid artery (ICA/CCA) PSV ratio) to describe cardiovascular physiology and health status (i.e., disease severity evaluation and/or risk stratification). They pointed out that fixed cut-off values (disregard of age or sex) have been proposed to define "significant" vascular disease from BFV-derived data. The authors highlighted that the use of single fixed cut-off values has limitations. They suggested that an accurate use of BFV-derived parameters requires physiological age-related profiles and the expected values for a specific subject. They evaluated the difference between left and right data and calculated mean, standard deviation and age-related profiles for BFV levels in 3,619 patients. It is of interest that left and right body-side derived data were not always equivalent. Sex-specific reference

interval (RI) was dependent on the parameter and/or age considered. RIs was defined for each studied artery: common carotid, internal carotid, external carotid, vertebral, femoral, and brachial arteries. They compared percentile curves with recommended fixed cut-off points. They reported equations for sex, body-side and age-specific BFV physiological profiles obtained in the investigated children, adolescents and adults, useful to determine the expected values and potential data-deviations for each person.

Taken together, the aforementioned articles showed a wide spectrum of the new experimental methods for measurement and analysis of multimodal data in vascular physiology. Looking at the successful issue of this Research Topic in 2021, we have launched the new Research Topic of Methods and Applications In Vascular Physiology: 2022 and welcome physiological experts to contribute and discuss the latest experimental, computational, statistical, and clinical methods in vascular physiology.

Author contributions

Acknowledgments

Conflict of Interest

The authors declare that the research was conducted in the absence of any commercial or financial relationships that could be construed as a potential conflict of interest.

Publisher's note

All claims expressed in this article are solely those of the authors and do not necessarily represent those of their affiliated organizations, or those of the publisher, the editors and the reviewers. Any product that may be evaluated in this article, or claim that may be made by its manufacturer, is not guaranteed or endorsed by the publisher.

Sex- and Age-Related Physiological Profiles for Brachial, Vertebral, Carotid, and Femoral Arteries Blood Flow Velocity Parameters During Growth and Aging (4–76 Years): Comparison With Clinical Cut-Off Levels

Yanina Zócalo* and Daniel Bia

Physiology Department, School of Medicine, CUiiDARTE, Republic University, Montevideo, Uruguay

Ultrasound-derived blood flow velocity (BFV) levels [e.g., peak systolic velocity (PSV)], intrabeat indexes (e.g., resistive), and intersegment ratios [e.g., internal/common carotid artery (ICA/CCA) PSV ratio] are assessed to describe cardiovascular physiology and health status (e.g., disease severity evaluation and/or risk stratification). In this respect, fixed cut-off values (disregard of age or sex) have been proposed to define "significant" vascular disease from BFV-derived data (parameters). However, the use of single fixed cut-off values has limitations. Accurate use of BFV-derived parameters requires knowing their physiological age-related profiles and the expected values for a specific subject. To our knowledge, there are no studies that have characterized BFV profiles in large populations taking into account: (i) data from different age-stages (as a continuous) and transitions (childhood–adolescence–adulthood), (ii) complementary parameters, (iii) data from different arteries, and (iv) potential sex- and hemibody-related differences. Furthermore, (v) there is little information regarding normative data [reference intervals (RIs)] for BFV indexes.

Aims: The aims of this study are the following: (a) to determine the need for age-, body side-, and sex-specific profiles for BFV levels and derived parameters (intrabeat indexes and intersegment ratios), and (b) to define RIs for BFV levels and parameters, obtained from CCA, ICA, external carotid, vertebral, femoral, and brachial arteries records.

Methods: A total of 3,619 subjects (3–90 years) were included; 1,152 were healthy (without cardiovascular disease and atheroma plaques) and non-exposed to cardiovascular risk factors. BFV data were acquired. The agreement between left and right data was analyzed (Concordance correlation, Bland–Altman). Mean and SD equations and age-related profiles were obtained for BFV levels and parameters (regression methods; fractional polynomials).

Results: Left and right body-side derived data were not always equivalent. The need for sex-specific RIs was dependent on the parameter and/or age considered. RIs were defined for each studied artery and parameter. Percentile curves were compared with recommended fixed cut-off points. The equations for sex, body-side, and age-specific BFV physiological profiles obtained in the large population (of children, adolescents, and adults) studied were included (spreadsheet formats), enabling to determine for a particular subject, the expected values and potential data deviations.

Keywords: adolescents, adults, blood flow velocity, brachial, carotid, children, femoral, physiological aging

INTRODUCTION

B-mode ultrasound (US) evaluation of peripheral arteries (e.g., carotid and femoral) morpho-structural characteristics (e.g., atherosclerotic plaques presence, diameters, and intima-media thickness) has been proposed as a valuable strategy to assess vascular health status and to improve risk stratification and/or disease diagnose in asymptomatic and healthy subjects. Data from US-derived vascular evaluation has also contributed to enhancing cardiovascular physiology and disease knowledge (e.g., expected vascular changes in relation to growth and aging; Naghavi et al., 2006; Sosnowski et al., 2007; Laclaustra et al., 2016; Marin et al., 2020). Structural assessment can be complemented by Doppler US evaluation, which allows quantifying blood flow velocity (BFV) levels and indexes that give data about micro- and macro-vascular status, and have shown to vary in association with physiological and pathological states (Hwang, 2017).

Using software integrated into conventional US devices, different BFV parameters can be evaluated: (i) BFV levels [e.g., peak systolic (PSV), end-diastolic velocity (EDV)], (ii) "intra-beat" indexes [e.g., resistive (RI), pulsate (PI)], and (iii) "inter-segment" velocity ratios. These complementary parameters are clinically important to assess the functional status of the macro and microvascular systems. As an example, low common carotid artery (CCA) PSV, and EDV are independently associated with cardiovascular disease (CVD) and events (e.g., stroke, heart disease) (Chuang et al., 2011, 2016); high internal carotid artery (ICA) PSV contributes to predict and grade ICA stenosis (Tokunaga et al., 2016); and low common femoral artery (CFA) PSV is predictive of ipsilateral iliac occlusion (Shaalan et al., 2003). On the other hand, CCA PI, and RI are associated with the prevalence of cerebral atherosclerosis and cardiovascular

events (e.g., ischemic stroke) (Hitsumoto, 2019), ICA PI is associated with the global burden of small vessels disease (Lau et al., 2018), and CFA PI contributes to detecting peripheral vascular disease (Clifford et al., 1981). In turn, ICA/CCA velocity ratios contribute to detect and define arterial stenosis (Kochanowicz et al., 2009).

Classically US-derived BFV indexes have been used in adults in whom the presence of an arterial alteration is suspected. In this context, single fixed cut-off points (without discriminating by age, hemibody, and/or sex) have been considered, mainly aiming at defining the significance (degree) of a stenosis (e.g., ICA PSV $\geq$125 cm/s or ICA PSV/CCA PSV $\geq$2 indicate arterial stenosis <50%) (Oates et al., 2009; Hodgkiss-Harlow and Bandyk, 2013; Freire et al., 2015; Santos et al., 2019). However, changes in BFV indexes could be found long before cut-off values (e.g., indicating significant stenosis) are reached. Indeed, early alterations in microvascular and macrovascular structures or functions (e.g., mimicking the effects of aging) can appear at any stage of life (even in childhood), reflecting a dissociation between chronologic and biologic vascular age and indicating a relative increase in cardiovascular risk (CVR) (Jani and Rajkumar, 2006; Bruno et al., 2020). Consequently, accurate use of BFV parameters in both clinical and cardiovascular research requires knowing the expected (physiological) age-related profiles and the predicted value for a specific subject. However, to our knowledge, there are no studies that have characterized BFV profiles in large populations: (i) considering several complementary indexes, (ii) analyzing data from different arteries, and taking into account potential (iii) differences between left and right hemibodies and/or (iv) sex-related differences, considering "age × sex" interaction (moderation). What is more important, in our understanding, is that no works are assessing BFV variations (as a continuous) considering data from different age stages and their transitions (childhood–adolescence–adulthood). It is to note that studies that aimed at analyzing age-related differences did not allow for their adequate and comprehensive characterization because of the following reasons: (i) considered small numbers of subjects [e.g., $n = 50$ (Seidel et al., 1999; Kuhl et al., 2000), $n = 78$ (Scheel et al., 2000), $n = 92$ (Zbornikova and Lassvik, 1986)], (ii) did not exclude subjects with vascular disease and/or exposed to factors known to impact on the vascular system (Kochanowicz et al., 2009), and/or (iii) compared "mean values" of defined groups considering wide age ranges [e.g., 10 (Zbornikova and Lassvik, 1986)], 20 (Scheel et al., 2000; Albayrak et al., 2007;

Abbreviations: ABI, ankle brachial index; BA, brachial artery; bDBP, brachial diastolic blood pressure; BFV, blood flow velocity; BH, body height; bMBP, brachial mean blood pressure; BMI, body mass index; BP, blood pressure; bPP, brachial pulse pressure; bSBP, brachial systolic blood pressure; BW, body weight; CCA, common carotid artery; CCC, concordance correlation coefficient; CFA, common femoral artery; CRFs, cardiovascular riskfactors; CVD, cardiovascular disease; CVR, cardiovascular risk; ECA, external carotid artery; EDV, end-diastolic blood flow velocity; ICA, internal carotid artery; MV, mean value; PI, pulsate index; PRV, peak reversal velocity; PSV, peak systolic blood flow velocity; PSVR, peak systolic velocity ratio; RI, resistive index; RIs, reference intervals; SD, standard deviation; SDI, systo-diastolic index; SMR, St Mary's ratio; taDBP, tibial artery diastolic blood pressure; taSBP, tibial artery systolic blood pressure; US, ultrasound or ultrasonographic; VA, vertebral artery; Vm, mean blood flowvelocity.

Nemati et al., 2009), or 30 (Yazici et al., 2005) years (difference in age of subjects in the same group).

Currently, it is unknown whether BFV parameters (i) provide equivalent data when obtained from left or right hemibodies and (ii) levels depend on the age and/or sex of the subjects. Furthermore, there is little information regarding physiological profiles and reference intervals (RIs) for BFV parameters obtained in a large healthy population including children, adolescents, and adults. The aims of this study were the following: (i) to evaluate the agreement between BFV parameters obtained from both hemibodies, (ii) to determine the need for age and/or sex-specific RIs, (iii) to define age-related physiological profiles and RIs for BFV parameters obtained from the assessment of CCA, ICA, external carotid artery (ECA), vertebral artery (VA), CFA, and brachial artery (BA) in a cohort of healthy children, adolescents, and adults.

MATERIALS AND METHODS

Study Population
The work was carried out in the context of the Centro Universitario de Investigación, Innovación y Diagnóstico Arterial (CUiiDARTE) project (Bia et al., 2011; Santana et al., 2012a,b; Zócalo et al., 2017; Bia and Zócalo, 2021; Zócalo and Bia, 2021), a population-based work developed in Uruguay. In this study, we considered data from 3,619 subjects included in the CUiiDARTE Database. This contains data on demographic and anthropometric variables, exposure to cardiovascular risk factors (CRFs), personal and family history of CVD, and data on hemodynamic, structural, and functional vascular parameters (Bia et al., 2011; Santana et al., 2012a,b; Zócalo and Bia, 2016, 2021; Zócalo et al., 2017; Castro et al., 2019; Bia and Zócalo, 2021). All procedures agree with the Declaration of Helsinki (1975 and reviewed in 1983). The work protocol was reviewed and approved by the Ethics Committee of Centro Hospitalario Pereira Rossell, Universidad de la República. The participants provided their written informed consent to participate in this study. In adults, written informed consent was obtained prior to the evaluation. In subjects <18 years, written consent of the parents and assent of the children were obtained before the work. Subjects or parents (in case of subjects aged <18 years) provided informed written consent to have data from their medical records used in research.

Anthropometric and Clinical Evaluation
A brief clinical and anthropometric evaluation enabled us to assess CRFs. A family history of CVD was defined by the presence of first-degree (all the subjects) and/or (for subjects ≤18 years) second-degree relatives with early (< 55 years in men; < 65 years in women) CVD. Body weight (BW) and height (BH) were measured with the subject wearing light clothing and no shoes. Standing BH was measured using a portable stadiometer and recorded to the nearest 0.1 cm. BW was measured with an electronic scale (841/843, Seca Inc., Hamburg, Germany; model HBF-514C, Omron Inc., Chicago, Illinois, USA) and recorded to the nearest 0.1 kg. Body mass index (BMI) was calculated as BW-to-squared BH ratio. In children and adolescents, BMI z-scores

(z-BMI) were calculated using software of WHO (Anthro-v.3.2.2; Anthro-Plus-v.1.0.4) (Castro et al., 2019).

Cardiovascular Evaluation
Participants were asked to avoid exercise, tobacco, alcohol, caffeine, and food-intake 4 h before the evaluation. All records were performed in a temperature-controlled room (21–23°C), with the subject in the supine position and after resting for at least 10–15 min, which enabled reaching steady hemodynamic states. Using an oscillometric device (HEM-433INT; Omron Healthcare Inc., Lake Forest, Illinois, USA), heart rate and brachial systolic and diastolic blood pressure (bSBP, bDBP) were recorded simultaneously and/or immediately before or after each US record. Then, brachial pulse pressure (bPP = bSBP–bDBP) and mean pressure (bMBP = bDBP+bPP/3) were obtained.

Cardiovascular evaluation in CUiiDARTE includes assessing the following: (i) peripheral (brachial, radial, and ankle) and central (aortic and carotid) blood pressure (BP) levels, central (aortic and carotid) pulse wave analysis and wave separation analysis-derived parameters (e.g., augmentation index, forward and backward pressure components); (ii) CCA, CFA, and BA beat-to-beat diameter waves and intima-media thickness; (iii) BA reactivity (e.g., flow-mediated dilation and low flow-mediated constriction); (iv) carotid, CA, CFA, and BA Doppler-derived BFV profiles and indexes; (v) ankle–brachial index (ABI); (vi) screening for carotid and femoral atherosclerotic plaques; (vii) CCA, CFA, and BA local stiffness (e.g., elastic modulus); (viii) systemic hemodynamic evaluation (e.g., vascular resistances, cardiac output, and index quantified from BA pulse contour analysis and/or cardiography impedance); (ix) regional stiffness (carotid–femoral and carotid–radial pulse wave velocity). In this study, we focused on US/Doppler-derived BFV data.

Carotid, Vertebral, Femoral, and Brachial Artery US
Morpho-Structural Parameters and Ankle-Brachial Index
Left and right CCA, ICA, ECA, VA, CFA, and left BA were examined (B-Mode and Doppler US, 7–13 MHz, linear transducer, M-Turbo, SonoSite Inc., Bothell, WA, USA) (Zócalo and Bia, 2016). Transverse and longitudinal arterial views were obtained to assess the presence of atherosclerotic plaques. Near and far walls were analyzed. Images were obtained from anterior, lateral, and posterior angles. An atherosclerotic plaque was defined as the following (i) focal wall thickening at least 50% greater than the adjacent segment (ii) focal thickening protruding into the lumen at least 0.5 mm, (iii) or an intima-media thickness ≥1.5 mm (Zbornikova and Lassvik, 1986; Marin et al., 2020).

Left and right bSBP and bDBPas well as tibial artery systolic and diastolic pressures (taSBP, taDBP) were obtained (no fixed order) at 5 min intervals (Hem-4030, Omron Inc., Illinois, USA). At least five measurements were obtained from each recording site. Then, ABI, a marker of arterial permeability and central-peripheral BP amplification, was calculated (Zócalo and Bia, 2016):

$$\text{ABI} = \frac{taSBP}{baSBP} \quad (1)$$

An ABI < 0.9 is conventionally used as a cut-off value to define the peripheral obstructive arterial disease and increased CVR. Right and left ABI values were used as screening to rule out arterial stenosis of at least 50% distal to CFA (Zócalo and Bia, 2016). None of the subjects included in the RIs group had ABI values <0.9.

Hemodynamic or BFV-Related Parameters

Common carotid artery, ICA, ECA, VA, CFA, and BA BFVs and patterns were examined by experienced investigators (Doppler US/color flow mapping; 7–13 MHz linear array) (**Figure 1**). The scan head was moved until the US beam was aligned with the arterial axis so that appropriate longitudinal images were obtained (Gerhard-Herman et al., 2006; Zócalo and Bia, 2016). Measurements were obtained in the longitudinal views, considering arterial segments as long as possible, in which both anterior and posterior walls were visualized (Oates et al., 2009). The insonation angle was always between 30° and 60° (angles > 60° would result in overestimation of the velocity) (Oates et al., 2009). The above enabled to ensure reliable center-line velocity data. Studies lasted for 30–40 min.

Carotid and vertebral evaluations were done with head of the subject rotated away from the side being examined. The sample volume was placed 15–20 mm proximal or distal to CCA bifurcation, defined as the tip of the flow divider, to obtain (right and left) ICA, ECA, or CCA BFV waveforms (Oates et al., 2009). Sample volume was placed below or above the standard site of measurements (e.g., in the ICA) if higher flow acceleration was identified with an aliasing artifact. VA was identified between the transverse processes of the vertebrae at the level of CCA bifurcation (V2 segment) (Kuhl et al., 2000). CFA data were obtained from the proximal straight arterial portion at the groin. Since changes in the BFV profile can occur at the bifurcation, care was taken to avoid it during data recording. BA data were obtained from a straight segment of at least 1 cm (elbow level).

The forward PSV reached during a beat, velocity at the end of the diastolic phase, excluding the notch before the next systole, and mean velocity (Vm) levels were computed from drawing the BFV waveform envelope. Peak reversal diastolic velocity (PRV; reverse, backward or upstream flow toward central aorta) was also computed in the CFA (**Figure 1**). PSV can vary in association with physiological (e.g., physical activity) or pathological (e.g., stenosis, arterio-venous fistula) conditions. In turn, EDV is usually a faithful mirror of vascular conditions and needs of the downstream territory; its reduction reflects an increase in the distal vascular resistance.

"Intra-beat" indexes, RI, PI, and systo-diastolic index (SDI) (unitless and independent of possible inaccuracies in the estimation of spectral velocity due to arterial diameter or angle correction), were calculated (**Figure 1**; Oates et al., 2009; Oglat et al., 2018). These indexes provide information about blood flow and resistance that cannot be obtained from measurements of absolute velocity alone (Oates et al., 2009). RI (Pourcelot's index), which reflects global resistance or needs of the downstream territory was calculated as follows:

$$RI = \frac{(PSV - EDV)}{PSV} \tag{2}$$

Resistive index reaches its limit in high resistance territories with no end-diastolic blood flow (EDV = 0), and so RI = 1. PI (or Gosling's Index) can be calculated from the equation:

$$PI = \frac{(PSV - MinV)}{Vm} \tag{3}$$

The minimal (negative or positive) velocity is denoted as MinV. MinV could be the PRV (e.g., for CFA) or EDV (e.g., for CCA). Vm (or TAMaxV), the time average of maximum velocities, should not be confused with TAMeanV (time average of mean velocities), which corresponds to the mean of the mean velocity envelope curve of a beat and is frequently used for estimation of blood flow volume. PI also reflects the vascular resistance of the downstream territory, even between territories of high resistance. Thus, PI can demonstrate the differences of resistance in territories incompatible with RI (territories where RI = 1). RI or PI and the range of downstream territory perfusion are inversely related; when the resistance increases (RI and PI increase), perfusion would decrease (Oglat et al., 2018). Both indexes are partially determined by vascular stiffness (e.g., higher the stiffness, lesser the wall buffering function, and consequently, higher PI). SDI was quantified as follows:

$$SDI = \frac{PSV}{EDV} \tag{4}$$

Several potential sources of variability in ICA PSV have been described (e.g., variations in the geometry of the bifurcations or bulb size, presence of collateral flow effects including intracranial/ECA collateral flow, and variations in US device parameters) (Oates et al., 2009). The effects of the described factors on ICA BFV would be mitigated by the use of "inter-segment" velocity ratios or indexes. These would also moderate intermachine (US devices) differences. Two different ratios were calculated: (i) PSV ratio (PSVR) and (ii) St Mary's ratio (SMR):

$$PSVR = \frac{ICA\ PSV}{CCA\ PSV} \tag{5}$$

$$SMR = \frac{ICA\ PSV}{CCA\ EDV} \tag{6}$$

Note that SMR is the ratio between a value increasing with the degree of stenosis and a value that decreases with increasing ICA resistance due to progressive stenosis. **Table 1** shows indexes obtained from measurement and calculations.

Data Analysis

A step-wise analysis was performed. First, after descriptive statistics were computed and checked (**Tables 2**, **3**; **Supplementary Material 1**: **Tables S1**, **S2**), it was analyzed whether the studied variables showed (in our population) the expected tendency in terms of age-related variations (**Figure 2**).

Second, a subgroup of subjects ($n = 1,688$, 864 women) was defined to determine the RIs following European reference values for arterial measurements collaboration group criteria (Engelen et al., 2013, 2015; Bossuyt et al., 2015). This subgroup included subjects who did not have any of the following: (i) CVD; (ii)
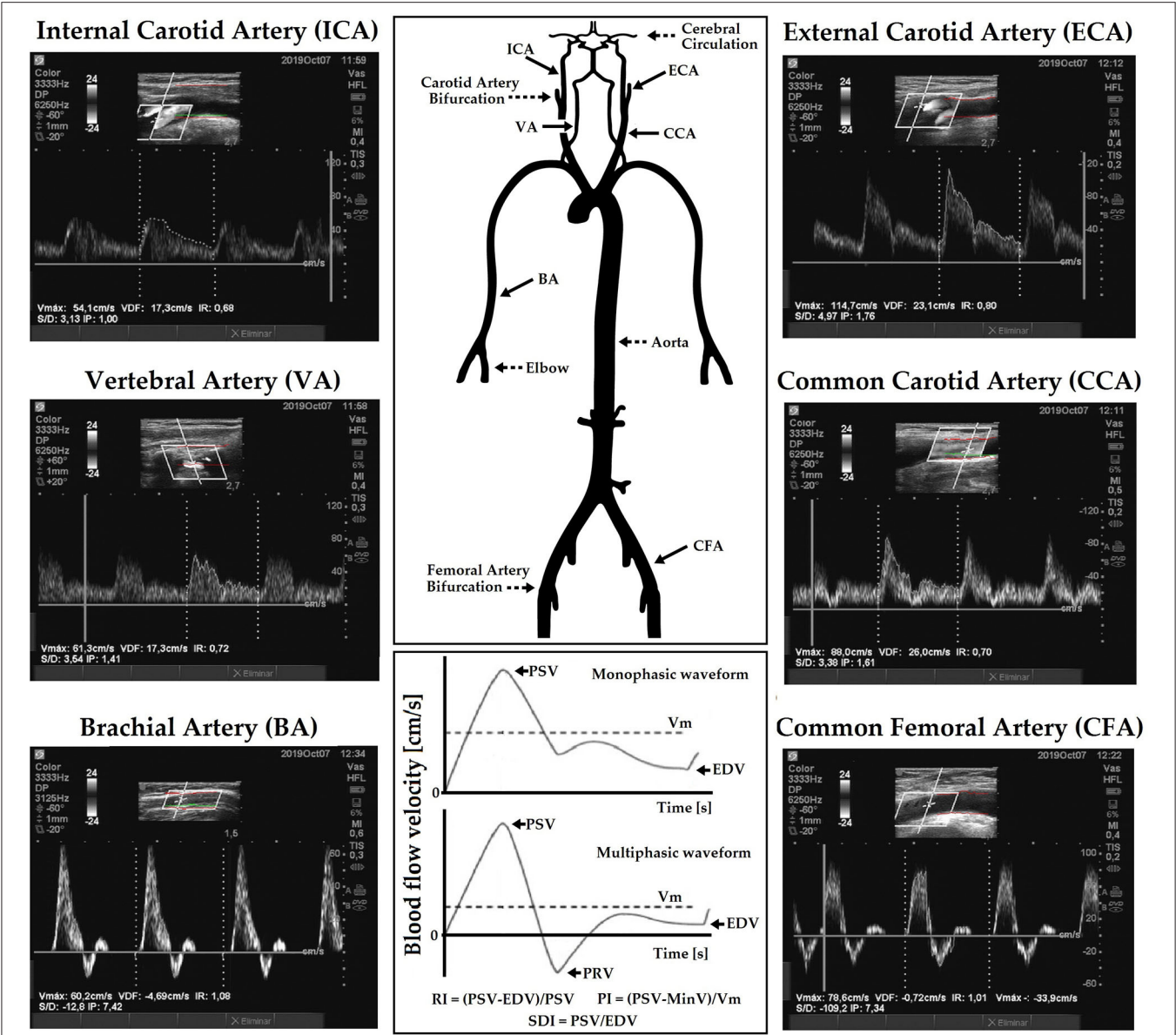
FIGURE 1 | Diagram showing arterial blood flow velocity (BFV) waves recordings and resistive (RI), pulsate (PI), and systo-diastolic index (SDI) calculus, for monophasic and multiphasic waves. Multiphasic waves cross the zero-flow baseline (0 cm/s) and contain both forward and reverse velocity components (e.g., common femoral artery, CFA; brachial artery, BA). Monophasic waves do not cross the zero-flow baseline (e.g., common carotid artery, CCA; Internal carotid artery, ICA) and reflect blood that flows in a single direction during the cardiac cycle. High-resistive waves have a sharp upstroke and a brisk downstroke and may be either multi (e.g., common femoral artery, CFA) or monophasic (e.g., external carotid artery, ECA). Low-resistive waves are monophasic, and contain a prolonged downstroke in the late systole with the continuous forward flow throughout diastole without an end-systolic notch (e.g., ICA). There is a "hybrid" waveform that is monophasic but has features of both high and low resistivity as it contains both brisk downstroke but also continuous forward flow throughout diastole (e.g., CCA).

TABLE 1 | Blood flow velocity (BFV) and related parameters.

Blood velocity parameters	Intra-segment velocity indexes	Inter-segment velocities ratios
Peak systolic velocity (PSV)	Resistive (RI) = PSV – EDV)/PSV	PSVR = ICA_{PSV}/CCA_{PSV}
End-diastolic velocity EDV	Pulsate (PI) = PSV – MinV)/Vm	SMR = ICA_{PSV}/CCA_{EDV}
Peak reversal velocity (PRV)	Systo-Diastolic (SDI) = PSV/EDV	–

PSVR, Peak Systolic Velocity Ratio; SMR, St Mary Ratio.

TABLE 2 | Demographic, anthropometric, and clinical characteristics of subjects.

Variable	All (n = 3,619; Age: 2.8–89.0 years)							Reference intervals group (n = 1,152; Age: 2.8–76.5 years)						
	MV	SD	Min	p25th	p50th	p75th	Max	MV	SD	Min	p25th	p50th	p75th	Max
Age (years)	33.9	24.2	2.8	11.6	24.0	56.5	89.0	17.3	13.5	2.8	6.2	15.1	20.5	76.5
BW (Kg)	61.2	25.3	12.3	45.6	63.2	78.1	150.6	46.1	22.4	12.3	22.1	50.5	64.0	105.0
BH (m)	1.5	0.2	0.9	1.5	1.6	1.7	2.0	1.5	0.3	0.9	1.2	1.6	1.7	1.9
BMI (Kg./m²)	24.1	6.0	11.5	19.7	23.7	27.8	71.3	20.0	4.1	11.5	16.5	19.5	23.1	30.0
z-BMI (SD)	0.9	1.5	−4.6	−0.1	0.7	1.8	8.0	0.3	0.9	−4.6	−0.3	0.4	1.0	2.0
TC (mg/dl)	200.2	44.3	94.3	170.0	196.0	227.0	379.0	192.2	26.0	99.0	174.0	194.5	212.0	238.0
HDL (mg/dl)	51.2	15.1	17.0	41.0	49.0	60.0	122.0	57.6	12.2	41.0	49.0	55.0	64.0	100.0
LDL (mg/dl)	123.4	39.8	28.0	95.0	119.0	146.0	323.0	114.7	26.0	31.0	98.0	116.0	132.0	180.0
TG (mg/dl)	133.2	86.0	24.0	80.0	111.0	158.5	783.0	95.8	42.3	24.0	62.0	86.0	120.0	272.0
Glicaemia (mg/dl)	94.4	18.7	40.0	85.0	92.0	100.0	307.0	86.9	9.1	40.0	83.0	87.0	92.0	114.0
bSBP (mmHg)	119.0	16.8	64.3	107.1	118.5	128.8	235.0	111.1	13.0	80.0	100.6	110.4	120.0	171.0
bDBP (mmHg)	68.9	10.4	41.3	60.8	67.7	75.8	129.2	64.1	7.9	46.7	58.6	62.8	69.0	97.4
TC ≥240 mg/dl (%)				7.2								0.0		
HDL <40 mg/dl (%)				8.9								0.0		
Glic ≥126 mg/dl (%)				0.9								0.0		
Current Smoke (%)				11.5								0.0		
Hypertension (%)				26.5								0.0		
Diabetes (%)				5.7								0.0		
History of CVD (%)				8.8								0.0		
Obesity (%)				21.9								0.0		
Familiar CVD (%)				13.5								6.4		
Sedentarism (%)				45.6								31.2		
Anti-HT (%)				21.8								0.0		
Anti-Hyperlip. (%)				13.5								0.0		
Anti-Diabetic (%)				4.1								0.0		
Atheroma Plaq. (%)				22.2								0.0		
Right ABI	1.14	0.08	0.71	1.08	1.14	1.19	1.61	1.14	0.08	0.90	1.08	1.13	1.19	1.61
Left ABI	1.15	0.08	0.68	1.09	1.15	1.20	1.45	1.14	0.08	0.90	1.09	1.14	1.20	1.45

MV, mean value; SD, standard deviation; Min, minimal; Max, maximal; p25th, p50th, p75th, 25, 50 and 75 percentile; BW, BH, BMI, Body weight, height and mass index; bSBP, bDBP, brachial systolic and diastolic pressure; ABI, ankle-brachial index; CVD, cardiovascular disease; TC, total cholesterol; Familiar CVD, familiar history of premature CVD; Anti-HT, antihypertensive agents; anti-hyperlip, anti-hyperlipidemic agents; anti-diabetic, antidiabetic agents; TG, triglycerides; Glic, Glicaemia; Atheroma Plaq., atherosclerotic plaques.

TABLE 3 | BFV parameters and derived indexes.

Variable	All (n = 3,619; Age: 2.8–89.0 years)							Reference intervals group (n = 1,152; Age: 2.8–76.5 years)						
	MV	SD	Min	p25th	p50th	p75th	Max	MV	SD	Min	p25th	p50th	p75th	Max
Left common carotid artery														
PSV (cm/s)	101.2	28.7	36.9	79.9	98.8	120.4	238.0	114.1	25.5	55.8	96.6	111.9	129.4	223.6
EDV (cm/s)	26.5	7.5	5.1	21.3	25.9	31.2	62.7	29.4	7.2	5.1	24.4	28.8	33.3	62.7
RI	0.73	0.06	0.49	0.69	0.73	0.77	1.01	0.74	0.06	0.54	0.70	0.74	0.78	1.01
PI	1.85	0.51	0.22	1.51	1.77	2.11	6.68	1.91	0.51	0.22	1.59	1.82	2.16	6.68
SDI	3.93	1.08	1.85	3.24	3.74	4.43	23.02	4.02	1.16	2.15	3.37	3.82	4.45	23.02
Left internal carotid artery														
PSV (cm/s)	81.2	25.8	27.2	62.4	76.1	94.4	217.0	91.3	26.2	35.1	72.6	86.8	106.6	213.9
EDV (cm/s)	30.6	10.4	0.7	23.6	28.9	36.0	87.5	34.6	10.5	9.1	27.4	33.0	40.3	87.5
RI	0.62	0.07	0.37	0.57	0.62	0.67	0.97	0.62	0.07	0.37	0.57	0.61	0.67	0.88
PI	1.15	0.30	0.28	0.95	1.11	1.28	4.15	1.16	0.31	0.28	0.95	1.12	1.30	4.15
SDI	2.75	0.92	1.60	2.34	2.63	3.00	38.06	2.69	0.54	1.60	2.30	2.60	3.00	5.21
Left external carotid artery														
PSV (cm/s)	91.0	24.2	34.3	74.0	88.3	105.2	249.9	92.1	23.3	38.1	75.0	89.8	106.0	196.7
EDV (cm/s)	14.3	5.9	0.7	10.7	13.7	17.3	57.1	13.5	5.6	0.8	10.1	12.9	16.0	45.4
RI	0.84	0.06	0.60	0.80	0.84	0.88	1.00	0.85	0.06	0.60	0.81	0.85	0.89	1.00
PI	2.52	0.77	0.15	2.02	2.41	2.86	9.39	2.68	0.79	0.15	2.15	2.55	3.04	7.39
SDI	8.80	13.9	2.53	5.08	6.26	8.17	179.31	10.47	17.44	2.53	5.31	6.61	8.80	165.30
Left ICA/CCA velocity ratios														
PSVR	0.83	0.23	0.32	0.68	0.80	0.95	3.00	0.81	0.20	0.32	0.67	0.80	0.93	1.56
SMR	3.20	1.12	1.12	2.53	3.00	3.62	19.04	3.16	0.92	1.30	2.55	3.03	3.59	8.45
Left vertebral artery														
PSV (cm/s)	59.4	19.9	19.5	45.4	55.9	70.0	181.5	67.03	21.26	21.30	52.50	63.90	79.30	181.50
EDV (cm/s)	17.2	5.9	3.1	13.0	16.7	20.6	54.1	18.59	6.06	3.81	14.40	17.80	22.80	54.10
RI	0.7	0.1	0.4	0.7	0.7	0.8	1.0	0.71	0.08	0.47	0.66	0.72	0.77	1.01
PI	1.5	0.5	0.6	1.2	1.4	1.7	7.2	1.56	0.47	0.68	1.22	1.50	1.80	4.37
SDI	3.8	3.0	1.5	2.8	3.4	4.2	74.2	3.94	3.25	1.52	2.95	3.57	4.37	70.90
Right common carotid artery														
PSV (cm/s)	94.3	27.2	30.8	74.3	91.3	111.8	227.2	106.7	24.23	46.40	90.10	104.60	121.90	210.60
EDV (cm/s)	25.2	7.2	7.2	20.2	24.4	29.7	57.7	28.12	6.95	9.01	23.10	27.40	32.00	56.60
RI	0.7	0.1	0.5	0.7	0.7	0.8	0.9	0.73	0.06	0.52	0.70	0.73	0.77	0.89
PI	1.8	0.5	0.4	1.5	1.8	2.1	4.6	1.92	0.50	0.78	1.58	1.84	2.16	4.61
SDI	3.8	1.0	1.2	3.2	3.7	4.3	10.0	3.90	0.92	1.82	3.28	3.69	4.34	9.51
Right internal carotid artery														
PSV (cm/s)	78.2	24.1	24.0	62.4	73.6	88.3	209.3	86.33	24.56	33.20	69.20	82.20	98.60	207.90

(Continued)

TABLE 3 | Continued

Variable	All (n = 3,619; Age: 2.8–89.0 years)							Reference intervals group (n = 1,152; Age: 2.8–76.5 years)						
	MV	SD	Min	p25th	p50th	p75th	Max	MV	SD	Min	p25th	p50th	p75th	Max
EDV (cm/s)	29.3	9.4	1.8	22.8	27.9	34.3	80.5	32.78	9.39	10.70	26.00	31.20	38.10	80.50
RI	0.6	0.1	0.4	0.6	0.6	0.7	0.9	0.61	0.07	0.38	0.57	0.62	0.66	0.88
PI	1.3	4.1	0.4	1.0	1.1	1.3	184.0	1.15	0.27	0.47	0.95	1.11	1.29	2.48
SDI	2.7	0.6	1.6	2.4	2.6	3.0	12.5	2.67	0.49	1.61	2.33	2.60	2.96	5.29
Right external carotid artery														
PSV (cm/s)	91.2	25.2	32.8	73.1	88.3	106.0	220.8	92.15	25.05	36.50	73.10	89.95	107.50	195.60
EDV (cm/s)	14.0	5.8	0.1	10.7	13.2	16.7	48.2	12.96	5.49	0.72	9.90	12.65	15.90	40.60
RI	0.8	0.1	0.6	0.8	0.9	0.9	1.0	0.86	0.06	0.66	0.82	0.86	0.89	1.02
PI	2.6	0.8	0.3	2.1	2.5	3.0	8.1	2.83	0.82	0.25	2.28	2.73	3.23	6.45
SDI	9.7	27.9	2.4	5.2	6.5	8.4	1157.0	11.53	19.16	2.91	5.51	6.91	9.00	152.20
Right ICA/CCA velocity ratios														
PSVR	0.87	0.24	0.31	0.72	0.84	0.98	3.46	0.82	0.20	0.33	0.69	0.81	0.93	1.74
SMR	3.28	1.12	1.00	2.58	3.06	3.68	14.23	3.13	0.84	1.19	2.56	3.00	3.56	7.34
Right vertebral artery														
PSV (cm/s)	53.5	20.6	22.4	41.8	49.8	61.7	487.0	58.28	17.08	22.70	45.40	56.30	67.20	139.40
EDV (cm/s)	15.2	5.3	3.6	11.5	14.8	18.3	38.1	16.17	5.42	3.61	12.30	15.20	19.00	38.10
RI	0.7	0.1	0.4	0.7	0.7	0.8	1.0	0.72	0.09	0.47	0.66	0.72	0.77	1.01
PI	1.5	0.6	0.5	1.2	1.4	1.8	10.0	1.59	0.50	0.69	1.22	1.52	1.84	3.86
SDI	3.8	2.4	1.8	2.9	3.4	4.2	51.1	3.83	1.26	1.76	2.90	3.55	4.43	9.22
Left common femoral artery														
PSV (cm/s)	114.5	31.5	39.6	91.3	111.6	134.5	278.5	120.6	30.7	41.1	99.5	118.2	139.4	278.5
PRV (cm/s)	−29.7	12.7	−77.4	−37.3	−30.0	−22.8	40.9	−28.4	14.3	−77.4	−37.3	−28.8	−20.9	38.1
RI	1.0	0.1	0.7	0.9	1.0	1.0	1.6	0.98	0.07	0.73	0.92	1.01	1.01	1.27
PI	7.6	9.7	1.7	4.5	6.2	8.3	206.2	6.59	6.48	1.71	4.00	5.58	7.38	122.20
SDI	78.5	55.0	−10.7	11.1	97.9	122.2	198.3	69.73	58.17	−10.7	10.00	89.05	122.20	192.30
Right common femoral artery														
PSV (cm/s)	114.4	31.1	34.3	91.3	110.4	134.5	236.0	120.6	29.91	44.00	99.70	117.70	138.90	224.60
PRV (cm/s)	−30.8	12.6	−80.0	−38.1	−31.0	−24.1	38.5	−30.55	14.38	−80.0	−38.9	−31.30	−23.10	33.00
RI	1.0	0.1	0.2	1.0	1.0	1.0	2.6	0.98	0.10	0.24	0.92	1.01	1.01	2.58
PI	8.0	7.8	1.2	4.7	6.3	8.7	101.1	7.17	6.86	1.89	4.23	5.66	7.71	83.90
SDI	82.5	52.9	−7.5	11.6	99.9	122.2	209.9	75.70	55.78	−7.48	10.50	95.90	123.90	192.20
Left brachial artery														
PSV (cm/s)	74.3	22.8	27.8	57.3	70.9	86.8	191.1	83.9	25.2	27.8	67.0	82.2	98.1	191.1
EDV (cm/s)	3.4	8.9	−48.1	0.0	0.0	9.4	52.6	3.6	10.9	−48.1	0.0	1.3	10.8	33.0
RI	1.0	0.1	0.6	0.9	1.0	1.0	1.4	0.94	0.10	0.56	0.88	0.98	1.00	1.41

MV, mean value; SD, standard deviation; Min., minimum; Max, maximum; p25th, p50th, p75th, 25, 50 and 75 percentiles; PSV, peak systolic velocity; PRV, peak reversal velocity; EDV, end-diastolic velocity; RI, PI, SDI, resistive, pulsate and systo-diastolic index; PSVR, PSV ratio; SMR, St' Mary ratio; ICA, internal carotid artery; CCA, common carotid artery.
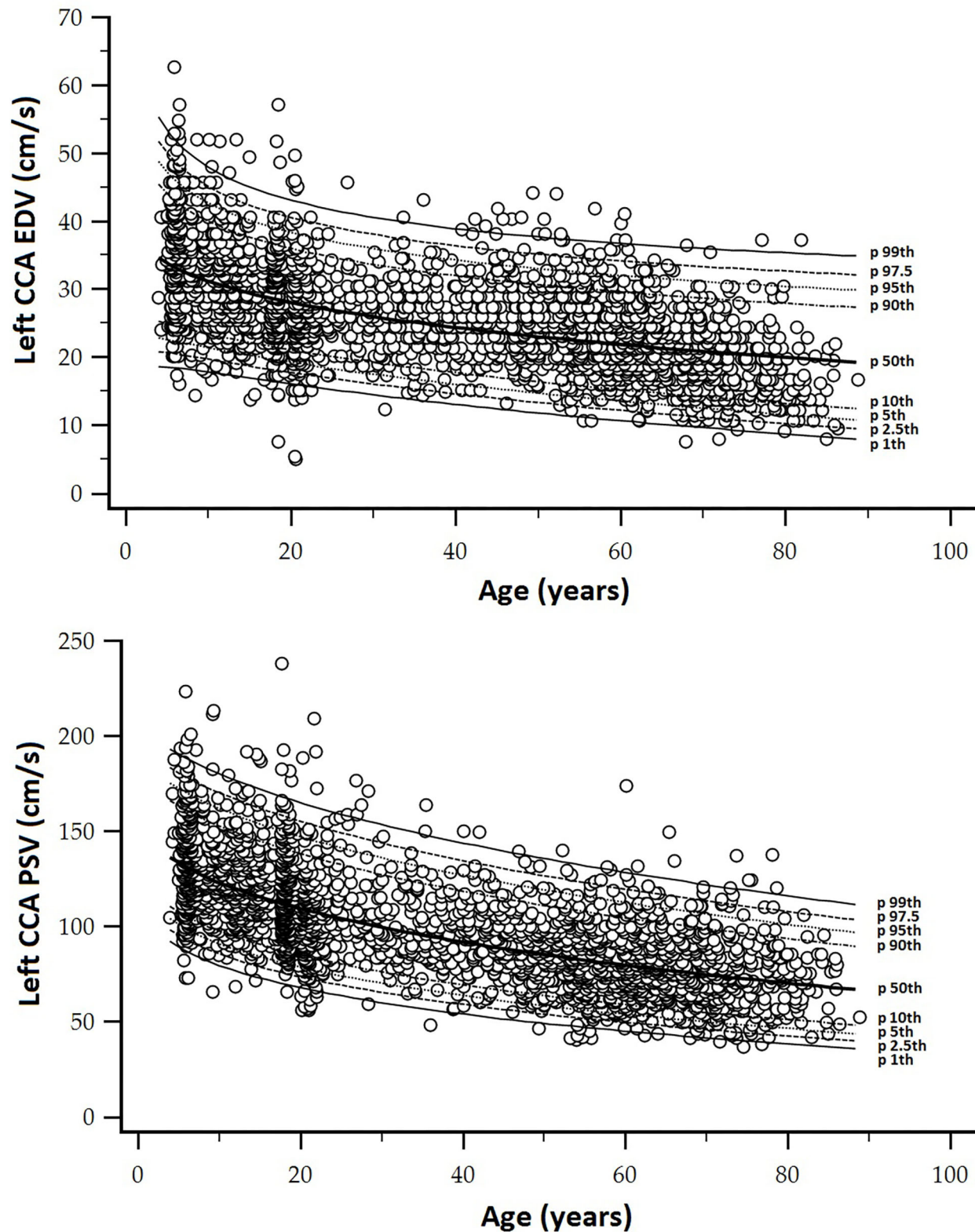
FIGURE 2 | (A) Top: Age-related profiles (1st, 2.5th, 5th, 10th, 50th, 90th, 95th, 97.5th, and 99th percentiles) for left CCA end-diastolic velocity (EDV). **(B)** Bottom: Age-related profiles (1st, 2.5th, 5th, 10th, 50th, 90th, 95th, 97.5th, and 99th percentiles) for left CCA peak systolic velocity (PSV).

use of BP-, lipid- and/or glucose-lowering drugs; (iii) arterial hypertension ($\geq$18 years: bSBP $\geq$ 140 and/or bDBP $\geq$ 90 mmHg; < 18 years: bSBP and bDBP < 95th percentile for sex, age, and BH); (iv) smoking; (v) diabetes (self-reported or fasting plasma glucose $\geq$126 mg/dl); (vi) dyslipidemia (self-reported or total cholesterol $\geq$240 mg/dl or HDL <40 mg/dl); (vii) obesity ($\geq$18 years: BMI $\geq$30 kg/m^2; <18 years: z-BMI $\geq$2.0). None of them had congenital, chronic, or infectious diseases, or heart rhythm other than sinus rhythm. In this subgroup, we analyzed the association of the presence of carotid and femoral atherosclerotic plaques with BFV indexes (partial correlations; age-adjusted) (**Supplementary Material 1: Tables S3, S4**). Results showed that the presence of plaques was associated with BFV levels. Then, subjects with plaques were excluded from the RIs subgroup (now called, BFV RIs subgroup; $n = 1,152$, women: 582) (**Tables 2, 3**; **Supplementary Material 1**: **Tables S1, S2**).

Third, aiming at determining if RIs for a similar BFV index from left and right body sides were necessary, we analyzed the degree of agreement between them by assessing the following (i) concordance correlation coefficients (CCC) and (ii) mean and proportional differences between data (Bland–Altman analysis) (**Supplementary Material 1: Tables S5–S10**). **Figure 3** exemplifies results obtained when comparing left and right CCA PSV and EDV. As a result, specific RIs for left and right CCA PSV and EDV, ICA PSV, and VA PSV and EDV were defined as necessary (**Supplementary Material 1: Table S11**). Some indexes (e.g., CCA RI) showed significant statistical differences between sides but were not clinically relevant for RIs construction (e.g., differences <1%).

Fourth, we evaluated whether age and/or sex-specific RIs were necessary using multiple linear regression models that included interaction analysis (Sex $\times$ Age) with Johnson–Neyman significance regions definition (**Supplementary Material 1: Tables S12–S18**). Variables "y," "x," and "w" (moderating variable) were assigned, respectively, to the BFV indexes, sex, and age. We identified the following indexes that (i) required sex-specific RIs only from a certain age, (ii) required sex-specific RIs regardless of age, (iii) did not require sex-specific RIs, (iv) did not require age and sex-specific RIs (**Supplementary Material 1: Table S11**). Even in the cases in which a difference was found between the left and right side, and/or by sex, the RIs were also expressed for hemibodies average, as well as for the entire RIs group (both sexes).

Finally, as a fifth step, age-related percentile curves and RIs were obtained. Age-related equations were obtained for mean values (MV) and SD. To this end, we implemented parametric regression methods based on fractional polynomials (FPs) (Royston and Wright, 1998), included in the European Reference Values for Arterial Measurements Collaboration Group methodological strategy and already used by our group (Diaz et al., 2018; Díaz et al., 2019, 2020; Zócalo et al., 2020; Bia and Zócalo, 2021). Briefly, fitting FPs age-specific MV and SD regression curves for the different variables (e.g., CCA EDV) were defined using an iterative procedure (generalized least squares). Then, age-specific equations were obtained for the different parameters. For instance, the CCA EDV MV equation would be "CCA EDV MV = a + b $\times$ Age^p + c $\times$ Age^q+...,"

where a, b, c, are the coefficients, and p, q, are the powers, with numbers selected from the set [-2, -1, -0.5, 0, 0.5, 1, 2, 3] estimated from the regression for mean CCA EDV curve, and similarly, from the regression for SD curve. FPs with powers [1,2], that is, with p = 1 and q = 2, illustrate an equation with the form a+b$\times$Age+c$\times$Age^2 (Royston and Wright, 1998). Residuals were used to assess the model fit, which was deemed appropriate if the scores were normally distributed, with a mean of 0 and an SD of 1, randomly scattered above and below 0 when plotted against age. Best fitted curves, considering visual and mathematical criteria (Kurtosis and Skewness coefficients) were selected. Using the equations obtained for MV and SD (**Supplementary Material 1: Table S19**), age-specific percentiles were defined using the standard normal distribution (Z). The 1st, 2.5th, 5th, 10th, 25th, 50th, 75th, 90th, 95th, 97.5th, and 99th percentiles were calculated, for example for CCA EDV: mean CCA EDV+Zp$\times$SD, where Zp assumed the values -2.3263, -1.9599, -1.6448, -1.2815, -0.6755, 0, 0.6755, 1.2815, 1.6448, 1.9599, and 2.3263, respectively. Year-by-year RIs data can be found in **Supplementary Material 1: Tables S20–S105**. **Figures 4, 5** illustrate percentile curves obtained for VA, CFA, BA, CCA, ICA, ECA, PSVR, and SMR. **Supplementary Material 2** (**Figures S1–S33**) shows BFV indexes age-related percentile curves (for all, women and men, and for left and right side, when appropriate).

The obtained percentiles were compared with data from other works, and the fixed cut-off values recommended to identify arterial stenosis > 50% (**Figures 7–12**) are as follows : (i) CCA PSV < 150 or < 182 cm/s (Freire et al., 2015), (ii) ICA PSV < 125 or < 140 cm/s (Oates et al., 2009; Freire et al., 2015), (iii) ICA EDV < 40 cm/s (Freire et al., 2015), (iv) ECA PSV < 150 cm/s (Freire et al., 2015), (v) VA PSV < 85 cm/s (Santos et al., 2019), (vi) VA EDV < 27 cm/s (Santos et al., 2019), PSVR < 2.0 (Oates et al., 2009), SMR < 8.0 (Oates et al., 2009), and CFA PI > 4 (Hodgkiss-Harlow and Bandyk, 2013).

The minimum sample size required was 377 (Bellera and Hanley, 2007). Like in previous works and according to the central limit theorem, normal distribution was considered (taking into account Kurtosis and Skewness coefficients distribution and sample size <30) (Lumley et al., 2002). Data analysis was done using MedCalc-Statistical Software (version 18.5, MedCalc Inc., Ostend, Belgium) and IBM-SPSS software (version 26, SPSS Inc., IL, USA). PROCESS version 3.5 (SPSS extension) was used for moderation (interaction) analysis (Hayes, 2020). A p < 0.05 was considered statistically significant.
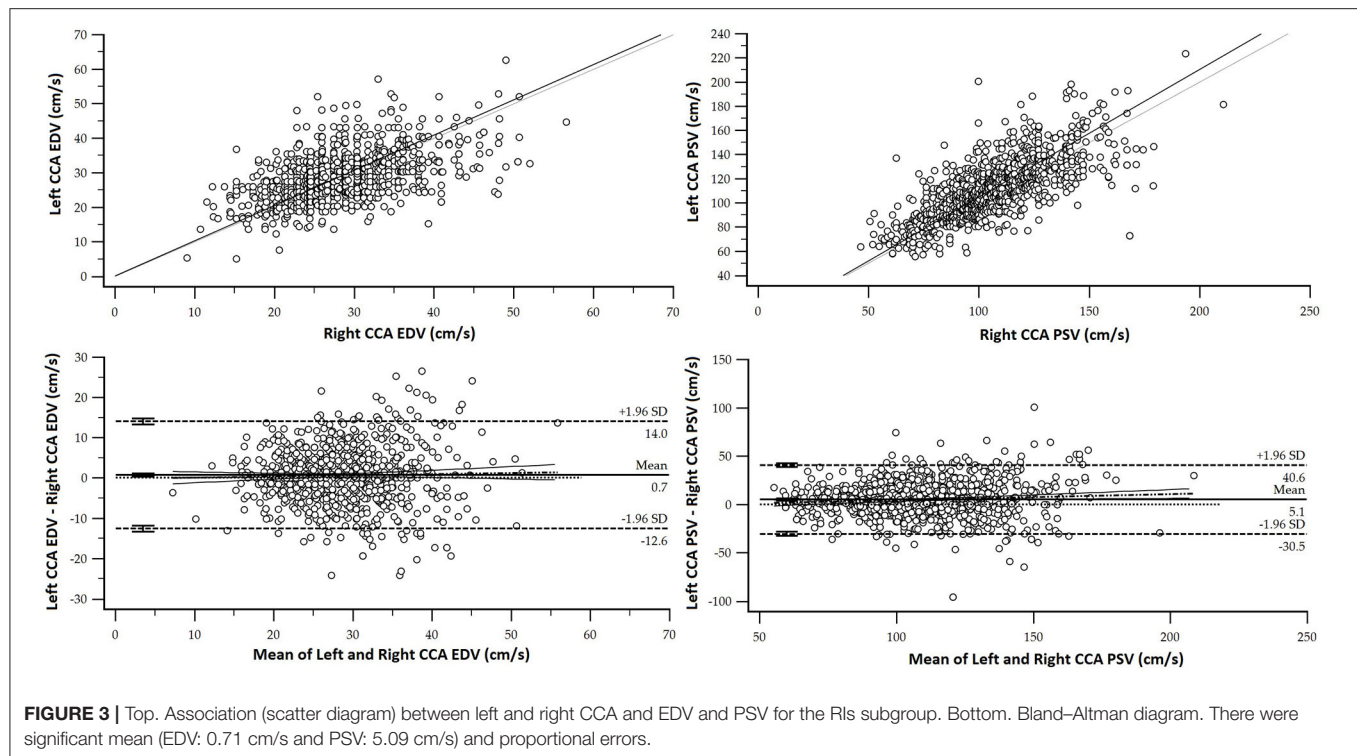
RESULTS

BFV and Atherosclerotic Plaques Presence in Asymptomatic Subjects

Several BFV levels, ratios, and indexes were associated with atherosclerotic plaque presence (**Supplementary Material 1: Tables S3, S4**).

Peak systolic velocity of BA and PRV of CFA were associated with atherosclerotic plaque presence in any of the studied segments (**Supplementary Material 1: Table S3**).

FIGURE 3 | Top. Association (scatter diagram) between left and right CCA and EDV and PSV for the RIs subgroup. Bottom. Bland–Altman diagram. There were significant mean (EDV: 0.71 cm/s and PSV: 5.09 cm/s) and proportional errors.

Right and left ICA PSV and EDV were positively associated with plaque presence in the evaluated segment and in CCA. In turn, ICA RI was associated with the existence of plaques in ICA and ECA. The associations described for ICA were not observed in CCA (**Supplementary Material 1: Table S4**). Then, the hemodynamic impact of atherosclerotic plaques presence would be greater in the former.

On the other hand, ICA/CCA ratios were associated with plaque presence in different arterial segments. The finding of atherosclerotic plaques in any segment, as well as in CCA, was associated with VA PSV level (irrespective of age), indicating that plaques in the carotid system may be associated with increased velocities in the vertebro-basilar territory (**Supplementary Material 1: Table S4**).

BFV and Hemibody and/or Sex-Related Differences

For some BFV indexes, data from the right and left sides were not equivalent (CCC and Bland-Altman tests) (**Supplementary Material 1: Tables S5–S11**). However, despite the statistical significance, in general the differences would not be clinically significant. In this regard, the statistically significant differences were (mean error) as follows: (i) 5.1 and 0.7 cm/s for CCA PSV and EDV, (ii) 1.5 cm/s for ICA PSV, (iii) 0.5 cm/s for ECA EDV, and (iv) 4.89 and 1.76 cm/s for VA PSV and EDV (the highest values were always obtained from left hemibody) (**Supplementary Material 1: Tables S5–S11**).

On the contrary, there were no statistical differences between RI, PI, and SDI data from left and right hemibodies, or they were not clinically significant (e.g., 0.005 for CCA RI). Then, in addition to hemibody-specific RIs, we

opted for defining RIs for left- and right-averaged data (**Supplementary Material 1: Table S11**).

We identified the following indexes that: (i) did not require sex-specific RIs (e.g. CCA EDV), (ii) did not require age and sex-specific RIs (e.g., BA EDV), (iii) require sex-specific RIs regardless of age (e.g., CCA PSV), and (iv) require sex-specific RIs only from a certain age (e.g., ICA EDV) (**Supplementary Material 1: Table S11**). It is to note, that compared to men, women showed the following: (i) lower CCA PSV or ECA EDV levels for almost all ages; (ii) lower CCA RI, PI and SDI, although values tend to be similar at 5–7 and over <70 years, (iii) lower ICA, PSV and PI, mainly in children, adolescents and young adults, (iv) higher PSVR, although at lower and higher ages the levels tend to be similar for both sexes, (v) similar CFA PSV values at low ages and then levels that exceeded those of men increasingly with age (**Supplementary Material 1: Tables S12–S18**).

Age-, Body Side- and Sex-Related RIs

Data for year-by-year RIs can be seen in **Supplementary Material 1: Tables S20–S105**. The 1st, 2.5th, 5th, 10th, 25th, 50th, 75th, 90th, 95th, 97.5th, and 99th percentiles were calculated. Equations for sex, body side, and age-specific percentiles were included in text and spreadsheet formats. Age-related profiles (considering both sexes, p50th) for the different arterial segments and BFV indexes are shown in **Figure 6**. The comparison of this work data (p2.5th, p50th and p97.5th) and that obtained by other authors [p50th (MV), p2.5th (MV−1.96 × SD), and p97.5th (MV+1.96 × SD)] is shown in **Figures 7–12**.

When comparatively analyzing p2.5th, p50th, and p97.5th curves obtained in this work with fixed cut-off values
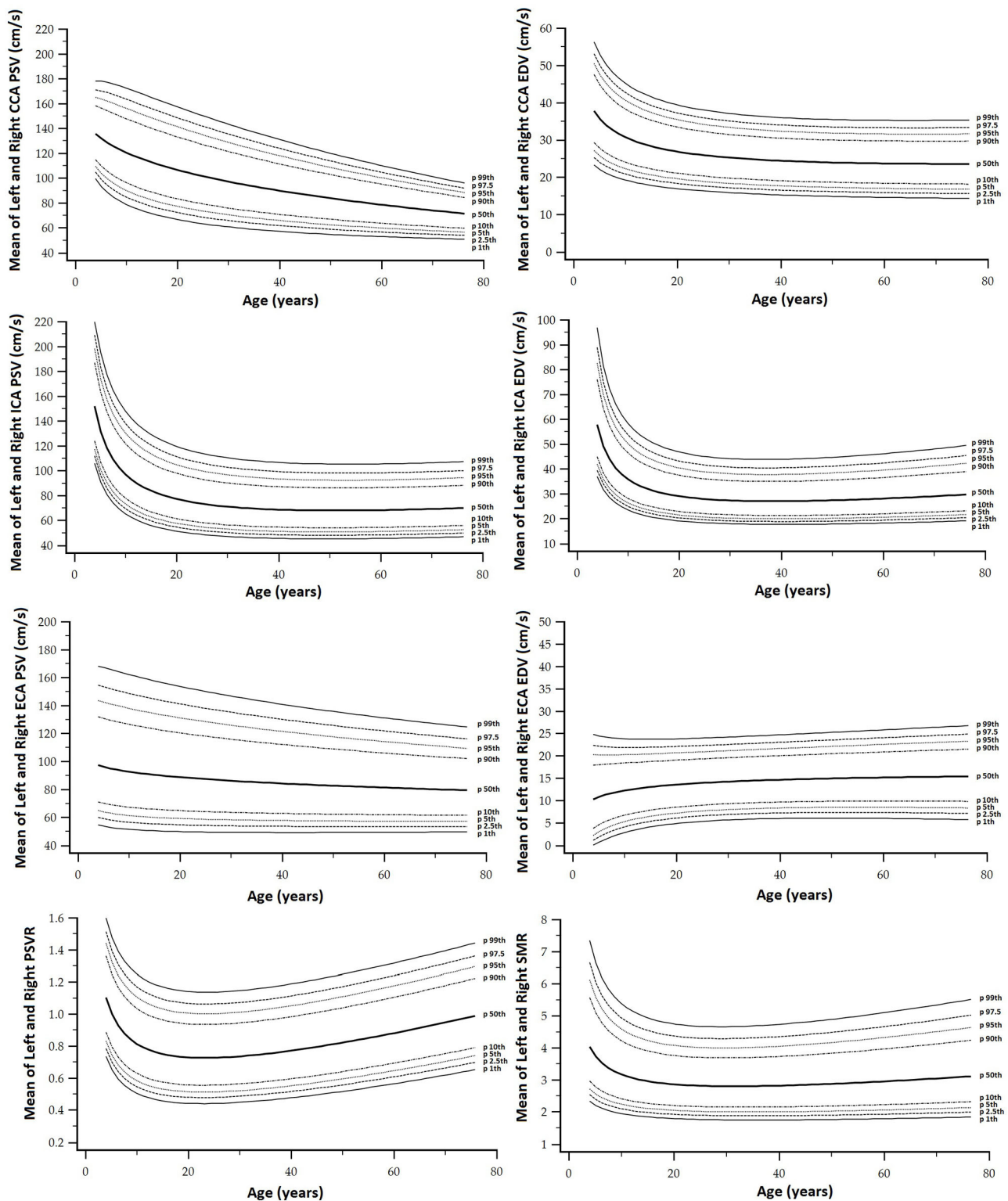
FIGURE 4 | Vertebral artery (VA), CFA, and BA PSV and EDV age-related percentile curves.

FIGURE 5 | CCA, ICA, and ECA and PSV ratio (PSVR), and St Mary ratio (SMR) age-related percentile curves.
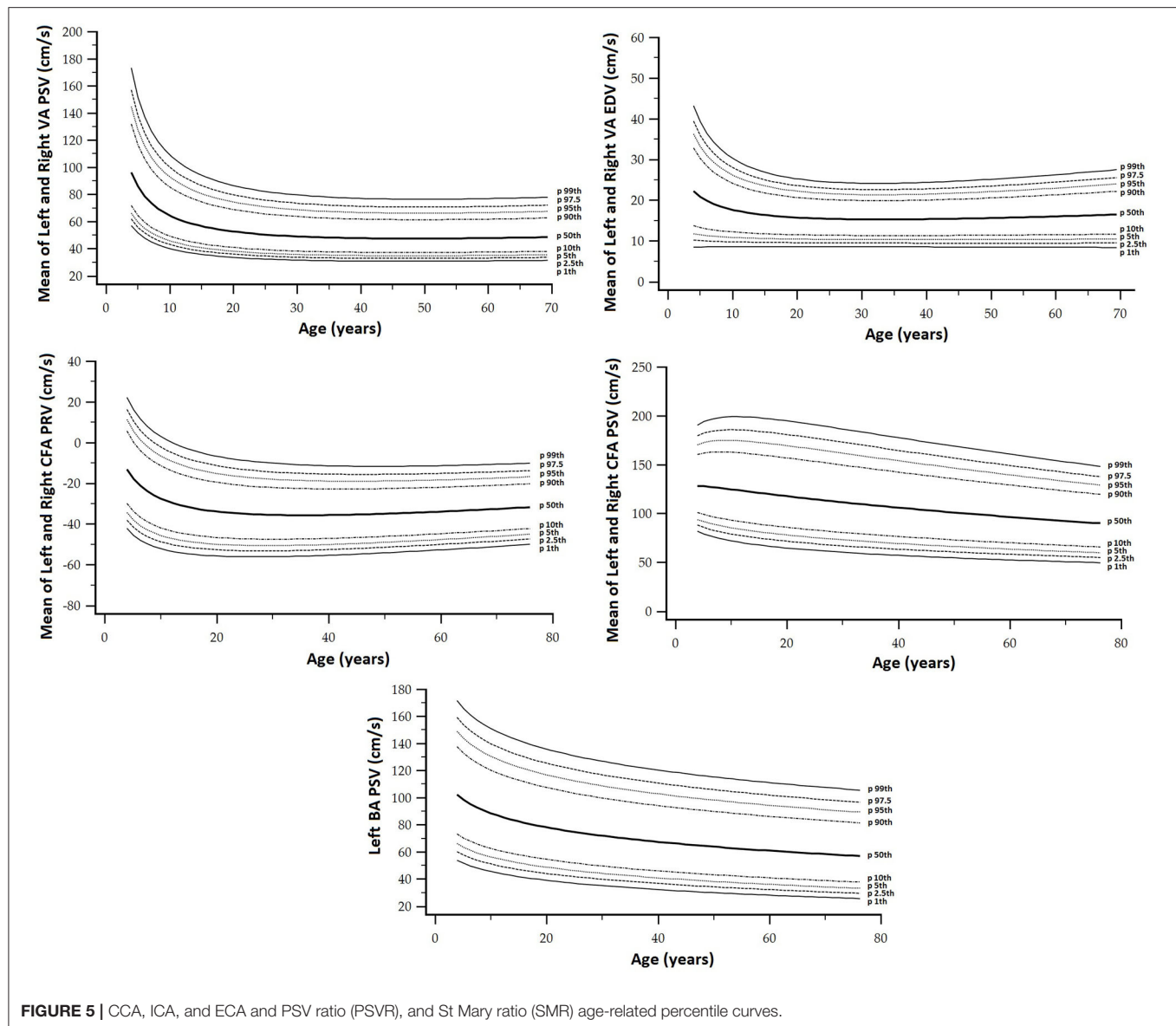
recommended to detect arterial stenosis >50%, the following was observed: (i) at low ages (children and/or adolescents) the thresholds were generally exceeded, whereas (ii) at old ages cut-off levels exceeded p97.5th values (more so at older ages) (**Figures 7–12**).

DISCUSSION

Age-Related Profiles

Carotid and Vertebral Arteries PSV and EDV

Common carotid artery ICA, ECA, and VA PSV levels were lower at higher ages but there were "regional" differences in the age-related profiles of arteries. The greatest reduction was observed in childhood/adolescence, however, whereas CCA PSV showed a continuous fall, ICA, ECA, and VA PSV levels stabilized at about 30–35 years (**Figure 6A**). The ratio between PSV levels in the carotid arteries showed age-related variations. During childhood

ICA PSV was higher than ECA PSV, but approximately at 10–15 years of age, the relationship reversed and, thereafter, ECA PSV remained higher than ICA PSV.

The ICA and VA PSV showed similar age-related profiles, but ICA PSV levels were always higher than those of the VA (**Figure 6A**). ECA EDV increased, whereas CCA, ICA, and VA EDV showed a reduction during childhood and adolescence. On the other hand, disregard of the arterial segment considered, the values stabilized at about 30–35 years (**Figure 6B**). CCA and ICA EDV level, as well as VA and ECA EDV remained at similar levels from ~20–30 years onward.

In general terms, age-related PSV and EDV values and variations observed for CCA (**Figures 7A,B**), ICA (**Figures 8A,B**), ECA (**Figures 9A,B**), and VA (**Figures 10A,B**) were in agreement with data (and differences) reported for children, adolescents, and/or adults (Zbornikova and Lassvik, 1986; Scheel et al., 2000; Yazici et al., 2005; Albayrak et al., 2007;

FIGURE 6 | Age-related percentile 50th curves for PSV **(A)**, EDV **(B)**, RI **(C)**, PI **(D)**, PSVR **(E)**, and SMR **(F)**.
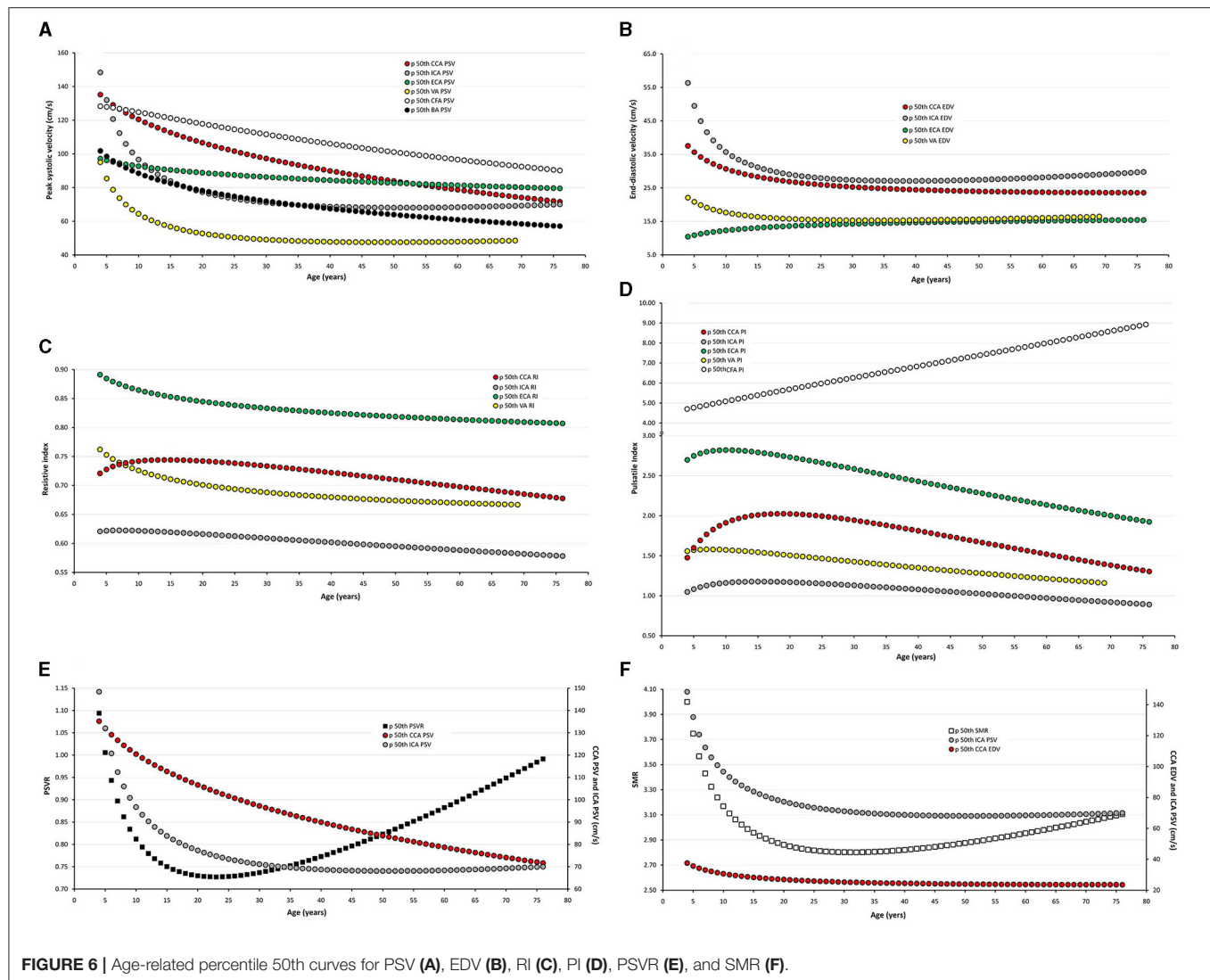
Demirkaya et al., 2008; Nemati et al., 2009; Kaszczewski et al., 2020; Trihan et al., 2020). In this regard, it should be noted that previous works compared (statistically) mean values obtained for groups of subjects within a wide age range [e.g., intervals of 10 (Zbornikova and Lassvik, 1986), 20 (Scheel et al., 2000), or 30 years (Yazici et al., 2005)], which would result in the finding of "step curves" that do not allow to visualize gradual physiological age-associated variations in BFV indexes. At the same time, the percentile curves obtained could show "deviations" that would not represent the real age-associated variations, determining (in some cases) non-physiological percentiles (e.g., CCA EDV p2.5th reached negative values) (**Figure 7B**).

Carotid and Vertebral Arteries RI and PI

In the first decades of life, RI and PI of carotid and vertebral arteries showed different behaviors (increases or falls), but they subsequently showed a gradual reduction with age (**Figures 6C,D**). CCA RI reached a maximum approximately at 15–20 years and then it fell to values even lower than the observed in childhood. The above described agrees with previous

works in children, adolescents, and young or middle-aged adults (Zbornikova and Lassvik, 1986; Scheel et al., 2000; Trihan et al., 2020) (**Figures 7C,D**).

On the other hand, some works described an increase in CCA RI and/or PI in subjects over 60 years (Zbornikova and Lassvik, 1986; Scheel et al., 2000) (**Figure 7C**). This could be explained by the inclusion of subjects with atherosclerotic plaques in ICA and/or ECA (whose prevalence increases with age) (Scheel et al., 2000). A similar consideration applies to ICA and ECA (see below).

Data obtained for ICA RI and PI (**Figures 8C,D**) agree with previous results (Trihan et al., 2020). Like us, other authors reported an age-related reduction in ICA RI and PI (Yazici et al., 2005; Trihan et al., 2020). However, works in which subjects with atherosclerotic plaques were not excluded showed an increase in ICA RI in <60 years (**Figures 8C,D**).

External carotid artery RI and PI showed an age-related reduction (mainly in the first two decades of life) (Trihan et al., 2020). Age-associated changes in ECA RI have been described in a limited way, and the available data are not coincident (e.g.,

FIGURE 7 | Common carotid artery. Comparison among curves of PSV **(A)**, EDV **(B)**, RI **(C)**, and PI **(D)**, obtained in our study (2.5th, 50th, and p97.5th percentiles) and mean values (p50th), and 2.5th (MV-1.96 × SD) and 97.5 (MV+1.96 × SD) percentiles obtained by other authors when studying groups of subjects of different ages. The fixed cut-off levels used to identify (graduate) levels of arterial stenosis are also shown.

FIGURE 8 | Internal carotid artery. Comparison among curves of PSV **(A)**, EDV **(B)**, RI **(C)**, and PI **(D)**, obtained in our study (2.5th, 50th, and p97.5th percentiles) and mean values (p50th), and 2.5th (MV-1.96 × SD) and 97.5 (MV+1.96 × SD) percentiles obtained by other authors when studying groups of subjects of different ages. The fixed cut-off levels used to identify (graduate) levels of arterial stenosis are also shown.

interspersed increases and decreases with variations depending on the age group considered have been reported) (Zbornikova and Lassvik, 1986; Scheel et al., 2000) (**Figures 9C,D**).

"Inter-Segment" Velocity Ratios: PSV and St Mary's Ratio

Peak systolic velocity ratio decreased until approximately 20–25 years (**Figure 6E**), and, thereafter, it increased markedly and

steadily. Despite both, CCA and ICA PSV decreased with age in the following stages: (i) in the first decade of life there was a reduction in PSVR, mainly explained by the significant reduction in ICA PSV, whereas (ii) from 20–25 years onward, it was observed an increase in PSVR, mainly attributed to the reduction in CCA PSV (**Figure 6E**). This agrees with data previously obtained in children and adolescents (Trihan et al., 2020) and in adults (Zbornikova and Lassvik, 1986; Kochanowicz et al., 2009) (**Figures 11A,B**).

FIGURE 9 | External carotid artery. Comparison among curves of PSV **(A)**, EDV **(B)**, RI **(C)**, and PI **(D)**, obtained in our study (2.5th, 50th, and p97.5th percentiles) and mean values (p50th), and 2.5th (MV−1.96 × SD) and 97.5 (MV+1.96 × SD) percentiles obtained by other authors when studying groups of subjects of different ages. The fixed cut-off levels used to identify (graduate) levels of arterial stenosis are also shown.

St Mary's ratio decreased until about 10–15 years (mainly due to the reduction in ICA PSV) and thereafter stabilized at 3.0. This agrees with data and trends previously described (Zbornikova and Lassvik, 1986; Scheel et al., 2000) (**Figures 6F**, **11C**).

Common Femoral and Brachial Artery Velocity and Indexes

There was a sustained age-related reduction in CFA PSV (**Figures 6A**, **12A**). This could be associated with a reduction in cardiac ejection rate.

During the first two decades of life, there was an age-related reduction in CFA PRV. Thereafter, it stabilized or showed a slight increase (**Figure 12B**). The degree of PRV variation (reversal level) in the first two decades would result from the interplay between vascular changes that would lead to higher (e.g., age-related increase in arterial stiffness and peripheral-to-aortic pressure gradient) or lower (e.g., age-related increase in arterial diameters) wave reflection levels (Hashimoto and Ito, 2010).

Opposite to the described carotid and vertebral arteries, there was a continuous age-associated increase in CFA PI. Although CFA PSV decreased with age, CFA PI increased, mainly due to an increase in forward–backward velocity oscillation around a mean value that decreases with age. It is to note that p2.5th for CFA PI data in adults overlapped the cut-off value (CFA PI = 4) proposed to define lower limb perfusion normality (Hodgkiss-Harlow and Bandyk, 2013) (**Figure 12C**).
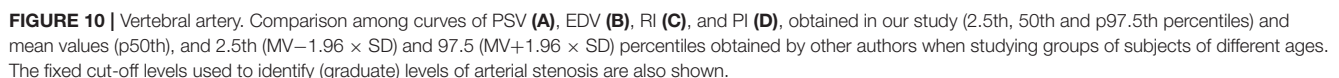
There was a gradual age-related reduction in left BA PSV (**Figures 6**, **12D**), which is in line with the described for other arteries.

Body Side-Related Differences

Despite for some BFV indexes there were statistical differences between right and left hemibodies data, the differences would not be significant in clinical practice. Previous works regarding this issue showed dissimilar findings, but in case there were differences, they were small.

Scheel et al. reported no significant side-to-side differences in flow velocities and waveform parameters in paired extracranial vessels (CCA, ICA, EC and VA), in a work that included 78 healthy adults (age MV/SD: 52/19 years, range: 20–85 years, both sexes) (Scheel et al., 2000). In turn, in healthy children and adolescents, Schoning and Hartig found no significant side-to-side differences in extracranial carotid velocity indexes (Schoning and Hartig, 1998). Other authors found higher flow velocities in left than in right CCA (Donis et al., 1988; Scheel et al., 2000) and VA (Nemati et al., 2009). Finally, higher PSV and EDV were observed in right than in the left ICA (Zbornikova and Lassvik, 1986).

There were no differences between left and right SMR, whereas the statistical differences in PSVR (higher values on the right side) would be clinically negligible (**Supplementary Material 1: Table S11**). This is in agreement with Kochanowicz et al. (Kochanowicz et al., 2009). In a population of healthy subjects (n = 343, mean age/SD: 43.5/18.3 years, range: 18–86 years) the authors did not find significant differences between left and right carotid ratios. Then, they proposed using the average of data from both hemibodies to define the reference limits for ICA/CCA ratios (Kochanowicz et al., 2009). Zbornikova and Lassvik did not find differences in PSVR between left and right sides (right: 1.00 ± 0.34, left: 0.96 ± 0.36), but they found SMR was higher in the right than in the left

FIGURE 10 | Vertebral artery. Comparison among curves of PSV **(A)**, EDV **(B)**, RI **(C)**, and PI **(D)**, obtained in our study (2.5th, 50th and p97.5th percentiles) and mean values (p50th), and 2.5th (MV−1.96 × SD) and 97.5 (MV+1.96 × SD) percentiles obtained by other authors when studying groups of subjects of different ages. The fixed cut-off levels used to identify (graduate) levels of arterial stenosis are also shown.

(3.93 ± 1.47 vs. 3.23 ± 1.29) which was explained by higher right ICA PSV (Zbornikova and Lassvik, 1986).

Sex-Related Differences

We identified the following indexes: (i) that did not require sex-specific RIs (e.g., CCA EDV), (ii) that did not require age and sex-specific RIs (e.g., BA EDV), (iii) that required sex-specific RIs regardless of age (e.g., CCA PSV), and (iv) that required sex-specific RIs only from a certain age (e.g., ICA EDV) (**Supplementary Material 1: Table S11**). Then, there was not a uniform behavior enabling to standardize the need for sex or age-related RIs, but it varied depending on the BFV index considered.

The finding of age-dependent differences between men and women ("age × sex" interaction), could contribute to explain the dissimilar or controversial findings. Scheel et al. reported non-significant sex-related differences in flow velocity- and waveform-derived parameters from extra-cranial vessels (Scheel et al., 2000). Zbosnikovaand Lassvick found (small) differences between women and men BFV (e.g., higher ICA PSV and EDV in women on the right-side) (Zbornikova and Lassvik, 1986). In turn, no sex-related differences were described for intracranial arteries (middle, anterior, and posterior cerebral arteries) BFV

(PSV, EDV, Vm) (Hashimoto and Ito, 2010). It is to note that similar to our work, Kochanowicz et al. reported data suggesting "age × sex" interaction (Kochanowicz et al., 2009). The authors found higher PSVR in women than in men for the age groups I (>40 years) and II (40–60 years), whereas similar ratios were observed for men and women in the age group III (>60 years). Then, sex-related differences would be moderated by age. Similarly, in this work p50th for PSVR in women and men showed differences in young or middle-aged adults, whereas data overlapped in older subjects (**Figure 11B**).

At least, in theory, the differences in BFV indexes age-related profiles observed between men and women could be explained by different age-related changes in CCA and ICA structure, and in the configuration of CCA bifurcation. In this regard, in women, ICA and CCA showed similar age-related dilatation, whereas, in men, CCA dilatation was greater and earlier than that of the ICA (Kochanowicz et al., 2009).

Percentiles vs. Fixed Cut-Off Points Indicative of Arterial Stenosis

The fixed threshold proposed for CCA PSV (150 cm/s) would not be useful for subjects <30 years, whose CCA PSV levels
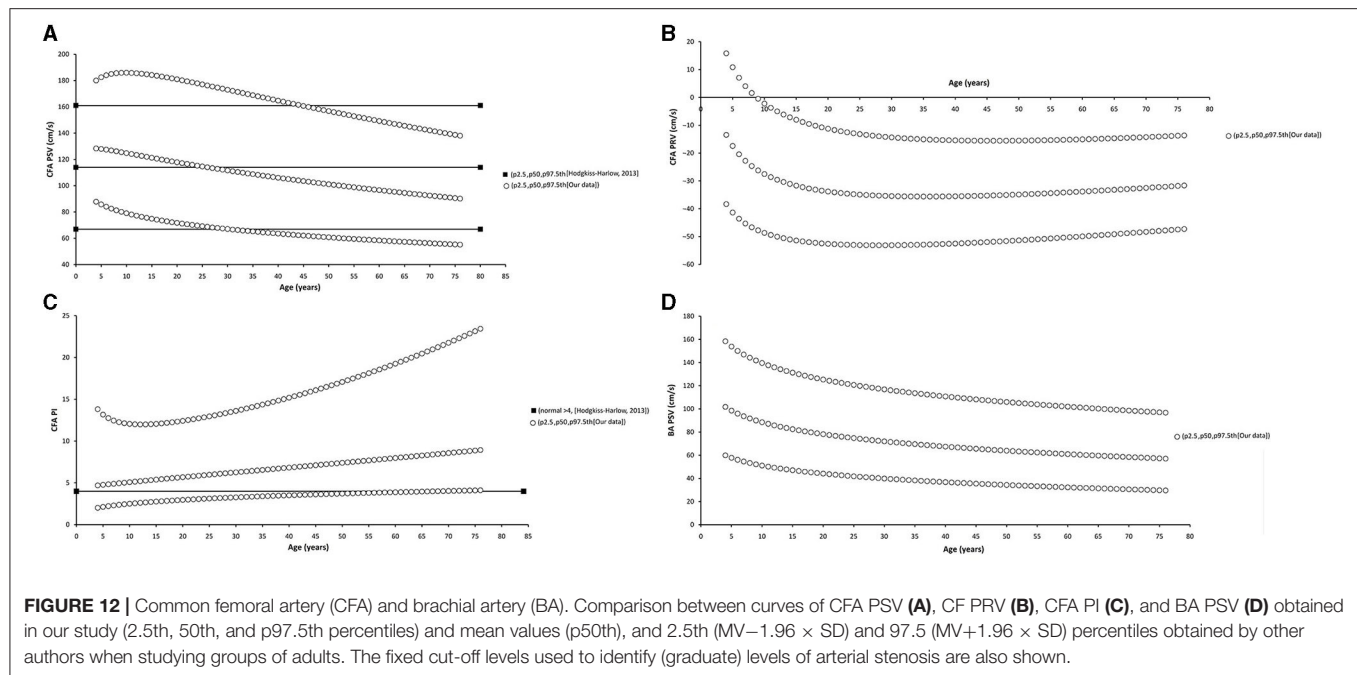
FIGURE 11 | Internal/common carotid artery velocity ratios. Comparison between curves of PSVR **(A)**, and SMR **(B)** obtained in our work (2.5th, 50th, and p97.5th percentiles) and mean values (p50th), and 2.5th (MV−1.96 × SD) and 97.5 (MV+1.96 × SD) percentiles obtained by other authors when studying groups of subjects of different ages. The fixed cut-off levels used to identify (graduate) levels of arterial stenosis are also shown.

are usually above that value (**Figure 7A**). On the other hand, the fixed cut-points (150 and 182 cm/s) are far above p97.5th for adults aged 50, 60, and 70 years (114, 105, and 97 cm/s, respectively). Similar considerations apply to ICA PSV

(120 and 140 cm/s) and ECA PSV (150 cm/s) thresholds (**Figures 8A**, **9A**). Although proposed thresholds would show high specificity for detecting significant stenosis and/or PSV deviations from expected values, they would not allow for early

FIGURE 12 | Common femoral artery (CFA) and brachial artery (BA). Comparison between curves of CFA PSV **(A)**, CF PRV **(B)**, CFA PI **(C)**, and BA PSV **(D)** obtained in our study (2.5th, 50th, and p97.5th percentiles) and mean values (p50th), and 2.5 (MV−1.96 × SD) and 97.5 (MV+1.96 × SD) percentiles obtained by other authors when studying groups of adults. The fixed cut-off levels used to identify (graduate) levels of arterial stenosis are also shown.

detection of vascular changes associated with disease and/or increased risk.

On the contrary, the threshold proposed for ICA EDV (40 cm/s) was below or overlapped the p97.5th obtained for children, adolescents, and adults (in several studies, including this one) (**Figure 8B**). Then, the use of the described cut-off point could be associated with over-diagnosis or over-estimation of the stenosis in subjects with atherosclerotic plaques.

Thresholds for VA PSV and EDV (85 and 27 cm/s) were below frequent values for children and adolescents, whereas they were near the p97.5th for adults (like in carotid arteries) (**Figures 10A,B**). Cut-off points for PSVR (2.0) and SMR (8.0) were far from the maximum values expected for any age (Oates et al., 2009). Therefore, they would not allow for detecting small and/or gradual departures from the "expected-for-age." (**Figures 11B,C**)

Common femoral artery PSV percentiles reported by Hodgkiss-Harlow and Bandyk (2013) were below or above the p97.5th obtained in this study for subjects younger or older than 45–50 years. On the other hand, fixed percentiles should not be used in CFA since PSV would not stabilize at any age. Finally, approximately after 45 years, CFA PI values ≤ 4 overlapped p2.5th values. Then, values above the threshold would be frequently found in healthy subjects (Hodgkiss-Harlow and Bandyk, 2013).

Clinical and Physiological Implications

Atherosclerosis evolves asymptomatically over time. Timely preventive strategies would limit disease progression and reduce the risk of complications (e.g., cardiovascular events) (Naghavi et al., 2006). US B-mode evaluation and Doppler-derived data are commonly used for the following: (i) to differentiate normal from diseased vessels, (ii) to define disease stages,

(iii) to assess collateral circulation (e.g., cerebral), doing so safely and cost-effectively. A primary aim of evaluations is to identify subjects with vascular conditions/disease associated with increased risk of cardiovascular events (e.g., stroke, vertebro-basilar ischemia), who would require specific treatments, and/or who would (particularly) benefit from preventive strategies. Another important aim is to document progressive or recurrent disease in patients already known to be at risk (Gerhard-Herman et al., 2006). In addition, it has been recently proposed that US studies could be used to identify subjects at increased risk, without the advanced disease (e.g., non-significant arterial narrowing) (Kochanowicz et al., 2009). In this sense, the deviation of BFV indexes of a particular subject from expected values could help to diagnose early stages of vascular disease and to determine individual risk. In this context, this work provides RIs for PSV, EDV, PRV, RI, PI, SDI, PSVR, and SMR data from different arterial segments (CCA, ICA, ECA, VA, CFA, and BA) obtained (in a single instance) from US studies performed in a large population of healthy children, adolescents, and adults.

Aiming at contributing with other groups and/or researchers, body side- sex- and age-related equations for MV, SD, and percentiles values were included in text and spreadsheet formats (**Supplementary Materials**). Thus, expected values for a given subject (and z-scores) could be calculated for clinical and/or research purposes.

Finally, it is to note that this work adds to the knowledge of the physiological variations in BFV levels and profiles that would be expected during growth and aging, analyzing at the same time (and comparatively) the behavior of different arteries. Furthermore, potential differences between left and right hemibodies as well as between men and women were considered and analyzed.

Strengths and Limitations

Our results should be understood within the context of the strengths and limitations that could be ascribed to the present work. First, as the work is a cross-sectional one, it provides no data on longitudinal age-related changes in BFV related indexes. Second, since no outcome data were considered, cut-off points (e.g., p75th, p90th, p95th) could not be defined based on CVR, but on values distribution in the studied group. It is not known whether the reference values should be used as cut-off values for diagnosis and treatment. In any case, if reference data were to be used in clinical practice it would be valuable to have a clear understanding of the factors that could modify the indexes levels and profiles. In this regard, further works would be necessary to define the impact that the exposure to traditional and emergent (new) CRFs, known to affect arterial vessels during aging, could have on BFV levels and indexes and their age-related variations. The analysis should be done taking into account factors influencing the findings (e.g., time of exposure, severity, the tendency of CRFs to aggregate and interact). Third, for any age, hemodynamic, structural, and functional vascular parameters can be acutely and temporarily modified by variations in the vascular smooth muscle tone (Bia et al., 2003, 2008). Systematization of recording conditions is necessary for the evaluation of arterial properties considering the modulating role of the smooth muscle tone. In this study, to systematize the records and as a way to minimize the impact of the referred source of variability, BFV levels were assessed and determined at rest under stable hemodynamic state conditions.

A major strength of the work is that BFV parameters were obtained in a large population sample (including children, adolescents, and adults), which enabled to define trends in mean values and percentiles for almost the whole range of life expectancy. The obtained data contribute to characterize the behavior of BFV (levels and parameters) in different arterial segments throughout life, providing information useful in clinical practice and physiological research. In this context, it is worth recalling that subjects with atherosclerotic plaques as well as those with ABI <0.9 were excluded from this study. This reinforces the value of the obtained data in terms of contribution to characterizing hemodynamic vascular parameters in physiological conditions.

CONCLUSION

This study adds to the knowledge of the physiological variations in BFV that would be expected during growth and aging, analyzing at the same time (and comparatively) the behavior of different indexes and arteries. Sex- and age-related profiles and RIs (normative data) for BFV levels and indexes obtained from US recordings of brachial, vertebral, carotid (common, internal, and external), and femoral arteries were determined in a large population (comprising children, adolescents, and adults) of asymptomatic subjects non-exposed to CRFs. Data

(percentile curves) were compared with fixed thresholds recommended for use in clinical practice. Equations (for mean and SD values; spreadsheet formats) were given to enable researchers and/or clinicians to determine expected values and potential deviations.

The presence of atherosclerotic plaques was associated (in asymptomatic subjects non-exposed to CRFs) with BFV levels, intrabeat indexes, and intersegment ratios. Some BFV-derived indexes showed statistical differences between hemibodies but the differences would not be significant in clinical practice. There was no uniform behavior to enable standardize the need for sex-related RIs (normative data), the need for sex-specific BFV RIs relied on the index and/or age considered.

Peak systolic velocity levels were lower at higher ages but there were "regional" differences in the age-related profiles of the arteries. The greatest reduction was observed in childhood/adolescence; however, though CCA, CFA, and BA PSV showed a continuous fall, ICA, ECA, and VA PSV levels stabilized at about 30–35 years. In the first decades of life, RI and PI of carotid and vertebral arteries showed different behaviors (increases or falls), but they subsequently showed a gradual reduction with age. In contrast, there was a continuous age-associated increase in CFA PI.

Currently used fixed thresholds would show high specificity for detecting significant stenosis and/or PSV deviations from expected values, but could result in misdiagnosis and/or would not allow detecting small and/or gradual departures from "expected-for-age," which could be associated with disease and/or increased risk.

DATA AVAILABILITY STATEMENT

The original contributions presented in the study are included in the article/**Supplementary Material**, further inquiries can be directed to the corresponding author.

ETHICS STATEMENT

The studies involving human participants were reviewed and approved by Comité de Ética de Investigación, Centro Hospitalario Pereira-Rossell, ASSE, Universidad de la República. Written informed consent to participate in this study was provided by the participants' legal guardian/next of kin.

AUTHOR CONTRIBUTIONS

YZ and DB contributed to conception and design of the study, performed the cardiovascular non-invasive recordings, constructed and organized the database, performed the statistical analysis, wrote the first draft and final version of the manuscript, contributed to manuscript revision, read, and approved the

submitted version. Both authors contributed to the article and approved the submitted version.

SUPPLEMENTARY MATERIAL

The Supplementary Material for this article can be found online at: https://www.frontiersin.org/articles/10.3389/fphys.2021.729309/full#supplementary-material

REFERENCES

Albayrak, R., Degirmenci, B., Acar, M., Haktanir, A., Colbay, M., and Yaman, M. (2007). Doppler sono-graphy evaluation of flow velocity and volume of the extracranial internal carotid and vertebral arteries in healthy adults. *J. Clin. Ultrasound.* 35, 27–33. doi: 10.1002/jcu.20301

Bellera, C. A., and Hanley, J. A. (2007). A method is presented to plan the required sample size when estimating regression-based reference limits. *J. Clin. Epidemiol.* 60, 610–615. doi: 10.1016/j.jclinepi.2006.09.004

Bia, D., and Zócalo, Y. (2021). Physiological age- and sex-related profiles for local (aortic) and regional (carotid-femoral, carotid-radial) pulse wave velocity and center-to-periphery stiffness gradient, with and without blood pressure adjustments: reference intervals and agreement between methods in healthy subjects (3–84 years). *J. Cardiovasc. Dev. Dis.* 8:3. doi: 10.3390/jcdd8010003

Bia, D., Zócalo, Y., Armentano, R., Camus, J., Forteza, E., and Cabrera-Fischer, E. (2008). Increased reversal and oscillatory shear stress cause smooth muscle contraction-dependent changes in sheep aortic dynamics: role in aortic balloon pump circulatory support. *Acta Physiol.* 192, 487–503. doi: 10.1111/j.1748-1716.2007.01765.x

Bia, D., Zócalo, Y., Farro, I., Torrado, J., Farro, F., Florio, L., et al. (2011). Integrated evaluation of age-related changes in structural and functional vascular parameters used to assess arterial aging, subclinical atherosclerosis, and cardiovascular risk in uruguayan adults: CUiiDARTE Project. *Int. J. Hypertens.* 2011:587303. doi: 10.4061/2011/587303

Bia, D.;, Armentano, R. L., Grignola, J. C., Craiem, D., Zócalo, Y. A., Ginés, F. F., et al. (2003). The vascular smooth muscle of great arteries: local control site of arterial buffering function? *Rev. Esp. Cardiol.* 56, 1202–1209. doi: 10.1016/S0300-8932(03)77039-0

Bossuyt, J., Engelen, L., Ferreira, I., Stehouwer, C. D., Boutouyrie, P., Laurent, S., et al. (2015). Reference values for arterial measurements collaboration. Reference values for local arterial stiffness. Part B: Femoral artery. *J. Hypertens.* 33, 1997–2009. doi: 10.1097/HJH.0000000000000655

Bruno, R. M., Nilsson, P. M., Engström, G., Wadström, B. N., Empana, J. P., Boutouyrie, P., et al. (2020). Early and supernormal vascular aging: clinical characteristics and association with incident cardiovascular events. *Hypertension* 76, 1616–1624. doi: 10.1161/HYPERTENSIONAHA.120.14971

Castro, J. M., García-Espinosa, V., Zinoveev, A., Marin, M., Severi, C., Chiesa, P., et al. (2019). Arterial structural and functional characteristics at end of early childhood and beginning of adulthood: impact of body size gain during early, intermediate, late and global growth. *J. Cardiovasc. Dev. Dis.* 6:33. doi: 10.3390/jcdd6030033

Chuang, S. Y., Bai, C. H., Chen, J. R., Yeh, W. T., Chen, H. J., Chiu, H. C., et al. (2011). Common carotid end-diastolic velocity and intima-media thickness jointly predict ischemic stroke in Taiwan. *Stroke* 42, 1338–1344. doi: 10.1161/STROKEAHA.110.605477

Chuang, S. Y., Bai, C. H., Cheng, H. M., Chen, J. R., Yeh, W. T., Hsu, P. F., et al. (2016). Common carotid artery end-diastolic velocity is independently associated with future cardiovascular events. *Eur. J. Prev. Cardiol.* 23, 116–124. doi: 10.1177/2047487315571888

Clifford, P. C., Skidmore, R., Bird, D. R., Woodcock, J. P., and Baird, R. N. (1981). The role of pulsatility index in the clinical assessment of lower limb ischaemia. *J. Med. Eng. Technol.* 5, 237–241. doi: 10.3109/03091908109018164

Demirkaya, S., Uluc, K., Bek, S., and Vural, O. (2008). Normal blood flow velocities of basal cerebral arteries decrease with advancing age: a transcranial Doppler sonography study. *Tohoku J. Exp. Med.* 14, 145–149. doi: 10.1620/tjem.214.145

Diaz, A., Bia, D., Zócalo, Y., Manterola, H., Larrabide, I., Lo Vercio, L., et al. (2018). Carotid intima media thickness reference intervals for a healthy argentinean population aged 11–81 years. *Int. J. Hypertens.* 2018:8086714. doi: 10.1155/2018/8086714

Díaz, A., Zócalo, Y., and Bia, D. (2019). Normal percentile curves for left atrial size in healthy children and adolescents. *Echocardiography* 36, 770–782. doi: 10.1111/echo.14286

Díaz, A., Zócalo, Y., and Bia, D. (2020). Percentile curves for left ventricle structural, functional and haemodynamic parameters obtained in healthy children and adolescents from echocardiography-derived data. *J. Echocardiogr.* 18, 16–43. doi: 10.1007/s12574-019-00425-0

Donis, J., Graf, M., and Sluga, E. (1988). Flussmessungen an den extrakraniellenKarotidenmitHilfe der Duplex-Sonographie. *ErgebnissebeiNormalpersonen. Ultraschall Med.* 9, 216–222. doi: 10.1055/s-2007-1011629

Engelen, L., Bossuyt, J., Ferreira, I., van Bortel, L. M., Reesink, K. D., Segers, P., et al. (2015). Reference values for arterial measurements collaboration. Reference values for local arterial stiffness. *Part A: Carotid artery. J. Hypertens.* 33, 1981–1996. doi: 10.1097/HJH.0000000000000654

Engelen, L., Ferreira, I., Stehouwer, C. D., Boutouyrie, P., and Laurent, S. (2013). Reference Values for Arterial Measurements Collaboration. Reference intervals for common carotid intima-media thickness measured with echotracking: Relation with risk factors. *Eur. Heart J.* 34, 2368–2380. doi: 10.1093/eurheartj/ehs380

Freire, C. M., Alcântara, M., Santos, S., Amaral, S., Veloso, O., Porto, C. L., et al. (2015). Recomendação para a quantificação pelo ultrassom da doença aterosclerótica das artérias carótidas e vertebrais: Grupo de trabalho do Departamento de Imagem Cardiovascular da Sociedade Brasileira de Cardiologia-DIC-SBC. *Arq Bras. Cardiol. Imagemcardiovasc.* 28, e1–64. doi: 10.5935/2318-8219.20150018

Gerhard-Herman, M., Gardin, J. M., Jaff, M., Mohler, E., Roman, M., and Naqvi, T. Z. (2006). Guidelines for noninvasive vascular laboratory testing: a report from the American Society of Echocardiography and the Society for Vascular Medicine and Biology. *Vasc Med.* 11, 183–200. doi: 10.1177/1358863x06070516

Hashimoto, J., and Ito, S. (2010). Pulse pressure amplification, arterial stiffness, and peripheral wave reflection determine pulsatile flow waveform of the femoral artery. *Hypertension* 56, 926–933. doi: 10.1161/HYPERTENSIONAHA.110.159368

Hayes, A. F. (2020). *Introduction to Mediation, Moderation, and Conditional Process Analysis (2nd Edition)*. Available online at: http://www.guilford.com/p/hayes3 (accessed on 13th Nov, 2020).

Hitsumoto, T. (2019). Relationships between the cardio-ankle vascular index and pulsatility index of the common carotid artery in patients with cardiovascular risk factors. *J. Clin. Med. Res.* 11, 593–599. doi: 10.14740/jocmr3914

Hodgkiss-Harlow, K. D., and Bandyk, D. F. (2013). Interpretation of arterial duplex testing of lower-extremity arteries and interventions. *SeminVasc. Surg.* 26, 95–104. doi: 10.1053/j.semvascsurg.2013.11.002

Hwang, J. Y. (2017). Doppler ultrasonography of the lower extremity arteries: anatomy and scanning guidelines. *Ultrasonography* 36, 111–119. doi: 10.14366/usg.16054

Jani, B., and Rajkumar, C. (2006). Ageing and vascular ageing. *Postgrad. Med. J.* 82, 357–362. doi: 10.1136/pgmj.2005.036053

Kaszczewski, P., Elwertowski, M., Leszczynski, J., Ostrowski, T., and Galazka, Z. (2020). Volumetric carotid flow characteristics in Doppler

ultrasonography in healthy population over 65 years old. *J. Clin. Med.* 9:1375. doi: 10.3390/jcm9051375

Kochanowicz, J., Turek, G., Rutkowski, R., Mariak, Z., Szydlik, P., Lyson, T., et al. (2009). Normal reference values of ratios of blood flow velocities in internal carotid artery to those in common carotid artery using Doppler sonography. *J. Clin. Ultrasound.* 37, 208–211. doi: 10.1002/jcu.20502

Kuhl, V., Tettenborn, B., Eicke, B. M., Visbeck, A., and Meckes, S. (2000). Color-coded duplex ultrasonography of the origin of the vertebral artery: normal values of flow velocities. *J. Neuroimaging* 10, 17–21. doi: 10.1111/jon200010117

Laclaustra, M., Casasnovas, J. A., Fernández-Ortiz, A., Fuster, V., León-Latre, M., Jiménez-Borreguero, L. J., et al. (2016). Femoral and carotid subclinical atherosclerosis association with risk factors and coronary calcium: the AWHS Study. *J. Am. Coll. Cardiol.* 67, 1263–1274. doi: 10.1016/j.jacc.2015.12.056

Lau, K. K., Pego, P., Mazzucco, S., Li, L., Howard, D. P., Küker, W., et al. (2018). Age and sex-specific associations of carotid pulsatility with small vessel disease burden in transient ischemic attack and ischemic stroke. *Int. J. Stroke* 13, 832–839. doi: 10.1177/1747493018784448

Lumley, T., Diehr, P., Emerson, S., and Chen, L. (2002). The importance of the normality assumption in large public health data sets. *Annu. Rev. Public Health* 23, 151–169. doi: 10.1146/annurev.publhealth.23.100901.140546

Marin, M., Bia, D., and Zócalo, Y. (2020). Carotid and femoral atherosclerotic plaques in asymptomatic and non-treated subjects: cardiovascular risk factors, 10-years risk scores, and lipid ratios' capability to detect plaque presence, burden, fibro-lipid composition and geometry. *J. Cardiovasc. Dev. Dis.* 7:11. doi: 10.3390/jcdd7010011

Naghavi, M., Falk, E., Hecht, H. S., Jamieson, M. J., Kaul, S., Berman, D., et al. (2006). From vulnerable plaque to vulnerable patient—Part III: Executive summary of the Screening for Heart Attack Prevention and Education (SHAPE) Task Force report. *Am. J. Cardiol.* 98, 2H–15H. doi: 10.1016/j.amjcard.2006.03.002

Nemati, M., Bavil, A. S., and Taheri, N. (2009). Comparison of normal values of Duplex indices of ver-tebral arteries in young and elderly adults. *Cardiovasc. Ultrasound.* 7:2. doi: 10.1186/1476-7120-7-2

Oates, C. P., Naylor, A. R., Hartshorne, T., Charles, S. M., Fail, T., Humphries, K., et al. (2009). Joint recommendations for reporting carotid ultrasound investigations in the United Kingdom. *Eur. J. Vasc. Endovasc. Surg.* 37, 251–261. doi: 10.1016/j.ejvs.2008.10.015

Oglat, A. A., Matjafri, M. Z., Suardi, N., Oqlat, M. A., Abdelrahman, M. A., and Oqlat, A. A. (2018). A review of medical Doppler ultrasonography of blood flow in general and especially in common carotid artery. *J. Med. Ultrasound.* 26, 3–13. doi: 10.4103/JMU.JMU_11_17

Royston, P., and Wright, E. (1998). A method for estimating age-specific reference intervals ('normal ranges') based on fractional polynomials and exponential transformation. *J. R. Stat. Soc. Ser. A Stat. Soc.* 161, 79–101. doi: 10.1111/1467-985X.00091

Santana, D. B., Zócalo, Y. A., and Armentano, R. L. (2012a). Integrated e-Health approach based on vascular ultrasound and pulse wave analysis for asymptomatic atherosclerosis detection and cardiovascular risk stratification in the community. *IEEE Trans. Inf. Technol. Biomed.* 16, 287–294. doi: 10.1109/TITB.2011.2169977

Santana, D. B., Zócalo, Y. A., Ventura, I. F., Arrosa, J. F., Florio, L., Lluberas, R., et al. (2012b). Health informatics design for assisted diagnosis of subclinical atherosclerosis, structural, and functional arterial age calculus and patient-specific cardiovascular risk evaluation. *IEEE Trans. Inf. Technol. Biomed.* 16, 943–951. doi: 10.1109/TITB.2012.2190990

Santos, S. N. D., Alcantara, M. L., Freire, C. M. V., Cantisano, A. L., Teodoro, J. A. R., Porto, C. L. L., et al. (2019). Vascular ultrasound statement from the department of cardiovascular imaging of the Brazilian Society of Cardiology—2019. *Arq. Bras. Cardiol.* 112, 809–849. doi: 10.5935/abc.20190106

Scheel, P., Ruge, C., and Schöning, M. (2000). Flow velocity and flow volume measurements in the extracranial carotid and vertebral arteries in healthy adults: reference data and the effects of age. *Ultrasound. Med. Biol.* 26, 1261–1266. doi: 10.1016/S0301-5629(00)00293-3

Schoning, M., and Hartig, B. (1998). The development of hemodynamics in the extracranial carotid and vertebral arteries. *Ultrasound. Med. Biol.* 24, 655–662. doi: 10.1016/S0301-5629(98)00029-5

Seidel, E., Eicke, B. M., Tettenborn, B., and Krummenauer, F. (1999). Reference values for vertebral artery flow volume by duplex sonography in young and elderly adults. *Stroke* 30, 2692–2696. doi: 10.1161/01.STR.30.12.2692

Shaalan, W. E., French-Sherry, E., Castilla, M., Lozanski, L., and Bassiouny, H. S. (2003). Reliability of common femoral artery hemodynamics in assessing the severity of aortoiliac inflow disease. *J. Vasc. Surg.* 37, 960–969. doi: 10.1067/mva.2003.282

Sosnowski, C., Pasierski, T., Janeczko-Sosnowska, E., Szulczyk, A., Dabrowski, R., Wozniak, J., et al. (2007). Femoral rather than carotid artery ultrasound imaging predicts extent and severity of coronary artery disease. *Kardiol. Pol.* 65, 760–766; discussion 767–8. Available online at: https://journals.viamedica.pl/kardiologia_polska/article/view/80839

Tokunaga, K., Koga, M., Yoshimura, S., Arihiro, S., Suzuki, R., Nagatsuka, K., et al. (2016). Optimal peak systolic velocity thresholds for predicting internal carotid artery stenosis greater than or equal to 50%, 60%, 70%, and 80%. *J. Stroke Cerebrovasc. Dis.* 25, 921–926. doi: 10.1016/j.jstrokecerebrovasdis.2015.12.021

Trihan, J. E., Perez-Martin, A., Guillaumat, J., and Lanéelle, D. (2020). Normative and pathological values of hemodynamic and Doppler ultrasound arterial findings in children. *Vasa* 49, 264–274. doi: 10.1024/0301-1526/a000860

Yazici, B., Erdogmuş, B., and Tugay, A. (2005). Cerebral blood flow measurements of the extracranial carotid and vertebral arteries with Doppler ultrasonography in healthy adults. *Diagn. Interv. Radiol.* 11, 195–198. Available online at: https://www.dirjournal.org/en/cerebral-blood-flow-measurements-of-the-extracranial-carotid-and-vertebral-arteries-with-doppler-ultrasonography-in-healthy-adults-1377

Zbornikova, V., and Lassvik, C. (1986). Duplex scanning in presumably normal persons of different ages. *Ultrasound. Med. Biol.* 12, 371–378. doi: 10.1016/0301-5629(86)90194-8

Zócalo, Y., and Bia, D. (2016). Ultrasonografía carotídea para detección de placas de ateroma y medición del espesor íntima-media; índice tobillo-brazo: Evaluación no invasiva en la práctica clínica: Importancia clínica y análisis de las bases metodológicas para su evaluación. *Rev. Urug. Cardiol.* 31, 47–60. Available online at: http://www.scielo.edu.uy/scielo.php?script=sci_arttext&pid=S1688-04202016000100012

Zócalo, Y., and Bia, D. (2021). Age- and sex-related profiles for macro, macro/micro and microvascular reactivity indexes: association between indexes and normative data from 2609 healthy subjects (3–85 years). *PloS ONE* 16:e0254869. doi: 10.1371/journal.pone.0254869

Zócalo, Y., Curcio, S., García-Espinosa, V., Chiesa, P., Giachetto, G., and Bia, D. (2017). Comparative analysis of arterial parameters variations associated with inter-individual variations in peripheral and aortic blood pressure: cross-sectional study in healthy subjects aged 2–84 years. *High Blood Press Cardiovasc. Prev.* 24, 437–451. doi: 10.1007/s40292-017-0231-2

Zócalo, Y., García-Espinosa, V., Castro, J. M., Zinoveev, A., Marin, M., Chiesa, P., et al. (2020). Stroke volume and cardiac output non-invasive monitoring based on brachial oscillometry-derived pulse contour analysis: explanatory variables and reference intervals throughout life (3–88 years). *Cardiol. J.* doi: 10.5603/CJ.a2020.0031

Conflict of Interest: The authors declare that the research was conducted in the absence of any commercial or financial relationships that could be construed as a potential conflict of interest.

Publisher's Note: All claims expressed in this article are solely those of the authors and do not necessarily represent those of their affiliated organizations, or those of the publisher, the editors and the reviewers. Any product that may be evaluated in this article, or claim that may be made by its manufacturer, is not guaranteed or endorsed by the publisher.

Check for
updates

Thoracic Outlet Syndrome: Fingertip Cannot Replace Forearm Photoplethysmography in the Evaluation of Positional Venous Outflow Impairments

Jeanne Hersant[1,2], Pierre Ramondou[1,2,3], Sylvain Durand[4], Mathieu Feuilloy[5,6], Mickael Daligault[7], Pierre Abraham[1,2,3]* and Samir Henni[1,2]

[1] Vascular Medicine, University Hospital, Angers, France, [2] UMR CNRS 1083 INSERM 6214, LUNAM University, Angers, France, [3] Sports and Exercise Medicine, University Hospital, Angers, France, [4] EA 4334 Motricité Interaction Performance, Le Mans University, Le Mans, France, [5] UMR CNRS 6613 LAUM, Le Mans, France, [6] School of Electronics (ESEO), Angers, France, [7] Department of Thoracic and Vascular Surgery, University Hospital, Angers, France

Objective: Fingertip photoplethysmography (PPG) resulting from high-pass filtered raw PPG signal is often used to record arterial pulse changes in patients with suspected thoracic outlet syndrome (TOS). Results from venous (low-pass filtered raw signal) forearm PPG (V-PPG) during the Candlestick-Prayer (Ca + Pra) maneuver were recently classified into four different patterns in patients with suspected TOS, two of which are suggestive of the presence of outflow impairment. We aimed to test the effect of probe position (fingertip vs. forearm) and of red (R) vs. infrared (IR) light wavelength on V-PPG classification and compared pattern classifications with the results of ultrasound (US).

Methods: In patients with suspected TOS, we routinely performed US imaging (US + being the presence of a positional compression) and Ca + Pra tests with forearm V-PPG$_{IR}$. We recruited patients for a Ca + Pra maneuver with the simultaneous fingertip and forearm V-PPG$_R$. The correlation of each V-PPG recording to each of the published pattern profiles was calculated. Each record was classified according to the patterns for which the coefficient of correlation was the highest. Cohen's kappa test was used to determine the reliability of classification among forearm V-PPG$_{IR}$, fingertip V-PPG$_R$, and forearm V-PPG$_R$.

Results: We obtained 40 measurements from 20 patients (40.2 ± 11.3 years old, 11 males). We found 13 limbs with US + results, while V-PPG suggested the presence of venous outflow impairment in 27 and 20 limbs with forearm V-PPG$_{IR}$ and forearm V-PPG$_R$, respectively. Fingertip V-PPG$_R$ provided no patterns suggesting outflow impairment.

Conclusion: We found more V-PPG patterns suggesting venous outflow impairment than US + results. Probe position is essential if aiming to perform upper-limb V-PPG

during the Ca + Pra maneuver in patients with suspected TOS. V-PPG during the Ca + Pra maneuver is of low cost and easy and provides reliable, recordable, and objective evidence of forearm swelling. It should be performed on the forearm (close to the elbow) with either PPG_R or PPG_{IR} but not at the fingertip level.

INTRODUCTION

Avenous origin is proposed as the second most frequent etiology of thoracic outlet syndrome (V-TOS) (Illig et al., 2016). Beyond effort venous thrombosis (Moore and Wei Lum, 2015; Cook and Thompson, 2021), transient positional compression of the subclavicular vein may result in venous outflow impairment during arm elevation, leading to positional upper limb pain and/or swelling (i.e., McCleery syndrome). Despite the absence of thrombosis, there is evidence that in McCleery syndrome, symptoms resulting from these positional outflow impairments can be improved with appropriate treatments (Likes et al., 2014; Moore and Wei Lum, 2015; Ryan et al., 2018; Wooster et al., 2019). Ultrasound (US) investigation is difficult in V-TOS, even in cases of chronic occlusion (Paget Schroetter syndrome) and does not measure positional upper limb volume changes (Jourdain et al., 2016; Brownie et al., 2020).

Photoplethysmography (PPG) is a low-cost and fairly established technique that estimates volume changes from the absorbance of red (R) or infrared (IR) light by illuminated tissues. There are two components within the raw PPG signal (Hickey et al., 2015). A high-pass filter can evaluate the small volume changes due to arterial pulsatility (A-PPG), while a low-pass filter removes the arterial pulsatility to assess limb volume changes mainly resulting from venous volume changes (V-PPG). It must be kept in mind that PPG is a semiquantitative technique with absolute values or absolute changes, being highly variable in test–retest recordings. We recently reported our experience with low-pass filtered reflectance infrared light forearm PPG (V-PPG_{IR}) during the Candlestick-Prayer (Ca + Pra) maneuver (Hersant et al., 2021). Our specific interest in the prayer position is because it can completely empty elevated upper limbs by opening the costoclavicular angle and thus might confirm whether venous outflow was impaired during the candlestick position. Therefore, the V-PPG signal varies between complete filling (arm lowered used as zero value) to complete emptying (upper limb elevated in the prayer position, used as 100% value). This approach seeks to normalize results and thereby improve the interpretation of this otherwise semiquantitative technique.

Fingertip A-PPG_R resulting from high-pass filtered raw PPG_R signal is often used to record arterial pulse changes in patients with suspected TOS (Colon and Westdorp, 1988; Baxter et al., 1990; Kleinert and Gupta, 1993). Using a low-pass filter to remove the arterial pulsatility, the resulting fingertip V-PPG_R might appear as an attractive tool for confirming the presence of upper-limb swelling (venous volume increase) during positional maneuvers in TOS. Since the V-PPG_{IR} probes were positioned on the forearm close to the elbow in our initial experiment, we aimed to test the hypothesis that patterns observed at the forearm level could be found at the fingertip level. Then, we recorded fingertip and forearm V-PPG_R simultaneously. Since light wavelength is described as an important determinant of the PPG responses (Chatterjee et al., 2018), we also aimed to compare forearm V-PPG_R results to those obtained through forearm V-PPG_{IR}.

In brief, this study was performed to test the influence of probe position (fingertip vs. forearm) and light wavelength (red vs. infrared) over V-PPG patterns and aimed to compare V-PPG results to the results of US imaging.

MATERIALS AND METHODS

Population

A prospective study was performed among patients who were referred to our laboratory from January 1 to December 31, 2020 for the investigation of symptoms suggesting the presence of TOS with upper-limb US imaging. As a routine during each visit, we recorded patient demographics and conditions, including age, sex, weight, height, history of the chest, shoulder or arm trauma or surgery, professional activity, and any ongoing treatments. All patients had bilateral forearm V-PPG_{IR} recording (2–3 cm distal to the elbow crease) with Vasolab320 (ELCAT®, Germany), as previously described (Hersant et al., 2021). In brief, it is stated that the Ca + Pra maneuver was performed with four consecutive phases: arm elevation to the candlestick position (in <5 s), maintenance of the "candlestick" (Ca) position until 30 s, rapid change to the "prayer" (Pra) position, which is maintained for 15 s, and then arm lowering (Hersant et al., 2021). For routine PPG_{IR}, after one training session, we waited for at least 1 min at rest with the arms along the torso before commencing recording (Hersant et al., 2021). It should be noted that ELCAT® starts from zero and records V-PPG_{IR} values in arbitrary units (AUs) at a sample rate of 4 Hz for 60 s and then automatically stops. It is also worth noting that increases in values correspond to decreases in volume. In parallel, US investigations were performed by trained operators, and maneuvers were left to the choice of the operator. US results were encoded limb by limb and considered positive (US[+]) when the report explicitly described positional compression (or occlusion) of the subclavicular vein regardless of which maneuver was performed. Otherwise, the US result was recorded as negative (US[−]) for venous compression. US and PPG_{IR} were systematically performed by different operators blinded to the results of the other test. All demography and clinical results were registered in an ethically approved database. Patients denying the use of their data, unable to understand the information for linguistic or cognitive reasons, and patients

TABLE 1 | Eligibility criteria for this study.

Inclusion Criteria:	• Age >18 years old
	• Patients referred for investigation of thoracic outlet syndrome
	• Affiliation to the French National healthcare system
	• French-speaking patients
	• Ability to stand still for half a minute
Exclusion Criteria:	○ Pregnancy
	○ Inability to understand the study goal
	○ Patients protected by decision of law

under 18 years of age were not recorded in the database and were considered to be ineligible for inclusion in the STOUT study.

Methods

The STOUT study was settled to allow the development of a homemade specific device allowing the recording of V-PPG$_R$ simultaneously at the forearm and fingertip levels and on both sides. The protocol was promoted by the university hospital in Angers, approved by the ethics committee, and registered in the clinicaltrial.gov website under identifier NCT03355274, before first inclusion. Patients were eligible to participate in this study if they fulfilled the inclusion and exclusion criteria (**Table 1**). Patients that agreed to participate provided signed informed consent after oral and written explanation of the protocol. The protocol and all related procedures were performed in compliance with the principles outlined in the Declaration of Helsinki. It is noted that inclusions were suspended during the coronavirus disease (COVID) wave. A schematic representation of the methods of this study is presented in **Figure 1**.

In patients included in the STOUT protocol, red light V-PPG (V-PPG$_R$) signals were recorded on both forearms and at the fingertip of the second finger of both hands, with the patient seated. Fingertip V-PPG$_R$ was recorded with adult finger soft-tip SpO2 sensors (Sino-K, China) as shown in **Figure 2**. On the forearms, we used flat red-light forehead SpO2 sensors (Nellcor Mansfield, MA, United States) placed 2–3 cm distal to the elbow crease covered with a Surgifix net (Urgo, France).

The system recorded fingertip and forearm V-PPG$_R$ values through a National instrument 4 channels 16-bit 9215 analog to digital converter, on both sides simultaneously at a sample rate of 200 Hz with a low pass filter of 0.2 Hz. The recording was started at least 15 s before the beginning of the Ca + Pra maneuver and stopped at least 1 min after the end of the procedure. Values are recorded in volts. Then, data were resampled to 4 Hz to allow comparison with ELCAT results.

For all PPG recordings, the Ca + Pra procedures were performed as previously reported (**Figure 1**) with the following four consecutive phases: arm elevation to the candlestick position (in <5 s), maintenance of the "candlestick" (Ca) position until 30 s, rapid change to the "prayer" (Pra) position that is maintained for 15 s, and then arm lowering.

Statistical Analysis

All V-PPG results were expressed in normalized emptying units (NEUs) using the starting voltage as a zero (0 NEU: arm fully filled) and the highest voltage observed during the candlestick or prayer maneuver as full emptying (100 NEU). Since the method and speed of arm lowering with the ELCAT was not normalized and as the recording period was too short to allow the return toward baseline value for routine IR V-PPG$_{IR}$, the analysis was performed over the first 45 s of the recording.

The data are presented as numbers (percentages), medians (25 and 75 percentiles), or means ± SD. Comparison of absolute values at the candlestick position and the prayer position with forearm V-PPG$_{IR}$ and with fingertip and forearm V-PPG$_R$ recordings were performed on a limb by limb basis, and the differences were tested with ANOVA and Scheffe post-tests.
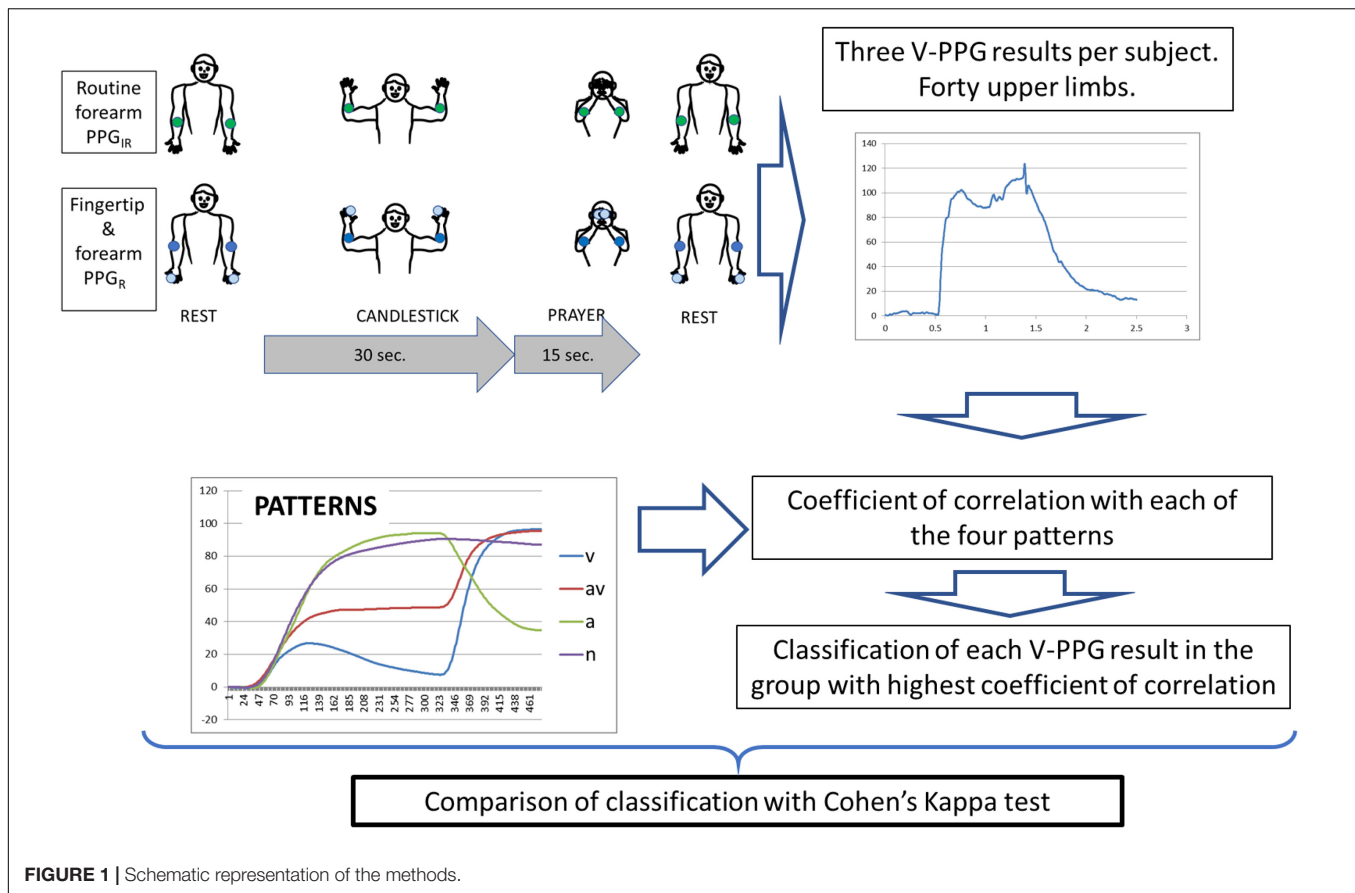
We calculated the coefficient of correlation of each recording to the reference curve of each of the four previously published representative patterns (Hersant et al., 2021). The reference curve was the mean of all recordings included in the cluster. Then, each recording was classified in the pattern that showed the highest correlation coefficient. Following this, Cohen's kappa test was used to analyze the concordance of classification observed between the forearm V-PPG$_{IR}$, the fingertip V-PPG$_R$, and the forearm V-PPG$_R$. Kappa is always ≤1. It is generally agreed that kappa <0.00, 0.00–0.20, 0.21–0.40, 0.41–0.60, 0.61–0.80, and 0.81–1 indicate no, slight, fair, moderate, substantial, and almost perfect to perfect agreements, respectively (Landis and Koch, 1977). Kappa values are reported with SE (± SE) and the 95% CI (minimum to maximum values). All statistical analyses were performed using SPSS® (IBM SPSS statistics version 15.0, Chicago, IL, United States) and Graphpad® for online Kappa calculation (Graphpad software, San Diego, CA, United States)[1]. For all tests, a two-tailed $P < 0.05$ was considered to be statistically significant.
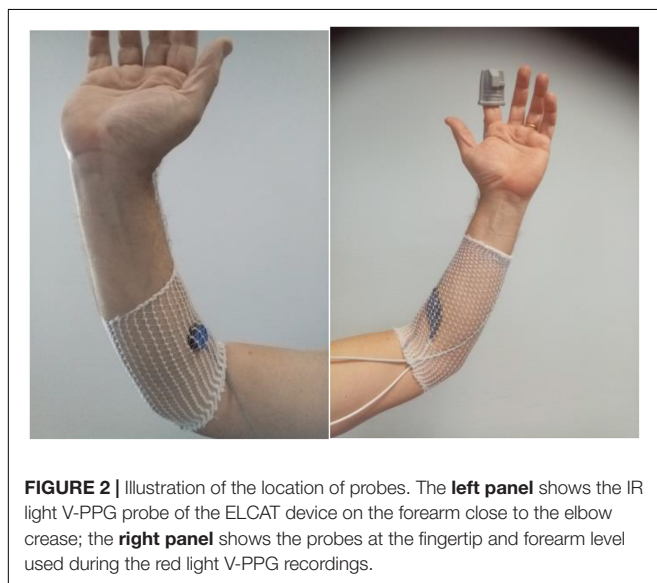
RESULTS

Among the included patients ($n = 21$), one patient did not have forearm V-PPG$_{IR}$ recordings for technical reasons and was excluded from this study. The remaining 20 patients (40 upper limbs) were 40.2 ± 11.3 years old, 11 males and 9 females, 171 ± 8 cm in height, and 77.2 ± 12.5 kg in weight. Notably, 10 patients had a history of chest shoulder or arm surgery or trauma. Half of the patients were unemployed, 8 of them due to their upper limb pain. Nine patients took pain killers, of whom three patients did so, on a daily basis. Of note, 2 patients reported unilateral right pain, 7 reported unilateral left pain, and 11 reported bilateral pain. US imaging in medical files reported the presence of right unilateral ($n = 2$), left unilateral ($n = 3$), or bilateral ($n = 4$) venous positional compression, resulting in 14 US$^+$ and 26 US$^-$ limbs.

Typical examples of recordings obtained for forearm V-PPG$_{IR}$ and for the fingertip and forearm V-PPG$_R$ test are presented in **Figure 3**. Of interest is that the outflow impairment found in both upper limbs of patient A and the left upper limb of patient B was

---

[1]https://www.graphpad.com

FIGURE 1 | Schematic representation of the methods.

FIGURE 2 | Illustration of the location of probes. The **left panel** shows the IR light V-PPG probe of the ELCAT device on the forearm close to the elbow crease; the **right panel** shows the probes at the fingertip and forearm level used during the red light V-PPG recordings.
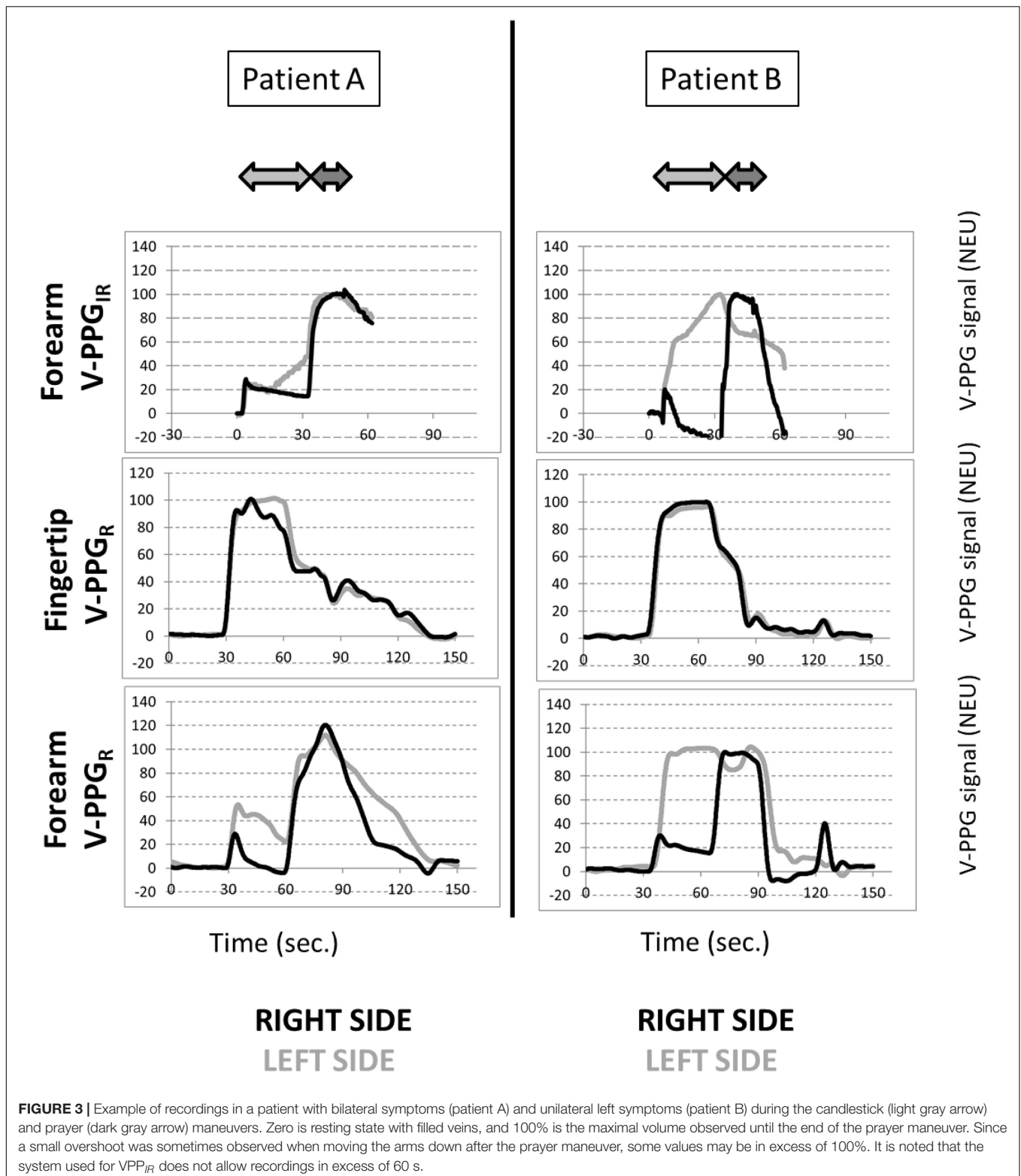
observed with the forearm V-PPG$_R$ and the forearm V-PPG$_{IR}$ but was not visible at the hand level with fingertip V-PPG$_R$.

On average, in the candlestick position, a significant difference was found between results at the fingertip level (88 ± 13 NEU) and those found during the forearm V-PPG$_{IR}$ (56 ± 45

NEU), between the forearm V-PPG$_R$ (53 ± 43 NEU) with $P < 0.05$, and between fingertip V-PPG$_R$ and forearm results tests. This difference was not observed for the prayer position with values being 71 ± 16 NEU, 86 ± 38 NEU, and 94 ± 11 NEU, respectively.

It should be noted that none of the 40 fingertip V-PPG$_R$ recordings was suggestive of the presence of outflow impairment (V or AV patterns). **Table 2** reports the comparison of V-PPG classification for results obtained for the different recordings. As shown, forearm V-PPG$_{IR}$ vs. forearm V-PPG$_R$ showed fair agreement as follows: number of observed agreements: 18 (45.0% of the observations), kappa = 0.235 ± 0.103, and 95% CI [0.034–0.437]. Forearm V-PPG$_{IR}$ vs. fingertip V-PPG$_R$ showed no agreement as follows: number of observed agreements: 7 (17.5% of the observations), kappa = −0.020 ± 0.061, and 95% CI [−0.140–0.100]. Finally, forearm V-PPG$_R$ vs. fingertip V-PPG$_R$ showed slight agreement as follows: number of observed agreements: 13 (35.1% of the observations), kappa = 0.092 ± 0.053, and 95% CI [−0.012–0.196].

When compared with US, among the limbs with US$^+$ ($n = 13$), nine upper limbs with forearm V-PPG$_{IR}$ and eight limbs with forearm V-PPG$_R$ had V-PPG patterns of V or AV type, but an additional 16 V or AV patterns were observed among forearm V-PPG$_{IR}$, 12 V or AV patterns among of the forearm V-PPG$_R$ recordings, and in the 27 US$^-$ limbs. Globally, there were many

FIGURE 3 | Example of recordings in a patient with bilateral symptoms (patient A) and unilateral left symptoms (patient B) during the candlestick (light gray arrow) and prayer (dark gray arrow) maneuvers. Zero is resting state with filled veins, and 100% is the maximal volume observed until the end of the prayer maneuver. Since a small overshoot was sometimes observed when moving the arms down after the prayer maneuver, some values may be in excess of 100%. It is noted that the system used for VPP$_{IR}$ does not allow recordings in excess of 60 s.

more forearm V-PPG tests showing a venous outflow impairment than during US imaging. Again, it is important to note that none of the 40 fingertip V-PPG$_R$ recordings was suggestive of the presence of venous outflow impairment.

DISCUSSION

The major results and points of interest of this study are as follows. First, we observed more V-PPG patterns

TABLE 2 | Classification of the patterns observed with red (R) or IR venous photoplethysmography (V-PPG) for each studied limb (n = 40).

A

		Forearm V-PPG$_{IR}$				
		V	AV	A	N	Total
Forearm V-PPG$_R$	V	9	2	2	3	**16**
	AV	1	2	1	0	**4**
	A	1	0	2	0	**3**
	N	5	5	2	5	**17**
	total	**16**	**9**	**7**	**8**	**40**

B

		Forearm V-PPG$_{IR}$				
		V	AV	A	N	Total
Fingertip V-PPG$_R$	V	0	0	0	0	0
	AV	0	0	0	0	0
	A	5	2	3	4	14
	N	11	7	4	4	26
	total	16	9	7	8	40

C

		Forearm V-PPG$_R$				
		V	AV	A	N	Total
Fingertip V-PPG$_R$	V	0	0	0	0	0
	AV	0	0	0	0	0
	A	8	2	0	4	14
	N	8	2	0	13	**26**
	total	16	4	3	17	40

Tables A–C are forearm V-PPG$_{IR}$ vs. forearm V-PPG$_R$, forearm V-PPG$_{IR}$ vs. fingertip V-PPG$_R$, forearm V-PPG$_R$ vs. fingertip V-PPG$_R$. V, AV, A, and N groups that are assumed indicative of isolated outflow impairment, arterial inflow/venous outflow simultaneous impairment, isolated inflow impairment, and normal responses, respectively (see text for details).

suggesting venous outflow impairment than US$^+$ results. Second, the agreement of V-PPG$_{IR}$ with the forearm V-PPG$_R$ was fair. Third and overall, fingertip V-PPG seems inadequate for detecting venous outflow impairment that is found at the forearm level, even in patients with positional venous compression at US imaging.

By the end of the 19th century, plethysmography was proposed in Physiology and Medicine for estimating volume changes in the limbs. Many techniques can be used to evaluate volume changes. Water immersion is one of the oldest tools but is inappropriate for upper limb recording during attitudinal tests. Strain gauge (Roos, 1969) plethysmography can be calibrated and expressed in volume increase normalized to the limb volume. Strain gauges are quite expensive, and the operators need to have a relatively large range of gauge lengths to adapt to individual anatomy. Air displacement (Coletta et al., 2001) or impedance (Nerurkar et al., 1990) plethysmography can also be proposed but remains more expensive than PPG. The use of red or infrared light combined with photosensitive detectors to estimate tissue light absorption of the finger was described in the late 1930s (Hertzman, 1937) and became popular in vascular physiology in the 1940s (Goldman and Schroeder, 1949). It was later computerized to enable routine

use. In reflectance PPG, the emitting and receiving diodes are positioned close one to the other, allowing for the use of PPG on upper or lower limbs.

While there are many reports of arterial PPG from fingertip recording in TOS, at present, only one study in the 1980s proposed forearm V-PPG to estimate the presence or absence of venous outflow impairment (Antignani et al., 1990). The enormous development and diffusion of US imaging is probably the major reason why V-PPG was not adopted in clinical routine in the last decades. US imaging is a simple and widely available tool. Its advantage is that it can detect not only the presence but also the level of venous compression, as well as potential anatomical vascular variations (Leonhard et al., 2017). Nevertheless, some limits of US must not be neglected. A debate persists to define whether a positive US test is a sign of decreased velocity in the subclavian vein on abduction (Adam et al., 2018) or of the loss of atrial and respiratory dynamics (Longley et al., 1992). Furthermore, recent reports question the accuracy of venous ultrasonography whether in diagnosing upper limb thrombosis (Moore and Wei Lum, 2015; Brownie et al., 2020) or confirming venous compression without thrombosis in patients with suspected TOS (Butros et al., 2013; Povlsen and Povlsen, 2018). Lastly, venous US imaging does not correlate with forearm volume changes (Czihal et al., 2015). Therefore, US imaging cannot diagnose forearm edema on its own (Matsumura et al., 1997; Landry and Liem, 2007). In fact, collateral veins may normalize venous outflow despite complete positional occlusion of the subclavicular vein. In such cases, no upper limb swelling occurs as a possible cause of pain or discomfort. Finally, it is worth noting that when arterial compression was reported, some reports did not mention the presence or absence of venous compression at all and were then recorded as negative for venous positional compression.

It is clear that, compared with US, V-PPG provides strictly no information on the presence and localization of positional venous compression. This appears to be a major weakness of the V-PPG technique. Nevertheless and on the contrary, V-PPG recording confirming upper limb swelling is expected to better support the idea that positional subclavicular vein compression is responsible for the symptoms. For this specific reason, we do believe that the two techniques (i.e., US and V-PPG) add information one to the other. There are two possible other issues with V-PPG. First, PPG remains a semiquantitative technique. Although it correlates with strain gauge plethysmography (Louisy and Schroiff, 1995), it is not reliable in absolute values (van den Broek et al., 1989). Second, there have been multiple studies showing that R and IR PPG probes may show different responses to volume changes (Moco et al., 2018; Chatterjee and Kyriacou, 2019). These two points may also have appeared as important limitations to the use and diffusion of V-PPG. Specifically, with a semiquantitative tool, it was difficult to define the volume decrease to be expected from arm elevation, and whether the candlestick position resulted in the expected complete forearm emptying. The Ca + Pra maneuver changes the semiquantitative results of the Roos test (that includes a candlestick position only)
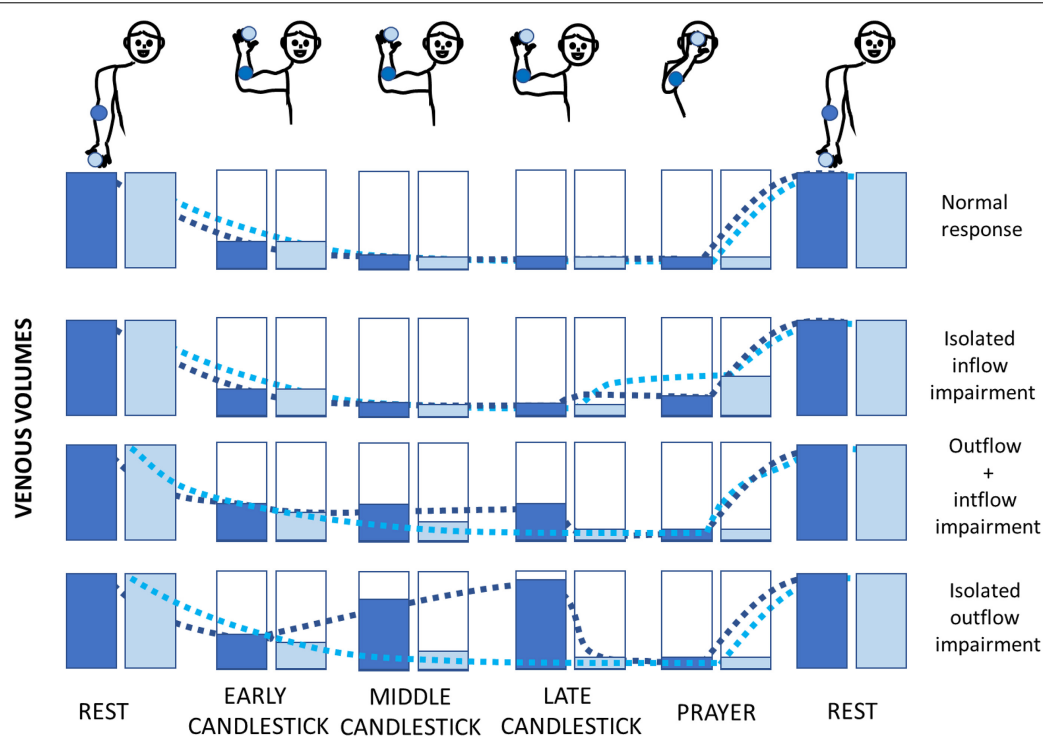
FIGURE 4 | Schematic representation of the hypotheses of the fingertip (light blue) and forearm (dark blue) volume changes during the Ca + Pra maneuver. Normally, the forearm and fingertip volumes decrease with arm elevation, and refilling will only occur during arm lowering (upper figure). In case of ischemia (isolated inflow impairment), it is expected that the decrease in adrenergic tone due to postischemic vasodilation would be better observed distally (at the fingertip level). If simultaneous inflow and outflow impairments occur, emptying of the forearm is stopped while fingertip veins may drain into the forearm veins due to hydrostatic pressure. Emptying of the forearm will be completed during the prayer attitude. In cases of isolated venous outflow impairment, arterial inflow during the candlestick attitude will fill the forearm from bottom to top (as in a filling bottle) and will increase the volume at the forearm far before the fingertip volume increases. It is noted that fingertip volume would increase too if the duration of the candlestick attitude was long enough.

to quantitative results. We believe that discordances between US and V-PPG should be interpreted neither as a lack of sensitivity of PPG because the presence of a venous compression at US does not necessarily induce forearm swelling, nor as a lack of specificity of PPG since we observed that some US reports just neglected the venous aspect when arterial imaging was positive. We put forward that V-PPG and US are complementary techniques. US detects venous compression but does not measure forearm swelling. V-PPG during the Ca + Pra maneuver is not a diagnostic test for subclavicular vein positional compression, but only (if a positional compression exists) for its hemodynamic consequences. While this could appear a limitation of the PPG technique, we believe that it is very interesting because it provides an objective argument for the presence of swelling during arm abduction as the cause of forearm discomfort in McCleery syndrome. In fact, when US of radio-vascular imaging shows the presence of venous attitudinal compression, it is unlikely that the venous compression itself results in symptoms if preclavicular collateral pathways normalize venous outflow.

The fair concordance between forearm V-PPG$_{IR}$ and forearm V-PPG$_R$ could result from the difference in light wavelengths; nevertheless, a fair to moderate relationship was predictable because a certain level of variability was expected from test–retest recordings. In fact, a difference by only a few degrees in abduction

angles (or by a few centimeters of elbows in the sagittal plane) may result in venous compression rather than venous occlusion, or even in the absence of compression.

The question that remains is why did fingertip recordings fail to detect the presence of volume changes in any of the upper limbs where US found a venous compression, while many profiles suggesting outflow impairment were observed at the forearm level? We believe that it is logical as detailed below, and a schematic representation of our interpretation of the volume changes expected at the forearm and fingertip level during the Ca + Pra maneuver is presented in **Figure 4**.

- A normal arterial inflow and venous outflow (N) should result in almost similar V-PPG results at the forearm and fingertip level, with venous emptying in "Ca" and no significant change between "Ca" and "Pra."
- If isolated arterial inflow impairment (A) occurs, fingertip and forearm volume would decrease to a minimum (veins should initially empty) during the candlestick phase. Then, during the "Pra" attitude, postischemic vasodilation at arterial decompression would be better observed distally (fingertip) than on the forearm.
- In case of simultaneous arterial inflow and venous outflow impairment (AV), finger veins would empty into the

forearm veins, after which finger volume is minimal and forearm volume stabilizes after the initial emptying. Then, only forearm volume further decreases in the prayer phase. As a result, a fingertip probe will not detect AV impairment.

- If isolated venous outflow impairment (V) occurs without arterial inflow impairment (e.g., as a result of isolated occlusion of the subclavicular vein without collateral pathways), once again the fingertip vein drains into the forearm veins due to gravity, and fingertip volume reaches a minimum. Then, the volume increases from bottom to top in the elevated forearm (just as a progressively filling bottle), and volume changes are optimally detected at the forearm close to the elbow (**Figure 4**), while the finger veins should remain completely emptied (at least for a few seconds of tenth of seconds). Only forearm volume decreases to its minimum during the "Pra" position while fingertip volume is already minimal. Here again, a fingertip probe does not detect the isolated venous outflow impairment (except when the candlestick position is prolonged long enough to have the progressive upward filling of the forearm veins with persistent arterial inflow, reaching the fingers).

These are interpretations, some of which are pure assumptions (i.e., postischemic vasodilation to explain the A-type pattern), but some are logical as a consequence of gravity (i.e., filling from bottom to top, emptying of hand to forearm veins when arms are elevated). Although only hypotheses, they seem to explain our observations quite well. Finally, it could be suggested that in patients with Paget-Schroetter syndrome, venous emptying should be slowed when arms are rapidly elevated both at the fingertip and the forearm levels, with no significant change between "Ca" and "Pra." This could not be observed in our experience because no patient with Paget Schroetter syndrome was included.

There are limitations to this study.

From a technical perspective, reported problems and sources of error with PPG are the individual variability in tissue to absorb, scatter, and reflect the emitted light (Blanc et al., 1993). These are not issues anymore during the Ca + Pra maneuver, with resting volume assumed to result from optimally filled veins (below heart level), and prayer position allowing for the optimal emptying of veins (above the heart level), defining the individual whole scale of minimal and maximal values. Simultaneous V-PPG$_{IR}$ and V-PPG$_R$ recordings might have been preferable to test the sole effect of wavelength difference on the results but were technically impossible, and interference between those two light-sensitive devices might have occurred despite differences in wavelengths.

From a methodological point of view, PPG can be contaminated by ambient light, cutaneous vasoconstriction and movements (Blanc et al., 1993). The former was limited by working in a moderately illuminated room. The latter is an issue mainly for the recording of small changes related to arterial pulsatility in arterial PPG recordings but shows minor influence on V-PPG results, with PPG routinely used during muscle contraction at the low limb level (Tucker et al., 1998). It is important to note that the V-PPG test was performed sitting or standing while US imaging may have been conducted

in the lying position. This might explain some underestimation of positive results with US since it was shown that positional compression of the subclavicular vessels is more frequent in the vertical than in the lying position (Cornelis et al., 2008). The relatively small number of subjects studied may limit the generalizability of our results, and future studies are required to confirm our observations and define whether differences may be observed between males and females, or during other provocative maneuvers. Finally, it could be suggested that clustering analysis applied to fingertip V-PPG recordings could result in specific fingertip V-PPG clusters and allow for the observation of four groups (as for the forearm) but with different mean curves. We believe that this is not the case because as previously explained and as shown in **Figure 4**, due to gravity emptying fingertip veins into forearm veins, our assumption is that the fingertip is just not the optimal location to detect outflow impairments.

From a physiological perspective, differences in anatomical vascular structure of the skin of the fingers compared with the skin of the forearm, as well as differences in innervation (in the fingers the vasomotor component is much higher than on proximal locations of the upper limb) may also result in the variations in volume being less visible at the fingertip compared to what can be seen on the forearm.

From a clinical perspective, it could be suggested that high central venous pressure may interfere with venous volume changes, as may be observed in cardiac failure or pulmonary hypertension. It cannot be excluded and requires further research. It could be also suggested that adrenergic vasoconstriction with positional pain will likely interfere with V-PPG results. If so, it is known that distal (i.e., hand or foot) vessels are more sensitive to adrenergic tone than vessels that are more proximal to the limbs. Therefore, recording at the forearm level is expected to be relatively insensitive to changes in adrenergic tone.

Finally, the limited number of subjects recruited in this pilot study limits the power of our results. Nevertheless, the total absence of profiles suggesting outflow impairment at the fingertip level, even in patients with US objective evidence of venous compression, was predictable (as explained in **Figure 4**), and we advocate that there is few if any need to further confirm this point in a larger population.

CONCLUSION AND PERSPECTIVES

Probe positioning on the forearm is essential if one aims to perform upper-limb V-PPG in patients with suspected TOS during the Ca + Pra maneuver. Both conceptually and as proven in this study, extracting the venous signal by a low-pass filter from fingertip PPG is inadequate for detecting volume changes suggesting outflow impairment. The additional value of forearm V-PPG in the diagnostic algorithm of patients with suspected TOS remains to be determined in a large population, but some immediate applications of the present findings may occur. Keeping in mind that the diagnosis of TOS remains difficult and its treatment is one of the most frequent

causes of lawsuits in cardiothoracic surgery (Ferguson, 1982), we suggest that in addition to imaging, forearm V-PPG$_{IR}$ during the Ca + Pra maneuver is easy and may provide recordable, objective arguments of forearm swelling in patients with suspected McCleery syndrome.

DATA AVAILABILITY STATEMENT

The raw data supporting the conclusions of this article will be made available by the authors, without undue reservation.

ETHICS STATEMENT

The studies involving human participants were reviewed and approved by the CPP of Ile de France VII (protocol STOUT on 15 March 2018). The patients/participants provided their written informed consent to participate in this study.

AUTHOR CONTRIBUTIONS

FUNDING

ACKNOWLEDGMENTS

REFERENCES

Adam, G., Wang, K., Demaree, C. J., Jiang, J. S., Cheung, M., Bechara, C. F., et al. (2018). A prospective evaluation of duplex ultrasound for thoracic outlet syndrome in high-performance musicians playing bowed string instruments. *Diagnostics* 8:11. doi: 10.3390/diagnostics8010011

Antignani, P. L., Pillon, S., Di Fortunato, T., and Bartolo, M. (1990). Light reflection rheography and thoracic outlet syndrome. *Angiology* 41, 382–386. doi: 10.1177/000331979004100505

Baxter, B. T., Blackburn, D., Payne, K., Pearce, W. H., and Yao, J. S. (1990). Noninvasive evaluation of the upper extremity. *Surg. Clin. N. Am.* 70, 87–97. doi: 10.1016/s0039-6109(16)45035-8

Blanc, V. F., Haig, M., Troli, M., and Sauve, B. (1993). Computerized photo-plethysmography of the finger. *Can. J. Anaesth.* 40, 271–278. doi: 10.1007/BF03037040

Brownie, E. R., Abuirqeba, A. A., Ohman, J. W., Rubin, B. G., and Thompson, R. W. (2020). False-negative upper extremity ultrasound in the initial evaluation of patients with suspected subclavian vein thrombosis due to thoracic outlet syndrome (Paget-Schroetter syndrome). *J. Vasc. Surg. Venous Lymphat. Disord.* 8, 118–126. doi: 10.1016/j.jvsv.2019.08.011

Butros, S. R., Liu, R., Oliveira, G. R., Ganguli, S., and Kalva, S. (2013). Venous compression syndromes: clinical features, imaging findings and management. *Br. J. Radiol.* 86:20130284. doi: 10.1259/bjr.20130284

Chatterjee, S., Abay, T. Y., Phillips, J. P., and Kyriacou, P. A. (2018). Investigating optical path and differential pathlength factor in reflectance photoplethysmography for the assessment of perfusion. *J. Biomed. Opt.* 23, 1–11. doi: 10.1117/1.JBO.23.7.075005

Chatterjee, S., and Kyriacou, P. A. (2019). Monte carlo analysis of optical interactions in reflectance and transmittance finger photoplethysmography. *Sensors* 19:789. doi: 10.3390/s19040789

Coletta, J. M., Murray, J. D., Reeves, T. R., Velling, T. E., Brennan, F. J., Hemp, J. R., et al. (2001). Vascular thoracic outlet syndrome: successful outcomes with multimodal therapy. *Cardiovasc. Surg.* 9, 11–15. doi: 10.1016/s0967-2109(00)00092-2

Colon, E., and Westdorp, R. (1988). Vascular compression in the thoracic outlet. Age dependent normative values in noninvasive testing. *J. Cardiovasc. Surg.* 29, 166–171.

Cook, J. R., and Thompson, R. W. (2021). Evaluation and management of venous thoracic outlet syndrome. *Thorac. Surg. Clin.* 31, 27–44. doi: 10.1016/j.thorsurg.2020.08.012

Cornelis, F., Zuazo, I., Bonnefoy, O., Abric, B., Borocco, A., Strainchamps, P., et al. (2008). [Diagnosis of thoracic outlet syndrome. Value of angiography in

the sitting position]. *J. Radiol.* 89(1 Pt 1), 47–52. doi: 10.1016/s0221-0363(08)70369-x

Czihal, M., Paul, S., Rademacher, A., Bernau, C., and Hoffmann, U. (2015). Lack of association between venous hemodynamics, venous morphology and the postthrombotic syndrome after upper extremity deep venous thrombosis. *Phlebology* 30, 105–112. doi: 10.1177/0268355513517226

Ferguson, T. B. (1982). The crisis of excellence. *J. Thorac. Cardiovasc. Surg.* 84, 161–171.

Goldman, M. L., and Schroeder, H. A. (1949). Coarctation of the aorta; photo-electric plethysmography and direct arterial blood pressure measurement as an aid in diagnosis. *Am. J. Med.* 7, 454–463. doi: 10.1016/0002-9343(49)90395-2

Hersant, J., Ramondou, P., Chavignier, V., Chavanon, A., Feuilloy, M., Picquet, J., et al. (2021). Forearm volume changes estimated by photo-plethysmography during an original candlestick/prayer maneuver in patients with suspected thoracic outlet syndrome. *Front. Physiol.* 12:652456. doi: 10.3389/fphys.2021.652456

Hertzman, A. (1937). Photoelectric plethysmography of the fingers and toes in man. *Proc. Soc. Exp. Biol. Med.* 37, 529–534. doi: 10.3181/00379727-37-9630

Hickey, M., Phillips, J. P., and Kyriacou, P. A. (2015). The effect of vascular changes on the photoplethysmographic signal at different hand elevations. *Physiol. Meas.* 36, 425–440. doi: 10.1088/0967-3334/36/3/425

Illig, K. A., Donahue, D., Duncan, A., Freischlag, J., Gelabert, H., Johansen, K., et al. (2016). Reporting standards of the society for vascular surgery for thoracic outlet syndrome: executive summary. *J. Vasc Surg.* 64, 797–802. doi: 10.1016/j.jvs.2016.05.047

Jourdain, V., Goldenberg, W. D., Matteucci, M., and Auten, J. (2016). Paget-Schroetter syndrome: diagnostic limitations of imaging upper extremity deep vein thrombosis. *Am. J. Emerg. Med.* 34, 683.e1–e3. doi: 10.1016/j.ajem.2015.07.018

Kleinert, J. M., and Gupta, A. (1993). Pulse volume recording. *Hand. Clin.* 9, 13–46. doi: 10.1016/s0749-0712(21)00947-1

Landis, J. R., and Koch, G. G. (1977). The measurement of observer agreement for categorical data. *Biometrics* 33, 159–174. doi: 10.2307/2529310

Landry, G. J., and Liem, T. K. (2007). Endovascular management of paget-schroetter syndrome. *Vascular* 15, 290–296. doi: 10.2310/6670.2007.00064

Leonhard, V., Caldwell, G., Goh, M., Reeder, S., and Smith, H. F. (2017). Ultrasonographic diagnosis of thoracic outlet syndrome secondary to brachial plexus piercing variation. *Diagnostics* 7:40. doi: 10.3390/diagnostics7030040

Likes, K., Rochlin, D. H., Call, D., and Freischlag, J. A. (2014). McCleery syndrome: etiology and outcome. *Vasc. Endovascular. Surg.* 48, 106–110. doi: 10.1177/1538574413512380

Longley, D. G., Yedlicka, J. W., Molina, E. J., Schwabacher, S., Hunter, D. W., and Letourneau, J. G. (1992). Thoracic outlet syndrome: evaluation of the subclavian vessels by color duplex sonography. *AJR Am. J. Roentgenol.* 158, 623–630. doi: 10.2214/ajr.158.3.1739007

Louisy, F., and Schroiff, P. (1995). Plethysmography with optoelectronic sensors: comparison with mercury strain gauge plethysmography. *Aviat. Space Environ. Med.* 66, 1191–1197.

Matsumura, J. S., Rilling, W. S., Pearce, W. H., Nemcek, A. A. Jr., Vogelzang, R. L., and Yao, J. S. (1997). Helical computed tomography of the normal thoracic outlet. *J. Vasc. Surg.* 26, 776–783. doi: 10.1016/s0741-5214(97)70090-9

Moco, A. V., Stuijk, S., and de Haan, G. (2018). New insights into the origin of remote PPG signals in visible light and infrared. *Sci. Rep.* 8:8501. doi: 10.1038/s41598-018-26068-2

Moore, R., and Wei Lum, Y. (2015). Venous thoracic outlet syndrome. *Vasc. Med.* 20, 182–189. doi: 10.1177/1358863X14568704

Nerurkar, S. N., Jindal, G. D., Pedhenekar, S. A., Gupta, D. K., Deshpande, A. K., Deshmukh, H. L., et al. (1990). Impedance plethysmographic observations in thoracic outlet syndrome. *J. Postgrad. Med.* 36, 154–157.

Povlsen, S., and Povlsen, B. (2018). Diagnosing thoracic outlet syndrome: current approaches and future directions. *Diagnostics* 8:21. doi: 10.3390/diagnostics8010021

Roos, D. B. (1969). Plethysmography: a simple method of studying and following peripheral vascular disorders. *Surg. Clin. N. Am.* 49, 1333–1342. doi: 10.1016/s0039-6109(16)38992-7

Ryan, C. P., Mouawad, N. J., Vaccaro, P. S., and Go, M. R. (2018). A patient-centered approach to guide follow-up and adjunctive testing and treatment after first rib resection for venous thoracic outlet syndrome is safe and effective. *Diagnostics* 8:4. doi: 10.3390/diagnostics8010004

Tucker, E. A., Lamb, L. E., Callicott, C., Cooke, S. D., and Cooke, E. D. (1998). Measurements of calf muscle pump efficiency during simulated ambulation. *Int. Angiol.* 17, 255–259.

van den Broek, T. A., Rauwerda, J. A., Kuijper, C. F., van Rij, G. L., and Bakker, F. C. (1989). Failure of quantitative venous photoplethysmography to assess venous insufficiency: a prospective clinical study. *Neth J. Surg.* 41, 104–107.

Wooster, M., Fernandez, B., Summers, K. L., and Illig, K. A. (2019). Surgical and endovascular central venous reconstruction combined with thoracic outlet decompression in highly symptomatic patients. *J. Vasc. Surg. Venous Lymphat Disord.* 7, 106.e3–112.e12. doi: 10.1016/j.jvsv.2018.07.019

Building a Mobile Stroke Unit Based on 5G Technology – A Study Protocol

Gangfeng Gu, Junyao Jiang, Bo Zheng, Xiao Du*, Ke Huang, Qinfang Yue and Jian Wang*

Department of Neurology, Ya'an People's Hospital, Ya'an, China

Background: In-time treatment of acute stroke is critical to saving people's lives and improving the quality of post-stroke life. A mobile stroke unit (MSU) with fifth-generation (5G) mobile networks strengthens the interaction of patient information and healthcare resources, thereby reducing response times and improving thrombolysis results. However, clinical evidence of better outcomes compared to regular care is still lacking.

Method and Design: In this randomized controlled trial, 484 patients with acute stroke are allocated into the MSU and regular care groups. We establish medical records for each patient and conduct a follow-up of 90 days. The primary outcomes are functional results as defined by utility-weighted modified Rankin Scale (uw-mRS) 90 days after the incidence occurred, whereas secondary outcomes include the alarm to CT scan completed time, the alarm to treatment decision time, the alarm to thrombolytic time, quality of life, and symptomatic intracranial hemorrhage combined with NIHSS score as well as cost-effectiveness.

Discussion: This study establishes an innovative MSU (based on 5G) to manage acute stroke, comparing its clinical and economic outcomes to regular care and informing decision-makers of the effectiveness of the stroke emergency system.

Clinical Trial Registration: [http://www.chictr.org.cn/showproj.aspx?proj=63874], identifier [ChiCTR2000039695].

Keywords: stroke treatment, 5G technology, randomized controlled trial (MeSH), utility weighted mRS, study protocol

INTRODUCTION

Patients with acute stroke require medical aid at the first moment to quickly work out suitable treatment options, thus minimizing adverse results after stroke (Peisker et al., 2017). Clinical guidelines propose that prehospital treatment, including ambulance arrangement and tissue plasminogen activator (t-PA) treatment, is essential to saving patients with acute stroke and improving their quality of life (Powers et al., 2018, 2019). To this end, an emergency medical system (EMS) with a quick response to stroke calling and well-trained emergency personnel is needed. Emergency experts have been searching for innovative approaches that transcend the conventional pathway to provide patients with better medical services. A mobile stroke unit (MSU) is a special ambulance that incorporates neurological examination, CT diagnosis, and intravenous

thrombolytic therapy by fitting a mobile CT and relevant point-of-care laboratory testing (Bowry and Grotta, 2017; Tsivgoulis et al., 2018).

As a timely administration of thrombolytic therapy, MSU has apparent benefits for acute stroke patients (Nyberg et al., 2018; Yamal et al., 2018). In China, the MSU equipped with a mobile CT was introduced in 2017, effectively reducing the "door to needle" from over 60 min to around 48 min. As a result, hospitals have established their MSUs across the country, in efforts to elevate the local medical services and social welfare (Zhou et al., 2021). Moreover, with the recent universalization of fifth-generation (5G) technology, the MSU has gradually transformed into a new model by equipping with the latest mobile networks and state-of-the-art monitoring devices, balancing essential functions of EMS and other advanced gadgets. Therefore, the highly informative and intelligent MSU enables rapid treatment of acute stroke, reducing stroke patients' disability and death rates and the economic burden on their family as well as the entire society. Furthermore, the highly integrated wearable devices could acquire the core medical data (including vital signs, cranial pressure monitoring, blood glucose, etc.) in real time, which is simultaneously uploaded to a stroke-specific cloud platform for remote consultation and better surveillance.

METHODS AND ANALYSIS

Study Design

We conduct a pragmatic, prospective trial to examine clinical and economic outcomes in patients eligible for thrombolytic administration who receive care from MSU, as compared with regular care in a blinded fashion (see **Figure 1**), determining. Through this, we aim to determine whether the deployment of MSU leads to better functional benefits for patients with acute stroke. Investigators randomly allocate one patient to either the MSU or the regular care group. To balance the two groups on potential confounding factors (such as weather) that may change in a year, we choose a block size of 4 weeks to limit the length of time to use the same program.

The protocol that is registered with No. ChiCTR2000039695 on 5 November 2020 (http://www.chictr.org.cn/showproj.aspx?proj=63874) has been approved by the ethical review committee of the Ya'an people's Hospital (NPSY202007002).

Participants

A total of 484 participants are recruited from the Ya'an people's Hospital, 242 of whom were randomized to the intervention group and the rest randomized to the comparison group.

Each participant must meet all of the inclusion criteria to be enrolled in this study, which are given as follows:

1. Patients need to be aged over 18 years, with a final diagnosis of ischemic stroke.
2. Patients' confirmed onset-to-alarm time is less than 4.5 h.
3. Patient is recognized as a t-PA candidate, with mRS scores less than 3.

4. Patients volunteer to participate and sign an informed consent.

The exclusion criteria include uncertain symptom onset, no focal stroke-like symptoms, severe malignant, or pregnancy.

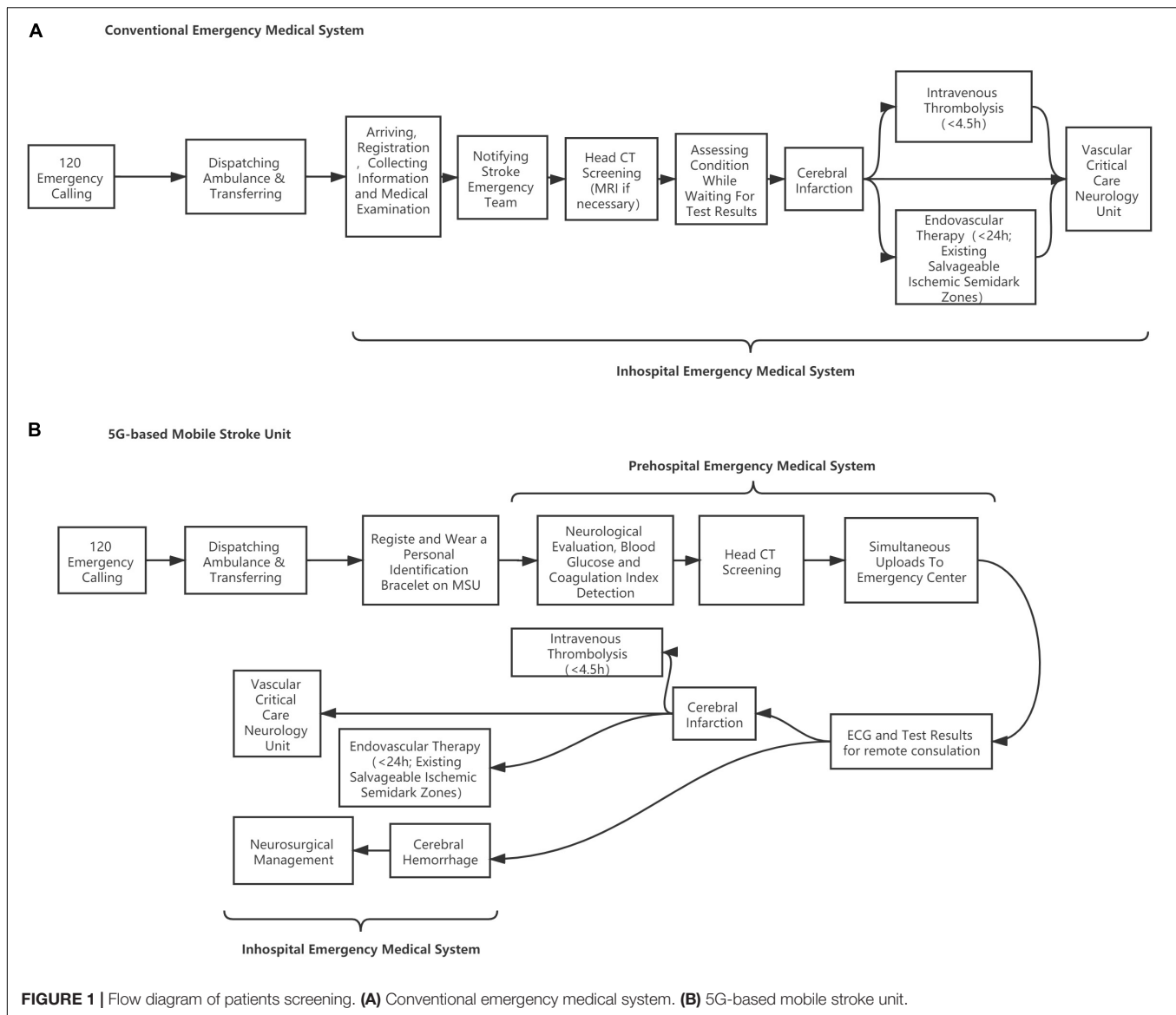### Intervention and Comparison

The case group is treated in the MSU, which is designed to establish a treatment unit integrating neurological symptom examination and CT diagnosis, achieving intravenous thrombolytic therapy and remote consultation at the first moment. During transportation, the physician can carry out neurological evaluation (NIHSS scores), blood glucose, coagulation index detection, and head CT scanning on the ambulance where data are transmitted to the stroke center in real time through 5G networks for technical support and treatment guidance from experts. Once the patient is recognized as suitable for thrombolysis, t-PA treatment will be given within the "golden time" of stroke management. The MSU team includes a paramedic, a stroke doctor, and a neuroradiologist, integrating the conventional EMS in a mixed urban–rural environment. The patient is evaluated for vital signs and neurological impairment followed by head CT screening and blood biochemical examination. The patients who meet the requirements of intravenous thrombolysis will be given t-PA treatment on the MSU vehicle after the informed consent is signed. Those who are not suitable for intravenous thrombolysis will be transported to the stroke center for further treatment. If necessary, remote consultation will be carried out through a customized telemedicine system based on 5G technologies. The MSU adopts a 7-day 24-h working system. In contrast, the control group is treated through conventional EMS in which the city emergency medical rescue center dispatches an ordinary ambulance. Head CT screening, blood biochemical examination, and the followed t-PA treatment (if suitable) will be performed after patients are delivered to the hospital's emergency center (Nor et al., 2005) (see **Figure 2**).

Primary and Secondary Outcomes

The primary endpoint is the utility-weighted modified Rankin Scale (uw-mRS) at 90 days assessed with a telephone interview. Secondary endpoints include time-dependent phenomena such as the alarm to CT scan completed time, the alarm to treatment decision time, the alarm to thrombolytic time, quality of life assessed with EQ-5D at follow-ups over 5 years, symptomatic intracranial hemorrhage combined with NIHSS score, as well as cost-effectiveness.

Sample Size Estimation

Previous studies suggested that the difference in mean 90d uw-mRS between groups ranged from 0.024 to 0.25. However, according to our pilot study data, we anticipate that the difference in 90d mean uw-mRS is 0.09 (0.59 vs. 0.50) with a standard deviation of 0.5 in both groups. Considering a type-I error of 0.05, a study power of 0.8, and a two-sided test, we included a total sample size of 484 participants after considering a 10% dropout rate, each group with 242 participants.

FIGURE 1 | Flow diagram of patients screening. **(A)** Conventional emergency medical system. **(B)** 5G-based mobile stroke unit.

Statistical Analysis

We calculate the sample size by comparing two independent samples. A *t*-test compares the mean uw-mRS at 90 days and corresponding two-sided 95% confidence intervals if the assumption of normality is not valid. Although the mRS is a primary endpoint, the difference among the uw-mRS categories is significant, and the *t*-test assumption and central limit theorem are probably met. The calculation of uw-mRS will be adjusted for baseline uw-mRS and baseline covariates associated with mRS in a linear regression model. Stratified analyses of the primary outcome and pooled measures are conducted by the Cochran–Mantel–Haenszel analyses and multiple ordinal regressions. We use a proportional odds model to process dichotomized outcomes of uw-mRS 0-1 vs. 2-6 with binary logistic regression. Participants in the intervention group who give up during the program will be excluded from the analysis. In addition, subjects in both treatment groups will be excluded from the

protocol analysis if any violations of the following protocols after randomization and during intervention and follow-up. All analyses are performed by SPSS 27.0.

Besides, we explore the missing data and compare the distribution of critical variables. Suppose there is a reasonable amount of missing data and the data summary indicates that the data are missing at random. In that case, all analyses will be performed after multiple imputations of missing data using baseline variables as auxiliary variables.

DISCUSSION

This study explores whether stroke patients clinically benefit from MSU deployment at 90 days. Given that many countries have encountered problems resulting from the increasing elderly population and related burden of cerebrovascular diseases,

FIGURE 2 | Regular care life chain versus 5G-based SSES life chain.
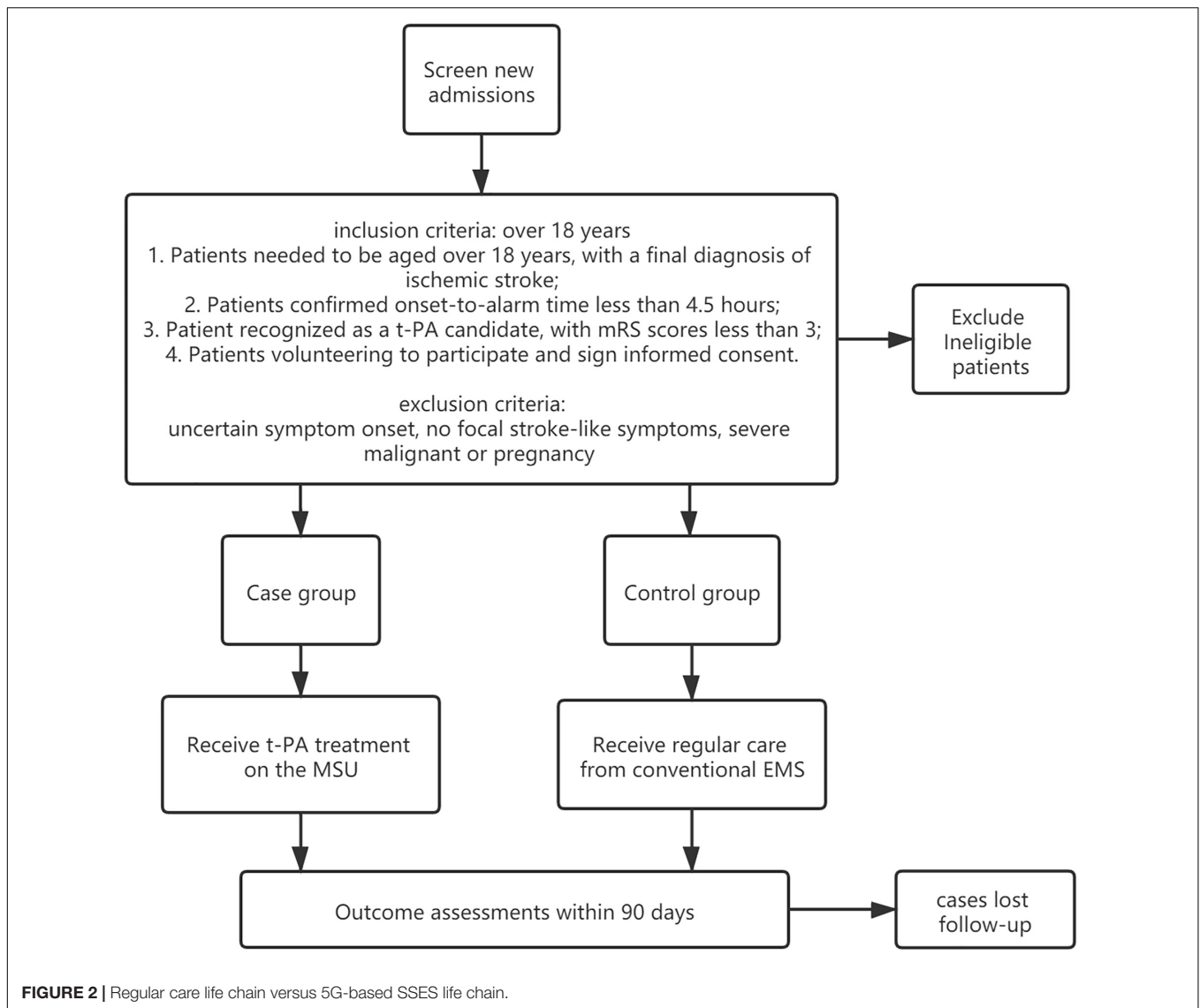
this finding could project some hope on emergency care based on the latest mobile networks and state-of-the-art devices to relieve stroke-related problems. As an expensive and complicated intervention, prehospital stroke management presents different models globally, making its clinical outcomes and cost-effectiveness difficult to evaluate, thus limiting its widespread utilization. Although some famous research works about the MSU gain better results about the clinical application (Kunz et al., 2016; Ebinger et al., 2021), the evidence is insufficient due to the limited sample size, unstandardized disposition of devices, and economic conditions of varied regions in the world. Therefore, a prospective controlled trial based on China's experience can provide healthcare decision-makers with clinical and administrative data in developing countries. However, selection bias by distributing patients according to MSU availability is hardly avoided, potentially causing the baseline information to be divided in the end. Second, the accurate data of uw-mRS are hardly accessed through telephone interviews. Therefore, we try to eliminate the offset by conducting multi-dimensional follow-ups through the Wechat survey applet. Third, a potential challenge is that it is difficult to identify patients with suspected stroke to suitable distribution in the dispatch center after an emergency call was made, thus making the prehospital stroke management unaccessible. Limited availability weakens a clear comparison group with all critical factors of a prospective study where MSU is compared to regular care. Overall, potential bias will be minimized by operationalized standards and adjustment for baseline parameters.

PATIENT AND PUBLIC INVOLVEMENT

Acute stroke patients are recruited for this research. The dissemination plan for the overview includes promotion via social media, presentation at conferences, and dissemination to patient advocacy groups.

ETHICS STATEMENT

The studies involving human participants were reviewed and approved by Ya'an People's Hospital (Approval No. 2020-24). The patients/participants provided their written informed consent to participate in this study.

AUTHOR CONTRIBUTIONS

JW provided the idea of this research and wrote the draft protocol. GG and BZ completed the details of the protocol. KH, QY, and JJ participated in the study design and literature review. XD was responsible for statistical analysis. All authors contributed to the article and approved the submitted version.

FUNDING

REFERENCES

Bowry, R., and Grotta, J. C. (2017). Bringing Emergency Neurology to Ambulances: mobile Stroke Unit. *Semin. Respir. Crit. Care Med.* 38, 713–717. doi: 10.1055/s-0037-1607994

Ebinger, M., Siegerink, B., Kunz, A., Wendt, M., Weber, J. E., Schwabauer, E., et al. (2021). Association Between Dispatch of Mobile Stroke Units and Functional Outcomes Among Patients With Acute Ischemic Stroke in Berlin. *JAMA* 325, 454–466. doi: 10.1001/jama.2020.26345

Kunz, A., Ebinger, M., Geisler, F., Rozanski, M., Waldschmidt, C., Weber, J. E., et al. (2016). Functional outcomes of prehospital thrombolysis in a mobile stroke treatment unit compared with conventional care: an observational registry study. *Lancet Neurol.* 15, 1035–1043. doi: 10.1016/S1474-4422(16)30209-6

Nor, A. M., Davis, J., Sen, B., Shipsey, D., Louw, S. J., Dyker, A. G., et al. (2005). The Recognition of Stroke in the Emergency Room (ROSIER) scale: development and validation of a stroke recognition instrument. *Lancet Neurol.* 4:727. doi: 10.1016/s1474-4422(05)70201-5

Nyberg, E. M., Cox, J. R., Kowalski, R. G., Vela-Duarte, D., Schimpf, B., and Jones, W. J. (2018). Mobile Stroke Unit Reduces Time to Image Acquisition and Reporting. *AJNR Am. J. Neuroradiol.* 39, 1293–1295. doi: 10.3174/ajnr.A5673

Peisker, T., Koznar, B., Stetkarova, I., and Widimsky, P. (2017). Acute stroke therapy: a review. *Trends Cardiovasc. Med.* 27, 59–66.

Powers, W. J., Rabinstein, A. A., Ackerson, T., Adeoye, O. M., Bambakidis, N. C., Becker, K., et al. (2018). 2018 Guidelines for the Early Management of Patients With Acute Ischemic Stroke: a Guideline for Healthcare Professionals From the American Heart Association/American Stroke Association. *Stroke* 49, e46–e110.

Powers, W. J., Rabinstein, A. A., Ackerson, T., Adeoye, O. M., Bambakidis, N. C., Becker, K., et al. (2019). Guidelines for the Early Management of Patients With Acute Ischemic Stroke: 2019 Update to the 2018 Guidelines for the Early Management of Acute Ischemic Stroke: a Guideline for Healthcare Professionals From the American Heart Association/American Stroke Association. *Stroke* 50, e344–e418.

Tsivgoulis, G., Geisler, F., Katsanos, A. H., Kõrv, J., Kunz, A., Mikulik, R., et al. (2018). Ultraearly Intravenous Thrombolysis for Acute Ischemic Stroke in Mobile Stroke Unit and Hospital Settings. *Stroke* 49, 1996–1999. doi: 10.1161/STROKEAHA.118.021536

Yamal, J. M., Rajan, S. S., Parker, S. A., Jacob, A. P., Gonzalez, M. O., Gonzales, N. R., et al. (2018). Benefits of stroke treatment delivered using a mobile stroke unit trial. *Int. J. Stroke* 13, 321–327.

Zhou, T., Zhu, L., Wang, M., Li, T., Li, Y., Pei, Q., et al. (2021). Application of Mobile Stroke Unit in Prehospital Thrombolysis of Acute Stroke: experience from China. *Cerebrovasc. Dis.* 50, 520–525. doi: 10.1159/000514370

Platelet Deposition Onto Vascular Wall Regulated by Electrical Signal

Mingyan Wang[1], Wei Zhang[1,2] and Zhi Qi[1]*

[1] Department of Basic Medical Sciences, School of Medicine, Xiamen University, Xiang'an Nan Lu, Xiamen, China, [2] Xiamen Institute of Cardiovascular Diseases, The First Affiliated Hospital of Xiamen University, School of Medicine, Xiamen University, Xiamen, China

Platelets deposition at the site of vascular injury is a key event for the arrest of bleeding and for subsequent vascular repair. Therefore, the regulation of platelet deposition onto the injured site during the process of platelet plug formation is an important event. Herein, we showed that electrical signal could regulate the deposition of platelets onto the injured site. On the one hand, the area of platelet deposition was reduced when the cathode of the applied electric field was placed at the injured site beforehand, while it was increased when the anode was at the site. On the other hand, if a cathode was placed at the injured site after the injury, the electrical signal could remove the outer layer of the deposited platelets. Furthermore, an electric field could drive rapid platelet deposition onto the blood vessel wall at the site beneath the anode even in uninjured blood vessels. Platelet deposition could thus be manipulated by externally applied electric field, which might provide a mechanism to drive platelet deposition onto the wall of blood vessels.

Keywords: platelet, deposition, primary hemostasis, transvascular electric potential, vascular injury

INTRODUCTION

Living cell responding to imposed electric field (EF) by migrating toward cathode or anode is known as electrotaxis or galvanotaxis. After its discovery one century ago (Sato et al., 2007), various cell types have been reported to migrate under EF. These cells include cancer cells (Djamgoz et al., 2001; Yan et al., 2009; Sun et al., 2012; Pu et al., 2015), human primary T cells (Arnold et al., 2019), lymphocytes (Lin et al., 2008), macrophages (Hoare et al., 2016; Sun et al., 2019), neural stem cells (Feng et al., 2012), and oligodendrocyte precursor cells (Li et al., 2015). Moreover, it has been shown that EF plays crucial roles in many physiological and pathophysiological processes, such as wound healing (Zhao et al., 2006), cell division (Zhao et al., 1999), stem cell migration (Feng et al., 2012; Funk, 2015), nerve regeneration (Song et al., 2004), metastatic process (Djamgoz et al., 2001), T cell functions (Arnold et al., 2019), and macrophage phagocytic uptake (Hoare et al., 2016; Sun et al., 2019). For example, under the stimulus of EF, cells could migrate in a specific direction to repair tissue damage (Zhao et al., 2006). Therefore, exogenous EF has been widely applied to accelerate the wound-healing process (Balakatounis and Angoules, 2008; Hunckler and de Mel, 2017; Luo et al., 2021).

Sialic acid (N-acetyl-neuraminic acid), a negatively charged sugar and constituent of many glycoproteins and gangliosides, is known to confer the bulk of negative charges to mammalian cell surfaces. Platelets contain sialic acid (Born and Palinski, 1985; Crook, 1991), which makes the platelet has an overall electronegative charge on its surface (Crook and Crawford, 1988). Due to this property, an electric field has been exerted on platelets suspended in the electrolytic medium for electrophoresis, which can be retrieved from the study by Abramson (1928). These electrophoretic

investigations of platelets have been carried out to determine the ionic groups responsible for the charge (Seaman and Vassar, 1966; Nomura and Takagi, 1974; Menashi et al., 1981), to judge the effect of drugs on platelets (Betts et al., 1968; Florence and Rahman, 2011; Wang et al., 2017), or to estimate the electrophoretic mobility of platelets in patients with various clinical conditions (Grottum, 1968; Karppinen and Halonen, 1970). In addition, an electric field has been applied onto a cylindrical chamber or capillary to study interactions between small molecules and platelets during their aggregation (Seaman and Vassar, 1966; Wang et al., 2015, 2017). However, whether the electric field could direct platelets toward the vascular wall *in vivo* to facilitate platelet deposition over there, especially in an injured blood vessel, has not been studied.

The main physiological function of platelets is to participate in primary hemostasis through three distinct steps: adhesion, activation, and aggregation. During these steps, a chain of events is triggered, ultimately leading to the formation of a platelet plug to prevent blood loss as rapidly as possible (Ruggeri and Mendolicchio, 2007; Versteeg et al., 2013). The first step to form the platelet plug is that the circulating platelets need to deposit to the exposed injured surface. Given their negative surface charge, it could be reasoned that EF might act as a potential guidance cue to regulate the deposition of platelet onto the injured surface of blood vessels. To test this hypothesis, we conducted experiments to investigate whether an applied EF could regulate the deposition of platelets onto the blood vessels.

MATERIALS AND METHODS

Animals

Male KM mice (weighing 20–30 g, Xiamen University Laboratory Animal Center) were anesthetized by intraperitoneal injection of 1.5% pentobarbital sodium. Animal care and experiments were performed in accordance with the procedures approved by the Animal Care and Use Committee of Xiamen University.

Experimental Materials

Pentobarbital sodium was from Sinopharm Chemical Reagent (China). 5, 6-carboxyfluorescein-succinimidyl-ester (CFSE) was from Invitrogen (Molecular Probes, Eugene, OR, United States). Poly-dimethyl-siloxane (PDMS; Sylgard 184, Dow Silicones, Midland, MI, United States) was from Dow Silicones Co. (United States). Stainless steel microwires were from Shanghai Lei Yu Materials Co. Ltd. (China). Neuraminidase was from Shanghai Canspec S&T Co. LTD (China).

Assessment of Platelet Deposition by Intravital Microscopy

Platelet deposition in the mesenteric vessels (diameter from 20 to 80 μm) of anesthetized mice was visualized using an inverted fluorescence microscope (IX7.1, Olympus, Japan) equipped with a digital camera. Images were collected as time series with acquisition rates of 10 frames/s. Images were analyzed using ImageJ (NIH, Bethesda, MD, United States). Vessel wall injury

was performed mechanically by puncturing the blood vessel wall with a glass microelectrode. The starting time of punctured injury was from the moment when the microelectrode was rapidly withdrawn from the puncture site.
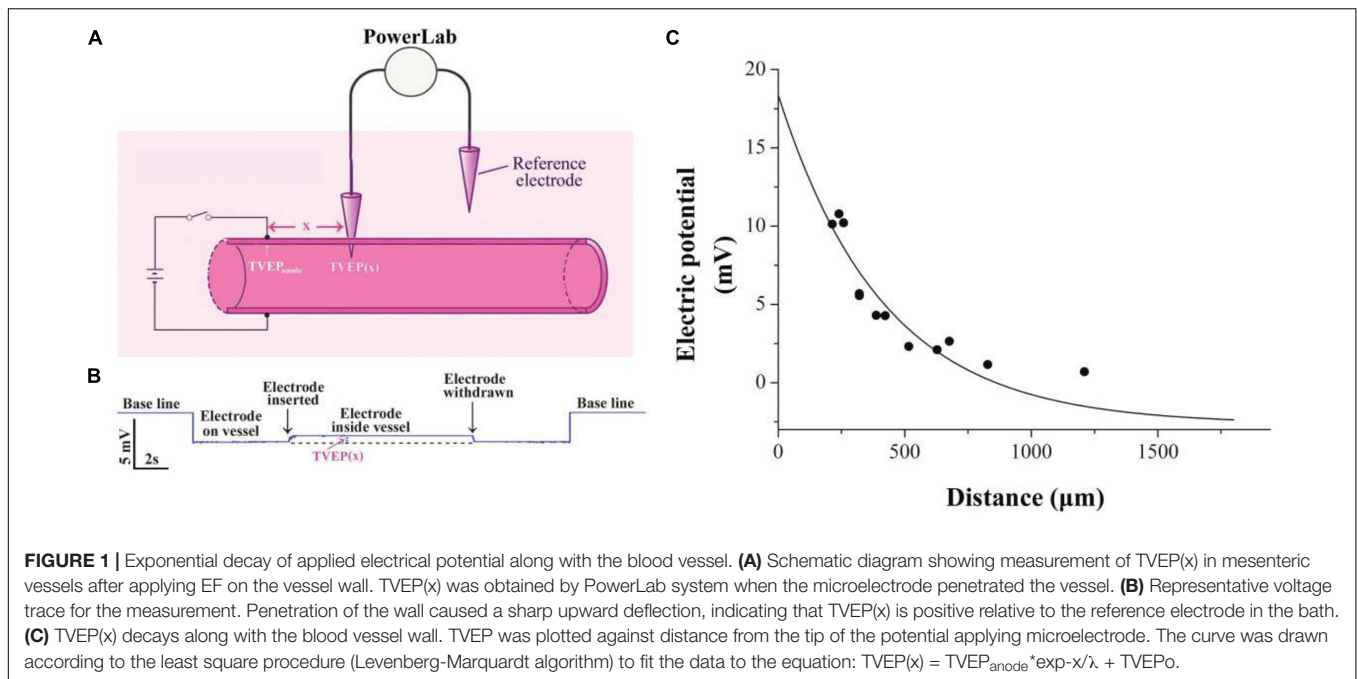
Transvascular Electric Potential Measurement

Transvascular electric potential (TVEP) is defined as the potential inside the blood vessel relative to the reference electrode outside (**Figure 1A**). Its measurement is essentially the same as described previously (Fajac et al., 1998) with slight modifications. Glass microelectrodes were pulled from thin-walled borosilicate capillary tubes using a micropipette puller (model P-10, Narishige) with resistance in a range of 2–5 MΩ (tip diameter, 2–4 μm) when filled with Hanks' balanced salt solution (HBSS; Gibco, in mM): 1.26 $CaCl_2$, 0.49 $MgCl_2$, 0.41 $MgSO_4$, 5.33 KCl, 0.44 KH_2PO_4, 4.17 $NaHCO_3$, 137.9 NaCl, 0.34 Na_2HPO_4, and 5.56 D-glucose. Silver wire, the end of which was covered by a layer of AgCl, was inserted into the tubes to make Ag/AgCl microelectrodes. The TVEP was measured by a potential-measuring circuit that was connected to Bio Amp device PowerLab System (PowerLab 8/30; ADInstruments, Australia) through a pair of Ag/AgCl microelectrodes (**Figure 1A**). The tip of one microelectrode was placed outside the adventitia of the blood vessel to serve as the reference electrode. The tip of the other microelectrode that gently penetrated the intima of the vessel with the use of a micromanipulator served as the recording electrode. All data were acquired and transferred to a computer for further analysis by using Chart or Scope software (ADInstruments).

Platelet Isolation and Transfer

To isolate platelets, blood was withdrawn from the inferior vena cava of anesthetized donor mice, and platelet-rich plasma was prepared through sequential centrifugation. Platelets were then pelleted from platelet-rich plasma and gently resuspended in Tyrode's buffer (10 mmol/L HEPES, 12 mmol/L $NaHCO_3$, pH 7.4, 137 mmol/L NaCl, 2.7 mmol/L KCl, 5 mmol/L glucose). Platelets were allowed to rest in Tyrode's buffer for 30 min at room temperature. Subsequently, platelets were labeled with CFSE (peak absorbance, 492 nm; peak emission, 518 nm) (5 mmol/L; Invitrogen) and centrifuged at 2000 g for 15 min to obtain the labeled platelets as described previously (Devi et al., 2010). Then, the platelets were slowly infused intravenously and visualized by using fluorescence microscope.

Fabrication of the Circular Microfluidic Channel

The microelectrode penetrable circular microfluidic channel with a diameter of 50 μm was fabricated according to a previous report (Qi et al., 2020). Briefly, a mixture of PDMS and its curing agent (10:1) was poured into an enclosed space, in which a stainless steel microwire with a diameter of 50 μm was aligned. After 30 min of heating under 75°C, the PDMS with the 50 μm microwire was placed into an ethanol pool for 12 h to swell slightly (swelling coefficient: 1.04) wetting the interface (Jia et al., 2008). Then, the

FIGURE 1 | Exponential decay of applied electrical potential along with the blood vessel. **(A)** Schematic diagram showing measurement of TVEP(x) in mesenteric vessels after applying EF on the vessel wall. TVEP(x) was obtained by PowerLab system when the microelectrode penetrated the vessel. **(B)** Representative voltage trace for the measurement. Penetration of the wall caused a sharp upward deflection, indicating that TVEP(x) is positive relative to the reference electrode in the bath. **(C)** TVEP(x) decays along with the blood vessel wall. TVEP was plotted against distance from the tip of the potential applying microelectrode. The curve was drawn according to the least square procedure (Levenberg-Marquardt algorithm) to fit the data to the equation: TVEP(x) = TVEP$_{anode}$*exp-x/λ + TVEPo.

wire in the PDMS was drawn out manually by applying a gentle force leading to the formation of a 50 μm circular microfluidic channel in the PDMS.

Blood Sample

Blood samples of the mice were collected from the inferior vena cava of anesthetized donor mice and anticoagulated using heparin. The collected whole blood was perfused through the microfluidic channel using a syringe pump (model Ph.D 2000, Harvard Apparatus, United Kingdom). Prior to the sample perfusion, degassed PBS buffer was used to prime the channels to remove air bubbles. For neuraminidase-treated groups, the blood samples were incubated with neuraminidase (1 U/ml) for 30 min under 37°C.

Statistical Analysis

All data were shown as mean $\pm$ SEM. Data were analyzed statistically by one-way ANOVA followed by the Bonferroni test for multiple comparisons with Origin7.0 (Microcal Software, Inc., Northampton, MA, United States). An unpaired Student's t-test was used for two-group comparisons. Values of $p < 0.05$ were considered to be statistically significant.

RESULTS

Exponential Decay of External Applied Electrical Potential Along With the Blood Vessel

Practically, it is very difficult to measure the electric potential directly beneath the anode. Therefore, the TVEP at different positions relative to the anode (**Figures 1A,B**) was measured

for the estimation of the TVEP directly beneath the anode. For instance, each datum point in **Figure 1C** was the experimental measured TVEP at a corresponding distance from the tip of the anode when the outside adventitia is defined to be at ground potential (0 mV, reference electrode). We found that these potentials decayed exponentially along with the blood vessel according to the following equation:

$$TVEP(x) = TVEP_{anode} * \exp - x/\lambda + TVEPo \qquad (1)$$

where x is the distance from the anode to the potential measuring microelectrode, TVEP(x) is the TVEP at position x, TVEP$_{anode}$ is the TVEP directly beneath the anode, and TVEPo is the TVEP of the blood vessel under physiological condition without any external applied EF. The spatial constant, λ, characterizes the attenuation and quantifies the extent of the spread of the TVEP$_{anode}$ along with the blood vessel. For mesenteric vessels, TVEPo = $- 2.65 \pm 0.05$ mV ($n = 163$) was obtained. The TVEP(x) was measured by the potential measuring microelectrode, which impaled the vessel wall at various positions along the vessel. Fitting the experimental data to Eq. 1, we obtained the spatial constant $\lambda = 415.5 \pm 68.1$ μm. Based on this parameter, TVEP$_{anode}$ for each of the experiments could be calculated by using Eq. 1. The EF in a given direction at any point is defined as the negative gradient of the potential in that direction at that point. Therefore, based on Eq. 1, the strength of the EF directly below the tip of the anode can be calculated as:

$$\begin{aligned} EF &= - d\{TVEP(x)\}/dx \\ &= -d\{TVEP_{anode} * \exp - x/\lambda + TVEPo\}/dx \qquad (2) \\ &= TVEP_{anode} * e^{-x/\lambda}/\lambda \end{aligned}$$

For example, the TVEP$_{anode}$ for the experiment in **Figure 1** is +18.4 mV, and thus, the EF directly below the tip of the

anode is 44.3 mV/mm. This strength of the EF is within the range of EF that regulates the cellular signaling pathways (McCaig et al., 2005, 2009).

Electrical Signal Regulates the Deposition of Platelets Onto the Surface of Injured Blood Vessels

To study whether the manipulation of electrical signal affects platelet deposition *in vivo*, we initiated platelet deposition by mechanically puncturing the vessel wall of mouse mesenteric vessels with a glass micropipette (tip diameter 4–6 mm). Representative time series of images showing platelet deposition when −EF (cathode on the injured site), +EF (anode on the injured site), and under default hemostasis (no EF) are shown in **Figures 2A–C**, respectively. These images demonstrated that the deposited platelets were not solely increased but alternatively increased or decreased with time. Comparing the images under default hemostasis, we can find that −EF reduced the platelet deposition, while +EF enhanced the platelet deposition. This is clearly shown in **Figure 3A**, which is the statistical summary for the mean area of platelet deposition onto the injured site at each time point within 1 s. As shown in the figure, the mean area of the deposited platelet was significantly reduced by −EF, but was increased by +EF relative to that without EF for each time point, respectively. The maximal area of platelet deposition within 1 s (**Figure 3B**) showed that the mean maximal area

within 1 s of punctured injury without EF was $118.6 \pm 18.1\ \mu m^2$. When −EF was applied, the maximal size was reduced to $55.0 \pm 5.8\ \mu m^2$. In contrast, the maximal size within 1 s of punctured injury was $182.7 \pm 25.2\ \mu m^2$ if +EF was applied. These results suggested that the electrical signal could regulate the degree of platelet deposition.
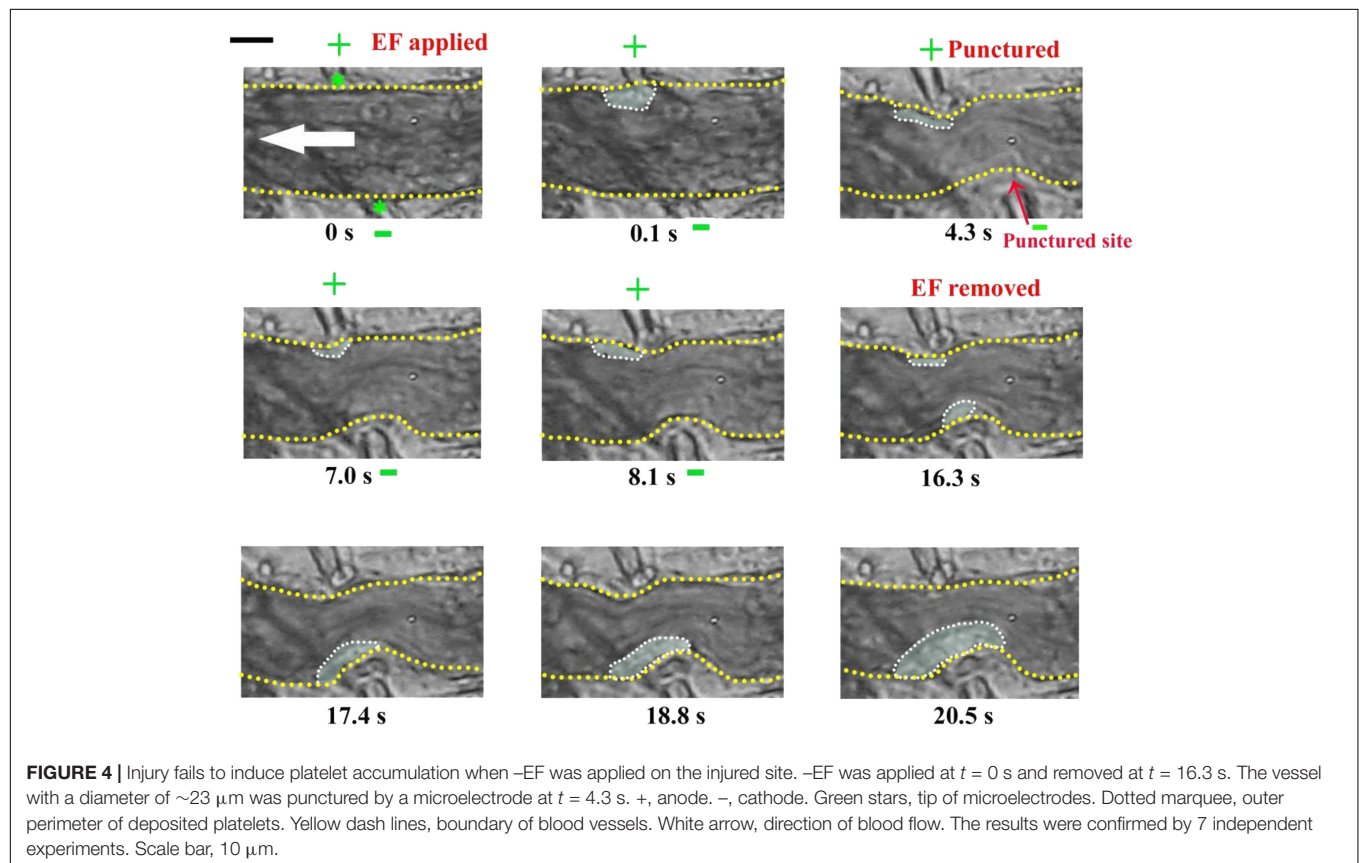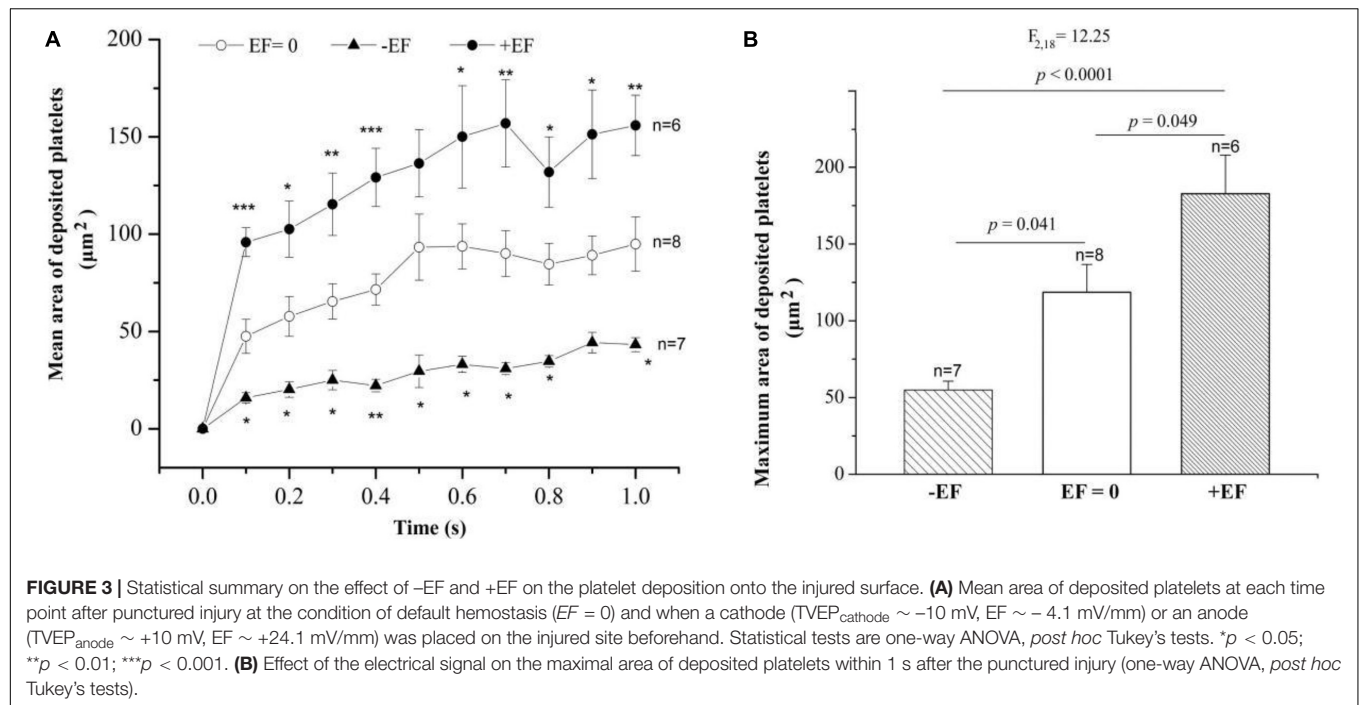
Interestingly, sometimes, the injury failed to induce platelet deposition if a cathode was placed at the injured site beforehand. For example, platelets did not deposit onto the punctured site from 4.3 to 8.1 s but deposited onto the uninjured area where the anode with TVEP$_{anode}$ of 8.4 mV (EF, 20.2 mV/mm) was placed on the injured site (0.1–8.1 s) (**Figure 4**). In contrast, when the applied EF was removed at t = 16.3 s, the platelet deposition appeared at the punctured site (white dotted marquee from 16.3 to 20.5 s). Meanwhile, the deposited platelets at the opposite side where the anode was once placed floated away. These data indicated that the polarity of the electrical signal plays an important role in platelet deposition onto the injured site.

The Outer Layer of the Deposited Platelets Could Be Removed if a Cathode Was Placed at the Injured Site After the Injury

To investigate whether the electrical signal could affect the injury-induced platelet deposition, we initiated platelet deposition by
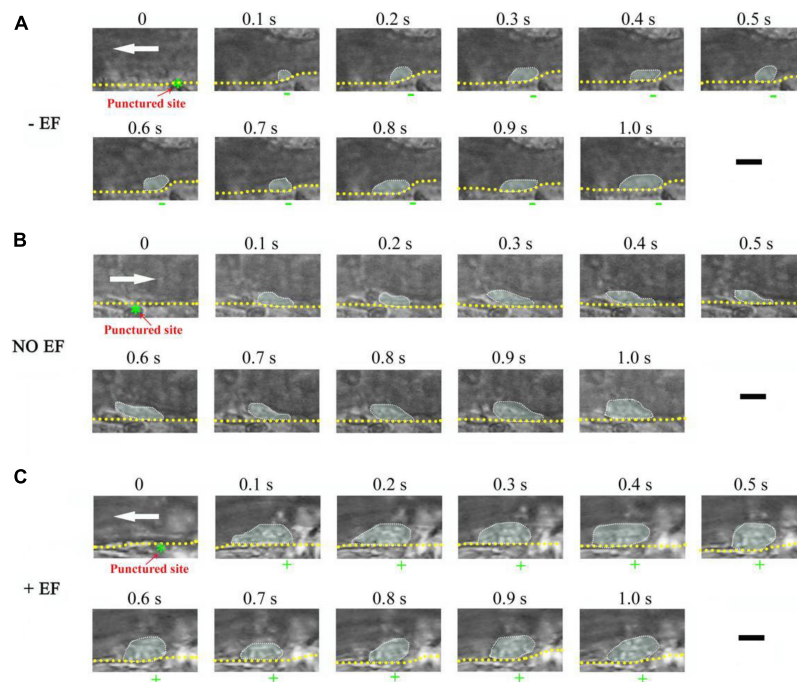
FIGURE 2 | Representative time series of images showing the effect of −EF and +EF on platelet deposition onto the injured surface of the mesenteric blood vessel. **(A)** Punctured injury induced platelet deposition when a cathode with TVEP$_{cathode}$ of −5.4 mV (EF, −13.0 mV/mm) was placed on the punctured site beforehand (vessel diameter, ∼28 μm). **(B)** Platelet deposition induced by punctured injury in the absence of EF (vessel diameter, 30 μm). **(C)** Punctured injury induced platelet deposition when an anode (green star) with TVEP$_{anode}$ of +6.7 mV (EF, 16.1 mV/mm) was placed on the punctured site beforehand (vessel diameter, 35 μm). The deposited platelets are highlighted and the outer perimeter of the area of the deposited platelets is circled with the dotted marquee according to the previous report (Nesbitt et al., 2009). +, anode. −, cathode. White arrow, direction of blood flow. Yellow dotted lines, boundary of blood vessels. Scale bar, 10 μm.

FIGURE 3 | Statistical summary on the effect of –EF and +EF on the platelet deposition onto the injured surface. **(A)** Mean area of deposited platelets at each time point after punctured injury at the condition of default hemostasis ($EF = 0$) and when a cathode ($TVEP_{cathode} \sim -10$ mV, EF ~ -4.1 mV/mm) or an anode ($TVEP_{anode} \sim +10$ mV, EF $\sim +24.1$ mV/mm) was placed on the injured site beforehand. Statistical tests are one-way ANOVA, *post hoc* Tukey's tests. *$p < 0.05$; **$p < 0.01$; ***$p < 0.001$. **(B)** Effect of the electrical signal on the maximal area of deposited platelets within 1 s after the punctured injury (one-way ANOVA, *post hoc* Tukey's tests).

FIGURE 4 | Injury fails to induce platelet accumulation when –EF was applied on the injured site. –EF was applied at $t = 0$ s and removed at $t = 16.3$ s. The vessel with a diameter of ~ 23 μm was punctured by a microelectrode at $t = 4.3$ s. +, anode. –, cathode. Green stars, tip of microelectrodes. Dotted marquee, outer perimeter of deposited platelets. Yellow dash lines, boundary of blood vessels. White arrow, direction of blood flow. The results were confirmed by 7 independent experiments. Scale bar, 10 μm.

puncturing the vessel wall of the mouse mesenteric vessel with a glass microelectrode. At this condition without an applied EF (default hemostasis), the platelet deposition clearly appeared in the injured area after the punctured injury (white dotted marquee from 0.1 to 21.4 s) (**Figure 5**). Interestingly, the inner layer of the deposited platelets could not be removed

even a cathode of the applied EF was placed on the injured site (from 21.5 to 22 s). At the same time, accompanying with the reduction of the size of the deposited platelets at the injured site, we observed that platelets accumulated at

the opposite side where the anode was placed, even though there was no vascular injury. These observations suggested that the electrical signal could eliminate platelets on the surface and suppress further platelet deposition, but could not
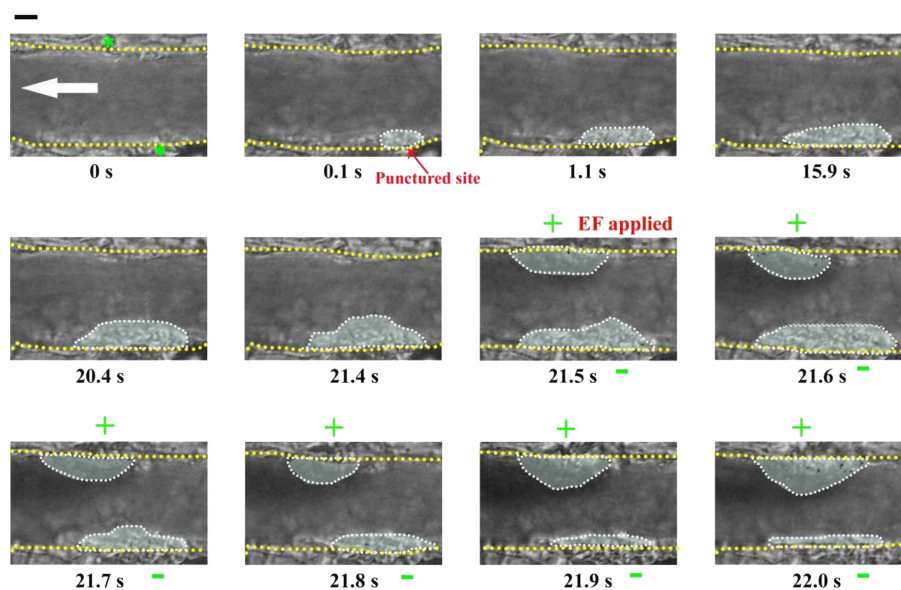
FIGURE 5 | Electrical signal could not eliminate platelets that had already been accumulated in the core region of the injury. First panel (t = 0 s): Configuration for applying EF on the mesenteric vessel with a diameter of ∼39 μm. Yellow dotted lines, boundary of the vessel walls. White arrow, direction of blood flow. Green stars, tip of microelectrodes. Dotted marquee, outer perimeter of deposited platelets. The vessel wall was punctured at t = 0 s by a microelectrode. EF was applied at t = 21.5 s with TVEP$_{anode}$ of +18.6 mV (EF, 44.8 mV/mm). +, anode. −, cathode. Scale bar, 10 μm. The results were reproduced in 9 independent experiments.
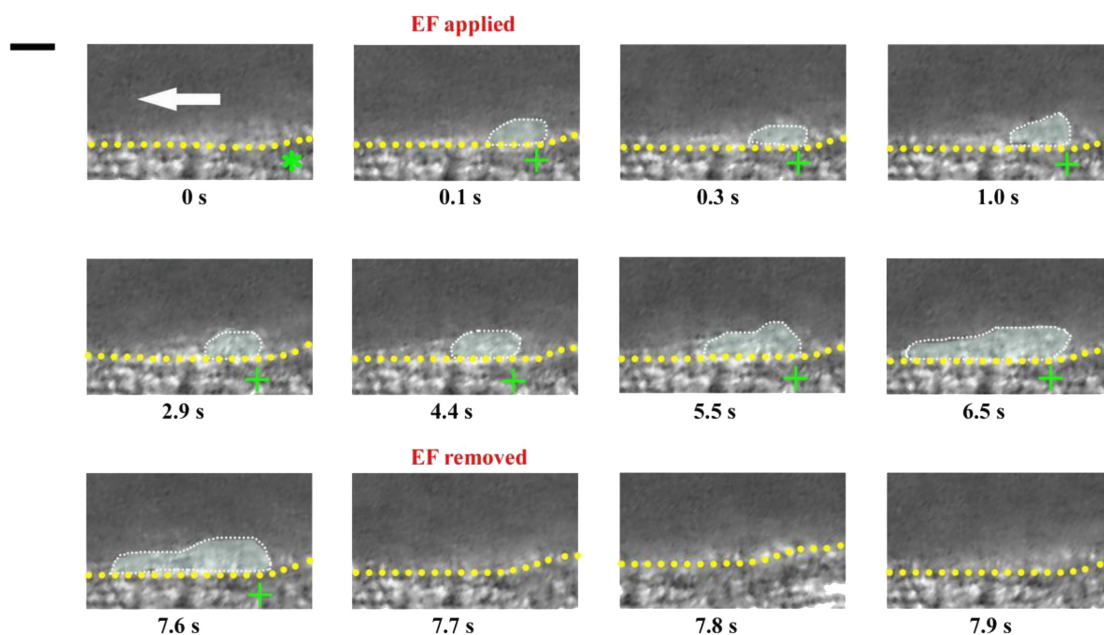
FIGURE 6 | Electrical signal causes platelet accumulation in uninjured mesenteric vessels. Intravital image sequence with TVEP$_{anode}$ of +6.9 mV (EF, 16.6 mV/mm) in an uninjured mesenteric vessel (diameter ∼ 55 μm). The EF was applied at t = 0 s and removed at t = 7.7 s. Green stars, tip of microelectrodes. Yellow dotted lines, boundary of blood vessels. White dotted marquee, deposited platelets. Scale bar, 10 μm. White arrow, direction of blood flow. +, anode. −, cathode. The results were reproduced in 9 independent experiments.
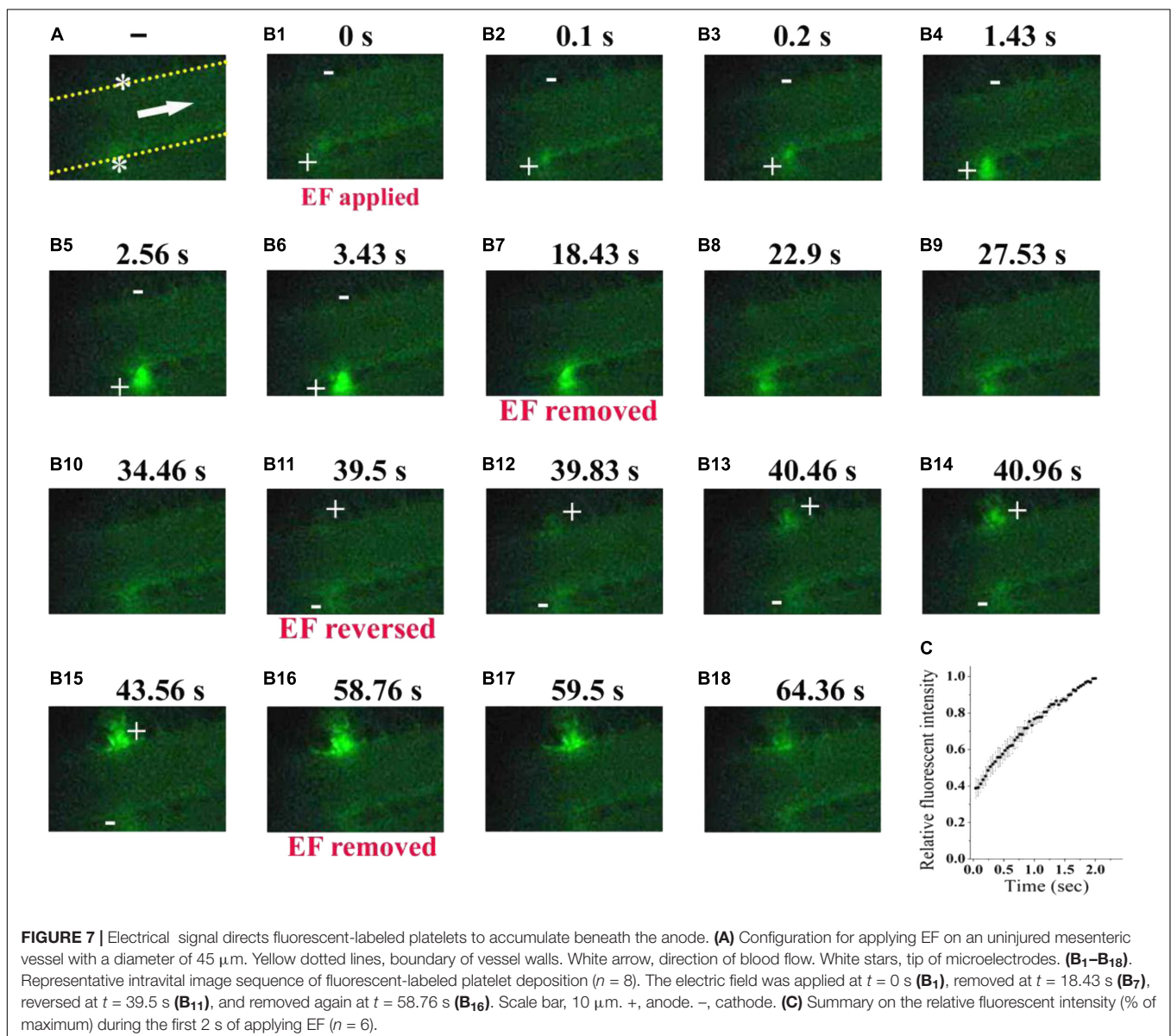
eliminate platelets that had already been deposited in the core region of the injury.

Electrical Signal Could Drive Platelet Deposition Beneath the Anode Even on Uninjured Blood Vessels

If an electrical signal *per se* could drive platelet deposition, its action should not be affected by other injury-induced biophysical or biochemical factors. This means that an EF could also drive platelet deposition even on uninjured blood vessels. To test this inference, we carried out experiments on mouse mesenteric vessels that were not injured. There was no platelet deposition before the application of an EF ($t = 0$, **Figure 6**). In contrast, small platelet deposition was present when the anode with $TVEP_{anode}$ of +6.9 mV (EF, 16.6 mV/mm) was applied in spite of no vascular

injury ($t = 0.1$ s, **Figure 6**). After that, the area of the deposited platelets was gradually increased to some extent. Notably, the deposited platelets were floating away once the applied EF was removed ($t = 7.7$ s **Figure 6**), indicating that electrical signal *per se* could cause platelet deposition at millisecond time scale even in the uninjured blood vessels *in vivo*.

To further confirm the ability of electrical signal to drive platelet deposition onto the uninjured vessel wall, we labeled platelets with fluorescent dye (**Figure 7A**). With $TVEP_{anode}$ of +16.5 mV 750 (EF, 39.7 mV/mm, **Figure 7B_1**), the fluorescent-labeled platelet accumulation clearly appeared underneath the anode after 100 ms of the EF application (**Figure 7B_2**), and the fluorescent intensity beneath the anode was gradually increased with time even without a vascular injury (**Figures 7B_2–B_6,C**). In contrast, the fluorescent intensity was gradually decreased when the EF was removed (**Figures 7B_7–B_10**). Furthermore,

FIGURE 7 | Electrical signal directs fluorescent-labeled platelets to accumulate beneath the anode. **(A)** Configuration for applying EF on an uninjured mesenteric vessel with a diameter of 45 μm. Yellow dotted lines, boundary of vessel walls. White arrow, direction of blood flow. White stars, tip of microelectrodes. **(B_1–B_18)**. Representative intravital image sequence of fluorescent-labeled platelet deposition ($n = 8$). The electric field was applied at $t = 0$ s **(B_1)**, removed at $t = 18.43$ s **(B_7)**, reversed at $t = 39.5$ s **(B_11)**, and removed again at $t = 58.76$ s **(B_16)**. Scale bar, 10 μm. +, anode. −, cathode. **(C)** Summary on the relative fluorescent intensity (% of maximum) during the first 2 s of applying EF ($n = 6$).

when the polarity of the EF was reversed (**Figure 7B$_{11}$**), the fluorescent intensity was gradually increased on the opposite side of the vessel (**Figures 7B$_{11}$–B$_{15}$**) and gradually decreased when the EF was removed (**Figures 7B$_{16}$–B$_{18}$**). These observations indicated that the electrical signal *per se* was sufficient to induce platelet deposition.

Electrical Signal-Triggered Platelet Deposition Is Significantly Reduced by Neuraminidase Treatment

The above results suggested that the underpinning mechanism of the electrical signal should be based on the surface charge of platelets. However, the platelet deposition onto the injured surface *in vivo* is a complex phenomenon. It has been reported that treatment with neuraminidase leads to a reduction in the electrokinetic charge (Seaman and Vassar, 1966) or electrophoretic mobility of platelets (Nomura and Takagi, 1974). Therefore, to further verify whether the effect of electrical signal is based on the surface charge of platelets, we reduced platelet surface charge by using neuraminidase to remove sialic acid residues and carried out experiment in a microfluidic system. There were no platelets on the tip of the anode without EF. By applying EF, we observed that platelets deposited onto the tip of the anode in the microfluidic channel within 100 ms (fps = 10) no matter whether the blood samples were treated with neuraminidase or not. However, the average area of the deposited platelets was significantly reduced by neuraminidase treatment at every time points comparing with that without neuraminidase treatment (**Figure 8**). The maximal area of the deposited platelets within 1 s was $19.9 \pm 3.1\ \mu m^2$ for neuraminidase-treated group, while it was $52.1 \pm 4.0\ \mu m^2$ for the group without neuraminidase treatment. These results provided further evidence that the effect of EF on platelet deposition was due to the surface charge of platelets.

DISCUSSION

The possible relationship between electrical signal and thrombus formation has been studied since more than half a century ago (Sawyer et al., 1953, 1960; Sawyer and Pate, 1953; Sawyer and Deutsch, 1955; Sawyer and Deutch, 1956; Schwartz, 1959; Schwarz and Richardson, 1961), but is neglected at the present time. From 1950s to 1970s, Sawyer and colleagues carried out a series of researches to show that electrical signal could not only trigger but also prevent thrombosis. However, most of their studies focused on how strong the electrical signal should be to cause thrombus formation. These experiments revealed that thrombosis occurs on electrodes in most cases when the potential of the electrode is equal to or greater than +300 mV (Sawyer et al., 1965; Sawyer and Sprinivasan, 1967). However, such electrical signal might be too strong. Since most of the blood cells carry negative surface charges (Born and Palinski, 1985), it is likely that a strong electrical signal (equal to or greater than +300 mV)
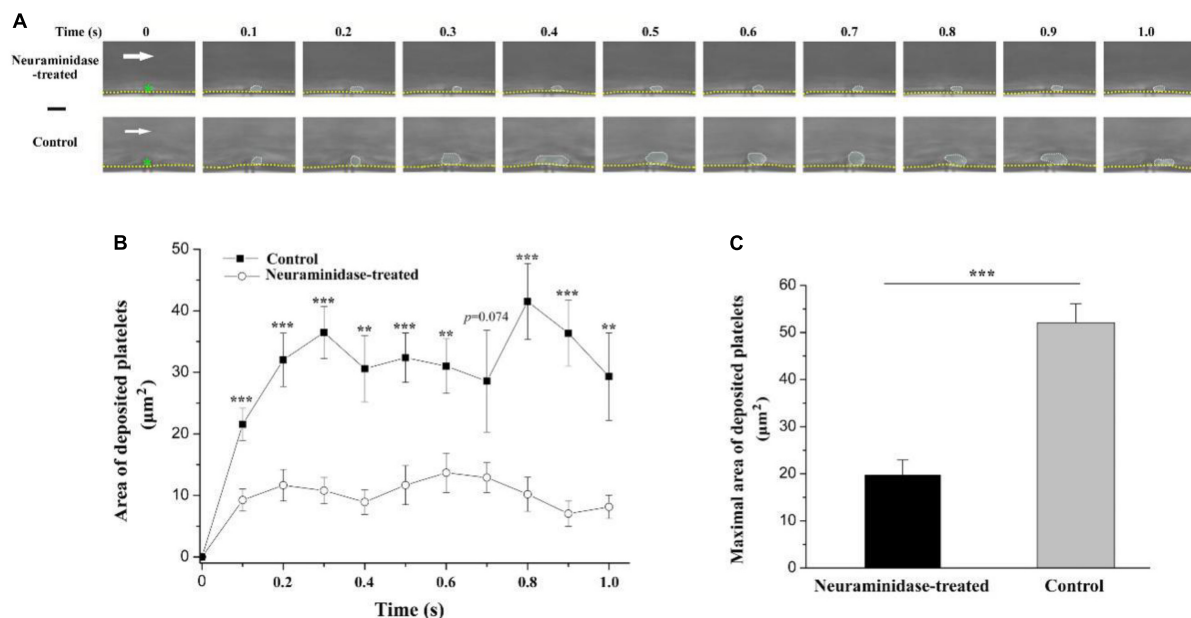
FIGURE 8 | Effect of neuraminidase treatment on EF-induced platelet deposition in microfluidic channel. **(A)** Representative time series of images on deposited platelets under shear rate of $200\ s^{-1}$ in the period of 1 s beginning from the start of the blood flow for neuraminidase-treated (1 U/ml) group (EF = 19.7 mV/mm) and control group (EF = 20.1 mV/mm). White dotted marquee, perimeter of deposited platelets. Green star, tip of microelectrode. Yellow dash lines, boundary of microfluidic channel. White arrow, direction of blood flow. Bar = 10 μm. **(B)** Statistical summary on the time courses of areas of deposited platelets for the group treated with (n = 10) or without (n = 9) neuraminidase (1 U/ml) under shear rate of $200\ s^{-1}$. The average values of EF for the group treated with or without neuraminidase were 20.6 ± 1.2 and 21.4 ± 1.3 mV/mm, respectively. **(C)** Statistical summary on the maximal area of deposited platelets for the group treated with or without neuraminidase. Unpaired Student's t-test was used for statistical analysis. $**p < 0.01$; $***p < 0.001$.

could result in the aggregation of blood cells, including red blood cells, white blood cells, and platelets, to the positive electrode.

There were no platelets on the tip of the microelectrode without EF. If an EF was applied, platelets were deposited onto the tip of the anode within 100 ms (fps = 10) in most of the experiments. It is noteworthy that the area of the deposited platelets at 100 ms was about half to two-third of the maximal area (**Figures 2C**, **3A**, **6**). Electrostatic interaction is mediated by an electric field, which takes action, not instantaneous, but propagates in time in a similar manner to that of light. Therefore, the applied electric field can take action immediately on the platelets from the moment of its application. That is, the platelets attracted by the tip of the anode microelectrode should be increased with time from the onset of the applied EF. As demonstrated in **Figure 3A**, the area of the deposited platelets reached about two-third of the maximal area after the first 100 ms. However, in the flowing blood, the larger the area of the deposited platelets, the larger the shear force on them. So, we observed that the area of the deposited platelets was not solely increased but was alternatively increased or decreased with time (**Figures 2**, **6**, **8**).

Circulating platelets are involved in different processes such as triggering inflammation, fighting microbial infection, promoting tumor metastasis, and embryonic blood/lymphatic vessel separation. Nevertheless, their principal function still remains stopping hemorrhage following vascular injury by forming platelet plug in primary hemostasis. Therefore, it is desired that only platelets but no other blood cells could be regulated to deposit onto the injured site during the process of platelet plug formation. The sizes of RBC and leukocyte are much larger than that of platelets, the mean diameter of which is 1.50 μm for mice (Tsakiris et al., 1999; Thon and Italiano, 2010). Therefore, based on the difference in sizes between platelets and other blood cells, we found that the deposited cells at the injured site were predominantly platelets when a smaller electrical signal (e.g., TVEP$_{anode}$, less than 20 mV) was applied. This might be due to the two following reasons: (1) The charge density of platelets is larger than that of other blood cells (Greger and Thomas, 1960;

Born and Palinski, 1985); (2) The platelet margination effect, i.e., the number of platelets in the vicinity of the vessel wall is much more than that in the center of the vessel (Tangelder et al., 1985; Tokarev et al., 2011a,b). It means that electrical signal could exert much larger force on the platelets than on other blood cells near the blood vessel wall. Therefore, platelets rather than other blood cells are overwhelmingly deposited onto the injured site when a smaller electrical signal was applied. For example, we found that the smaller electrical signal with TVEP$_{anode}$ of less than 20 mV could only cause transient platelet deposition, as the deposited platelets were washed away if the applied EF was removed. Thus, our data suggest that manipulation of the electrical signal might be a useful method to regulate platelet deposition onto the vascular vessel wall.

DATA AVAILABILITY STATEMENT

The raw data supporting the conclusions of this article will be made available by the authors, without undue reservation.

ETHICS STATEMENT

The animal study was reviewed and approved by Animal Care and Use Committee of Xiamen University.

AUTHOR CONTRIBUTIONS

ZQ designed the research. MW performed the experiments. All authors analyzed the data and wrote the manuscript.

FUNDING

REFERENCES

Abramson, H. A. (1928). The electrophoresis of the blood platelets of the horse with reference to their origin and to thrombus formation. *J. Exp. Med.* 47, 677–683. doi: 10.1084/jem.47.5.677

Arnold, C. E., Rajnicek, A. M., Hoare, J. I., Pokharel, S. M., Mccaig, C. D., Barker, R. N., et al. (2019). Physiological strength electric fields modulate human T cell activation and polarisation. *Sci. Rep.* 9:17604. doi: 10.1038/s41598-019-53898-5

Balakatounis, K. C., and Angoules, A. G. (2008). Low-intensity electrical stimulation in wound healing: Review of the efficacy of externally applied currents resembling the current of injury. *Eplasty* 8:e28.

Betts, J. J., Betts, J. P., and Nicholson, J. T. (1968). Significance of ADP, Plasma and Platelet Concentration in Platelet Electrophoretic Studies. *Nature* 219:1280. doi: 10.1038/2191280b0

Born, G. V., and Palinski, W. (1985). Unusually high concentrations of sialic acids on the surface of vascular endothelia. *Br. J. Exp. Pathol.* 66, 543–549.

Crook, M. (1991). Sialic acid: its importance to platelet function in health and disease. *Platelets* 2, 1–10. doi: 10.3109/09537109109005496

Crook, M., and Crawford, N. (1988). Platelet surface charge heterogeneity: characterization of human platelet subpopulations separated by high voltage

continuous flow electrophoresis. *Br. J. Haematol.* 69, 265–273. doi: 10.1111/j.1365-2141.1988.tb07632.x

Devi, S., Kuligowski, M. P., Kwan, R. Y., Westein, E., Jackson, S. P., Kitching, A. R., et al. (2010). Platelet recruitment to the inflamed glomerulus occurs via an alphaIIbbeta3/GPVI-dependent pathway. *Am. J. Pathol.* 177, 1131–1142. doi: 10.2353/ajpath.2010.091143

Djamgoz, M. B. A., Mycielska, M., Madeja, Z., Fraser, S. P., and Korohoda, W. (2001). Directional movement of rat prostate cancer cells in direct-current electric field: involvement of voltage gated Na$^+$ channel activity. *J. Cell. Sci.* 114(Pt 14), 2697–2705.

Fajac, I., Lacronique, J., Lockhart, A., Dall'Ava-Santucci, J., and Dusser, D. J. (1998). Silver/silver chloride electrodes for measurement of potential difference in human bronchi. *Thorax* 53, 879–881. doi: 10.1136/thx.53.10.879

Feng, J. F., Liu, J., Zhang, X. Z., Zhang, L., Jiang, J. Y., Nolta, J., et al. (2012). Guided Migration of Neural Stem Cells Derived from Human Embryonic Stem Cells by an Electric Field. *Stem Cells* 2, 349–355. doi: 10.1002/stem.779

Florence, A. T., and Rahman, R. (2011). The effect of some oral contraceptive steroids on platelet electrophoretic mobility in vitro. *J. Pharm. Pharmacol.* 24, 983–985. doi: 10.1111/j.2042-7158.1972.tb08932.x

Funk, R. H. W. (2015). Endogenous electric fields as guiding cue for cell migration. *Front. Physiol.* 6:143. doi: 10.3389/fphys.2015.00143

Greger, W. P., and Thomas, P. M. (1960). Micro-electrophoresis of human white cells and platelets. *Nature* 186, 171–172. doi: 10.1038/186171b0

Grottum, K. A. (1968). Influence of aggregating agents on electrophoretic mobility of blood platelets from healthy individuals and from patients with cardiovascular diseases. *Lancet* 291, 1406–1408. doi: 10.1016/S0140-6736(68)91979-X

Hoare, J. I., Rajnicek, A. M., McCaig, C. D., Barker, R. N., and Wilson, H. M. (2016). Electric fields are novel determinants of human macrophage functions. *J. Leukoc. Biol.* 6, 1141–1151. doi: 10.1189/jlb.3A0815-390R

Hunckler, J., and de Mel, A. (2017). A current affair: Electrotherapy in wound healing. *J. Multidiscip. Health* 10, 179–194. doi: 10.2147/JMDH.S127207

Jia, Y., Jiang, J., Ma, X., et al. (2008). PDMS microchannel fabrication technique based on microwire-molding. *Chin. Sci. Bull.* 53, 3928–3936. doi: 10.1007/s11434-008-0528-6

Karppinen, K., and Halonen, P. I. (1970). Red cell and platelet electrophoresis in coronary heart disease. *Advan. Cardiol.* 4, 175–178. doi: 10.1159/000387614

Li, Y., Wang, X., and Yao, L. (2015). Directional migration and transcriptional analysis of oligodendrocyte precursors subjected to stimulation of electrical signal. *Am. J. Physiol. Cell Physiol.* 309, C532–C540. doi: 10.1152/ajpcell.00175.2015

Lin, F., Baldessari, F., Gyenge, C. C., Sato, T., Chambers, R. D., Santiago, J. G., et al. (2008). Lymphocyte electrotaxis in vitro and in vivo. *J. Immunol.* 181, 2465–2471. doi: 10.4049/jimmunol.181.4.2465

Luo, R. Z., Dai, J. Y., Zhang, J. P., and Li, Z. (2021). Accelerated Skin Wound Healing by Electrical Stimulation. *Adv. Healthc. Mater.* 16:e2100557. doi: 10.1002/adhm.202100557

McCaig, C. D., Rajnicek, A. M., Song, B., et al. (2005). Controlling Cell Behavior Electrically: Current Views and Future Potential. *Physiol. Rev.* 85, 943–978. doi: 10.1152/physrev.00020.2004

McCaig, C. D., Song, B., and Rajnicek, A. M. (2009). Electrical dimensions in cell science. *J. Cell. Sci.* 122, 4267–4276. doi: 10.1242/jcs.023564

Menashi, S., Weintroub, H., and Crawford, N. (1981). Characterization of human platelet surface and intracellular membranes isolated by free flow electrophoresis. *J. Biol. Chem.* 256, 4095–4101. doi: 10.1016/0165-022X(81)90075-0

Nesbitt, W. S., Westein, E., Tovar-Lopez, F. J., et al. (2009). A shear gradient-dependent platelet aggregation mechanism drives thrombus formation. *Nat. Med.* 15, 665–673. doi: 10.1038/nm.1955

Nomura, Y., and Takagi, H. (1974). Effects of certain drugs and enzymes on the electrophoretic mobility of rabbit blood platelets. *Jpn. J. Pharmacol.* 24, 205–212. doi: 10.1254/jjp.24.205

Pu, J., Cao, L., and McCaig, C. D. (2015). Physiological extracellular electrical signals guide and orient the polarity of gut epithelial cells. *Tissue Barriers* 3:e1037417. doi: 10.1080/21688370.2015.1037417

Qi, Z., Wang, M., Ke, D., et al. (2020). *inventor; Xiamen University, assignee. A microchannel structure which can be directly inserted into microelectrode. People's Republic of China patent ZL 2020 2 1425661.6.* Beijing: Chinese trademark office.

Ruggeri, Z. M., and Mendolicchio, G. L. (2007). Adhesion mechanisms in platelet function. *Circ. Res.* 100, 1673–1685. doi: 10.1161/01.RES.0000267878.97021.ab

Sato, M. J., Ueda, M., Takagi, H., Watanabe, T. M., Yanagida, T., and Ueda, M. (2007). Input-output relationship in galvanotactic response of Dictyostelium cells. *Biosystems* 88, 261–272. doi: 10.1016/j.biosystems.2006.09.008

Sawyer, P. N., and Deutch, B. (1956). Use of electric current to delay intravascular thrombosis in experimental animals. *Am. J. Physiol.* 187, 473–478. doi: 10.1152/ajplegacy.1956.187.3.473

Sawyer, P. N., and Deutsch, B. (1955). The experimental use of oriented electrical fields to delay and prevent intravascular thrombosis. *Surg. Forum.* 5, 173–178.

Sawyer, P. N., and Pate, J. W. (1953). Bioelectric phenomena as an etiologic factor in intravascular thrombosis. *Am. J. Physiol.* 175, 103–107. doi: 10.1152/ajplegacy.1953.175.1.103

Sawyer, P. N., and Sprinivasan, S. (1967). Studies on the biophysics of intravascular thrombosis. *Am. J. Surg.* 114, 42–60. doi: 10.1016/0002-9610(67)90038-4

Sawyer, P. N., Pate, J. W., and Weldon, C. S. (1953). Relations of abnormal and injury electric potential differences to intravascular thrombosis. *Am. J. Physiol.* 175, 108–112. doi: 10.1152/ajplegacy.1953.175.1.108

Sawyer, P. N., Reardon, J. H., and Ogoniak, J. C. (1965). Irreversible electrochemical precipitation of mammalian platelets and intravascular thrombosis. *Proc. Natl. Acad. Sci. U S A.* 53, 200–207. doi: 10.1073/pnas.53.1.200

Sawyer, P. N., Suckling, E. E., and Wesolowski, S. A. (1960). Effect of small electric currents on intravascular thrombosis in the visualized rat mesentery. *Am. J. Physiol.* 198, 1006–1010. doi: 10.1152/ajplegacy.1960.198.5.1006

Schwartz, S. I. (1959). Prevention and production of thrombosis by alternations in electric environment. *Surg. Gynecol. Obstet.* 108, 533–536.

Schwarz, S. I., and Richardson, J. W. (1961). Prevention of thrombosis with the use of a negative electric current. *Surg. Forum.* 12, 46–48.

Seaman, G. V. F., and Vassar, P. S. (1966). Changes in the electrokinetic properties of platelets during their aggregation. *Arch. Biochem. Biophys.* 117, 10–17. doi: 10.1016/0003-9861(66)90119-6

Song, B., Zhao, M., Forrester, J., and McCaig, C. (2004). Nerve regeneration and wound healing are stimulated and directed by an endogenous electrical field in vivo. *J. Cell Sci.* 117(Pt 20), 4681–4690. doi: 10.1242/jcs.01341

Sun, Y. H., Reid, B., Ferreira, F., Luxardi, G., Ma, L., Lokken, K. L., et al. (2019). Infection-generated electric field in gut epithelium drives bidirectional migration of macrophages. *PLoS Biol.* 17:e3000044. doi: 10.1371/journal.pbio.3000044

Sun, Y. S., Peng, S. W., Lin, K. H., and Cheng, J. Y. (2012). Electrotaxis of lung cancer cells in ordered three-dimensional scaffolds. *Biomicrofluidics* 6, 14102–1410214. doi: 10.1063/1.3671399

Tangelder, G. J., Teirlinck, H. C., Slaaf, D. W., and Reneman, R. S. (1985). Distribution of blood platelets flowing in arterioles. *Am. J. Physiol.* 248, H318–H323. doi: 10.1152/ajpheart.1985.248.3.H318

Thon, J. N., and Italiano, J. E. (2010). Platelet formation. *Semin. Hematol.* 47, 220–226. doi: 10.1053/j.seminhematol.2010.03.005

Tokarev, A. A., Butylin, A. A., and Ataullakhanov, F. I. (2011a). Platelet adhesion from shear blood flow is controlled by near-wall rebounding collisions with erythrocytes. *Biophys. J.* 100, 799–808. doi: 10.1016/j.bpj.2010.12.3740

Tokarev, A. A., Butylin, A. A., Ermakova, E. A., Shnol, E. E., Panasenko, G. P., and Ataullakhanov, F. I. (2011b). Finite platelet size could be responsible for platelet margination effect. *Biophys. J.* 101, 1835–1843. doi: 10.1016/j.bpj.2011.08.031

Tsakiris, D. A., Scudder, L., Hodivala-Dilke, K., et al. (1999). Hemostasis in the mouse (Mus musculus): a review. *Thromb. Haemost.* 81, 177–188. doi: 10.1055/s-0037-1614439

Versteeg, H. H., Heemskerk, J. W., Levi, M., and Reitsma, P. H. (2013). New fundamentals in hemostasis. *Physiol. Rev.* 93, 327–358. doi: 10.1152/physrev.00016.2011

Wang, F. Q., Li, Q. Q., Zhang, Q., et al. (2017). Determination of Platelet Aggregation by Capillary Electrophoresis. *Chromatographia* 80, 341–345. doi: 10.1007/s10337-016-3231-9

Wang, F. Q., Zhang, Q., Li, C. H., et al. (2015). Evaluation of affinity interaction between small molecules and platelets by open tubular affinity capillary electrochromatography. *Electrophoresis* 37, 736–743. doi: 10.1002/elps.201500414

Yan, X., Han, J., Zhang, Z., Wang, J., Cheng, Q., Gao, K., et al. (2009). Lung cancer A549 cells migrate directionally in DC electric fields with polarized and activated EGFRs. *Bioelectromagnetics* 30, 29–35. doi: 10.1002/bem.20436

Zhao, M., Forrester, J. V., and McCaig, C. D. (1999). A small, physiological electric field orients cell division. *Proc. Natl. Acad. Sci. U S A.* 96, 4942–4946. doi: 10.1073/pnas.96.9.494

Zhao, M., Song, B., Pu, J., Wada, T., Reid, B., Tai, G. P., et al. (2006). Electrical signals control wound healing through phosphatidylinositol-3-OH kinase-gamma and PTEN. *Nature* 442, 457–460. doi: 10.1038/nature04925

Improved Quantification of Cell Density in the Arterial Wall—A Novel Nucleus Splitting Approach Applied to 3D Two-Photon Laser-Scanning Microscopy

Koen W. F. van der Laan[1], Koen D. Reesink[1], Myrthe M. van der Bruggen[1], Armand M. G. Jaminon[2], Leon J. Schurgers[2], Remco T. A. Megens[1,3,4], Wouter Huberts[1], Tammo Delhaas[1] and Bart Spronck[1,5]*

[1] Department of Biomedical Engineering, CARIM School for Cardiovascular Diseases, Maastricht University, Maastricht, Netherlands, [2] Department of Biochemistry, CARIM School for Cardiovascular Diseases, Maastricht University, Maastricht, Netherlands, [3] Institute for Cardiovascular Prevention, Ludwig Maximilian University, Munich, Germany, [4] German Center for Cardiovascular Research (DZHK), Partner Site Munich Heart Alliance, Munich, Germany, [5] Department of Biomedical Engineering, School of Engineering and Applied Science, Yale University, New Haven, CT, United States

Accurate information on vascular smooth muscle cell (VSMC) content, orientation, and distribution in blood vessels is indispensable to increase understanding of arterial remodeling and to improve modeling of vascular biomechanics. We have previously proposed an analysis method to automatically characterize VSMC orientation and transmural distribution in murine carotid arteries under well-controlled biomechanical conditions. However, coincident nuclei, erroneously detected as one large nucleus, were excluded from the analysis, hampering accurate VSMC content characterization and distorting transmural distributions. In the present study, therefore, we aim to (1) improve the previous method by adding a "nucleus splitting" procedure to split coinciding nuclei, (2) evaluate the accuracy of this novel method, and (3) test this method in a mouse model of VSMC apoptosis. After euthanasia, carotid arteries from SM22α-hDTR $Apoe^{-/-}$ and control $Apoe^{-/-}$ mice were bluntly dissected, excised, mounted in a biaxial biomechanical tester and brought to *in vivo* axial stretch and a pressure of 100 mmHg. Nuclei and elastin fibers were then stained using Syto-41 and Eosin-Y, respectively, and imaged using 3D two-photon laser scanning microscopy. Nuclei were segmented from images and coincident nuclei were split. The nucleus splitting procedure determines the likelihood that voxel pairs within coincident nuclei belong to the same nucleus and utilizes these likelihoods to identify individual nuclei using spectral clustering. Manual nucleus counts were used as a reference to assess the performance of our splitting procedure. Before and after splitting, automatic nucleus counts differed $-26.6 \pm 9.90\%$ ($p < 0.001$) and $-1.44 \pm 7.05\%$ ($p = 0.467$) from the manual reference, respectively. Whereas the slope of the relative difference between the manual and automated counts as a function of the manual count was significantly negative before splitting ($p = 0.008$), this slope became insignificant after splitting ($p = 0.653$). Smooth

muscle apoptosis led to a 33.7% decrease in VSMC density (p = 0.008). Nucleus splitting improves the accuracy of automated cell content quantification in murine carotid arteries and overcomes the progressively worsening problem of coincident nuclei with increasing cell content in vessels. The presented image analysis framework provides a robust tool to quantify cell content, orientation, shape, and distribution in vessels to inform experimental and advanced computational studies on vascular structure and function.

INTRODUCTION

Vascular smooth muscle cells (VSMCs) are a crucial component of blood vessels because they regulate extracellular matrix (ECM) production, maintain mechanical homeostasis in larger vessels, and enable autoregulation in smaller vessels (Owens, 1995; Brozovich et al., 2016). Changes in VSMC functionality, phenotype, and content, potentially lead to changes in diameter, wall thickness, structure, and mechanical properties of the vessel (Jaminon et al., 2019). Accurate information about a vessel's VSMC content, orientation, and distribution under well-controlled conditions is indispensable to improve modeling of active biomechanics of the vessel wall, thereby helping to further our understanding of the role VSMC play in vascular remodeling.

VSMC content is commonly determined from histological cross-sections of vessels stained with a nucleic acid dye (Clarke et al., 2010; Pai et al., 2011; Yu et al., 2011; Roostalu et al., 2018). VSMC density and distribution estimates obtained from histological cross sections are potentially disturbed, as this histological technique requires fixation and sectioning of the vessel. In addition, experience shows that it is difficult to control the orientation of smaller vessels fixed in paraffin wax for sectioning, making it nearly impossible to obtain accurate VSMC orientation data from histological cross sections of small vessels. Thus, while histology is a useful tool for assessing VSMC content of vessels, it seems ill-suited for providing accurate, quantitative information about VSMC density and distributions, especially in murine vessels.

To address this problem, we previously developed a method that uses two-photon laser scanning microscopy (TPLSM) to image intact pressurized and stretched mouse carotid arteries stained with a nucleic acid fluorescent dye (Spronck et al., 2016). Using this method, one can quantify the transmural location and/or orientation distributions of VSMC nuclei under well-controlled mechanical conditions in 3D, avoiding the need to fixate and section the vessel. Our results showed that VSMCs in mouse carotid arteries have significant non-zero helix angles and distinctly layered transmural distributions. This level of detail contrasts with computational models of artery biomechanics, in which VSMCs are often assumed to be oriented exclusively circumferentially (Zulliger et al., 2004; Masson et al., 2011; Spronck et al., 2015).

A significant limitation of our previous method for quantifying VSMC nucleus content is that nuclei which are situated closely together may be identified as a single nucleus (Spronck et al., 2016). Consequently, the shape and orientation of the resulting identified structures do not resemble those of normal nuclei and, if noticed, these structures may/should be excluded from further analysis. In our previous study, on average 6.5% of the detected nuclear structures had to be rejected because they exceeded the maximum size threshold. Furthermore, it is possible for structures within the size thresholds to consist of multiple nuclei. Clearly, correct identification of nucleus structures would enable more accurate estimates of VSMC density and distribution.

While several methods exist for splitting segmented structures consisting of multiple nuclei into their corresponding nuclei, these are generally optimized for spherical nuclei, or for image stacks with consistent contrast levels throughout, or developed for 2D images (Daník et al., 2009; Mathew et al., 2015; Atta-Fosu et al., 2016; Abdolhoseini et al., 2019; Ruszczycki et al., 2019). VSMC nuclei are typically twice to six times as long as they are wide and applying the above-mentioned methods to multiple elongated nuclei structures often leads to over segmentation (Daly et al., 2002). Additionally, non-fixated tissue cannot be optically cleared, resulting in decreasing contrast with increasing sample penetration. Although contrast compensation methods exist for TPLSM image stacks, these will be difficult to apply due to the curved and multilayered nature of vessels. Hence, existing methods are ill-suited for splitting multiple elongated nuclei segmented from TPLSM image stacks of intact, non-fixated vessels.

The aim of the present paper is to develop a procedure for splitting structures of touching elongated nuclei and to evaluate the accuracy of the resulting automatic characterization of the blood vessel's cell density. The performance of the "nucleus splitting" procedure will be compared with manually determined nucleus counts from TPLSM data obtained from mouse carotid arteries containing a wide range of cell density.

MATERIALS AND METHODS

Experimental Animals and Vessel Samples

All animal studies were performed under an approved protocol by the Ethics Committee for animal experiments of Maastricht University. In the present study, we utilized an inducible VSMC

apoptosis mouse model (*SM22α-hDTR Apoe*$^{-/-}$, Clarke et al., 2006). A total of 12 *Apoe*$^{-/-}$ animals were used, six of which had the *hDTR* knock-in receptor (*SM22α-hDTR Apoe*$^{-/-}$) and served as the VSMC apoptosis group, while the other six (control *Apoe*$^{-/-}$) served as the control group. After 8 weeks, both groups were treated with diphtheria toxin (DT), inducing VSMC apoptosis in the *hDTR* knock-in receptor group but not in the control group. Both groups were euthanized through an overdose of isoflurane 2 weeks after the injection. Left carotid arteries, generally 5–7 mm in length, were harvested from the animals. After isolation, as much connective tissue as possible was bluntly removed from the arteries. Samples were immediately stored at 4 degrees Celsius in Hank's balanced salt solution (HBSS) (Thermo Fisher Scientific, Paisley, United Kingdom) containing 1.0 µM sodium nitroprusside (Sigma-Aldrich, St. Louis, MO, United States) to ensure full vasodilation.

Sample Mounting and Preparation

Within 4 h after excision, samples were mounted on glass pipets in a custom biaxial biomechanical testing setup (van der Bruggen et al., 2021), a schematic of which is shown in **Figure 1A**. Samples were stretched to their *in vivo*-like length and pressurized to 100 mmHg, as described previously (van der Bruggen et al., 2021). Finally, 1.5 µM Syto-41 (Thermo Fisher Scientific, Paisley, United Kingdom) and 0.5 µM Eosin-Y (Sigma-Aldrich, St. Louis, MO, United States) were added to the organ bath to stain nuclei and elastin fibers, respectively. Samples were left to stain for 30 min before imaging. Syto-41 and Eosin-Y were left in the organ bath during imaging.

Imaging Setup

Fluorescence microscopy images were acquired using a Radiance2100 two-photon laser scanning setup (Bio-Rad,
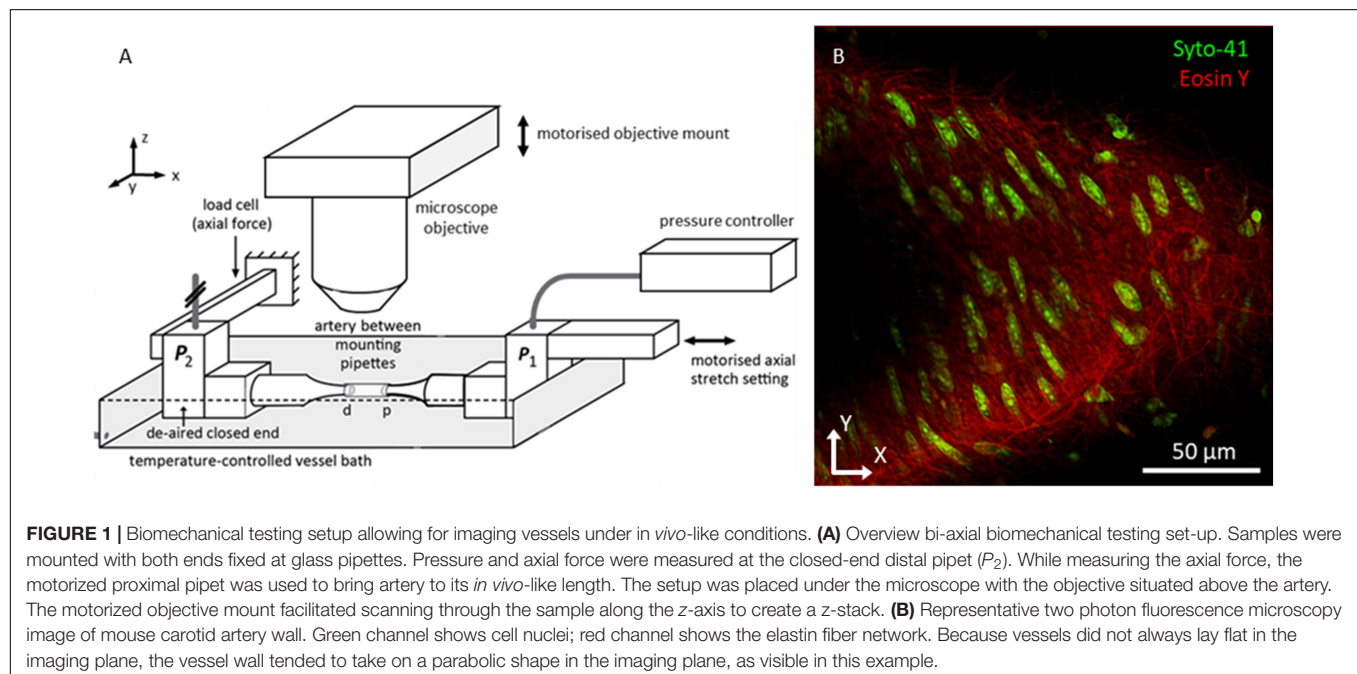
Hercules, CA, United States) equipped with a 60x CFI APO NIR Objective (NA 1.0, WD 2.8 mm) (Nikon, Minato City, Tokyo, Japan). The center wavelength of the Tsunami tunable pulsed femtosecond laser (Spectra-Physics, Santa Clara, California, United States) was tuned to 810 nm. Using preinstalled optical filters in the microscope, the spectral ranges of two detection channels were set to 440–510 and 580–650 nm, and displayed in green and red, respectively. In this configuration, the green channel captured the light emitted by the Syto-41 staining, whilst the red channel captured the light emitted by the Eosin-Y staining, the results of which can be seen in **Figure 1B**. These ranges were chosen to minimize overlapping fluorescence emission spectra within the channels. Image resolution was set to $1,024 \times 1,024$ pixels^2 with a pixel size of 0.2×0.2 µm^2, resulting in a field of view of 205×205 µm^2. Microscope focus was positioned above the vessel and images were taken sequentially, moving down 0.45 µm between every image, until the near vessel wall was passed completely. In this manner, image stacks were made for every sample, generally 30–40 µm deep.

Image Stack Analysis

The steps in the proposed image stack analysis method are displayed in **Figure 2**. The analysis method produces manual and automated counts, without and with splitting, as well as medial cell densities and transmural cell density distributions derived from the automated counts.

Deconvolution

Recorded image stacks were sharpened using Huygens professional image deconvolution software (Scientific Volume Imaging, Hilversum, Netherlands). The classic maximum likelihood estimation algorithm was used to perform the deconvolution. For each channel of the image stack, a theoretical

FIGURE 1 | Biomechanical testing setup allowing for imaging vessels under in *vivo*-like conditions. **(A)** Overview bi-axial biomechanical testing set-up. Samples were mounted with both ends fixed at glass pipettes. Pressure and axial force were measured at the closed-end distal pipet (P_2). While measuring the axial force, the motorized proximal pipet was used to bring artery to its *in vivo*-like length. The setup was placed under the microscope with the objective situated above the artery. The motorized objective mount facilitated scanning through the sample along the *z*-axis to create a z-stack. **(B)** Representative two photon fluorescence microscopy image of mouse carotid artery wall. Green channel shows cell nuclei; red channel shows the elastin fiber network. Because vessels did not always lay flat in the imaging plane, the vessel wall tended to take on a parabolic shape in the imaging plane, as visible in this example.

FIGURE 2 | Schematic overview of the steps taken during image stack analysis to produce the manual and automated counts, medial cell densities and transmural cell distributions, with and without nucleus splitting.

point spread function was constructed from the microscopic parameters mentioned previously (microscope type, excitation and emission wavelengths, embedding medium refractive index, voxel dimensions, objective magnification, and numerical aperture) and entered into the program. The deconvolution algorithm was set to run for a maximum of thirty iterations or until a quality threshold, set to 0.005, was reached. All further image analysis for nucleus quantification was performed using custom scripts written in MATLAB R2019b (MathWorks, Natick, MA, United States).

Determination of Vessel Orientation

A straight cylinder was fitted through the obtained elastin data to determine the vessel centerline. For this procedure, voxels from the red (elastin) channel were used when they exceeded a background threshold of 15% of the maximum possible intensity

value. The optimal straight cylinder was determined by finding the centerline position and orientation for which the variance in the radial distance from the voxels to the centerline was minimized. The radial distance from a voxel to the vessel centerline equals the minimal distance from the centerline to that voxel and is determined by the length of the vector, $\vec{r}_i$, between the voxel and the point along the centerline closest to the voxel, as defined by $r_i = |\vec{r}_i| = (r_{i,1}^2 + r_{i,2}^2 + r_{i,3}^2)^{1/2}$. The radial distance was calculated according to

$$r_i = \left| \vec{X}_i - \vec{X}_{\text{ves},\, i} \right|, \tag{1}$$

where $\vec{X}_i$ describes the position vector of voxel i and $\vec{X}_{\text{ves},i}$ describes the position vector of the point along the vessel centerline closest to $\vec{X}_i$. The vessel centerline is defined by $\vec{X}_{\text{ves}}$ and $\vec{V}_{\text{ves}}$, the position vector of a point along the centerline and the orientation unit vector of the centerline, respectively. $\vec{X}_{\text{ves},\, i}$ is found by moving the magnitude of the projection of $(\vec{X}_i - \vec{X}_{\text{ves}})$ on the centerline in the direction of $\vec{V}_{\text{ves}}$ from $\vec{X}_{\text{ves}}$, as shown in **Figure 3A**, according to

$$\vec{X}_{\text{ves},\, i} = \vec{X}_{\text{ves}} + \vec{V}_{\text{ves}}(\vec{V}_{\text{ves}} \cdot (\vec{X}_i - \vec{X}_{\text{ves}})). \tag{2}$$

The vessel centerline was determined by optimizing $\vec{X}_{\text{ves}}$ and $\vec{V}_{\text{ves}}$ so that the variance in r_i was minimized for the n selected elastin voxels, as shown in **Figure 3B**, using the cost (error) function

$$\varepsilon_{\text{ves}}(r_i) = \sum_{i=1}^{n} \frac{(r_i - \bar{r})^2}{n-1}, \tag{3}$$
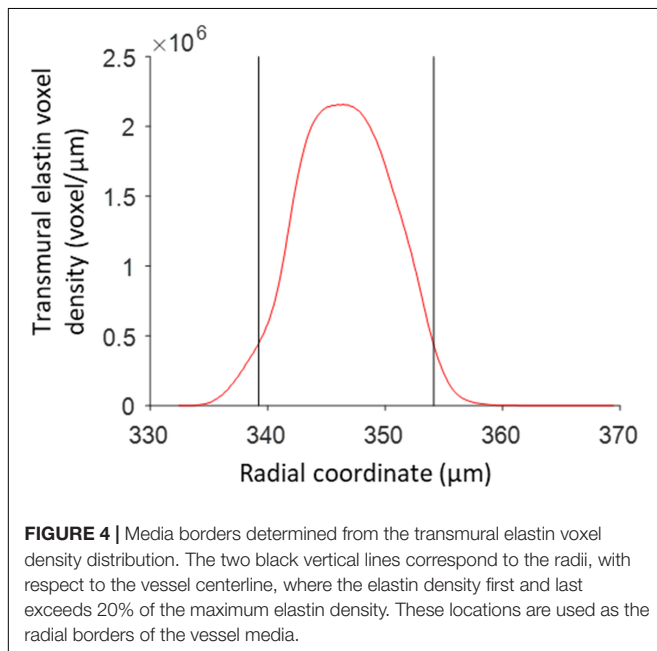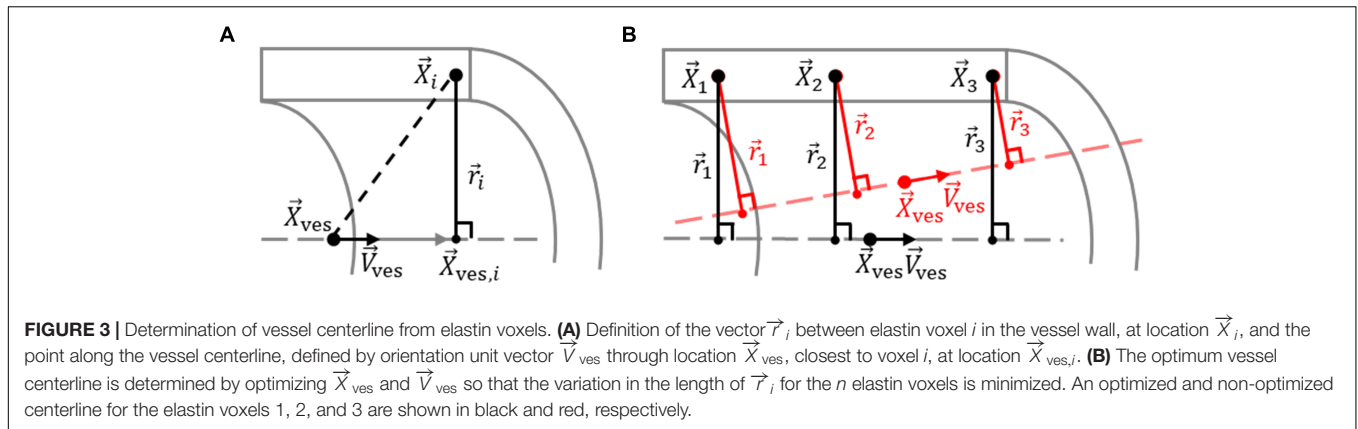
where $\bar{r}$ represents the expected value of r_i for the n selected elastin voxels. The cost function was minimized by varying the first and third coordinates of $\vec{X}_{\text{ves}}$ and $\vec{V}_{\text{ves}}$ using a trust-region-reflective non-linear least-squares algorithm. The second coordinate of $\vec{X}_{\text{ves}}$ was kept fixed at half the width of an image stack to ensure that the least squares algorithm would converge to a single point along the vessel centerline for $\vec{X}_{\text{ves}}$.

Medial Thickness Determination

The radial positions of the inner and outer borders of the media, with respect to the vessel centerline, were determined using voxels in the red channel that exceeded a background threshold of 6% of the maximum possible intensity value. A transmural density distribution of these voxels was determined using the *ksdensity* MATLAB function. The distribution was evaluated for the complete range of radial distances corresponding with the selected voxels, with a resolution of 0.1 μm and with a bandwidth of 0.8 for the kernel smoothing window (Bowman and Azzalini, 2004). The borders of the media were set at the edges of the region where the density distribution exceeds 20% of the maximum value of the distribution (**Figure 4**).

Manual Nucleus Counting

The number of nuclei within each 3D image were counted by two independent experienced people (KWFL and RTAM), and

FIGURE 3 | Determination of vessel centerline from elastin voxels. **(A)** Definition of the vector $\vec{r}_i$ between elastin voxel i in the vessel wall, at location $\vec{X}_i$, and the point along the vessel centerline, defined by orientation unit vector $\vec{V}_{ves}$ through location $\vec{X}_{ves}$, closest to voxel i, at location $\vec{X}_{ves,i}$. **(B)** The optimum vessel centerline is determined by optimizing $\vec{X}_{ves}$ and $\vec{V}_{ves}$ so that the variation in the length of $\vec{r}_i$ for the n elastin voxels is minimized. An optimized and non-optimized centerline for the elastin voxels 1, 2, and 3 are shown in black and red, respectively.

FIGURE 4 | Media borders determined from the transmural elastin voxel density distribution. The two black vertical lines correspond to the radii, with respect to the vessel centerline, where the elastin density first and last exceeds 20% of the maximum elastin density. These locations are used as the radial borders of the vessel media.

the average count per scan was used as a reference to determine the accuracy of the image analysis method.

Vesselness Filtering

After deconvolution, the intensity of the green channel was adjusted so that the lowest 99.6% of voxels, based on intensity, spanned the whole intensity range. The previously reported Vesselness filtering-based approach was adopted to enhance elongated structures in the green channel and suppress background noise (Spronck et al., 2016). 3D kernels based on the 2nd order Gaussian derivatives with a standard deviation of 1.2 μm in all three directions were used. Kernel voxel size was chosen to fit ± 3 standard deviations in each direction, yielding a kernel size of 37 × 37 × 17 voxels. Vesselness filtering parameters α, β, and c were all set to 0.15 and an intensity threshold of 0.1 was subsequently used to segment the nuclei from the Vesselness-filtered image stacks into binary image stacks. These parameters were chosen to visually give the best trade-offs between sensitivity

and reliability in enhancing nuclei, as well as minimize the frequency of multiple enhanced nuclei touching each other.

In addition to enhancing elongated structures, Vesselness filtering was used to assign each voxel the orientation of the elongated structure at that location. These orientations correspond to the smallest absolute eigenvalue produced by the Hessian matrix used during Vesselness filtering. The orientation of voxels in an elongated nucleus were therefore predominantly in line with the orientation of that nucleus.

Nucleus Extraction

Nucleus structures were extracted from binary image stacks using a 3D 6-connectivity neighborhood connected-component analysis. This groups high binary voxels that are directly in front, behind, above, below, left, or right of each other into structures representing nuclei. A minimum volume threshold, set to 54 μm³, was applied to the extracted structures to exclude structures that were too small to reasonably be nuclei. The number of remaining nucleus structures was used as the automated cell count, without nucleus splitting.

Transmural Cell-Density Distribution Estimation

Radial locations of the n extracted nucleus structures compared to the vessel centerline, $r_{c,i}$, were determined from their centroids using

$$r_{c,i} = \left| \vec{X}_{c,i} - (\vec{X}_{ves} + \vec{V}_{ves}(\vec{V}_{ves} \cdot (\vec{X}_{c,i} - \vec{X}_{ves}))) \right|, \quad (4)$$

where $\vec{X}_{c,i}$ represents the structure centroid location for extracted nucleus structure i. A transmural density distribution of $r_{c,i}$ was determined using the *ksdensity* MATLAB function. The distribution was evaluated for the complete range of radial distances corresponding with the selected structures, using a resolution of 0.1 μm and with a bandwidth of 1 for the kernel smoothing window (Bowman and Azzalini, 2004).

Nucleus Splitting

The proposed nucleus splitting procedure was used to detect whether extracted nucleus structures consisted of multiple nuclei

and, if so, to split these structures into their separate nuclei. The procedure consists of three major steps: (1) determining the likelihood for each combination of two voxels within a structure that they are part of the same nucleus based on their location and orientation; (2) using these likelihoods to build a Laplacian matrix for spectral clustering and identify individual nucleus cores; and (3) assigning voxels that were excluded from the Laplacian matrix to cores according to their highest likelihood of belonging to a specific core. While the last step is not strictly necessary for improving cell count accuracy, it does allow further analysis of split nuclei in terms of size, shape, or orientation analysis.

Step 1: Voxel Pair Likelihood Determination

The likelihood that any two voxels in a structure are part of the same nucleus was determined based on the assumptions that VSMC nuclei are predominantly long and cylindrically-shaped, organized in distinct layers within the vessel wall, and oriented primarily in the circumferential-axial plane, compared to the vessel centerline. A likelihood that two voxels are part of the same nucleus was defined for each of these assumptions.

The first likelihood, $p_{rd,i,j} \in [0, 1]$, is determined using the shortest distance from voxel i to the line represented by the location and orientation of voxel j, $r_{i,j}$, and the shortest distance from voxel j to the line represented by the location and orientation of voxel i, $r_{j,i}$. Since the orientation of a voxel is in line with the elongated structure at that location, if both $r_{i,j}$ and $r_{j,i}$ are relatively short, compared to the thickness of the elongated structure, the voxels are likely part of the same elongated structure. The likelihood $p_{rd,i,j}$ was calculated according to Gaussian distribution

$$p_{rd,i,j} = e^{\left(\frac{-r_{i,j}{}^2 - r_{j,i}{}^2}{2\sigma_r{}^2} \right)}, \quad (5)$$

with the standard deviation σ_r set to 0.8 µm, based on the width of a VSMC nucleus (O'Connell et al., 2008). Similar to the radial location of nucleus centroids compared to the vessel centerline, $r_{i,j}$ and $r_{j,i}$ were calculated according to

$$r_{i,j} = \left| \vec{X}_i - (\vec{X}_j + \vec{E}_j(\vec{E}_j \cdot (\vec{X}_i - \vec{X}_j))) \right|, \quad (6)$$

and

$$r_{j,i} = \left| \vec{X}_j - (\vec{X}_i + \vec{E}_i(\vec{E}_i \cdot (\vec{X}_j - \vec{X}_i))) \right|, \quad (7)$$

where $\vec{X}_i$ and $\vec{X}_j$ are the position vectors of voxels i and j, respectively, and $\vec{E}_i$ and $\vec{E}_j$ denote the orientations of voxel i and j, respectively. $p_{rd,i,j}$ is defined so that it will be high if the voxels are situated close together, regardless of their orientation, as $r_{i,j}$ and $r_{j,i}$ will always be equal to or smaller than the distance between the two voxels. However, the value of $p_{rd,i,j}$ can still be high when the voxels are relatively far away if their positions and orientations are all in line, as illustrated in **Figure 5A**. This allows for voxel pairs situated at opposite ends of the same elongated nucleus to have a high $p_{rd,i,j}$.

The second likelihood, $p_{td,i,j} \in [0, 1]$, was determined using the transmural distance between voxels i and j, $d_{td,i,j}$. If this

distance is relatively large, compared to the thickness of a nucleus, then the two voxels likely lay in separate VSMC layers and, as illustrated in **Figure 5B**, were therefore unlikely to be part of the same nucleus. The likelihood $p_{td,i,j}$ was calculated according to the Gaussian distribution

$$p_{td,i,j} = e^{\frac{-d_{td,i,j}{}^2}{2\sigma_{td}{}^2}}, \quad (8)$$

with the standard deviation σ_{td} set to 0.8 µm, based on the thickness of a VSMC nucleus in the vessel media. The transmural distance between voxels i and j, $d_{td,i,j}$, was determined by the magnitude of the positioning vector between the voxels i and j on the transmural orientation unit vector at the centroid of the structure to be split according to

$$d_{td,i,j} = \frac{\vec{V}_{tm} \cdot (\vec{X}_i - \vec{X}_j)}{\left| \vec{V}_{tm} \right|}. \quad (9)$$

Here $\vec{V}_{tm}$ represents the transmural orientation vector and was defined by the shortest possible vector from the vessel centerline to the structure's centroid according to

$$\vec{V}_{tm} = \vec{X}_c - (\vec{X}_{ves} + \vec{V}_{ves}(\vec{V}_{ves} \cdot (\vec{X}_c - \vec{X}_{ves}))). \quad (10)$$

Here X_c is the location of the centroid of the structure that is to be split, given by the average location of the voxels comprising the structure.

The third likelihood, $p_{ta,i,j} \in [0, 1]$, was determined by whether the orientation of voxels i and j were primarily in the circumferential-axial plane of the vessel. Voxels in between touching nuclei from different layers typically had a transmural orientation and, because VSMCs are oriented in the circumferential-axial plane, it was difficult to discern which nucleus these voxels belonged to. Rather than informing whether two voxels are likely part of the same nucleus, $p_{ta,i,j}$ serves as an exclusion criterion of transmurally orientated voxels for determining nucleus cores in the next nucleus splitting step. By excluding transmural oriented voxels that do not clearly belong to a specific nucleus, the reliability and accuracy of spectral clustering for determining nucleus cores was improved. $p_{ta,i,j}$ is calculated using the magnitude of the voxel orientations unit vectors $\vec{E}_i$ and $\vec{E}_j$ on the transmural orientation vector, $\vec{V}_{tm}$, according to

$$p_{ta,i,j} = \left(1 - \frac{\left| \left(\vec{V}_{tm} \cdot \vec{E}_i \right) \right|}{\left| \vec{V}_{tm} \right|} \right) \left(1 - \frac{\left| \left(\vec{V}_{tm} \cdot \vec{E}_j \right) \right|}{\left| \vec{V}_{tm} \right|} \right). \quad (11)$$

In this manner, $p_{ta,i,j}$ only produces a high likelihood if both voxel orientations are primarily along the circumferential-axial plane of the vessel, as illustrated in **Figure 5C**.

Step 2: Nucleus Core Determination

Spectral clustering uses the similarity between the data points in a dataset to define clusters of similar data points (von Luxburg, 2007). In the nucleus splitting procedure a normalized spectral
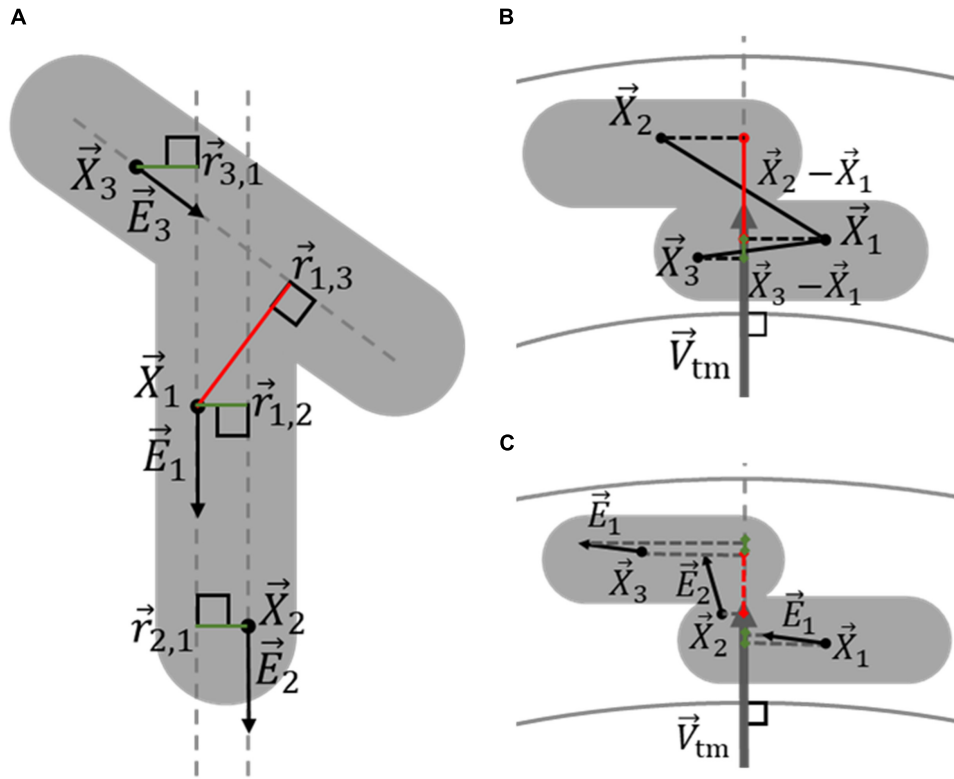
FIGURE 5 | Determination of the likelihood that two voxels belong to the same nucleus, based on their orientation and location. **(A)** Voxels within a multiple-nucleus structure, shown in gray, can still likely be part of the same elongated structure, and thus the same nucleus, even when relatively far apart. Voxels 1 and 2, with locations $\vec{X}_1$ and $\vec{X}_2$, respectively, have similar orientations, given by $\vec{E}_1$ and $\vec{E}_2$, respectively. Because the line between $\vec{X}_1$ and $\vec{X}_2$ is relatively in line with both $\vec{E}_1$ and $\vec{E}_2$, vectors $\vec{r}_{1,2}$ and $\vec{r}_{2,1}$ are both short enough to produce high likelihoods that voxels 1 and 2 belong to the same nucleus, indicated by the green lines. On the other hand, because the orientation of voxel 3, $\vec{E}_3$, is dissimilar to that of the line between $\vec{X}_1$ and $\vec{X}_3$, $\vec{r}_{1,3}$ is too long for voxel 1 and 3 to likely be part of the same nucleus, indicated by the red color, even though $\vec{r}_{3,1}$ is small. **(B)** The transmural distance between voxels influences whether they are likely part of the same VSMC layer, and thus the same nucleus. The projection of $\vec{X}_1 - \vec{X}_3$ on $\vec{V}_{tm}$ is relatively small, making it likely that voxel 1 and 3 belong to the same VSMC layer. Conversely, the projection of $\vec{X}_1 - \vec{X}_2$ on $\vec{V}_{tm}$ is relatively large, making it unlikely that voxel 1 and 2 belong to the same VSMC layer. **(C)** The transmural components of voxel orientations indicate whether voxels are oriented in the axial-circumferential plane of the vessel, similar to VSMCs, and whether they likely belong to a specific nucleus. The green and red colors of the projections of $\vec{E}_1$, $\vec{E}_2$, and $\vec{E}_3$ on $\vec{V}_{tm}$ indicates voxels 1 and 3 are oriented primarily in the axial-circumferential plane, while voxel 2 is not.

clustering algorithm was adopted to cluster structure voxels into cores representing the separate nuclei by using the likelihood that voxels were part of the same nucleus as the similarity between them. The adopted algorithm requires the construction of a normalized random walk Laplacian matrix from the weighted adjacency matrix **R** and the degree matrix **D** according to

$$\mathbf{L}_{rw} = \mathbf{I} - \mathbf{D}^{-1}\mathbf{R}, \tag{12}$$

where **I** is the identity matrix. The weighted adjacency matrix **R,** is a symmetric matrix in which the columns and rows represent the voxels in the structure and the non-diagonal elements describe the undirected similarity between voxels. The elements of the weighted adjacency matrix were calculated by multiplying the three likelihoods that two voxels within a structure were part of the same nucleus with each other according to

$$\mathbf{R} = \left[\rho_{i,j}\right] = \begin{cases} p_{rd,i,j} \cdot p_{ta,i,j} \cdot p_{td,i,j}, & i \neq j \\ 0, & i = j \end{cases}, \tag{13}$$

in which $\rho_{i,j} \in [0, 1]$ denotes the similarity between voxels i and j are part of the same nucleus. The degree matrix **D** contains along its diagonal the degree of each voxel, d_i, which describes the combined similarity of that voxel with all voxels in the structure and is otherwise filled with zeros. The degree of a voxel is determined by its summed similarity with all voxel in the structure according to

$$d_i = \sum_{j=1}^{n} \rho_{i,j}. \tag{14}$$

During spectral clustering, a degree threshold was chosen below which voxels were excluded from the Laplacian matrix. This improved the accuracy and reliability of the algorithm as visually it was confirmed that, without the exclusion of low degree voxels, the algorithm inconsistently produced additional cores in and between nuclei. On the other hand, if the threshold was set too high, it was possible that small nuclei were not assigned to

a core as most voxels in that core were excluded. The degree threshold was set at $d_{min} = 40$ as this visually produced the most consistent results.

The spectral clustering algorithm utilizes the eigenvalues and eigenvectors of the Laplacian matrix to cluster structure voxels that exceeded the degree threshold into nucleus cores. The algorithm was limited to split a structure in no more than $k = 10$ cores. Consequently, the k smallest absolute eigenvalues, with their corresponding eigenvectors, were determined from the Laplacian matrix using a Krylov method. First, it was determined whether a structure consisted of a single or multiple nuclei. If the total volume of voxels exceeding the degree threshold was smaller than 1.8 μm^3, the structure was deemed to consist of a single nucleus as there were not enough voxels to facilitate multiple cores. Additionally, if the first and second eigenvalue were smaller than 0.01 and larger than 0.02, respectively, indicating that all voxels are sufficiently likely to be part of the same nucleus with each other, the structure was deemed to consist of a single nucleus.

If the structure was not deemed to consist of a single nucleus, the algorithm performed k-means clustering using the eigenvectors of the Laplacian matrix corresponding to the k smallest absolute eigenvalues as cluster indicators to create nucleus cores (Bowman and Azzalini, 2004). The highest average silhouette value, describing how close a voxel is to its own core centroid compared to other core centroids, was used to determine the k cores to split the structure in, with k ranging from 2 to 10 (Rousseeuw, 1987). To prevent the k-means clustering algorithm from converging to a local minimum due to a poor starting point, it was repeated 20 times for each value of k. The result with the smallest mean within-cluster point-to-centroid distance was selected for each value of k, as this value is small for well-grouped clusters.

Step 3: Assignment of Low-Degree Voxels to Cores

In the last step of the nucleus splitting procedure, the voxels which were excluded from the Laplacian matrix, were divided between the nucleus cores to produce whole nuclei. Voxels were allocated to the core which they were deemed to have the highest likelihood of belonging to. This likelihood was based on the shortest distance from a voxel to a core centerline and the distance from a voxel to the edge of a core in the direction of the core centroid. The likelihood $p_{ij} \in [0, 1]$ that voxel i belonged to core j, was calculated according to

$$p_{i,j} = e^{\left(\frac{-r_{vc,i,j}^2}{2\sigma_{vc}^2}\right)} e^{\left(\frac{-d_{vs,i,j}^2}{2\sigma_{vs}^2}\right)}, \qquad (15)$$

where $r_{vc,i,j}$ and $d_{vs,i,j}$ are the shortest distance from voxel i to core centerline j and the distance from voxel i to the surface of core j, in the direction of core centroid j, respectively. Standard deviations σ_{vc} and σ_{vs} were set to 2 and 5 μm, respectively. The vector $r_{vc,i,j}$ was calculated according to

$$r_{vc,i,j} = |\vec{X}_{v,i} - (\vec{X}_{c,j} + \vec{V}_{c,j}(\vec{V}_{c,j} \cdot (\vec{X}_{v,i} - \vec{X}_{c,j})))|, \quad (16)$$

where $\vec{X}_{c,j}$ and $\vec{X}_{v,i}$ represent core centroid j and excluded voxel i locations, respectively, and $\vec{V}_{c,j}$ represents the core centerline j orientation vector. **Figure 6A** illustrates how $\vec{r}_{vc,i,j}$ was used to assign excluded voxels to cores.

Core centerline orientations were determined in one of two ways. If a core consisted of 12 voxels or less, the core centerline orientation was calculated from the mean orientation of the voxels in the core, and then normalized. Otherwise, the core centerline orientation was determined by finding the orientation on which the summed projected magnitude of core voxel orientations was maximized by minimizing the cost (error) function

$$\varepsilon_{co}(\vec{V}_{c,j}) = \sum_{i=1}^{n} \left(1 - \left|\left(\vec{E}_{c,i} \cdot \vec{V}_{c,j}\right)\right|\right), \qquad (17)$$

using a trust-region-reflective non-linear least-squares algorithm. Here $\vec{E}_{c,i}$ represent the orientations of the core's voxels.

To determine the distance from an excluded voxel to the edge of a core, an ellipsoid approximation of the core's shape was made. The eigenvectors of the covariance matrix of the core's voxel locations were used as the principal axes of the ellipsoid, while two times the square root of the eigenvalues of the covariance matrix were used as the size of the ellipsoid along those axes (Nielsen and Bhatia, 2014). The distance from excluded voxel i to the surface of the ellipsoid approximation of core j in the direction of the core's centroid, $d_{vs,i,j}$, was determined, as illustrated in **Figure 6B**, according to

$$d_{vs,i,j} = |\vec{X}_{v,i} - \vec{X}_{c,j}| - d_{cs,i,j}. \qquad (18)$$

Here $\vec{X}_{v,i}$ and $\vec{X}_{c,j}$ are the position vectors of excluded voxel i and the centroid of core j, and $d_{cs,i,j}$ represents the distance from the centroid to the surface of core j in the direction of $\vec{X}_{v,i}$. The distance $d_{ce,i,j}$ was calculated from the length along each of the principle ellipsoid axes at which the vector $\vec{X}_{v,i} - \vec{X}_{c,j}$ crosses the ellipsoid surface, defined as $x'_{i,j}$, $y'_{i,j}$, and $z'_{i,j}$, according to

$$d_{cs,i,j} = \sqrt{x'_{i,j}{}^2 + y'_{i,j}{}^2 + z'_{i,j}{}^2}. \qquad (19)$$

The distances $x'_{i,j}$, $y'_{i,j}$, and $z'_{i,j}$, were calculated by multiplying the size of a core ellipsoid along each axis, $s_{x',j}$, $s_{y',j}$, and $s_{z',j}$, with the amplitude of the projection of the normalized vector between $\vec{X}_{c,j}$ and $\vec{X}_{v,i}$ on the corresponding axis, $\vec{V}_{x'}$, $\vec{V}_{y'}$, and $\vec{V}_{z'}$, respectively, according to
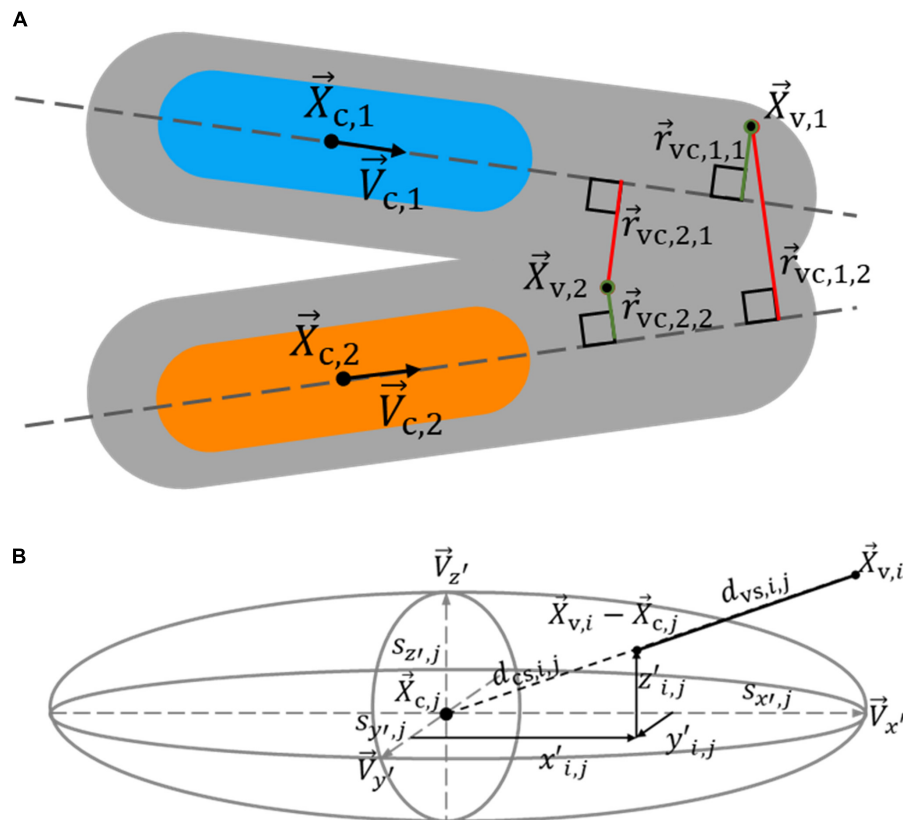
$$x'_{i,j} = s_{x',j}\left(\vec{V}_{x',j} \cdot \frac{\left(\vec{X}_{c,j} - \vec{X}_{v,i}\right)}{|\vec{X}_{c,j} - \vec{X}_{v,i}|}\right), \qquad (20)$$

$$y'_{i,j} = s_{y',j}\left(\vec{V}_{y',j} \cdot \frac{\left(\vec{X}_{c,j} - \vec{X}_{v,i}\right)}{|\vec{X}_{c,j} - \vec{X}_{v,i}|}\right), \qquad (21)$$

and

$$z'_{i,j} = s_{z',j}\left(\vec{V}_{z',j} \cdot \frac{\left(\vec{X}_{c,j} - \vec{X}_{v,i}\right)}{|\vec{X}_{c,j} - \vec{X}_{v,i}|}\right). \qquad (22)$$

FIGURE 6 | Determination of the likelihood that voxels excluded from spectral clustering belong to a nucleus core. An excluded voxel is assigned to a nucleus core based on its distance to core centerlines and the distance to core surfaces, as estimated by an ellipsoid. **(A)** The shortest distance from excluded voxels 1 and 2 to core centerlines 1 and 2 influences which core they likely belong to. Since $\vec{r}_{vc,1,1}$ is shorter than $\vec{r}_{vc,1,2}$, indicated by the green and red colors, respectively, voxel 1 is more likely to belong to core 1 than 2, shown in blue and orange, respectively. Voxel 2 more likely belongs to core 2 than 1, as $\vec{r}_{vc,2,2}$ is shorter than $\vec{r}_{vc,2,1}$. **(B)** The graph shows the path from excluded voxel i to the surface of core j, as estimated by an ellipsoid, in the direction of the core centroid. A voxel is more likely to belong to a core it has a shorter distance to its surface to.

Determination of Medial Cell Density

The media volume within an image stack was determined by multiplying the number of voxels that had a radial distance to the vessel centerline between the inner and outer borders of the media with the volume of one voxel ($18 \cdot 10^{-3}$ μm³). The nucleus count, with identical radial distance restrictions, was divided by the media volume to determine the media cell density for the sample.

Choice of Image Analysis Parameters

Table 1 lists all image analysis parameter values used in this study. These values where chosen based on preliminary results, using manual nucleus counts as a reference. Parameter estimation was limited to six of the 12 scans: three from both the control and VSMC apoptosis groups, whilst the image analysis procedure's performance was judged using all 12 scans. In this manner we sought to evaluate whether the proposed image analysis method improved nucleus structure identification, instead of only determining which parameters provided the best results for this dataset.

Statistical Analysis

Paired t-tests were used to determine whether differences between the mean absolute manual and automated nucleus counts were significant. One-sample two-sided t-tests were used to determine whether relative differences between manual nucleus count and automated nucleus counts were significant. Linear regression was used to analyze the relation of the relative differences between the automated and manual nucleus counts with the manual nucleus count. Lastly, independent t-test was used to analyze whether the media cell density of the VSMC apoptosis group was significantly different from the control group, using the automated nucleus count with the nuclear splitting procedure. All statistical tests were performed using two tails and with α = 0.05.

RESULTS

Nucleus Count Without Splitting

Mean automated nucleus counts without nucleus splitting are significantly smaller than manual counts

TABLE 1 | Parameter values for nucleus quantification from TPLSM 3D images.

Parameter description	Value	Unit	Step in protocol
Red channel background threshold	15	%*	Vessel orientation
Red channel background threshold	6	%*	
Kernel smoothing function bandwidth	1.2	—	Medial thickness determination
Transmural distribution threshold for edge detection	20	%**	
Second-order Gaussian kernel SD	1.2	μm	
Vesselness filtering parameter α	0.15	—	
Vesselness filtering parameter β	0.15	—	Vesselness filtering
Vesselness filtering parameter c	0.15	—	
Intensity threshold for nucleus detection	0.1	—	
Min. size nucleus structure	54	μm^3	Nucleus extraction
Kernel smoothing function bandwidth	1.0		Cell density distribution estimation
Voxel-voxel radial distance SD (σ_r)	0.8	μm^3	Nucleus splitting, step 1
Transmural distance SD (σ_{td})	0.8	μm^3	
Minimum degree for spectral clustering (d_{min})	40	—	
Min. structure size for splitting threshold	1.8	μm^3	
Max. spectral clustering 1st eigenvalue	0.01	—	
Min. spectral clustering 2nd eigenvalue	0.02	—	Nucleus splitting, step 2
Number of k-means clustering repetitions	20	—	
Max. number of cores (k)	10	—	
Voxel-core radial distance SD (σ_{vc})	2.0	μm	
Voxel-ellipsoid surface distance SD (σ_{vs})	5.0	μm	Nucleus splitting, step 3
Voxel count threshold for core centerline determination	12	Voxels	

*Percentage with respect to maximum possible channel intensity value; **percentage with respect to maximum transmural distribution value. SD, standard deviation.

($\Delta = -36.9$, $p < 0.001$) (**Table 2**). Mean relative differences between manual and automated nucleus counts without splitting were significant as well ($\Delta = -26.6\%$ $p = <0.001$). Visually, it was confirmed that this mismatch was primarily caused by closely situated nuclei that were recognized as a single structure, as is demonstrated in **Figure 7A**. Linear regression showed that the relative underestimation of the number on nuclei by the automated count without splitting increased significantly with increasing sample cell density (slope = -0.201, $p = 0.008$) (**Figure 8**). This indicates that the error from identifying multiple nuclei as a single structure got progressively worse with increasing cell density.

Nucleus Count With Nucleus Splitting

The accuracy of the automated nucleus count improved when splitting structures of multiple elongated nuclei with the nucleus splitting procedure, as the mean manual and automated counts was no longer significantly different ($\Delta = -2.2$, $p = 0.467$) (**Table 2**). Furthermore, mean relative differences between manual and automated nucleus counts with splitting were no longer significant ($\Delta = -1.44\%$ $p = 0.493$). Linear regression shows that the difference between manual and automated count with splitting no longer significantly depends on the number of nuclei in the sample (slope = -0.029, $p = 0.653$) (**Figure 8A**).

Transmural Nucleus Distribution

Nucleus splitting has a marked impact on the transmural nucleus density distributions produced from the automated counts

(**Figure 9**). Since the procedure increased the number of nuclei counted in each sample, the area beneath the transmural nucleus distribution curves increased correspondingly. Additionally, the local maxima were more pronounced in the transmural cell distribution curves of high cell content samples (**Figure 9A**). Interestingly, multiple nuclei were more frequently extracted as a single structure near the adventitial side of the vessel wall compared to the luminal side.

Induced Vascular Smooth Muscle Cell Apoptosis Mouse Model

The medial nucleus density of the VSMC apoptosis group was, on average, 33.7% lower than the control group in the induced VSMC apoptosis case study (**Table 2**). Besides the decrease in cell content, fewer strongly pronounced local maxima and minima were present in the transmural nucleus distributions for the VSMC apoptosis group (**Figure 9**).
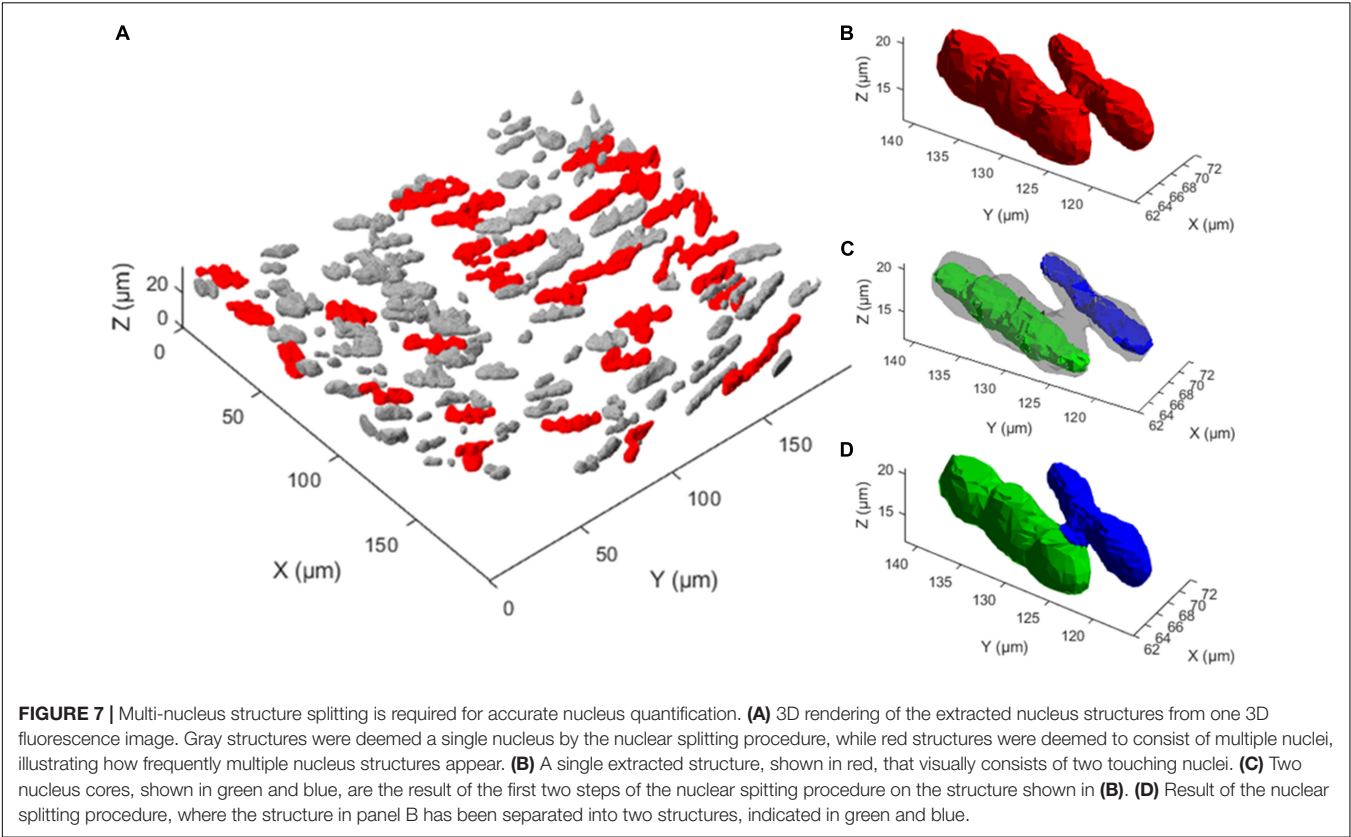
DISCUSSION

The aim of this study was to develop a method for splitting touching elongated nucleus structures segmented from TPLSM image stacks of intact non-fixated blood vessels into their corresponding nuclei and to evaluate the accuracy of the automatic characterization of the blood vessel's cell content.

The results show that the spectral clustering-based nucleus splitting procedure successfully split structures of multiple elongated nuclei into their individual nuclei, as illustrated in

TABLE 2 | Nuclear splitting results in insignificant differences between mean manual and automated nucleus counts.

Method/Measure	Unit	n	Mean $\pm$ SD	p-value
Manual reference			129.8 ± 35.7	–
Automated count without splitting	Nuclei per scan	12	92.9 ± 18.8	$<0.001^*$
Automated count with splitting			127.6 ± 34.9	0.467^*
Relative difference manual and automated count without splitting	%	12	-26.6 ± 9.90	$<0.001^{**}$
Relative difference manual and automated count with splitting			-1.44 ± 7.05	0.493^{**}
Control group	10^4 nuclei per mm^3	6	10.9 ± 2.57	–
VSMC apoptosis group			7.23 ± 0.85	0.008^{***}

*Percentages for the relative differences are calculated with respect to manual count results. * Paired t-test vs. manual count. ** One sample t-test. *** Two sample t-test vs. control group. SD, standard deviation.; n, number of image stacks included in analysis.*

FIGURE 7 | Multi-nucleus structure splitting is required for accurate nucleus quantification. **(A)** 3D rendering of the extracted nucleus structures from one 3D fluorescence image. Gray structures were deemed a single nucleus by the nuclear splitting procedure, while red structures were deemed to consist of multiple nuclei, illustrating how frequently multiple nucleus structures appear. **(B)** A single extracted structure, shown in red, that visually consists of two touching nuclei. **(C)** Two nucleus cores, shown in green and blue, are the result of the first two steps of the nuclear spitting procedure on the structure shown in **(B)**. **(D)** Result of the nuclear splitting procedure, where the structure in panel B has been separated into two structures, indicated in green and blue.

Figure 7, based on the likelihood that voxels within those structures were part of the same elongated nucleus. The implementation of the nucleus splitting method significantly improved the accuracy of the automated nucleus count (**Table 2**). In addition to this, the relative difference between the manual and automated counts was no longer significantly dependent on the samples cell content (**Figure 8**). With regard to transmural nucleus distributions, the nucleus splitting procedure generally made local maxima more pronounced, making the layered distribution of VSMCs in the media more apparent (**Figure 9**). This effect was stronger in vessels with higher cell density, because touching nuclei from different layers needed to be split more often. This makes the nucleus splitting procedure valuable, especially for higher cell density vessels, as these have more nuclei situated close enough to be recognized as a single structure.

While previous studies have analyzed VSMCs segmented from fluorescence microscopy image stacks of non-sectioned vessels before, their focus was on pattern and orientation analysis, rather than cell content quantification (Daly et al., 2002; McGrath et al., 2005; Spronck et al., 2016; Cordoba and Daly, 2019). So far, histological tissue analysis has been the standard for quantifying cell content in vessels (Clarke et al., 2010; Pai et al., 2011; Yu et al., 2011; Roostalu et al., 2018). The proposed image analysis method provides a useful new tool for quantifying cell content in vessels from 3D image stacks. Compared to histology, our method provides several benefits as it does not require vessel fixation and sectioning, making it possible to determine cell content, densities and distributions within the vessel wall under *in vivo*-like loading conditions without disturbing them. Therefore, our method can help provide
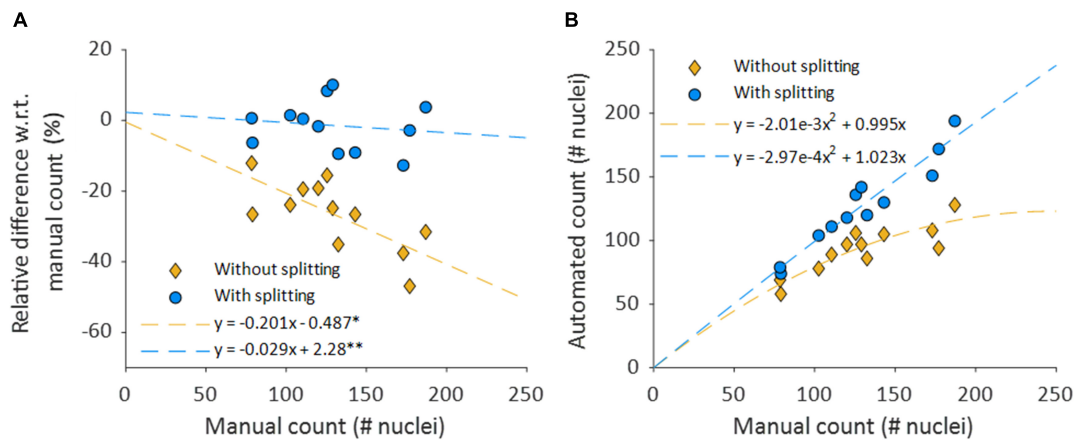
FIGURE 8 | Nuclear splitting improves accuracy of cell content quantification. **(A)** Shows the differences between the manual and automated counts, normalized with respect to the manual count. The dashed lines depict simple linear regression lines of both counts. *$p = 0.008$ and $p = 0.953$ for the slope and intercept, respectively. **$p = 0.653$ and $p = 0.789$ for the slope and intercept, respectively. **(B)** Automated nucleus counts without and with splitting, against the manual count. The formulas for the dashed lines in panel B are directly derived from the linear regression coefficients of their respective relative data shown in **(A)**.
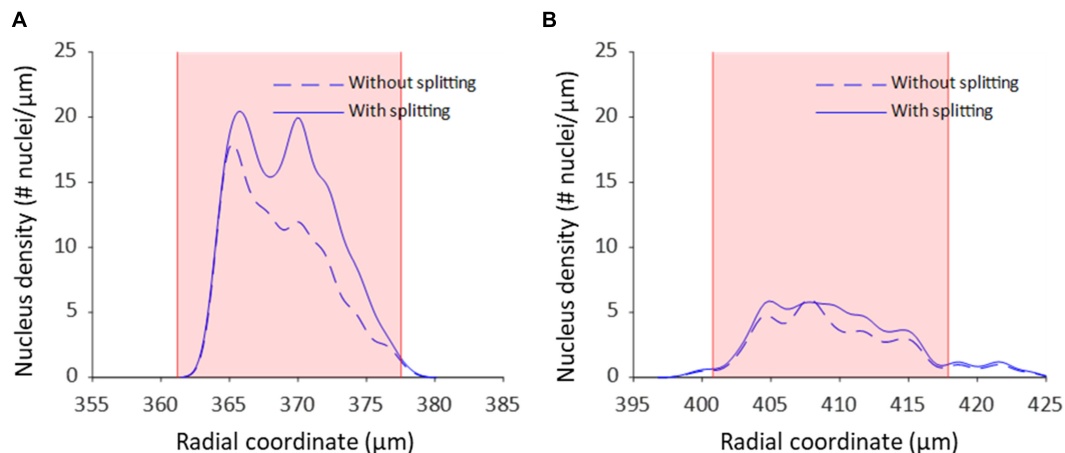
FIGURE 9 | Nucleus splitting makes VSMC layers more distinct in transmural cell density distributions. **(A)** Nucleus density as a function of radial location for a sample of a wild type animal (control $Apoe^{-/-}$) with high cell content. By splitting structures with nuclei from different layers the layered organization of VSMCs becomes more prominent. Multi-nucleus structures are predominantly on the adventitial side of the vessel wall. **(B)** Nucleus density as a function radial location for a sample from the VSMC apoptosis group ($SM22\alpha$-hDTR $Apoe^{-/-}$) with low cell content. Multi-nucleus structures are less frequent and spread more evenly throughout the vessel wall of the low cell content vessel compared to the high cell content vessel. Shaded (pink) areas denote the media in each sample.

potential new insights and possibilities for research on active vessel biomechanics, vessel pathophysiology, and modeling of the vessel wall.

The induced VSMC apoptosis case study served to illustrate the usefulness of the proposed image analysis method as the measured 33.7% decrease in medial nucleus density for the VSMC apoptosis group, as compared to the control group, was in line with literature (Clarke et al., 2006). Additionally, the transmural distributions of VSMC apoptosis group displayed less profound local maxima compared to the control group, as illustrated in **Figure 9**, indicating that induced VSMC apoptosis disturbed the layered distribution of VSMCs in the vessel wall. This level of detailed transmural cell distribution analysis would not be feasible with histological slides, as vessel cell content would

not be quantified under well-controlled biomechanical *in vivo*-like conditions.

Interestingly, throughout the dataset multi-nucleus structures were more frequent at the adventitial than the luminal side of the vessel wall, as demonstrated in **Figure 9**. It is likely that, as fluorescence intensity decreases with increased sample penetration, dim extra-nuclear fluorescent structures became undetectable and no longer linked neighboring nuclei. Alternatively, it could be that spacing between nuclei increased toward the luminal side of the vessel wall, resulting in fewer multi-nucleus structures. Perhaps the intravenous injection of DT, and subsequent penetration into the vessel wall from the luminal side, may have caused an uneven level of cell death throughout the vessel, thereby influencing nucleus spacing.

However, the current dataset is insufficient to determine whether this observation was due to pathophysiological model properties or imaging artifacts.

While the proposed nucleus splitting procedure significantly improved the accuracy of automated cell content quantification, the spread in the relative differences between automated and manual counts remained similar (**Table 2**). Because the Syto-41 fluorescent staining also labeled mRNA to a lesser extent, other structures were visible near nuclei in the green channel throughout the dataset, to various extents. Consequently, parameters α, β, c, and the intensity threshold used during the Vesselness filtering step were tuned to filter out (most of) these structures, preventing them from acting as bridges between extracted nuclei and resulting in more multi-nucleus structures. Conversely, this makes the Vesselness filtering less sensitive to low intensity nuclei, and more sensitive to brightness variations throughout and between samples, resulting in a larger spread in relative differences the automated and manual counts. To minimize this problem, it is advisable for future research to use a more selectively nucleic acid stain.

The memory required to perform the proposed image stack analysis method should be considered when selecting a computer to run the image stack analysis on. Since large Laplacian matrixes are generated when splitting large multi-nucleus structures, it is possible to run out of memory when processing these structures. While a modern computer, with an i7-9700 CPU @ 3.00 GHz (Intel, Santa Clara, CA, United States) and 16 GB of RAM, was used to process the data, some image stacks had to be excluded from the dataset as they contained excessively large structures that could therefore not be processed. To prevent the exclusion of image stacks, for future research, it is recommended to use a computer with more memory or further optimize the code for large structures.

CONCLUSION

The proposed nucleus splitting procedure greatly improves the accuracy of the automated quantification of cell content in mouse carotid arteries. The presented image analysis framework now provides a robust tool to quantitatively characterize VSMC content, orientation and distribution to inform experimental and advanced computational studies on vascular structure and function.

DATA AVAILABILITY STATEMENT

The raw data supporting the conclusions of this article will be made available by the authors, without undue reservation.

ETHICS STATEMENT

The animal study was reviewed and approved by the Ethics Committee for Animal Experiments of Maastricht University.

AUTHOR CONTRIBUTIONS

KWFL: conceptual design, setting up imaging protocol and data analysis procedure, performing manual nucleus count and data analysis, and drafting the article. KDR and BS: conceptual design, data interpretation, and critical revision of the article. MMB: sample preparation and data collection. AMGJ and LJS: provided animal model. RM: contributed to setting up imaging protocol and performing manual nucleus count. WH: critical revision of the article, with a focus on the mathematical aspects of the image analysis method. TD: critical revision of the article. All authors contributed to the article and approved the submitted version.

FUNDING

REFERENCES

Abdolhoseini, M., Kluge, M. G., Walker, F. R., and Johnson, S. J. (2019). Segmentation of heavily clustered nuclei from histopathological images. *Sci. Rep.* 9:4551. doi: 10.1038/s41598-019-38813-2

Atta-Fosu, T., Guo, W., Jeter, D., Mizutani, C. M., Stopczynski, N., and Sousa-Neves, R. (2016). 3D clumped cell segmentation using curvature based seeded watershed. *J. Imaging* 2:31. doi: 10.3390/jimaging2040031

Bowman, A. W., and Azzalini, A. (2004). *Applied Smoothing Techniques for Data Analysis : The Kernel Approach With S-Plus Illustrations*. Oxford: Clarendon Press.

Brozovich, F. V., Nicholson, C. J., Degen, C. V., Gao, Y. Z., Aggarwal, M., and Morgan, K. G. (2016). Mechanisms of vascular smooth muscle contraction and the basis for pharmacologic treatment of smooth muscle disorders. *Pharmacol. Rev.* 68, 476–532. doi: 10.1124/pr.115.010652

Clarke, M. C., Talib, S., Figg, N. L., and Bennett, M. R. (2010). Vascular smooth muscle cell apoptosis induces interleukin-1-directed inflammation: effects of hyperlipidemia-mediated inhibition of phagocytosis. *Circ. Res.* 106, 363–372. doi: 10.1161/CIRCRESAHA.109.208389

Clarke, M. C. H., Figg, N., Maguire, J. J., Davenport, A. P., Goddard, M., Littlewood, T. D., et al. (2006). Apoptosis of vascular smooth muscle cells induces features of plaque vulnerability in atherosclerosis. *Nat. Med.* 12, 1075–1080. doi: 10.1038/nm1459

Cordoba, C. G., and Daly, C. J. (2019). The organisation of vascular smooth muscle cells; a quantitative fast fourier transform (FFT) based assessment. *Transl. Res. Anat.* 16:100047. doi: 10.1016/j.tria.2019.100047

Daly, C., McGee, A., Vila, E., Briones, A., Giraldo, J., Arribas, S., et al. (2002). Analysing the 3D structure of blood vessels using confocal microscopy. *Microsc. Anal.* 92, 5–8.

Danìk, O., Matula, P., Ortiz-de-Solórzano, C., Muñoz-Barrutia, A., Maška, M., and Kozubek, M. (2009). *Segmentation of Touching Cell Nuclei Using a Two-Stage Graph Cut Model*. Berlin Heidelberg: Springer, 410–419.

Jaminon, A., Reesink, K., Kroon, A., and Schurgers, L. (2019). The role of vascular smooth muscle cells in arterial remodeling: focus on calcification-related processes. *Int. J. Mol. Sci.* 20:694. doi: 10.3390/ijms20225694

Masson, I., Beaussier, H., Boutouyrie, P., Laurent, S., Humphrey, J. D., and Zidi, M. (2011). Carotid artery mechanical properties and stresses quantified using

in vivo data from normotensive and hypertensive humans. *Biomech. Model. Mechanobiol.* 10, 867–882. doi: 10.1007/s10237-010-0279-6

Mathew, B., Schmitz, A., Munoz-Descalzo, S., Ansari, N., Pampaloni, F., Stelzer, E. H., et al. (2015). Robust and automated three-dimensional segmentation of densely packed cell nuclei in different biological specimens with Lines-of-Sight decomposition. *BMC Bioinform.* 16:187. doi: 10.1186/s12859-015-0617-x

McGrath, J. C., Deighan, C., Briones, A. M., Shafaroudi, M. M., McBride, M., Adler, J., et al. (2005). New aspects of vascular remodelling: the involvement of all vascular cell types. *Exp. Physiol.* 90, 469–475. doi: 10.1113/expphysiol.2005.030130

Nielsen, F., and Bhatia, R. (2014). *Matrix Information Geometry*. Berlin: Springer Berlin.

O'Connell, M. K., Murthy, S., Phan, S., Xu, C., Buchanan, J., Spilker, R., et al. (2008). The three-dimensional micro- and nanostructure of the aortic medial lamellar unit measured using 3D confocal and electron microscopy imaging. *Matrix Biol.* 27, 171–181. doi: 10.1016/j.matbio.2007.10.008

Owens, G. K. (1995). Regulation of differentiation of vascular smooth muscle cells. *Physiol. Rev.* 75, 487–209.

Pai, A., Leaf, E. M., El-Abbadi, M., and Giachelli, C. M. (2011). Elastin degradation and vascular smooth muscle cell phenotype change precede cell loss and arterial medial calcification in a uremic mouse model of chronic kidney disease. *Am. J. Pathol.* 178, 764–773. doi: 10.1016/j.ajpath.2010.10.006

Roostalu, U., Aldeiri, B., Albertini, A., Humphreys, N., Simonsen-Jackson, M., Wong, J. K. F., et al. (2018). Distinct cellular mechanisms underlie smooth muscle turnover in vascular development and repair. *Circ. Res.* 122, 267–281. doi: 10.1161/CIRCRESAHA.117.312111

Rousseeuw, P. J. (1987). Silhouettes: a graphical aid to the interpretation and validation of cluster analysis. *J. Comput. Appl. Math.* 20, 53–65. doi: 10.1186/1471-2164-6-35

Ruszczycki, B., Pels, K. K., Walczak, A., Zamlynska, K., Such, M., Szczepankiewicz, A. A., et al. (2019). Three-dimensional segmentation and reconstruction of neuronal nuclei in confocal microscopic images. *Front. Neuroanat.* 13:81. doi: 10.3389/fnana.2019.00081

Spronck, B., Heusinkveld, M. H., Donders, W. P., de Lepper, A. G., Op't Roodt, J., Kroon, A. A., et al. (2015). A constitutive modeling interpretation of the relationship among carotid artery stiffness, blood pressure, and age in

hypertensive subjects. *Am. J. Physiol. Heart. Circ. Physiol.* 308, H568–H582. doi: 10.1152/ajpheart.00290.2014

Spronck, B., Megens, R. T., Reesink, K. D., and Delhaas, T. (2016). A method for three-dimensional quantification of vascular smooth muscle orientation: application in viable murine carotid arteries. *Biomech. Model. Mechanobiol.* 15, 419–432. doi: 10.1007/s10237-015-0699-4

van der Bruggen, M. M., Reesink, K. D., Spronck, P. J. M., Bitsch, N., Hameleers, J., Megens, R. T. A., et al. (2021). An integrated set-up for ex vivo characterisation of biaxial murine artery biomechanics under pulsatile conditions. *Sci. Rep.* 11:2671. doi: 10.1038/s41598-021-81151-5

von Luxburg, U. (2007). A tutorial on spectral clustering. *Stat. Comput.* 17, 395–416. doi: 10.1007/s11222-007-9033-z

Yu, H., Clarke, M. C., Figg, N., Littlewood, T. D., and Bennett, M. R. (2011). Smooth muscle cell apoptosis promotes vessel remodeling and repair via activation of cell migration, proliferation, and collagen synthesis. *Arterioscler. Thromb. Vasc. Biol.* 31, 2402–2409. doi: 10.1161/ATVBAHA.111.235622

Zulliger, M. A., Rachev, A., and Stergiopulos, N. (2004). A constitutive formulation of arterial mechanics including vascular smooth muscle tone. *Am. J. Physiol. Heart Circ.* 287, 1335–1343. doi: 10.1152/ajpheart.00094.2004

Phenylephrine-Induced Cardiovascular Changes in the Anesthetized Mouse: An Integrated Assessment of *in vivo* Hemodynamics Under Conditions of Controlled Heart Rate

Rajkumar Rajanathan[1]*, Tina Myhre Pedersen[1], Morten B. Thomsen[2], Hans Erik Botker[3] and Vladimir V. Matchkov[1]

[1] Department of Biomedicine, Aarhus University, Aarhus, Denmark, [2] Department of Biomedical Sciences, University of Copenhagen, Copenhagen, Denmark, [3] Department of Cardiology, Aarhus University Hospital, Aarhus, Denmark

Objective: Investigating the cardiovascular system is challenging due to its complex regulation by humoral and neuronal factors. Despite this complexity, many existing research methods are limited to the assessment of a few parameters leading to an incomplete characterization of cardiovascular function. Thus, we aim to establish a murine *in vivo* model for integrated assessment of the cardiovascular system under conditions of controlled heart rate. Utilizing this model, we assessed blood pressure, cardiac output, stroke volume, total peripheral resistance, and electrocardiogram (ECG).

Hypothesis: We hypothesize that (i) our *in vivo* model can be utilized to investigate cardiac and vascular responses to pharmacological intervention with the α_1-agonist phenylephrine, and (ii) we can study cardiovascular function during artificial pacing of the heart, modulating cardiac function without a direct vascular effect.

Methods: We included 12 mice that were randomly assigned to either vehicle or phenylephrine intervention through intraperitoneal administration. Mice were anesthetized with isoflurane and intubated endotracheally for mechanical ventilation. We measured blood pressure *via* a solid-state catheter in the aortic arch, blood flow *via* a probe on the ascending aorta, and ECG from needle electrodes on the extremities. Right atrium was electrically paced at a frequency ranging from 10 to 11.3 Hz before and after either vehicle or phenylephrine administration.

Results: Phenylephrine significantly increased blood pressure, stroke volume, and total peripheral resistance compared to the vehicle group. Moreover, heart rate was significantly decreased following phenylephrine administration. Pacing significantly decreased stroke volume and cardiac output both prior to and after drug administration. However, phenylephrine-induced changes in blood pressure and total peripheral resistance were maintained with increasing pacing frequencies compared to the vehicle

group. Total peripheral resistance was not significantly altered with increasing pacing frequencies suggesting that the effect of phenylephrine is primarily of vascular origin.

Conclusion: In conclusion, this *in vivo* murine model is capable of distinguishing between changes in peripheral vascular and cardiac functions. This study underlines the primary effect of phenylephrine on vascular function with secondary changes to cardiac function. Hence, this *in vivo* model is useful for the integrated assessment of the cardiovascular system.

BACKGROUND

Cardiovascular morbidity is the leading cause of mortality worldwide (Mc Namara et al., 2019). Understanding the molecular mechanisms underlying cardiovascular morbidity is, therefore, of utmost importance to provide new therapeutic insight and preventive strategies to reduce mortality and improve the quality of life for patients. Many great discoveries have been made through *in vivo* assessment of cardiovascular function. Animal models, particularly mice, are often used for this purpose as they are easily accessible and compatible with research on molecular mechanisms underlying cardiovascular physiology and pathology (Janssen et al., 2002; Zaragoza et al., 2011; Camacho et al., 2016). However, many of the suggested molecular mechanisms important for cardiovascular function are based on studies that are limited to isolated organ functions or basic phenotyping reports on tissue perfusion and blood pressure changes. Thus, a comprehensive cardiovascular functional phenotype is rarely described. Existing models have provided significant improvements to the therapeutic armamentarium against cardiovascular diseases, however, it remains the leading cause of death and disability worldwide (Pandya et al., 2013). Hence, new research modalities and an improvement of existing methods are essential to further progress our understanding of mechanisms underlying cardiovascular morbidity (Wier, 2014; Figtree et al., 2021).

Studying the cardiovascular system is a complex task. The cardiovascular system is a closed system consisting of the heart as a pump and blood vessels in which blood flows through. Thus, the efficiency of the circulation is determined by cardiac function, i.e., contractility and heart rate, in conjunction with vascular diameter changes determining total peripheral resistance (Mayet and Hughes, 2003). This interplay between cardiac and vascular functions is further complicated by tight regulation from numerous humoral factors and the autonomic nervous system under normal physiological conditions (Holmes et al., 2004; Gordan et al., 2015; Song et al., 2015; Paz Ocaranza et al., 2020). Evidently, there is a vast number of regulators of the cardiovascular system complicating the mechanistic assessment of the molecular background underlying cardiovascular function under normal physiological conditions. Apart from biological variation including aging and fitness level, deviation from normal physiological conditions due to pathology, e.g., changed sympathetic activity in hypertension, may further contribute to

the complexity of the cardiovascular system (Kougias et al., 2010). All these factors must be considered when extrapolating *ex vivo* knowledge onto whole body homeostasis.

Most conventional ways to investigate the cardiovascular system lack the integrated assessment. For instance, cardiac function is extensively assessed *in vivo* through various imaging modalities, e.g., echocardiography and magnetic resonance imaging (Ram et al., 2011; Botnar and Makowski, 2012; Li et al., 2020). Albeit this provides great knowledge on cardiac function *in vivo*, the results from these studies are often seen in isolation and not in conjunction to any physiological changes in peripheral vascular resistance and blood pressure. Vascular function is routinely studied *ex vivo*, for instance, through different forms of myography, but this is a highly simplified approach as it does not permit simultaneous assessment of changes in blood flow and transmural pressure that take place *in vivo* (Mulvany and Aalkjaer, 1990). Perfusion of the hind limb or another vascular bed provides a good insight into changes in the peripheral resistance, but this procedure can only be done under conditions of either constant flow or constant pressure (Bomzon and Naidu, 1985). Many studies conclude on vascular function based on blood pressure measurements (Zhao et al., 2011) or tissue perfusion assessment with imaging techniques (Moroz and Reinsberg, 2018), but the conclusions are limited due to lacking information on cardiac output or volume blood flow and driving perfusion pressure, respectively, which are key components for tissue perfusion. Hence, the conventional models are unable to properly address current pressing issues in cardiovascular physiology. One of the challenges is elucidating the mechanisms of molecular signaling or a pathological state with multifarious cardiovascular effects (Tisdale and Gheorghiade, 1992; Holmes et al., 2004; Song et al., 2015; Nielsen et al., 2019; Paz Ocaranza et al., 2020). Moreover, the concurrent assessment of load-dependent and independent parameters is valuable in all disease states and after drug administration. This can be achieved in an integrated model that makes the separation of intrinsic cardiac parameters and vascular responses feasible.

Consequently, the field of cardiovascular physiology demands a comprehensive model for the integrated assessment of the cardiac and vascular functions and their responses to pharmacological intervention. Considering this, we propose an experimental protocol for the integrated assessment of hemodynamic parameters of anesthetized mice before and after pharmacological intervention. By fully elucidating the

cardiovascular mechanisms, including load-dependent and independent parameters, our method may contribute to providing valuable new therapeutic targets. In this study, we have challenged mice with a selective α_1 adrenoreceptor agonist, phenylephrine, which has been described to affect both cardiac and vascular functions *in vivo* (Crosley et al., 1951; Malhotra et al., 1998). We aimed to validate our experimental protocol by distinguishing between phenylephrine-induced vascular and subsequent cardiac changes. We hypothesize that artificial pacing of the heart controls the cardiac function and, hence, can be helpful to differentiate between vascular and cardiac responses. The hemodynamic assessment includes blood pressure, cardiac output, stroke volume, total peripheral resistance, and electrophysiological parameters derived from the electrocardiogram (ECG), and their changes to increasing pacing frequencies.

MATERIALS AND METHODS

Animals

Male mice (C57BL/6, Janvier Labs, France) at the age of approximately 9 months with a mean weight of approximately 33 g were used in this study. Mice were housed in rooms with temperature (21.5°C) and humidity (55%) regulation and with a 12:12 h light-dark cycle. Animals had access to *ad libitum* food and tap water. All animal experiments conformed to the guidelines from Directive 2010/63/EU of the European Parliament on the protection of animals used for scientific purposes. The experimental protocol was approved by the Animal Experiments Inspectorate of the Danish Ministry of Environment and Food and reported in accordance with the ARRIVE (Animal Research: Reporting *in vivo* Experiments) guidelines. Mice were euthanized immediately at the end of protocol under deep anesthesia by cervical dislocation.

Anesthesia and Mechanical Ventilation

Anesthesia of mice was induced with 3% isoflurane mixed with 100% O_2 for 5 min. Mice were then placed on a homeothermic blanket system (50-7222F, Harvard Apparatus, United States) to control core temperature (37 $\pm$ 5°C) and anesthesia was adjusted and maintained at 2% of isoflurane throughout. Hair was removed from the thorax and cervical regions of the supine mice with a depilatory agent (Veet, Canada). A microscope was used for the surgical procedures. Following a midline cervical incision, the trachea was visualized, and endotracheal intubation was performed. The intubation tube was connected to a MiniVent Ventilator (model 845, Harvard Apparatus, United States). The expired air was connected to a capnograph (Type 340, Harvard Apparatus, United States) reporting the end-tidal CO_2 (% $etCO_2$). Furthermore, positive end-expiratory pressure of 2 cm H_2O was attained with a water lock consisting of a water-filled tube (Schwarte et al., 2000). An actuator head was connected to the inspiratory air circuit monitoring airway pressure and flow, and this was set to a maximum threshold of 15 cm H_2O to prevent pulmonal barotrauma (Wilson et al., 2012). Tidal volume was kept constant

at 10 µl/g body mass (Hauber et al., 2010). Ventilation rate was adjusted based on % $etCO_2$ at approximately 3.5% (Hansen et al., 2020). Next, pancuronium-bromide (0.4 mg/h i.p., P1918, Sigma, United States), an M_2-acetylcholine receptor blocker, was used to immobilize the mouse for the rest of protocol duration (Uhlirova et al., 2016), and 0.9% NaCl solution (1 ml i.p., 9 mg/ml NaCl, Fresenius Kabi, Germany) was provided to balance out any fluid loss.

Arterial Blood Pressure Measurements

A 1.0 F solid-state catheter (SPR-1000, Millar, United States) connected to a bioamplifier unit (ADInstruments, Australia) was introduced into the common carotid artery and placed in the aortic arc for continuous blood pressure measurements. The right carotid artery was visualized and bluntly dissected using forceps. Special precaution was taken to prevent damage of the vagal nerve. To prevent the artery from drying out, it was kept wet during the implantation procedure with warm 0.9% NaCl saline. Three silk sutures (Multifilament 5-0, Teleflex Medical, United States) were used for cannulation and fixation of the catheters. The first suture was tightened in a double knot around the artery to occlude it as far cranially as possible. The second suture was placed under the artery and pulled caudally to temporarily occlude the artery. The third suture was prepared as a loose knot in the caudal end of the artery segment. The tip of a needle (25G × 5/8", 0.5 mm × 16 mm, BD Microlance, United States) was bent in a 90° angle and used to puncture the carotid artery. The solid-state catheter was then introduced in the caudal direction through the puncture, and it was secured by tightening of the third suture. Once secured, the second suture was removed, and the catheter tip was advanced and placed in the aortic arc. The position of the catheter tip was confirmed by evaluations of the blood pressure pulse profile corresponding to blood pressure in aorta, and its location was also anatomically verified at the end of the experiment following dissection. To prevent loss of fluid through evaporation, the surgical area was covered with gauze wet with warm 0.9% NaCl saline.

Transit-Time Flow Probe

A transit-time flow probe (1.5 SL, Transonic, United States) was mounted on the ascending aorta assessing the blood flow as surrogate measure for cardiac output (Janssen et al., 2002). Following a midsternal longitudinal incision exposing tissue on the right thoracic side, the mouse was repositioned on the left side exposing the right side of thorax to access the heart and the ascending aorta as described previously (Tarnavski et al., 2004). A longitudinal incision was made spanning from the first to third intercostal space 1–2 mm laterally from the sternal midline. The thoracotomy was expanded to approximately 1 cm in width using a small mouse retractor. The right anterior surface of the heart and ascending aorta were identified, and pericardiectomy was carefully performed. In case of thymus covering the ascending aorta, a partial thymectomy was performed. A blunt vascular hook (0.3 mm) and forceps were used for final blunt dissection and isolation of the ascending aorta. The transit-time flow probe was prepared by soaking it in ultrasound gel (Kruuse, Denmark) until signal quality was optimal. Once

prepared, the flow probe was positioned on the ascending aorta. Successful placement of the flow probe was evident from stable representable flow recordings indicating no aortic compression. Cardiac output was calculated as the integral of the transit-time flow probe measurements.

Electrical Pacing and Electrocardiogram Recording

Platinum bipolar electrodes connected to a dual bioamplifier/stimulator unit (ADInstruments, Australia) were positioned on the right atrium in the area of the sinus node for electrical pacing of the heart. The electrical pulse width was 0.2 ms, and the current was 3 mA. ECG electrodes (MLA2505, ADInstruments, Australia) connected to a shielded 5-lead bioamplifier cable (MLA2540, ADInstruments, Australia) were placed on each limb for the recording of leads that correspond to lead I and II in humans as shown in **Figure 1**. The bioamplifier unit for the ECG recording was set to detect signals within a range of 10 mV with a low-pass filter (500 Hz), a high-pass filter (0.3 Hz), and a mains filter activated.

Experimental Protocol

The experimental protocol consisted of two electrical pacing sessions with pharmacological intervention in between them. After ensuring steady baseline recordings of blood pressure, blood flow, and ECG parameters, the first pacing session was commenced. For each pacing session, the heart was initially paced at 10 Hz with stepwise increase to 10.3, 10.6, 11, and 11.3 Hz. Each frequency was maintained for a period of 20 s. Following a pause of 1 min an injection of either phenylephrine (0.3 mg/kg i.p., P6126, Sigma, United States) or a corresponding volume of 0.9% NaCl was given, with animals being allocated to each group according to a random number generator. The second pacing session was initiated 10 min after the injection. Data was collected for 6 min following the end of the second pacing session. Data were acquired using LabChart Pro 8 (ADInstruments, Australia) with a sampling rate of 1 k/s. Hemodynamic and electrophysiological parameters were averaged over a period of 20 s.

Statistics

Data were analyzed using Prism 9 (GraphPad, United States) and presented as means ± SEM. Baseline values between the two groups were compared using unpaired *t*-test. The cardiovascular parameters obtained during pacing protocols and following pharmacological intervention were compared using two-way ANOVA with Bonferroni correction. Results were considered statistically significant at $P < 0.05$.

RESULTS

Instrumentation of blood pressure and flow probes was successful in all six mice, however, ECG data were only available for $n = 5$. The protocol was completed in all mice. Baseline parameters in the two groups of mice were comparable (**Table 1**).

Electrical Pacing and Intervention With α_1 Adrenergic Agonist Did Not Significantly Alter the Electrocardiogram or Cause Arrhythmia

Electrical pacing of the right atrium did not interrupt atrioventricular conduction (**Figures 2A–F**). In both the first and second pacing sessions, PR interval and width of QRS complex were not significantly affected (**Figures 2G,H**). Furthermore, baseline values for the length of the PR interval and width of the QRS complex were similar between the phenylephrine and vehicle groups. Similarly, no differences were seen between the phenylephrine and vehicle groups in PR interval and width of QRS complex in between and after pacing sessions (**Figures 2G,H**).

α_1 Adrenergic Stimulation Significantly Elevated Blood Pressure but Not Cardiac Output Through Changes in Total Peripheral Resistance

As expected, following administration of phenylephrine, both systolic and diastolic blood pressures were significantly elevated (**Figures 3**, **4A**). Stroke volume was also increased after administration of phenylephrine (**Figure 4B**) while heart rate was significantly reduced in comparison with the vehicle group (**Figure 4C**). Accordingly, cardiac output was not changed after phenylephrine administration and was not different from the vehicle group (**Figure 4D**). Total peripheral resistance was calculated as blood pressure divided by the corresponding values for cardiac output for the analyzed period. The calculated total peripheral resistance was significantly increased after phenylephrine administration (**Figure 4E**). Altogether, our data suggest that phenylephrine elevated blood pressure primarily due to an increased total peripheral resistance.

Pacing Frequency Affects Cardiac Output but Not Total Peripheral Resistance

The increasing pacing frequency from 10 to 11.3 Hz significantly reduced systolic and diastolic blood pressures under control conditions in both the phenylephrine and vehicle groups (**Figure 5A**). In contrary, increasing pacing frequencies had no significant effect on systolic and diastolic blood pressures during the second pacing session for the vehicle or phenylephrine groups (**Figure 5B**). Stroke volume and cardiac output was significantly reduced with increasing pacing frequency both under control conditions and following phenylephrine and vehicle administration (**Figures 5C,D**). We did not observe changes in total peripheral resistance with increasing pacing frequencies, neither during control conditions or following phenylephrine and vehicle administration (**Figure 5E**). Moreover, the increased blood pressure and total peripheral resistance following phenylephrine administration compared to the vehicle group remained unaltered during the second pacing session (**Figures 5B,E**).
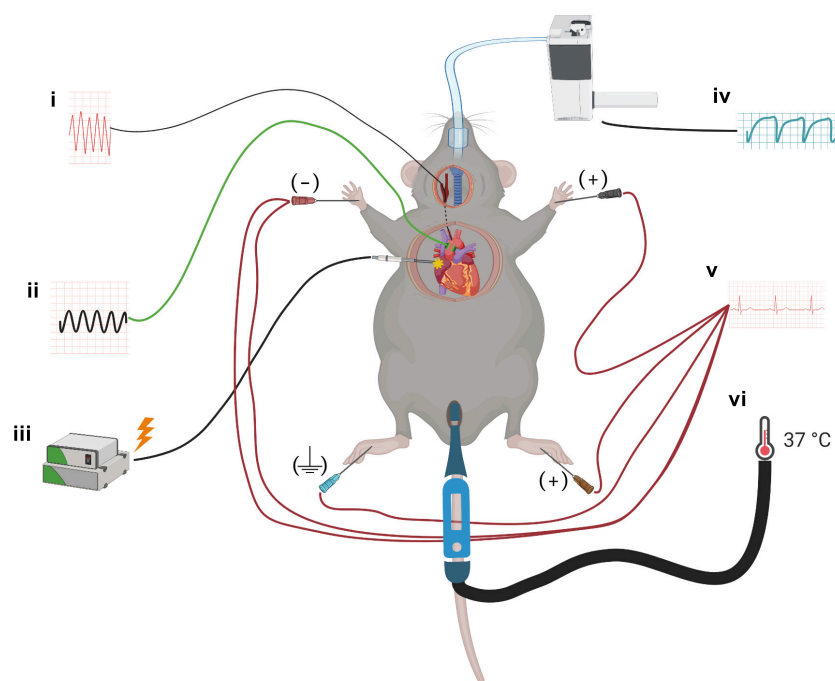
FIGURE 1 | A schematic for the experimental setup. Mice were anesthetized with isoflurane, and probes to monitor the cardiovascular parameters were implanted: (i) solid-state pressure catheter was inserted through the common carotid artery and placed in the arcus aorta, (ii) transit-time flow probe was mounted on the ascending aorta to measure cardiac output, (iii) bipolar electrodes were placed at the right atrium for cardiac pacing, (iv) mice were intubated endotracheally for mechanical ventilation, (v) ECG needle electrodes were placed on all four limbs to monitor heart rate and ECG parameters, and (vi) throughout the surgery and protocol, mice were placed on a homeothermic blanket system with a rectal probe to maintain core temperature.

DISCUSSION

This study reports on a mouse model for the assessment of cardiovascular parameters upon *in vivo* experimental interventions in a comprehensive and integrated manner. This model allows for distinction between interventions that have primary cardiac or vascular actions. We used α_1 adrenoceptor

TABLE 1 | Bodyweight, age, and baseline ventilatory, and cardiovascular parameters of anesthetized mice prior to administration of either phenylephrine (0.3 mg/kg, i.p.) or vehicle, and prior to cardiac pacing.

Parameters	Vehicle group	Phenylephrine group	*P*
Body weight, g	33.2 ± 0.6	32.1 ± 0.8	0.31
Age, weeks	38.7 ± 1.2	37.3 ± 0.9	0.40
Systolic blood pressure, mmHg	73.2 ± 5.2	69.3 ± 4.8	0.44
Diastolic blood pressure, mmHg	46.1 ± 4.8	41.1 ± 3.9	0.58
Heart rate, BPM	537 ± 19	542 ± 7	0.79
Stroke volume, µl	16.4 ± 1.9	15.6 ± 1.8	0.78
Cardiac output, ml/min	8.8 ± 1.0	8.5 ± 0.9	0.83
Peripheral resistance, mmHg·min/ml	6.5 ± 0.5	6.2 ± 0.5	0.72
End-tidal CO_2, %	3.4 ± 0.1	3.3 ± 0.2	0.68
Ventilation rate, min^{-1}	81.3 ± 2.9	87.0 ± 2.2	0.15

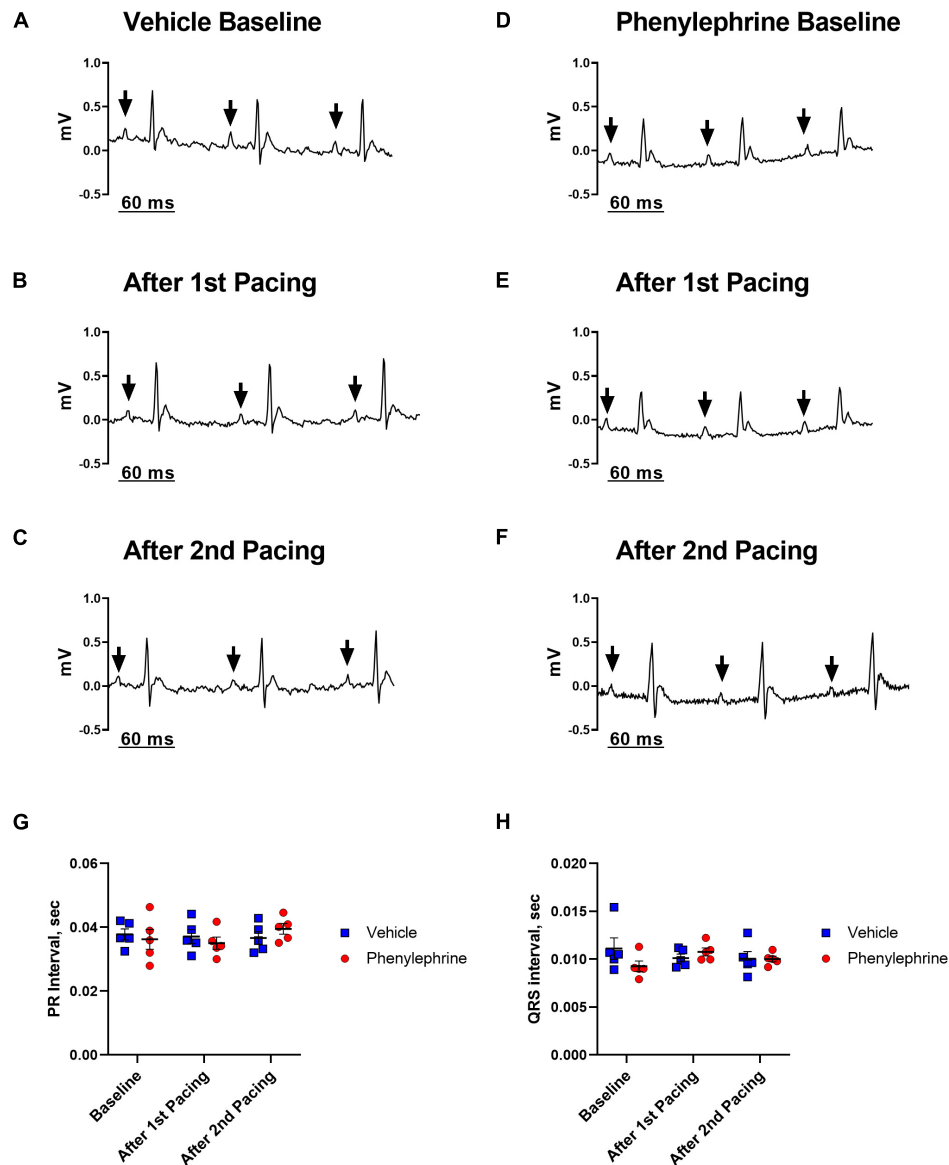*Data were compared with unpaired t-test with n = 6 in both groups.*

agonist stimulation to modulate vascular function and observed the subsequent effects on overall cardiovascular function. By assessing the response to increasing pacing frequencies compared to periods of rest both with and without phenylephrine, we were able to differentiate between cardiac and vascular effects. We reported complex changes in blood pressure, heart rate, cardiac output, and total peripheral resistance following the interventions.

We chose a selective α_1-adrenergic receptor agonist, phenylephrine, as it is known to increase blood pressure *via* elevation of systemic vascular resistance without any direct effect on myocardial contractility (Thiele et al., 2011). Phenylephrine is often used clinically as a vasopressor to treat arterial hypotension induced by general anesthesia (Kalmar et al., 2018). Moreover, phenylephrine is broadly used in *ex vivo* organ bath assessments of vascular functions (Gutierrez et al., 2019), but also *in vivo* in rodent experimental models (Boguslavskyi et al., 2021; Ralph et al., 2021) where it is used to provoke blood pressure changes. The α_1-adrenergic mechanism underlying the vasopressor effect of phenylephrine is well-described (Dessy et al., 1998; Jumrussirikul et al., 1998; Brozovich et al., 2016; Boguslavskyi et al., 2021). Accordingly, we suggest that the significant phenylephrine-induced elevation of blood pressure in this study is a result of vascular constriction with consequent increase in total peripheral resistance. Furthermore, these elevations in blood pressure and total peripheral resistance were accompanied by a decrease in heart rate. We attributed this heart rate change to be a

FIGURE 2 | Representative electrocardiograms (lead I) recorded prior to and after both the first and second pacing sessions for the vehicle **(A–C)** and phenylephrine groups **(D–F)**. Black arrows indicate P waves with consecutive QRS complexes, thus, describing sinus rhythm before and after electrical pacing of the heart. **(G)** There were no differences between the mean PR interval between vehicle and phenylephrine groups before and after both pacing sessions ($P = 0.92$). **(H)** No differences in width of QRS complex were seen between the vehicle and phenylephrine groups ($P = 0.47$). Data were compared with two-way ANOVA, $n = 5$.

response to increased activation of baroreceptors, i.e., baroreflex. Upon blood pressure induced activation, the baroreceptors, mediated through the activity of the autonomic nervous system, exercise changes to both cardiac and vascular functions, thus, counteracting any acute pressure changes (Andresen and Kunze, 1994; Jumrussirikul et al., 1998; Boguslavskyi et al., 2021). In our experiments, the baroreceptors failed to return the blood pressure to resting values following phenylephrine injection. This is most likely because phenylephrine-mediated α_1-adrenergic activation of vascular smooth muscle cells bypassed the baroreceptor-mediated inhibition of sympathetic outflow. As a result, phenylephrine maintained vasoconstriction

increasing total peripheral resistance and blood pressure. These phenylephrine-induced changes in blood pressure, total peripheral resistance, and heart rate are also described in humans (Crosley et al., 1951; Malhotra et al., 1998).

Phenylephrine administration increased stroke volume. We suggest that this may be result of both increased preload because of phenylephrine-induced venous constriction (Jumrussirikul et al., 1998; Kalmar et al., 2018; Boguslavskyi et al., 2021) and a baroreceptor mediated reduction in heart rate with subsequent increased diastolic filling time. However, this stroke volume elevation is limited by simultaneous elevation of afterload due to increased total peripheral resistance as described previously
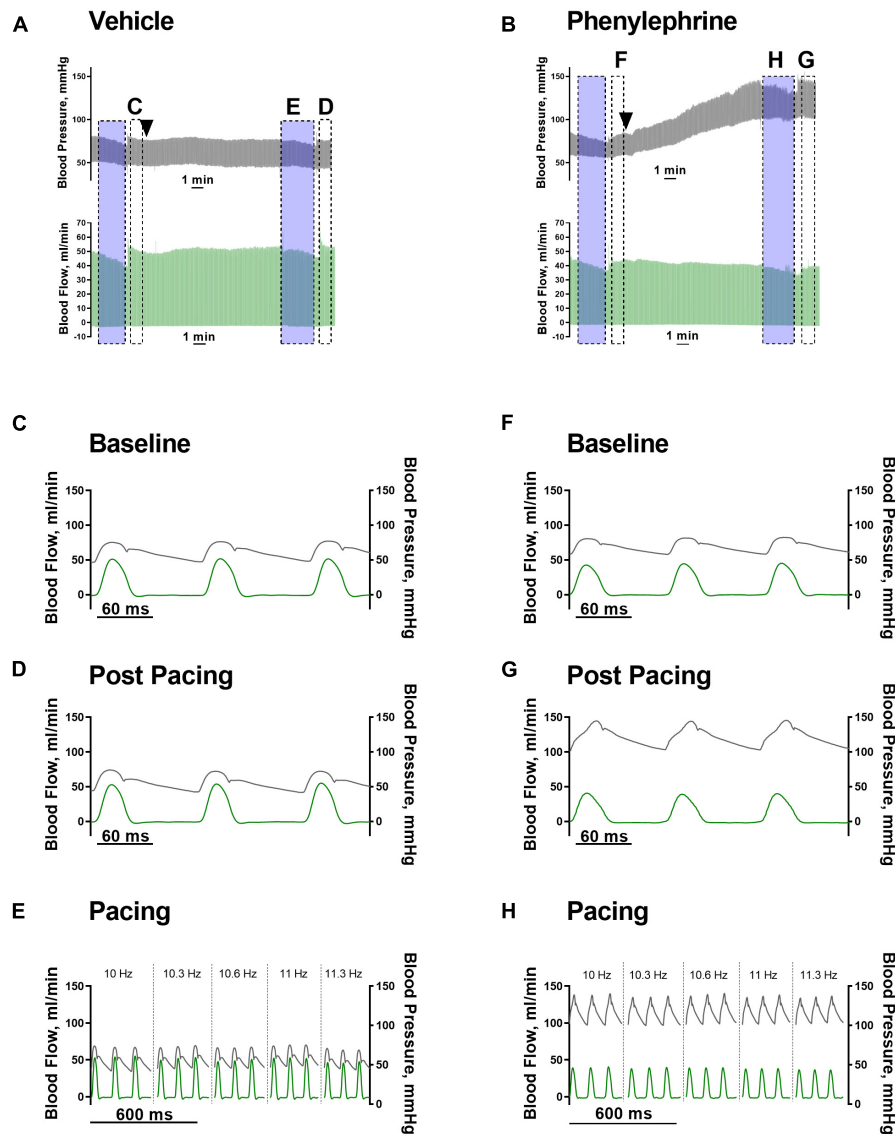
FIGURE 3 | (A,B) Representative traces of blood pressure (black traces) and blood flow (green traces) after vehicle or phenylephrine administration (black arrow heads). Transparent blue boxes indicate periods of pacing. Panels **(C–H)** are indicated in panels **(A,B)**. **(C,F)** Hemodynamic parameters prior to vehicle or phenylephrine administration. **(D,G)** Hemodynamic parameters after vehicle or phenylephrine administration and post second atrial pacing. **(E,H)** Hemodynamic parameters during second atrial pacing and after vehicle or phenylephrine administration.

(Yang et al., 2013; Kalmar et al., 2018). As a product of stroke volume and heart rate, cardiac output did not change significantly. Studies in humans reported both decreased and increased cardiac output following phenylephrine administration because of either increased afterload or reduced heart rate and an increased preload, respectively (Mon et al., 2017; Kalmar et al., 2018). A previous study in pigs suggested this bi-directional effect of phenylephrine to be related to changes to preload and, thus, preload level (Cannesson et al., 2012). Hence, in situations with significantly reduced end-diastolic ventricular filling, e.g., hemorrhage and hypotension, phenylephrine increases preload with consequent elevation in stroke volume and cardiac output (Cannesson et al., 2012). This is supported by observations of

increased cardiac output following phenylephrine administration to hypotensive patients (Kalmar et al., 2018). This effect of phenylephrine is predominantly mediated by venous constriction and elevation of venous return leading to increased preload and stroke volume. The lack of a significant increase of cardiac output in this study may suggest that these mice were under relatively mild hypotensive conditions, or that the relation between preload-dependence and cardiac output in mice is different in comparison with humans and pigs (Georgakopoulos and Kass, 2001; Cannesson et al., 2012; Mon et al., 2017; Kalmar et al., 2018).

Mice have high resting heart rates ranging from 500 to 700 beats per minute depending on the time of day
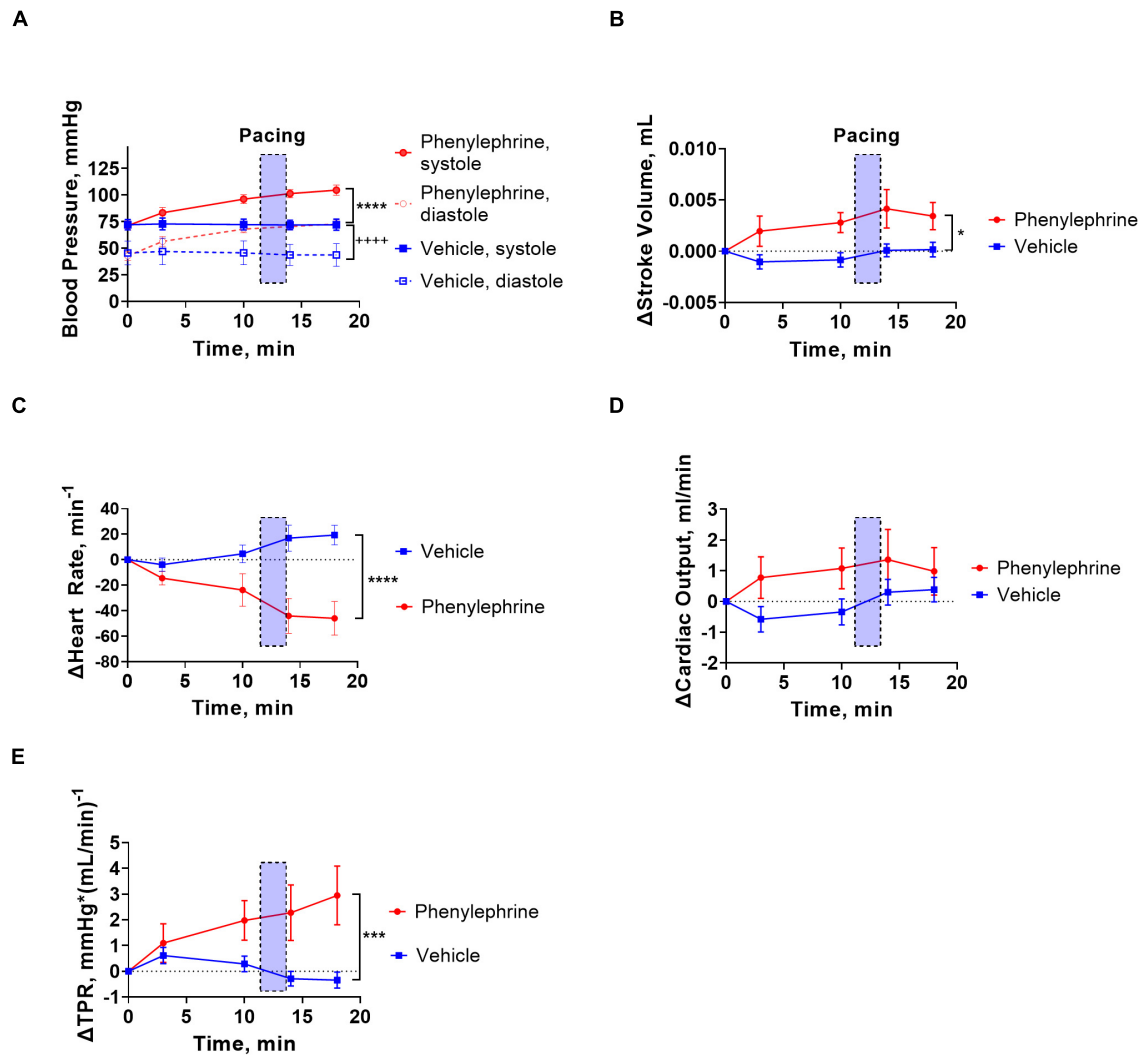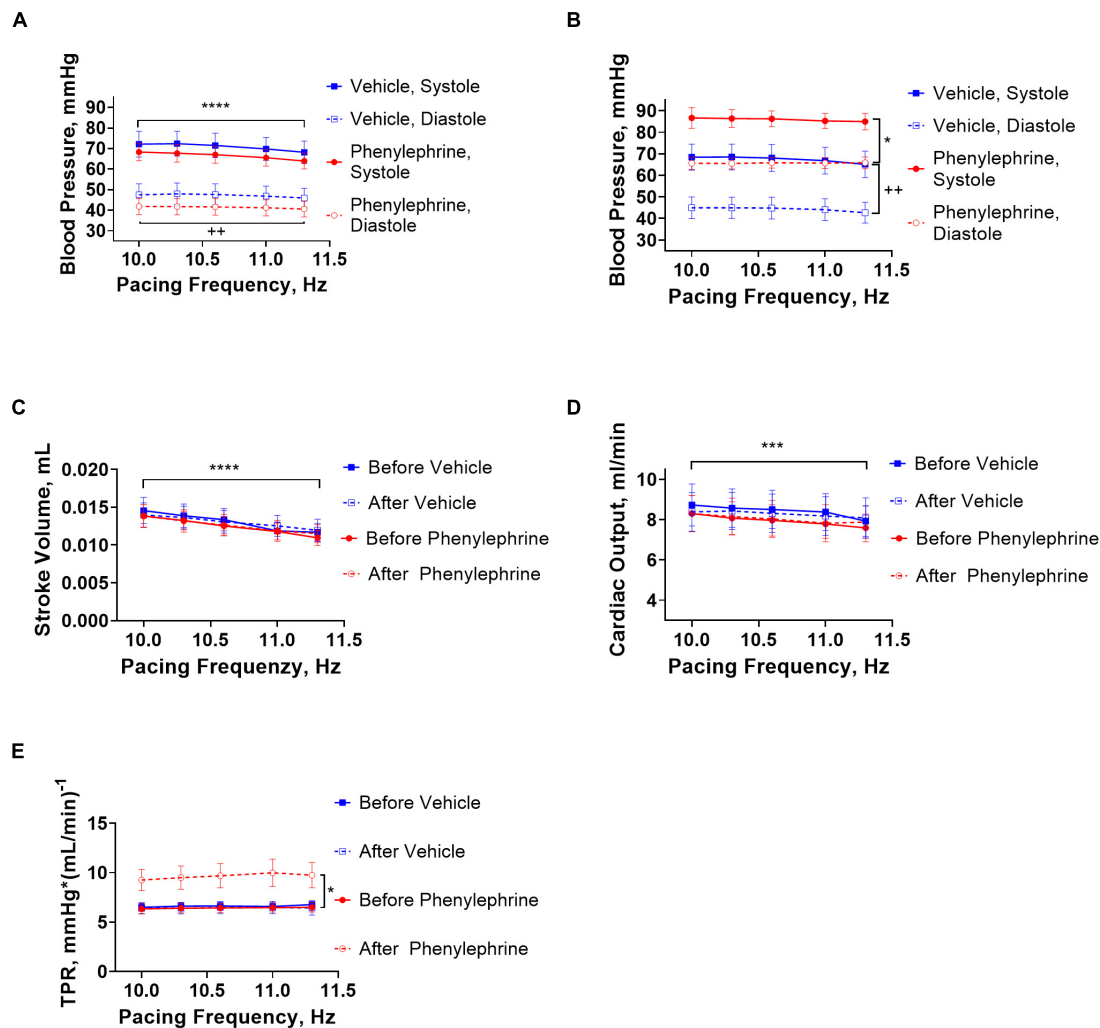
FIGURE 4 | Vehicle or phenylephrine injection was given at the beginning of the traces ($x = 0$). Transparent blue boxes indicate the second pacing session corresponding to the panels in **Figures 3E,H**. **(A)** Following intervention with phenylephrine or vehicle, both systolic and diastolic blood pressures were significantly elevated in the phenylephrine group (****$P < 0.0001$ systolic pressure and $^{++++}P < 0.0001$ for diastolic pressure). **(B)** Stroke volume was also increased significantly following phenylephrine administration (*$P = 0.027$). **(C)** Heart rate was significantly decreased after phenylephrine administration in comparison with vehicle (****$P < 0.0001$). **(D)** Cardiac output was not changed significantly following phenylephrine administration ($P = 0.21$). **(E)** After phenylephrine administration, total peripheral resistance (TPR) significantly increased compared to vehicle group (***$P = 0.0006$). Data were compared with two-way ANOVA, $n = 6$.

(Kaese and Verheule, 2012) corresponding to a very short cardiac cycle length of 80–110 ms. Thus, minimal changes in heart rate can have significant consequences for diastolic duration, diastolic filling time, and stroke volume. The importance of increased ventricular filling time for stroke volume in mice is debated (Georgakopoulos and Kass, 2001). In our study, stroke volume and cardiac output decreased significantly with increasing pacing frequencies suggesting that the ventricular filling time is indeed important. Additionally, the observed difference in stroke volume between the phenylephrine and vehicle groups was abolished during electrical pacing. This implies the importance of reduced heart rate and increase in diastolic filling time for the phenylephrine-induced increments in stroke volume in mice.

A load-dependent biphasic force-frequency relation has previously been described for the murine heart with a positive relation at 400–600 beats per minute (bpm) and a negative force-frequency relation above 600 bpm (Georgakopoulos and Kass, 2001). Accordingly, we saw a negative force-frequency relation during the first pacing session when we paced the hearts with increasing pacing frequencies starting from 10 Hz that corresponds to 600 bpm (**Supplementary Figure 1**). However, the force-frequency relations were significantly changed for the vehicle and phenylephrine groups during the second pacing session (**Supplementary Figure 1**). This change may be due to volume loss leading to compensatory endogenous catecholamine release from the sympathetic nerves and adrenal medulla with consequent increase in venous return (Funk et al., 2013).

FIGURE 5 | (A) During the first pacing session, prior to administration of vehicle or phenylephrine, blood pressure was decreased with increasing pacing frequencies in both groups (****$P < 0.0001$ for systolic pressure and [++]$P = 0.0028$). **(B)** During the second pacing session after administration of phenylephrine, blood pressure did not change with increasing pacing frequencies, but elevation of blood pressure compared to vehicle group was maintained (*$P = 0.028$ for systolic blood pressure and [++]$P = 0.0064$ for diastolic pressure). **(C)** Stroke volume decreased significantly with increasing pacing frequencies (****$P < 0.0001$). **(D)** Cardiac output was also affected with increasing pacing frequencies (***$P = 0.0002$). **(E)** Total peripheral resistance did not change with increasing pacing frequencies, but the phenylephrine-induced increments in total peripheral resistance were maintained during the second pacing session compared to the vehicle group (*$P = 0.04$). Data were compared with two-way ANOVA, $n = 6$.

Thus, alterations in preload may have changed the force-frequency relation in our model. Normalizing the murine biphasic force-frequency relation to preload has been suggested to flatten the force-frequency relation curve at high frequencies (Georgakopoulos and Kass, 2001). This may in part explain the decrease in blood pressure seen in both vehicle and phenylephrine groups during the first pacing session and the diminished effect of increasing pacing frequency during the second pacing session. The component of venous return may have been greater following phenylephrine administration compared to vehicle when taking into account phenylephrine-induced venous constriction (Cannesson et al., 2012). Further measurements of pressure-volume relations in the caval vein or right atrium would answer this question.

The versatility of this model should be stated. For instance, this *in vivo* model can further be elaborated to include myocardial ischemia and reperfusion with temporary occlusion of a coronary artery and, thus, the systemic effects of acute myocardial infarction can be investigated (Michael et al., 1995). Additionally, the protocol may also be applied to other animal models, e.g., the rat model. However, considerations must be taken in regards of different electrophysiological properties of the heart beckoning other settings for the electrical pacing. This remains to be validated in the specific animal models.

Our protocol can distinguish between vascular and cardiac changes and possibly answer important questions in cardiovascular research. This can be particularly pertinent to disease states with multimorbid cardiovascular pathology. For

example, cardiovascular morbidity in diabetes and hypertension can comprise pathological changes to both cardiac and vascular functions and lead to heart failure with preserved ejection fraction (Borlaug, 2020). Differentiating between the intrinsic cardiac properties and vascular function may shed light on the mechanism underlying this type of heart failure potentially improving treatment strategies. Currently, this can be examined by a combination of *in vivo* and *ex vivo* models, while our protocol offers a purely *in vivo* setting (Pedersen et al., 2018). Another important issue in cardiovascular research relates to molecules, e.g., ketone bodies and cardiac glycosides, that exert complex responses in the body (Tisdale and Gheorghiade, 1992; Nielsen et al., 2019). Ketone bodies have been described to increase cardiac output (Nielsen et al., 2019). However, due to possible multifarious effects on the cardiovascular system, it is unclear whether this increase in cardiac output is (i) due to increase in contractility or a decrease in heart rate, i.e., a direct cardiac effect, (ii) due to reduced total peripheral resistance, i.e., a direct vascular effect, or (iii) due to a combination of both vascular and cardiac effects. Thus, our model may be a helpful approach to illuminate such intricate research questions.

LIMITATIONS

This experimental protocol provides a possibility to assess valuable comprehensive information on the cardiovascular system, but some limitations must be highlighted and considered for future elaboration of the model. The limited translational value of mouse studies must be considered (Perlman, 2016), yet, mouse experimental models are indispensable in mechanistic studies with genetic expression manipulations (Chinwalla et al., 2002) as well as for initial pharmacological trials and other high throughput analyses (Perlman, 2016). Presently, multiple animal studies must be performed to gain comprehensive knowledge on the effects of a pharmacological treatment. In this regard, our protocol is helpful in reducing the number of animal experiments needed for the comprehensive assessment of *in vivo* pharmacological interventions in the cardiovascular system.

The established protocol is technically challenging as it is an invasive procedure and requires the introduction of several probes. In this regard, smaller animals may yield a lower surgical success rate due to lower surgical accessibility and increased vulnerability compared to bigger animals. This demands higher surgical skill level and precision. In our experiments, we used 9 months old mice which had suitable size for the surgery required.

Several other aspects related to the surgical procedure must also be mentioned. Opening the thorax alters pressure dynamics in the thoracic cave, e.g., pressure alterations related to natural respiration are eliminated, and this may affect venous return and cardiac function. Additionally, anesthesia and open-thorax interventions have previously been reported to lead to a significant drop in blood pressure (Hoit et al., 1997; Janssen et al., 2004). To reduce the significance of mechanical ventilation between the vehicle and phenylephrine groups, the ventilation parameters were maintained throughout

the entire experiment and were comparable between the two groups. In addition, parameters such as positive end-expiratory pressure, airway pressure, and flow were monitored and kept constant in all experiments. Partially, these factors are probably also the reason for the slight hypotensive condition during the experiment. The hypotensive conditions can be corrected by vasopressor administration, e.g., phenylephrine. However, considerations must be taken for the possible interference of several cardiovascular parameters including a direct effect on peripheral vascular resistance with indirect effects on cardiac function as has been shown in this study. Lastly, pancuronium bromide was used in this open-thorax protocol as a muscle relaxant to eliminate intrinsic respiratory reflexes. Pancuronium has been reported to increase heart rate and contractility in rat atrial preparations (Gursoy et al., 2011). Similarly, heart rate but also blood pressure has been described to increase following administration of pancuronium in anesthetized patients (Pauca and Skovsted, 1981). However, we did not see any significant cardiovascular changes in response to intraperitoneal injection of pancuronium used in our study.

Overdriving of heart rate with electrical pacing is not a normal physiological condition. Electrical pacing of the heart with increasing frequency is commonly used in arrhythmia research, e.g., programmed electrical stimulation protocols. However, the pacing settings in our study did not modify the electrical properties of the heart nor introduce arrhythmias evident from ECGs. Electrical pacing successfully and consistently controlled the heart rhythm in the frequency range of 10–11.3 Hz corresponding to a physiological heart rate of 600–678 BPM. Pacing with frequencies below 10 Hz or above 11.3 Hz did not always translate into a 1:1 capture of the heart rhythm. Moreover, recovery of hemodynamic parameters after electrical pacing indicates that cardiovascular functions were not damaged compared to their normal physiological state. Lastly, our results suggest that the electrical pacing had no direct effect on vascular function.

We measured blood flow in the ascending aorta as surrogate for cardiac output. This did not include the blood flow through the coronary arteries and, thus, underestimates the true value of cardiac output. Moreover, change in venous return is an important parameter in our mechanistic assessment, yet, this was not measured directly as this will further complicate the setup. These improvements, e.g., venous blood flow or an atrial pressure-volume assessment, would be an advantage for future technical development. Lastly, despite the importance of neurohumoral regulation for the cardiovascular system, this was not assessed in this study, but this can be considered in future research.

CONCLUSION

In conclusion, this *in vivo* protocol provides a method of controlling heart rate in cardiovascular studies in the murine model with pharmacological intervention. Phenylephrine administration increased total peripheral resistance, blood pressure, and stroke volume. However, during atrial pacing

there were no differences in stroke volume and cardiac output between the phenylephrine and vehicle groups. Thus, our model suggests that the decrease in heart rate with consequent increase in ventricular filling may be a significant contributor to the phenylephrine-induced increase in stroke volume rather than increase in venous return. This model underlines the primary vascular effects of phenylephrine with secondary cardiac changes. Although technically challenging, this protocol enables the assessment of a broad range of parameters for an integrated understanding of the cardiovascular system under normal and pathological conditions, and it may be helpful in answering important questions in cardiovascular physiology.

DATA AVAILABILITY STATEMENT

The animal study was reviewed and approved by the raw data supporting the conclusions of this article will be made available by the authors, without undue reservation.

ETHICS STATEMENT

The experimental protocol was approved by the Animal Experiments Inspectorate of the Danish Ministry of Environment and Food and reported in accordance with the ARRIVE (Animal Research: Reporting *in vivo* Experiments) guidelines.

AUTHOR CONTRIBUTIONS

RR and VM performed the experiments and made the draft of the manuscript. RR, TP, and VM performed the data analysis. RR, TP, MT, and VM took part in the conception and designed the study. All authors provided critical feedback and approved the final version of the manuscript.

FUNDING

SUPPLEMENTARY MATERIAL

The Supplementary Material for this article can be found online at: https://www.frontiersin.org/articles/10.3389/fphys. 2022.831724/full#supplementary-material

REFERENCES

Andresen, M. C., and Kunze, D. L. (1994). Nucleus tractus solitarius–gateway to neural circulatory control. *Annu. Rev. Physiol.* 56, 93–116. doi: 10.1146/annurev.ph.56.030194.000521

Boguslavskyi, A., Tokar, S., Prysyazhna, O., Rudyk, O., Sanchez-Tatay, D., Lemmey, H. A. L., et al. (2021). Phospholemman phosphorylation regulates vascular tone, blood pressure, and hypertension in mice and humans. *Circulation* 143, 1123–1138. doi: 10.1161/CIRCULATIONAHA.119.040557

Bomzon, A., and Naidu, S. G. (1985). Perfusion of the isolated rat hind limb. An analysis of the technique. *J. Pharmacol. Methods* 14, 285–296. doi: 10.1016/0160-5402(85)90004-x

Borlaug, B. A. (2020). Evaluation and management of heart failure with preserved ejection fraction. *Nat. Rev. Cardiol.* 17, 559–573.

Botnar, R. M., and Makowski, M. R. (2012). Cardiovascular magnetic resonance imaging in small animals. *Prog. Mol. Biol. Transl. Sci.* 105, 227–261. doi: 10.1016/B978-0-12-394596-9.00008-1

Brozovich, F. V., Nicholson, C. J., Degen, C. V., Gao, Y. Z., Aggarwal, M., and Morgan, K. G. (2016). Mechanisms of vascular smooth muscle contraction and the basis for pharmacologic treatment of smooth muscle disorders. *Pharmacol. Rev.* 68, 476–532. doi: 10.1124/pr.115.010652

Camacho, P., Fan, H., Liu, Z., and He, J.-Q. (2016). Small mammalian animal models of heart disease. *Am. J. Cardiovasc. Dis.* 6, 70–80.

Cannesson, M., Jian, Z., Chen, G., Vu, T. Q., and Hatib, F. (2012). Effects of phenylephrine on cardiac output and venous return depend on the position of the heart on the Frank-Starling relationship. *J. Appl. Physiol.* 113, 281–289. doi: 10.1152/japplphysiol.00126.2012

Chinwalla, A. T., Cook, L. L., Delehaunty, K. D., Fewell, G. A., Fulton, L. A., Fulton, R. S., et al. (2002). Initial sequencing and comparative analysis of the mouse genome. *Nature* 420, 520–562. doi: 10.1038/nature01262

Crosley, A. P., Clark, J. K., and Barker, H. G. (1951). The renal hemodynamic effects of phenylephrine (neosynephrine) hydrochloride in man. *J. Pharmacol. Exp. Ther.* 101, 153–155.

Dessy, C., Kim, I., Sougnez, C. L., Laporte, R., and Morgan, K. G. (1998). A role for MAP kinase in differentiated smooth muscle contraction evoked by alpha-adrenoceptor stimulation. *Am. J. Physiol.* 275, C1081–C1086. doi: 10.1152/ajpcell.1998.275.4.C1081

Figtree, G. A., Broadfoot, K., Casadei, B., Califf, R., Crea, F., Drummond, G. R., et al. (2021). A call to action for new global approaches to cardiovascular disease drug solutions. *Circulation* 144, 159–169. doi: 10.1161/cir.0000000000000981

Funk, D. J., Jacobsohn, E., and Kumar, A. (2013). Role of the venous return in critical illness and shock: part II-shock and mechanical ventilation. *Crit. Care Med.* 41, 573–579. doi: 10.1097/CCM.0b013e31827bfc25

Georgakopoulos, D., and Kass, D. (2001). Minimal force-frequency modulation of inotropy and relaxation of in situ murine heart. *J. Physiol.* 534, 535–545. doi: 10.1111/j.1469-7793.2001.00535.x

Gordan, R., Gwathmey, J. K., and Xie, L. H. (2015). Autonomic and endocrine control of cardiovascular function. *World J. Cardiol.* 7, 204–214. doi: 10.4330/wjc.v7.i4.204

Gursoy, S., Bagcivan, I., Durmus, N., Kaygusuz, K., Kol, I. O., Duger, C., et al. (2011). Investigation of the cardiac effects of pancuronium, rocuronium, vecuronium, and mivacurium on the isolated rat atrium. *Curr. Ther. Res. Clin. Exp.* 72, 195–203. doi: 10.1016/j.curtheres.2011.09.001

Gutierrez, A., Contreras, C., Sanchez, A., and Prieto, D. (2019). Role of phosphatidylinositol 3-kinase (PI3K), mitogen-activated protein kinase (MAPK), and protein kinase C (PKC) in calcium signaling pathways linked to the alpha1-adrenoceptor in resistance arteries. *Front. Physiol.* 10:55. doi: 10.3389/fphys.2019.00055

Hansen, K. B., Staehr, C., Rohde, P. D., Homilius, C., Kim, S., Nyegaard, M., et al. (2020). PTPRG is an ischemia risk locus essential for HCO(3)(-)-dependent regulation of endothelial function and tissue perfusion. *eLife* 9:e57553. doi: 10.7554/eLife.57553

Hauber, H. P., Karp, D., Goldmann, T., Vollmer, E., and Zabel, P. (2010). Effect of low tidal volume ventilation on lung function and inflammation in mice. *BMC Pulm. Med.* 10:21. doi: 10.1186/1471-2466-10-21

Hoit, B. D., Ball, N., and Walsh, R. A. (1997). Invasive hemodynamics and force-frequency relationships in open- versus closed-chest mice. *Am. J. Physiol. Heart Circ. Physiol.* 273, H2528–H2533. doi: 10.1152/ajpheart.1997.273.5.H2528

Holmes, C. L., Landry, D. W., and Granton, J. T. (2004). Science review: vasopressin and the cardiovascular system part 2 - clinical physiology. *Crit. Care* 8, 15–23. doi: 10.1186/cc2338

Janssen, B., Debets, J., Leenders, P., and Smits, J. (2002). Chronic measurement of cardiac output in conscious mice. *Am. J. Physiol. Regul. Integr. Comp. Physiol.* 282, R928–R935. doi: 10.1152/ajpregu.00406.2001

Janssen, B. J., De Celle, T., Debets, J. J., Brouns, A. E., Callahan, M. F., and Smith, T. L. (2004). Effects of anesthetics on systemic hemodynamics in mice. *Am. J. Physiol. Heart Circ. Physiol.* 287, H1618–H1624. doi: 10.1152/ajpheart.01192.2003

Jumrussirikul, P., Dinerman, J., Dawson, T. M., Dawson, V. L., Ekelund, U., Georgakopoulos, D., et al. (1998). Interaction between neuronal nitric oxide synthase and inhibitory G protein activity in heart rate regulation in conscious mice. *J. Clin. Investig.* 102, 1279–1285. doi: 10.1172/JCI2843

Kaese, S., and Verheule, S. (2012). Cardiac electrophysiology in mice: a matter of size. *Front. Physiol.* 3:345. doi: 10.3389/fphys.2012.00345

Kalmar, A. F., Allaert, S., Pletinckx, P., Maes, J. W., Heerman, J., Vos, J. J., et al. (2018). Phenylephrine increases cardiac output by raising cardiac preload in patients with anesthesia induced hypotension. *J. Clin. Monit. Comput.* 32, 969–976. doi: 10.1007/s10877-018-0126-3

Kougias, P., Weakley, S. M., Yao, Q., Lin, P. H., and Chen, C. (2010). Arterial baroreceptors in the management of systemic hypertension. *Med. Sci. Monit.* 16, RA1–RA8.

Li, H., Abaei, A., Metze, P., Just, S., Lu, Q. W., and Rasche, V. (2020). Technical aspects of in vivo small animal CMR imaging. *Front. Phys.* 8:183. doi: 10.3389/fphy.2020.00183

Malhotra, R., Banerjee, G., Brampton, W., and Price, N. C. (1998). Comparison of the cardiovascular effects of 2.5% phenylephrine and 10% phenylephrine during ophthalmic surgery. *Eye* 12(Pt 6), 973–975. doi: 10.1038/eye.1998.252

Mayet, J., and Hughes, A. (2003). Cardiac and vascular pathophysiology in hypertension. *Heart* 89, 1104–1109.

Mc Namara, K., Alzubaidi, H., and Jackson, J. K. (2019). Cardiovascular disease as a leading cause of death: how are pharmacists getting involved? *Integr. Pharm. Res. Pract.* 8, 1–11. doi: 10.2147/IPRP.S133088

Michael, L. H., Entman, M. L., Hartley, C. J., Youker, K. A., Zhu, J., Hall, S. R., et al. (1995). Myocardial ischemia and reperfusion: a murine model. *Am. J. Physiol. Heart Circ. Physiol.* 269, H2147–H2154.

Mon, W., Stewart, A., Fernando, R., Ashpole, K., El-Wahab, N., MacDonald, S., et al. (2017). Cardiac output changes with phenylephrine and ephedrine infusions during spinal anesthesia for cesarean section: a randomized, double-blind trial. *J. Clin. Anesth.* 37, 43–48. doi: 10.1016/j.jclinane.2016.11.001

Moroz, J., and Reinsberg, S. A. (2018). Dynamic contrast-enhanced MRI. *Methods Mol. Biol.* 1718, 71–87. doi: 10.1007/978-3-540-78423-4_7

Mulvany, M. J., and Aalkjaer, C. (1990). Structure and function of small arteries. *Physiol. Rev.* 70, 921–961. doi: 10.1152/physrev.1990.70.4.921

Nielsen, R., Møller, N., Gormsen, L. C., Tolbod, L. P., Hansson, N. H., Sorensen, J., et al. (2019). Cardiovascular effects of treatment with the ketone body 3-hydroxybutyrate in chronic heart failure patients. *Circulation* 139, 2129–2141. doi: 10.1161/CIRCULATIONAHA.118.036459

Pandya, A., Gaziano, T. A., Weinstein, M. C., and Cutler, D. (2013). More Americans living longer with cardiovascular disease will increase costs while lowering quality of life. *Health Aff.* 32, 1706–1714. doi: 10.1377/hlthaff.2013.0449

Pauca, A. L., and Skovsted, P. (1981). Cardiovascular effects of pancuronium in patients anaesthetized with enflurane and fluroxene. *Can. Anaesth. Soc. J.* 28, 39–45. doi: 10.1007/BF03007288

Paz Ocaranza, M., Riquelme, J. A., Garcia, L., Jalil, J. E., Chiong, M., Santos, R. A. S., et al. (2020). Counter-regulatory renin-angiotensin system in cardiovascular disease. *Nat. Rev. Cardiol.* 17, 116–129. doi: 10.1038/s41569-019-0244-8

Pedersen, T. M., Boardman, N. T., Hafstad, A. D., and Aasum, E. (2018). Isolated perfused working hearts provide valuable additional information during phenotypic assessment of the diabetic mouse heart. *PLoS One* 13:e0204843. doi: 10.1371/journal.pone.0204843

Perlman, R. L. (2016). Mouse models of human disease: an evolutionary perspective. *Evol. Med. Public Health* 2016, 170–176. doi: 10.1093/emph/eow014

Ralph, A. F., Grenier, C., Costello, H. M., Stewart, K., Ivy, J. R., Dhaun, N., et al. (2021). Activation of the sympathetic nervous system promotes blood pressure salt-sensitivity in C57BL6/J mice. *Hypertension* 77, 158–168. doi: 10.1161/HYPERTENSIONAHA.120.16186

Ram, R., Mickelsen, D. M., Theodoropoulos, C., and Blaxall, B. C. (2011). New approaches in small animal echocardiography: imaging the sounds of silence. *Am. J. Physiol. Heart Circ. Physiol.* 301, H1765–H1780. doi: 10.1152/ajpheart.00559.2011

Schwarte, L. A., Zuurbier, C. J., and Ince, C. (2000). Mechanical ventilation of mice. *Basic Res. Cardiol.* 95, 510–520.

Song, W., Wang, H., and Wu, Q. (2015). Atrial natriuretic peptide in cardiovascular biology and disease (NPPA). *Gene* 569, 1–6. doi: 10.1016/j.gene.2015.06.029

Tarnavski, O., McMullen, J. R., Schinke, M., Nie, Q., Kong, S., and Izumo, S. (2004). Mouse cardiac surgery: comprehensive techniques for the generation of mouse models of human diseases and their application for genomic studies. *Physiol. Genomics* 16, 349–360. doi: 10.1152/physiolgenomics.00041.2003

Thiele, R. H., Nemergut, E. C., and Lynch, C. III. (2011). The clinical implications of isolated alpha(1) adrenergic stimulation. *Anesth. Analg.* 113, 297–304. doi: 10.1213/ANE.0b013e3182120ca5

Tisdale, J. E., and Gheorghiade, M. (1992). Acute hemodynamic effects of digoxin alone or in combination with other vasoactive agents in patients with congestive heart failure. *Am. J. Cardiol.* 69, 34g–47g.

Uhlirova, H., Kılıç, K., Tian, P., Thunemann, M., Desjardins, M., Saisan, P. A., et al. (2016). Cell type specificity of neurovascular coupling in cerebral cortex. *eLife* 5:e14315. doi: 10.7554/eLife.14315

Wier, W. G. (2014). More in vivo experimentation is needed in cardiovascular physiology. *Am. J. Physiol. Heart Circ. Physiol.* 307, H121–H123. doi: 10.1152/ajpheart.00326.2014

Wilson, M. R., Patel, B. V., and Takata, M. (2012). Ventilation with "clinically relevant" high tidal volumes does not promote stretch-induced injury in the lungs of healthy mice. *Crit. Care Med.* 40, 2850–2857. doi: 10.1097/ccm.0b013e31825b91ef

Yang, B., Larson, D. F., and Ranger-Moore, J. (2013). Biphasic change of tau (tau) in mice as arterial load acutely increased with phenylephrine injection. *PLoS One* 8:e60580. doi: 10.1371/journal.pone.0060580

Zaragoza, C., Gomez-Guerrero, C., Martin-Ventura, J. L., Blanco-Colio, L., Lavin, B., Mallavia, B., et al. (2011). Animal models of cardiovascular diseases. *J. Biomed. Biotechnol.* 2011:497841.

Zhao, X., Ho, D., Gao, S., Hong, C., Vatner, D. E., and Vatner, S. F. (2011). Arterial pressure monitoring in mice. *Curr. Protoc. Mouse Biol.* 1, 105–122.

Check for updates

Lymphatic Vessel Regression and Its Therapeutic Applications: Learning From Principles of Blood Vessel Regression

Faisal Masood, Rohan Bhattaram, Mark I. Rosenblatt, Andrius Kazlauskas, Jin-Hong Chang* and Dimitri T. Azar

Department of Ophthalmology and Visual Sciences, Illinois Eye and Ear Infirmary, College of Medicine, University of Illinois at Chicago, Chicago, IL, United States

Aberrant lymphatic system function has been increasingly implicated in pathologies such as lymphedema, organ transplant rejection, cardiovascular disease, obesity, and neurodegenerative diseases including Alzheimer's disease and Parkinson's disease. While some pathologies are exacerbated by lymphatic vessel regression and dysfunction, induced lymphatic regression could be therapeutically beneficial in others. Despite its importance, our understanding of lymphatic vessel regression is far behind that of blood vessel regression. Herein, we review the current understanding of blood vessel regression to identify several hallmarks of this phenomenon that can be extended to further our understanding of lymphatic vessel regression. We also summarize current research on lymphatic vessel regression and an array of research tools and models that can be utilized to advance this field. Additionally, we discuss the roles of lymphatic vessel regression and dysfunction in select pathologies, highlighting how an improved understanding of lymphatic vessel regression may yield therapeutic insights for these disease states.

Keywords: lymphatic vessel regression, blood vessel regression, antilymphangiogenesis, lymphangiogenesis, angiogenesis

INTRODUCTION

Increasingly implicated in various pathologies, the lymphatic system plays important roles in immune cell transport, gastrointestinal nutrient absorption, and interstitial fluid transport (Alitalo et al., 2005; Tammela and Alitalo, 2010; Petrova and Koh, 2020; Landau et al., 2021). The identification of lymphatic-specific markers such as vascular endothelial growth factor receptor 3 (VEGFR-3), lymphatic vessel endothelial hyaluronan receptor 1 (LYVE-1), prospero-related homeobox 1 (Prox-1), and podoplanin in the late 1990s was instrumental in paving the way for research on lymphangiogenesis, or the production of new lymphatic vessels (LVs) from extant LVs. There has been a steady stream of research conducted on lymphangiogenesis since the identification of lymphatic endothelial cell (LEC) markers, culminating in approximately 4152 publications by 2021; however, despite its importance in phenomena such as tumor cell metastasis (Detmar and Hirakawa, 2002; Stacker et al., 2002, 2014) and organ transplantation rejection (Yamakawa et al., 2018), the field of lymphangiogenesis is largely overshadowed by its blood vessel (BV) counterpart,

angiogenesis. In 2021, approximately 124,224 publications exist in the field of angiogenesis, nearly 30-fold more publications than for lymphangiogenesis.

This exploration of vessel formation and progression is only one side of the coin; a detailed understanding of the regression of both newly formed and extant vasculature is the other half of this story. At the time of writing, there are approximately 525 publications on LV regression compared to 25,037 publications on BV regression, a 47.8-fold difference. The phenomenon of BV regression and its therapeutic implications were explored as early as the 1940s and 50s, roughly a half century prior to the discovery of the aforementioned markers of LECs that enabled the study of LV regression (Terry, 1942; Michaelson and Schreiber, 1956), with researchers subsequently proposing that modulation of vascular endothelial growth factor (VEGF) signaling pathways and other angiogenic pathways would prove fruitful in anti-tumor therapies (Kowanetz and Ferrara, 2006; Kong et al., 2017).

Considering the discovery of increased LV density in certain pathologies, such as inflammatory bowel disease (Zhang et al., 2021), where LV regression could be therapeutic, in addition to the identification of decreased lymphatic clearance in other pathologies, such as Alzheimer's disease (Tarasoff-Conway et al., 2015; Petrova and Koh, 2020), a clear understanding of the mechanisms underlying LV regression is urgently needed. Herein, we summarize what is known about LV regression, extend insights from the prolific field of BV regression to shed light on LV regression, discuss the implications of the newly identified roles of lymphatics in a variety of pathologies, and describe research models and modalities that can be utilized to further advance the understudied field of LV regression. By applying salient BV regression principles, we explore how concepts such as homeostasis, inflammation, negative feedback, and apoptosis may elucidate findings in LV regression.

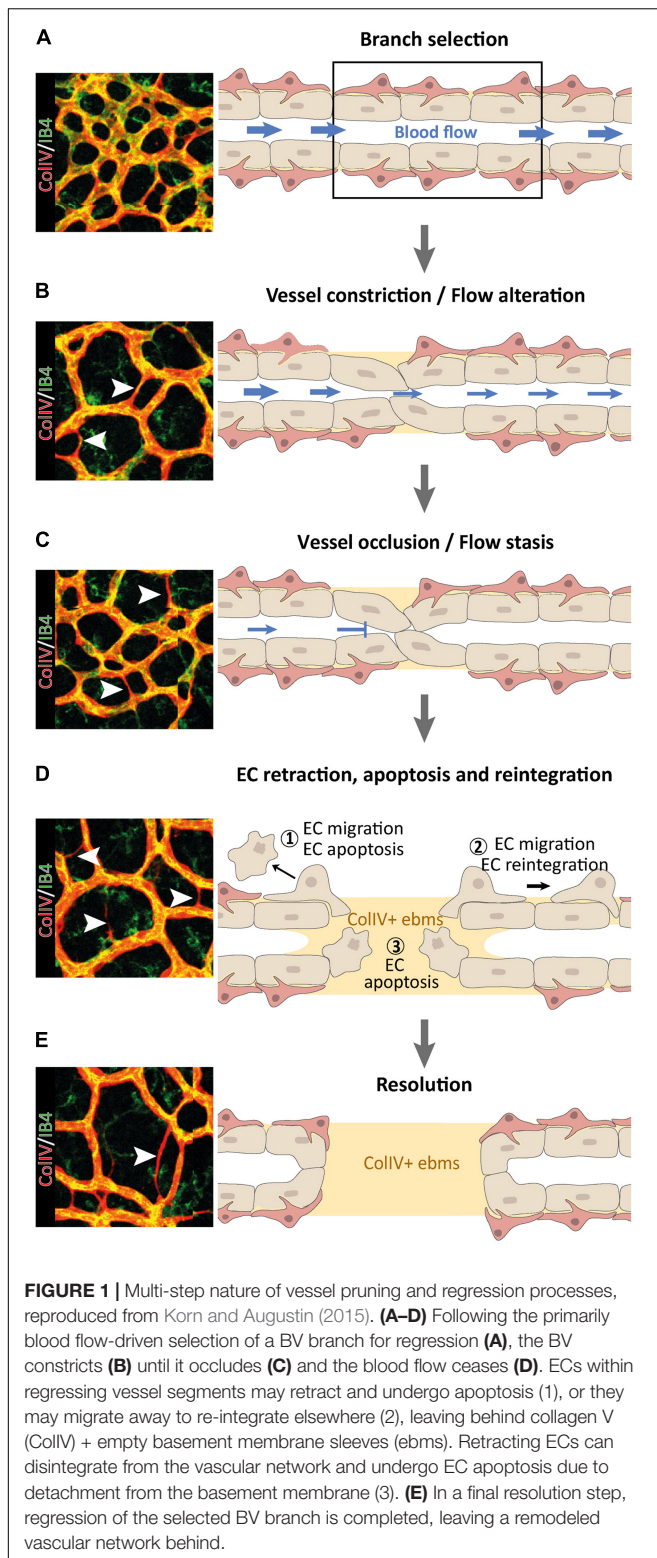## (Lymph)angiogenesis in Physiology and Disease

Angiogenesis, the growth and development of new BVs from extant BVs, is a well-studied and characterized process (Carmeliet and Jain, 2011). While vasculogenesis refers to the development of the heart and basic vascular structures (Patan, 2004), angiogenesis is the process by which this network expands and matures into a fully functional system. The primary driver of angiogenesis is VEGF-A, which binds to VEGF receptors 1 and 2 (VEGFR-1/2) and induces vasodilation and cellular permeability. A detailed overview of the protein families and molecular mediators implicated in angiogenesis can be found in the review by Carmeliet and Jain (2011). Lymphangiogenic progression follows growth patterns like those observed in angiogenesis, with some key distinctions (Adams and Alitalo, 2007; Lohela et al., 2009). Similar to VEGF-A being the primary factor behind angiogenesis, VEGF-C is the driving factor for lymphangiogenesis, with VEGF-D exhibiting a lesser effect. A detailed mechanism of lymphangiogenesis is expertly reviewed by Oliver et al. (2020).

The lymphatic system plays an important role in both the vascular and immune systems. It regulates and returns fluid to the venous system while also transporting immune cells to appropriate locations. Lymph nodes are key in antigen presentation and generating humoral and cell-mediated immune responses. Although necessary for healthy tissue homeostasis, the development of lymphatic vasculature can also contribute to immunopathologies, such as chronic autoimmune disease (Kesler et al., 2013). In such chronic inflammatory states, lymphangiogenesis can create tertiary lymphatic organs (TLOs), which are very similar to normal lymph nodes. TLOs have been found in organ transplant recipients and corneal transplant recipients as well as in patients with rheumatoid arthritis and inflammatory bowel disease (Kesler et al., 2013). Pathologic lymphatic drainage is also a mechanism for tumor metastasis (Kesler et al., 2013). Tumor cells can induce lymphangiogenesis to connect to existing lymphatic vasculature, thereby increasing the risk of metastasis (Karpanen et al., 2001; Skobe et al., 2001). Although tumor-induced lymphangiogenesis may result in dysfunctional intratumoral lymphatics, Padera et al. (2002) demonstrated that VEGF-C–induced lymphangiogenesis promotes metastasis through the functional lymphatics formed at the tumor border. Unlike treatments targeting BV-mediated metastasis, anti-lymphangiogenic therapy is still underdeveloped clinically (Kesler et al., 2013; Yamakawa et al., 2018).

Blood and Lymphatic Vessel Regression

Blood vessel regression is a complex, multifaceted process that is still poorly understood compared to angiogenic growth (Korn and Augustin, 2015). BV regression has been studied in the context of vessel pruning, which is the process of microvessel regression during BV maturation and is known to involve a diverse set of molecular markers and pathways. Korn and Augustin described multiple mechanisms of BV regression (**Figure 1**), with VEGF, Wnt/Notch, angiopoietin (Ang)/tyrosine kinase with immunoglobulin-like and EGF-like domains (TIE), and other signaling pathways playing key roles (Korn and Augustin, 2015). Claxton and Fruttiger (2003) used an induced hyperoxia mouse model in which VEGF was downregulated to demonstrate that FGF2, ANG2, platelet-derived growth factor (PDGF), and Delta-like canonical Notch ligand 4 (DLL4) are involved in maintaining vessel stability independent of VEGF. A mouse model study of Parkinson's disease focused specifically on the vascular pathologic effect, and VEGF was shown to maintain mature vessels and induce plasticity in response to external factors (Elabi et al., 2021). Korn et al. (2014) demonstrated how the Wnt/Notch signaling pathway also has a key role in BV maturation and stabilization (Korn and Augustin, 2015), with improper signaling potentially resulting in inducing spontaneous vessel regression and death. DLL4 expressed by ECs can bind with Notch as well and downregulate VEGF, a key signaling event for capillary remodeling (Lobov et al., 2011). As Notch ligand interactions are primarily involved in cell death and apoptosis (Miele and Osborne, 1999), there appear to be multiple approaches to induce cell apoptosis. These pathways occur concurrently with the Ang/TIE2 pathway, which regulates vessel plasticity, and are crucial for vessel pruning and

FIGURE 1 | Multi-step nature of vessel pruning and regression processes, reproduced from Korn and Augustin (2015). **(A–D)** Following the primarily blood flow-driven selection of a BV branch for regression **(A)**, the BV constricts **(B)** until it occludes **(C)** and the blood flow ceases **(D)**. ECs within regressing vessel segments may retract and undergo apoptosis (1), or they may migrate away to re-integrate elsewhere (2), leaving behind collagen V (ColIV) + empty basement membrane sleeves (ebms). Retracting ECs can disintegrate from the vascular network and undergo EC apoptosis due to detachment from the basement membrane (3). **(E)** In a final resolution step, regression of the selected BV branch is completed, leaving a remodeled vascular network behind.

ending the vessel maturation process (Welti et al., 2013). Other pathways include Hairy/enhancer-of-split related with YRPW motif protein (HEY)/p53, cysteine-rich transmembrane BMP regulator 1 (CRIM1), and C-X-C motif chemokine ligand 10

(CXCL10)/C-X-C motif chemokine receptor 3 (CXCR3), which increase VEGFR-1, stimulate VEGF-A signaling, and detach ECs to prepare for apoptosis, respectively, all of which are key processes in BV pruning and regression (Bodnar et al., 2009; Fan et al., 2014). Researchers have observed a unique pattern in these complex pathways, termed the "anti-angiogenic switch," which represents a modified form of the "angiogenic switch" concept from tumor vasculature. Essentially, the mere addition or inhibition of VEGF does not necessarily change the angiogenic direction. Gosain et al. (2006) assessed the abilities of exogenous VEGF, FGF, PDGF, and a combination of VEGF and FGF to reverse vascular regression. They only observed a transient increase in vessel density, and regression continued after an observed period. Conversely, Irani et al. (2017) tested the ability of an anti-VEGF-B antibody fragment to induce BV regression and found that the antibody fragment alone could not significantly reduce BV density. These findings indicate that signaling pathways are not simply "pro" or "anti" angiogenesis; instead, a myriad of concurrent signals with a basal level of VEGF make angiogenic regression a resilient state (Elabi et al., 2021).

Physiological BV regression occurs to facilitate the maturation of developing blood vessels and to prevent excessive BV growth (Korn and Augustin, 2015). There are many instances in which blood vessels regress almost completely in healthy states. Hyaloid vessels, which are present in the eye during embryonic development, completely regress after complete eye development, primarily through pathways involving Wnt signaling (Wang et al., 2019a,b). The menstrual cycle also presents a unique BV growth and regression cycle; during luteolysis of the ovarian corpus luteum, Goede et al. (1998) observed an association between upregulated Ang2 expression (relative to Ang1) and BV regression. Another unique physiological example of BV regression is in the context of embryological finger patterning, a process involving apoptosis of embryologic interdigital webbing to form free digits (Hurle et al., 1985). Prior to physiologic apoptosis of interdigital webbing, robust interdigital angiogenesis increases the local oxygen concentration, resulting in the generation of reactive oxygen species (ROS) that impart cellular damage (Eshkar-Oren et al., 2015; Cordeiro et al., 2019). This oxidative stress culminates in interdigital webbing apoptosis, which is followed by remodeling and regression of the interdigital vasculature. Pathological BV regression has been seen in a wide variety of conditions. Retinopathy of prematurity (Keshet, 2003), pulmonary fibrosis (Ebina et al., 2004; Parra et al., 2005; Johnson and DiPietro, 2013; Barratt and Millar, 2014), chronic kidney disease (Polichnowski, 2018), kidney microvessel rarefaction (Goligorsky, 2010; Chade, 2013), Parkinson's disease (Elabi et al., 2021), spinal cord injury (Trivedi et al., 2016), and initial tumor BV co-option (Holash et al., 1999) have all been linked to BV regression during specific pathological time frames (**Table 1**).

The phenomenon of LV regression is not well understood compared to BV regression. The exact mechanisms responsible for LV regression are not well defined, but TH1- and TH2-derived cytokines have been shown to play a role in negative regulation of lymphangiogenesis (Shao and Liu, 2006;

TABLE 1 | Pathologic blood vessel (BV) regression.

Organ system	References	pathologies/disease	Mechanism	Affected BVs
Eye	Keshet, 2003	Retinopathy of prematurity	Oxygen supplementation in premature infants can lead to hyperoxia-induced underexpression of VEGF, resulting in pathologic regression of retinal BVs. As the infant returns to room air, the deficit in retinal BVs results in a relatively hypoxic state, causing robust angiogenesis. This compensatory response results in the excessive formation of leaky BVs that may infiltrate the inner layer of the retina and vitreous, potentially causing retinal detachment and blindness.	Retinal BVs
Lung	Parra et al., 2005; Johnson and DiPietro, 2013; Barratt and Millar, 2014	Fibrosis	Injury to alveolar epithelium results in an inflammatory response and robust angiogenesis; ongoing inflammation results in fibrotic parenchymal remodeling and vascular regression by apoptosis of VECs.	Pulmonary microvessels
Kidney	Goligorsky, 2010; Fligny and Duffield, 2013; Polichnowski, 2018	CKD, Microvessel rarefaction	Altered peritubular capillary caliber, increased recruitment of renal immune cells, altered mechanical forces, and potentially other mechanisms contribute to pericyte dysfunction and detachment from BVs, ultimately leading to BV rarefaction and regression.	Tubular microvessels
Brain	Elabi et al., 2021	Parkinson's, Spinal cord injury	Pericyte activation leads to compensatory angiogenesis, followed by regression. Immediate regression could be due to impaired Wnt/ß-catenin signaling, and lack of MMP-2 in spinal cord injury can lead to angiogenic regression (again possibly due to pericyte disruption).	Brain and spine BVs
Cancer	Holash et al., 1999	Initial tumor co-option and BV regression	Some subset of malignancies may initially co-opt into extant vasculature, resulting in BV regression, local hypoxia, and subsequent angiogenesis. BV regression was physically characterized by separation of ECs from supporting mural cells and molecularly characterized by the up-regulation of Ang-2 in the absence of VEGF. The investigators hypothesized that this upregulation of Ang-2 may serve as a host defense mechanism to mark the coopted BVs for regression	Tumor-coopted BVs

VEC, vascular endothelial cell; CKD, chronic kidney disease; MMP-2, matrix metalloproteinase-2.

Kataru et al., 2011; Savetsky et al., 2015). LV regression has been observed in experimental settings. In a study by Zhang et al. (2011) lymphatic regression was found to be transient as vessels eventually grew back, but this is not true for all LV regression states. Shi et al. (2020) observed LV regression due to aqueous humor in both healthy and inflamed states. They linked alpha-melanocyte–stimulating hormone (a-MSH), vasoactive intestinal peptide (VIP), thrombospondin-1 (TSP-1), transforming growth factor beta (TGF-β), and Fas ligand (FasL) found in aqueous humor to LV regression, but the roles of these factors in induced LV regression have yet to be confirmed (Shi et al., 2020).

Similar to LV regression mechanism knowledge, the knowledge of LV functions in both physiology and pathology is limited. LV regression in the endometrium has been linked to the menstrual cycle (Tomita and Mah, 2014), as Girling and Rogers found fewer vessels in the functionalis layer and reduced vessel density in the subepithelium in a pig uterus model (Girling and Rogers, 2005). Tomita and Mah (2014) demonstrate that LVs in the functionalis layer undergo a cycle of "proliferation and degeneration" that is synchronized with cyclic menstrual changes of endometrial arteries. Additionally, it has been noted that embryologic pulmonary LVs undergo physiological regression, with a persistence of these vessels implicated in the pathophysiology behind pulmonary lymphangiectasia (Esther and Barker, 2004). As mentioned above, promotion of LV regression was also observed in relation to eye development and aqueous humor (Shi et al., 2020). Although limited, these physiological and pathological examples of LV regression can be probed and further dissected to potentially yield context-specific information on the mechanisms of LV regression.

LEARNING FROM BLOOD VESSEL REGRESSION

As discussed in the previous Section "Pathologies Involving Lymphangiogenic Regression and Dysfunction," much remains to be discovered regarding LV regression. Here, we identify salient BV regression principles, extend these concepts to LV regression, and highlight pertinent lymphatic literature that supports these claims (**Table 2**).

Survival Signals and Homeostasis

The basal state of BVs is one of quiescence and homeostasis. Stabilized networks are remarkably unperturbed by both pro- and anti-angiogenic factors various protective mechanisms ensure that a vascular network does not undergo inappropriate pruning or proliferation. These stabilizing factors include pericyte coverage (Bergers et al., 2003), vascular endothelial (VE)-cadherin cell–cell junctions (Murakami, 2012), and autocrine VEGF-A signaling (Lee et al., 2007). Factors promoting either homeostasis or BV regression are illustrated in **Figure 2**. For a more detailed summary of the factors involved in BV homeostasis and quiescence, see the review by Murakami (2012). The signaling required to maintain BV homeostasis is a result of upstream phenomena. For example, HIF-1 alpha accumulates in cells exposed to hypoxic conditions

TABLE 2 | Extending BV regression hallmarks to lymphatic vessels (LV) regression.

Overarching theme	References	Insights for LV regression
Survival signals and homeostasis	Bergers et al., 2003; Keshet, 2003; Lee et al., 2007; Murakami, 2012; Ji, 2014; Korn and Augustin, 2015; Zhong et al., 2017; Fallah and Rini, 2019; Schito, 2019; Iyer et al., 2020; Stritt et al., 2021	Although largely uncharacterized, it is established that pro-survival and homeostatic signaling occur in LVs. The impact of absent shear stress and interstitial fluid flow on LV regression deserves further exploration. In contrast to BVs' dependence on autocrine VEGF-A for survival, only the intestinal and meningeal lymphatics require VEGF-C signaling for maintenance and survival.
Inflammation	Folkman et al., 1983; Cursiefen et al., 2006; Logie et al., 2010; Kelley et al., 2011; Steele et al., 2011; Martínez-Corral et al., 2012; Mumprecht et al., 2012; Liao and von der Weid, 2014; Sajib et al., 2018; Filiberti et al., 2020; Ocansey et al., 2021	Inflammation serves as a stimulus for both angiogenesis and lymphangiogenesis. Inflammatory cytokines such as IL-6, IL-8, and TNF-α, have been implicated in neovascularization. Suppressing inflammation with glucocorticoids can prevent neovascularization. Further characterization of the effects of glucocorticoids through continuous live-imaging may allow for elucidation of the link between anti-inflammatory treatments and LV regression.
Anti-angiogenic switch and negative feedback	Lingen et al., 1996; Alitalo and Carmeliet, 2002; Watanabe et al., 2004; Gosain et al., 2006; Sato and Sonoda, 2007; Kataru et al., 2011; Wietecha et al., 2011; Shirasuna et al., 2012	Just as in BVs, negative feedback mechanisms likely regulate the balance between a lymphangiogenic and anti-lymphangiogenic state. Thus far, paracrine T-cell signaling through interferon-γ and vasohibin-1 inhibition of VEGF-A induced lymphangiogenesis have been implicated as potential negative feedback modulators of lymphangiogenesis. Endogenous mediators of the anti-lymphangiogenic switch remain largely uncovered. Further characterization of these molecules may reveal potent drivers of LV regression.
Apoptosis of regressing vessels	Ito and Yoshioka, 1999; Zhu et al., 2000; Mäkinen et al., 2001; Kim et al., 2010; Franco et al., 2015; Korn and Augustin, 2015; Watson et al., 2017; Gur-Cohen et al., 2019; Schafer et al., 2020; Hou et al., 2021	In certain contexts, apoptosis is a primary driver of BV regression. In other cases, apoptosis is a result of another determinant of BV regression. In another subset of cases, migration of VECs into neighboring BVs allows for a cell death-independent mechanism of BV regression. Although studies on the role of apoptosis in LV regression are currently lacking, it is possible that these mechanisms of BV regression hold similarly true in LV regression. Further work is required to characterize the nuances of apoptosis in LV regression.

and consequently leads to the transcription of pro-angiogenic genes including VEGF-A (Fallah and Rini, 2019). Absence of this upstream requirement for homeostasis can lead to dramatic BV regression. For example, in retinopathy of prematurity, administration of high concentration oxygen to premature infants obliterates the local hypoxic signaling required to maintain the immature retinal vessels, leading to pathological BV regression (Keshet, 2003). Another upstream phenomenon that promotes BV survival signaling is shear stress imparted by laminar blood flow in a properly perfused vessel (Korn and Augustin, 2015).

Extending these findings to LVs, it is certain that these vessels similarly experience pro-survival signaling, the disruption of which can lead to LV regression (**Figure 3**). Although the LV network experiences less shear stress than the BV network, Stritt et al. (2021) showed that LVs have greater sensitivity to shear stress and further elucidated the mechanisms by which shear stress may lead to LEC proliferation *in vitro*. In addition to LEC proliferation and potential survival, shear stress has also been implicated in the survival of lymphatic valves (Iyer et al., 2020). Although not as clear as in the BV context, shear stress signaling on a perfused LV has been seen to play a role in LV proliferation, and further studies may evaluate its role in LV regression. Additionally, similar to the angiogenic context, local hypoxia and subsequent HIF signaling induces lymphangiogenesis through increased expression of VEGF-C and VEGF-D (Ji, 2014; Schito, 2019). This commonality between angiogenesis and lymphangiogenesis may allude to normoxia as a survival signal for both BVs and LVs. The murine oxygen-induced retinopathy model is a tool that allows for the study of BV regression under hyperoxic conditions. Because the retina is physiologically

devoid of LVs, another model must be utilized to study the effects of hyperoxia on LV regression. As our laboratory has demonstrated previously, Prox1-green fluorescent protein (GFP)/Flt1-DsRed transgenic mice can be utilized as a model to observe the physiologic LV regression that occurs postnatally in mice (Zhong et al., 2017). Application of this research tool in conjunction with administration of high concentration oxygen may allow for elucidation of the effects of hyperoxia on LV regression.

In contrast to BVs' dependence on autocrine VEGF-A, most LVs do not seem to require continuous VEGF-C signaling for homeostasis; intestinal and meningeal lymphatics are cited as exceptions (Stritt et al., 2021). Thus, it is likely that there are more nuances left to be unearthed in lymphatic vessel maintenance signaling. As evidenced by the example of retinopathy of prematurity in the BV context, further characterization of these LV survival signals will allow for an increased understanding of LV regression.

Inflammation

Inflammation-induced angiogenesis has been studied in a variety of contexts, including herpes simplex virus 1–induced corneal neovascularization, *helicobacter pylori* infection, cancer, and inflammatory bowel disease (Sajib et al., 2018; Filiberti et al., 2020). Sajib et al. (2018) described the intimate relationship between inflammation and angiogenesis, citing the dual role inflammatory markers such as IL-8 and cyclooxygenase-2 may play in both inflammation and promoting angiogenesis. As inflammatory markers may induce angiogenesis, it follows that inhibition of inflammation may block angiogenesis, and indeed, Folkman described this phenomenon as early as Folkman et al. (1983). Summarized
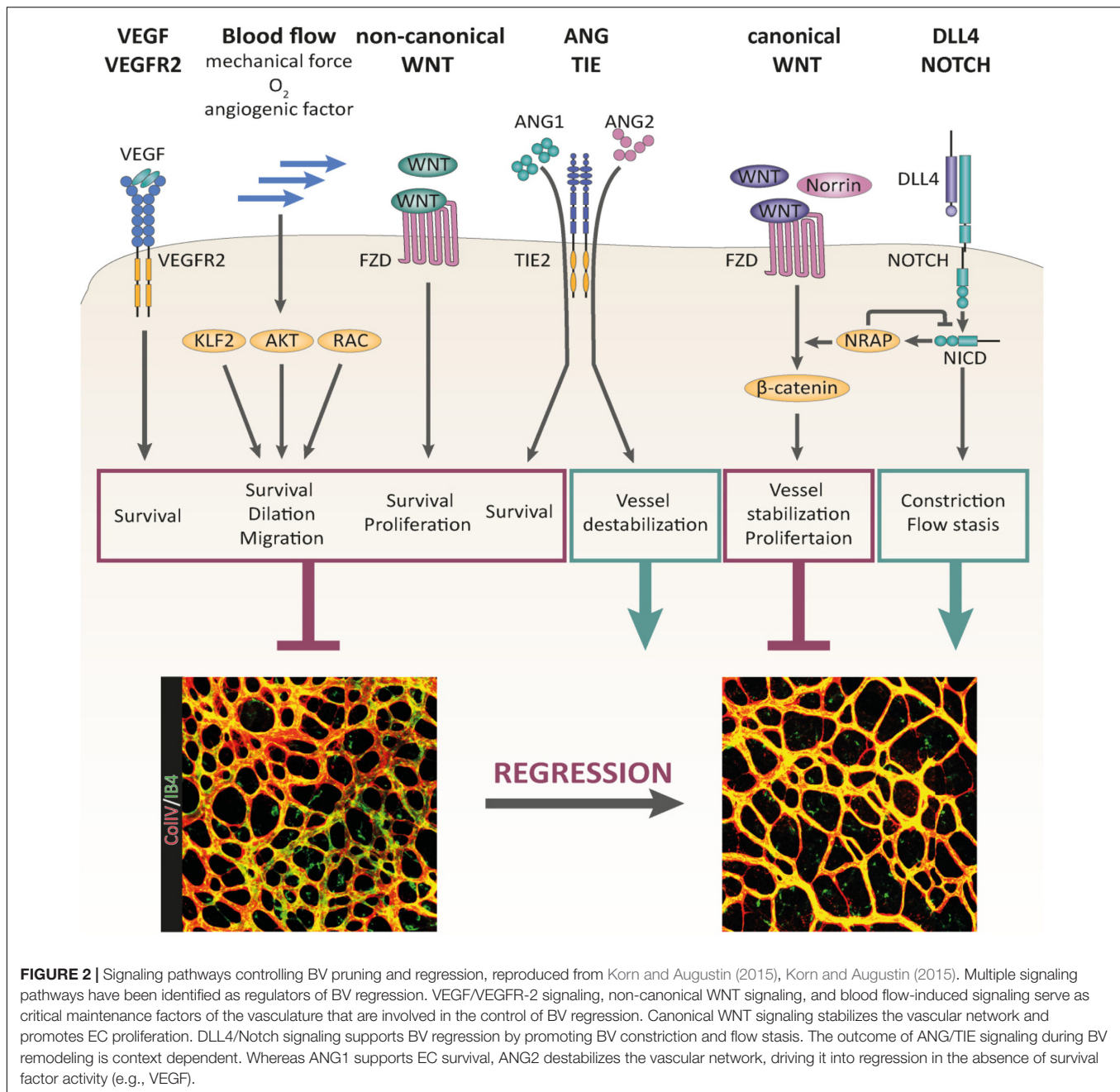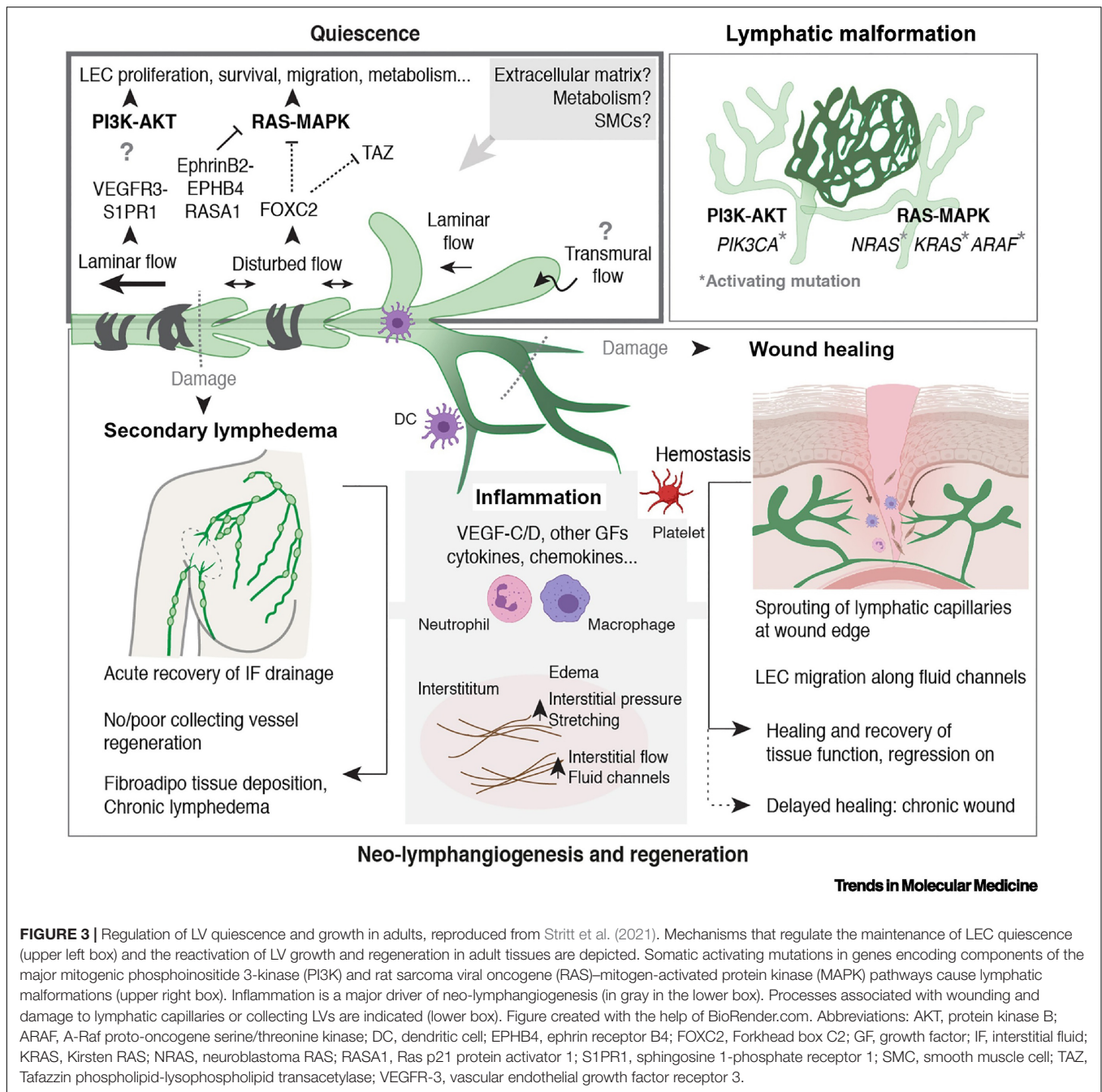
FIGURE 2 | Signaling pathways controlling BV pruning and regression, reproduced from Korn and Augustin (2015), Korn and Augustin (2015). Multiple signaling pathways have been identified as regulators of BV regression. VEGF/VEGFR-2 signaling, non-canonical WNT signaling, and blood flow-induced signaling serve as critical maintenance factors of the vasculature that are involved in the control of BV regression. Canonical WNT signaling stabilizes the vascular network and promotes EC proliferation. DLL4/Notch signaling supports BV regression by promoting BV constriction and flow stasis. The outcome of ANG/TIE signaling during BV remodeling is context dependent. Whereas ANG1 supports EC survival, ANG2 destabilizes the vascular network, driving it into regression in the absence of survival factor activity (e.g., VEGF).

by Logie et al. (2010), the literature is rich with examples of glucocorticoids, potent inflammatory inhibitors, preventing inflammation-induced angiogenesis.

Inflammation has also been implicated in lymphangiogenesis (**Figure 4**; Cursiefen et al., 2006; Kelley et al., 2011; Liao and von der Weid, 2014), and glucocorticoids have been shown to inhibit inflammation-induced lymphangiogenesis (Steele et al., 2011; Martínez-Corral et al., 2012). Although Steele et al. (2011) demonstrated that glucocorticoids inhibit corneal lymphangiogenesis, they found that this anti-inflammatory treatment does not induce LV regression. However, their definition of regressing vessels was determined

visually and perhaps further speaks to the lack of a standardized definition for LV regression (Steele et al., 2011). Additionally, this work utilized corneal removal and fixation, therefore necessitating comparison of samples from different mice; a similar methodology using transgenic mice with fluorescent lymphatic detection would allow for continuous live-imaging and determination of the fate of lymphatic vessels, thereby allowing for verification of LV regression. Another study found that upon resolution of inflammation, newly proliferated lymph node LVs do indeed undergo regression (Mumprecht et al., 2012). Further research of the effects of both inflammation resolution and anti-inflammatory therapy on LV regression are

FIGURE 3 | Regulation of LV quiescence and growth in adults, reproduced from Stritt et al. (2021). Mechanisms that regulate the maintenance of LEC quiescence (upper left box) and the reactivation of LV growth and regeneration in adult tissues are depicted. Somatic activating mutations in genes encoding components of the major mitogenic phosphoinositide 3-kinase (PI3K) and rat sarcoma viral oncogene (RAS)–mitogen-activated protein kinase (MAPK) pathways cause lymphatic malformations (upper right box). Inflammation is a major driver of neo-lymphangiogenesis (in gray in the lower box). Processes associated with wounding and damage to lymphatic capillaries or collecting LVs are indicated (lower box). Figure created with the help of BioRender.com. Abbreviations: AKT, protein kinase B; ARAF, A-Raf proto-oncogene serine/threonine kinase; DC, dendritic cell; EPHB4, ephrin receptor B4; FOXC2, Forkhead box C2; GF, growth factor; IF, interstitial fluid; KRAS, Kirsten RAS; NRAS, neuroblastoma RAS; RASA1, Ras p21 protein activator 1; S1PR1, sphingosine 1-phosphate receptor 1; SMC, smooth muscle cell; TAZ, Tafazzin phospholipid-lysophospholipid transacetylase; VEGFR-3, vascular endothelial growth factor receptor 3.

warranted and may provide insights into novel mechanisms of LV regression.

Anti-angiogenic Switch and Negative Feedback

In the context of wound healing, Gosain et al. (2006) described that after robust angiogenesis, exogenous application of pro-angiogenic stimuli, such as VEGF, FGF, and PDGF, is insufficient for preventing the BV regression characteristic of wound healing resolution. Thus, it follows that there must be a summation

of anti-angiogenic stimuli that supersede the effects of pro-angiogenic molecules in physiologic BV regression. This concept, termed the anti-angiogenic switch, refers to the negative feedback mechanism by which VECs may be protected from excessive angiogenesis and VEGF stimulation. This notion was referred to as early as 1996 when Lingen et al. (1996) described the ability of retinoic acid to "switch [cultured oral squamous cell carcinomas] from an angiogenic to an anti-angiogenic phenotype". Over time, proteins in the vasohibin and mammalian Sprouty families have emerged as negative feedback modulators of angiogenesis (Watanabe et al., 2004;
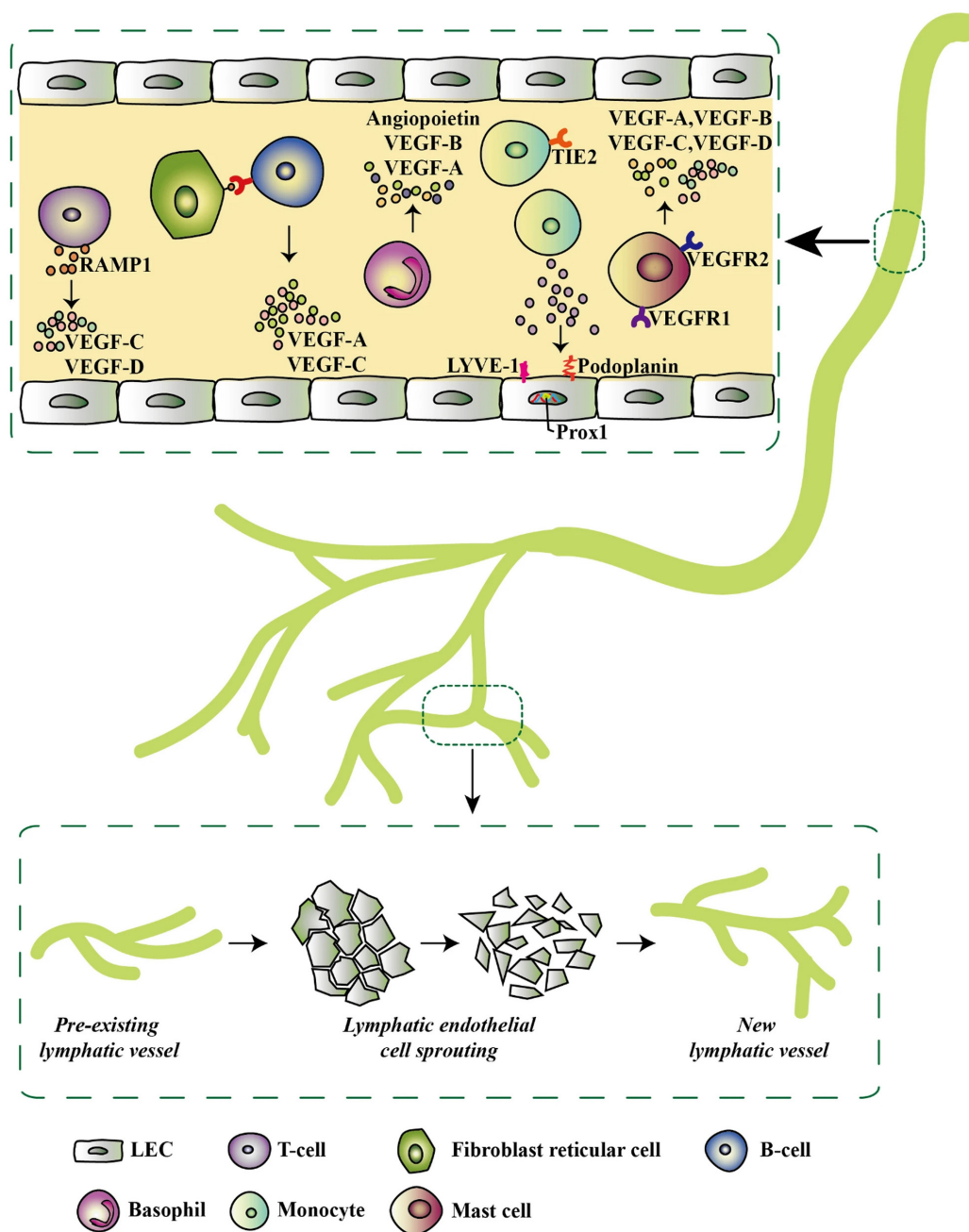
FIGURE 4 | Inflammatory-associated cells and their secretome that initiates lymphatic expansion, reproduced from Ocansey et al. (2021). Most of the inflammatory cells do not only secrete lymphangiogenic factors but also exhibit lymphangiogenic phenotypes by expressing specific lymphatic endothelial markers such as LYVE-1, Prox-1, and podoplanin. These factors trigger pre-existing LVs in the inflammatory environment to give rise to new LVs via LEC sprouting.

Sato and Sonoda, 2007; Wietecha et al., 2011). This research provides evidence for the existence of endogenous mediators that through a negative-feedback mechanism inhibit angiogenesis and prime BVs for physiological regression.

Negative feedback mechanisms are pervasive in biology, as they prevent overstimulation and excessive action. Within the context of inflammation-associated lymphangiogenesis in regional lymph nodes, Kim et al. (2014) described some of the

antilymphatic signaling pathways that occur upon inflammation resolution. The authors describe a balancing act between prolymphangiogenic molecules, derived from intranodal follicular B cells, CD11b macrophages, and fibroblast-type reticular stromal cells, and antilymphatic molecules, derived from T lymphocytes. This dynamic tug-of-war accounts for the ability of the lymphatic vasculature to adapt to the situation at hand, with prolymphangiogenic molecules dominating the early

phase of inflammation and antilymphatic molecules dominating the resolution of inflammation.

As described by Kim et al. (2014) several antilymphatic molecules derived from T lymphocytes have been identified. Shao and Liu (2006) utilized a pig thoracic duct assay to demonstrate that interferon-α and interferon-γ treatment cause a dose-dependent decline in LEC proliferation *in vitro*; the authors hypothesize this effect may be through the induction of apoptosis (Shao and Liu, 2006). A 2011 study similarly implicated interferon-γ signaling as a main driver in lymph node LV regression (Kataru et al., 2011); through the transfer of T cells to athymic nude mice, demonstrated the role of TH1 cell signaling as a negative feedback regulator of lymph node LV formation. In addition to the effects of TH1 interferon signaling, studies published in 2015 asserted the anti-lymphangiogenic function of TH2 cytokine signaling, with IL-4 and IL-13 as the TH2-derived cytokines implicated in negative regulation of lymphangiogenesis (Savetsky et al., 2015; Shin et al., 2015). Two other studies in 2008 confirmed that TGF-β also serves as a negative regulator of lymphangiogenesis (Clavin et al., 2008; Oka et al., 2008). While the story of negative regulation of lymphangiogenesis is likely incomplete, TH1-derived interferon signaling, TH2-derived IL-4 and IL-13 signaling, and TGF-β signaling all play roles in inhibiting lymphangiogenesis.

Apoptosis of Regressing Endothelial Cells

The role of apoptosis in regressing BVs seems to be context dependent. Based on high-resolution imaging of murine cornea and zebrafish models, Franco et al. (2015) concluded that BV regression in these models is apoptosis-independent and, instead, reliant upon VEC migration into neighboring vessels. In contrast, the physiological regression of the hyaloid vessels and pupillary membrane occurs in a cell-death dependent manner (Ito and Yoshioka, 1999; Zhu et al., 2000; Kim et al., 2010; Schafer et al., 2020). In consideration of these diametrically opposite means of vascular regression, one involving VEC migration and the other necessitating cell death, apoptosis plays a nuanced role in BV regression. Korn and Augustin (2015) extended the apoptotic mechanism a step further, contending that apoptosis may be the primary driver of BV regression in some cases or a consequence of depleted survival signaling. Through this nuanced understanding of apoptosis in BV regression and much ingenuity, Schafer et al. (2020) were able to repurpose YK-4-279, a small molecule inhibitor of E-26 transformation-specific transcription factors, to further promote apoptosis and enhance hyaloid vessel regression *in vivo*. These findings in a hyaloid vessel regression murine model successfully translated to human *in vitro* culture, demonstrating YK-4-279's efficacy in regressing human umbilical vein endothelial cell tubes. Their discovery, facilitated by an understanding of apoptosis in BV regression, may prove fruitful in therapeutic applications for pathological neovascularization (Schafer et al., 2020). For an expert review on EC apoptosis in BV regression, readers are referred to the review by Watson et al. (2017).

We have arrived at this nuanced understanding of apoptosis in BV regression as a result of much research, and to our knowledge, there have been few investigations of the role of apoptosis in LV regression. In a study, Hou et al. (2021) utilized ultraviolet A light crosslinking to induce regression of corneal LVs and BVs in an apoptosis-dependent manner. Perhaps in an example of migration-dependent temporary LV regression, Gur-Cohen et al. (2019) demonstrated a transient dissociation of LVs from the hair follicle stem cell niche after the onset of the hair cycle and noted the absence of apoptosis in this context. In Mäkinen et al. (2001) demonstrated that expression of soluble VEGFR-3 in the skin of transgenic mice starting at embryonic day (E)15 lead to regression of dermal LVs with noted apoptosis of LECs in the embryo. Apart from these studies, there has been little research on the role of apoptosis in LV regression. Extending what is known from the BV regression literature, it is similarly possible that LV regression may proceed through migration of LECs into neighboring vessels or through apoptosis of pruned LV segments. Further studies are warranted to unpack the context-specific role of apoptosis in LV regression.

PATHOLOGIES INVOLVING LYMPHANGIOGENIC REGRESSION AND DYSFUNCTION

In health, the lymphatic system plays a key role in fluid homeostasis, lipophilic nutrient absorption in the gastrointestinal tract, and immune surveillance (Tammela and Alitalo, 2010; Yamakawa et al., 2018; Johnson, 2021). Disruption of these roles can result in interstitial fluid imbalance and edema, nutrient malabsorption, and inflammatory pathologies, respectively (Tammela and Alitalo, 2010; Saito et al., 2013; Abouelkheir et al., 2017). Lymphatic dysfunction has long been implicated in diseases such as lymphedema, tumor metastasis, and chronic inflammatory diseases such as rheumatoid arthritis (Rockson, 2001; Detmar and Hirakawa, 2002; Alitalo, 2011). Although research on the lymphatic system still lags behind that for the vascular system (Adamczyk et al., 2016), dysfunction of lymphatic networks has been increasingly identified as a novel player in different pathologies. For a more complete overview of the recently uncovered roles of general lymphatic dysfunction in pathologies such as obesity, inflammatory bowel disease, glaucoma, cardiovascular disease, and neurodegenerative disease, see the 2020 review by Oliver et al. (2020). Here, we describe pathologies with a recently uncovered LV regression component.

Neurodegenerative Disease: Lymphatic Vessel Regression in the Aging Brain

Prior to the discovery of meningeal LVs by Louveau et al., 2015, it had long been accepted that the central nervous system lacked a lymphatic vascular system (Louveau et al., 2015; Petrova and Koh, 2020). On the heels of this initial discovery, Antila et al. (2017) utilized *Prox1-eGFP* transgenic mice to modulate and observe meningeal LV development. Through their work, they elucidated that meningeal LVs develop postnatally

through VEGF-C and VEGFR-3 signaling. Lymphangiogenesis from meningeal LVs was observed upon injection of AAV-VEGF-C, demonstrating that meningeal LVs are capable of dynamically regressing or undergoing lymphangiogenesis dependent on VEGF-C concentrations. This ability to modulate meningeal LV density may have additional therapeutic implications in neurodegenerative diseases such as Alzheimer's disease and Parkinson's disease. In Ma et al. (2017) demonstrated that LVs are the primary conduit for CSF drainage and also observed an age-dependent decline in CSF lymphatic outflow. Considering an age-related decline in CSF outflow along with the important role of CSF in waste removal, Da Mesquita et al. (2018) posited a role for lymphatic flow impairment in Alzheimer's disease pathology. Their studies of photodynamic meningeal lymphatic ablation in murine models showed that LV impairment translates into impaired efflux of interstitial macromolecules as well as impaired cognitive function (Da Mesquita et al., 2018). Similar studies utilizing mouse models overexpressing α-synuclein demonstrated that LV ligation and the subsequent decrease in CSF clearance increase α-synuclein accumulation, increase neuronal loss, and impair motor function, suggesting that age-related LV dysfunction may also contribute to the pathogenesis of Parkinson's disease (Zou et al., 2019). In support of this hypothesis, Ding et al. (2021) used magnetic resonance imaging to visualize lymphatic outflow in patients with Parkinson's disease and found significantly reduced meningeal lymphatic flow in these patients as compared to controls. The current literature suggests that age-related regression of LVs may underpin and exacerbate both Alzheimer's disease and Parkinson's disease, and thus, an improved understanding of LV regression could support the development of therapeutics that can modulate this pathological lymphatic impairment.

Cardiovascular Disease and Atherosclerosis Progression

Lymphatic vessel regression has been hypothesized to exacerbate atherosclerotic cardiovascular disease, the leading cause of death worldwide (Csányi and Singla, 2019; Vourakis et al., 2021). In health, the lymphatic system serves as a conduit for reverse cholesterol transport, the process by which peripheral cholesterol is retrieved and shuttled to the liver by high-density lipoproteins (HDLs) (Huang et al., 2015). Some evidence suggests that reverse cholesterol transport may hamper the pathogenesis of atherosclerosis, although Huang et al. (2015) highlighted that clinical studies have yet to corroborate the athero-protective role of HDL-mediated cholesterol transport (Rosenson et al., 2012). By serving as a channel for cholesterol retrieval, LVs may play a role in reducing the cholesterol burden in atherosclerosis (Fernández-Hernando, 2013; Csányi and Singla, 2019). Studies have suggested that adventitial lymphatics of atherosclerotic vessels undergo regression, leading to potentially impaired drainage of inflammatory cytokines and pro-atherosclerotic lipids, thereby exacerbating atherosclerosis (Taher et al., 2016; Csányi and Singla, 2019). While a component of LV regression may exacerbate atherosclerotic disease, therapeutic lymphangiogenesis is seen to promote

recovery of cardiac tissue post-myocardial infarction in mice (Houssari et al., 2020). Using an adeno-associated viral gene delivery of VEGF-C, Houssari et al. (2020) demonstrate that induced-lymphangiogenesis accelerates the resolution of cardiac inflammation following experimental myocardial infarction. A separate work by Liu et al. (2020) demonstrates that LECs play a cardioprotective role through the release of a molecule called Reelin, corroborating the role of lymphatic vessels in cardiac homeostasis. Overall, LVs are hypothesized to have an athero-protective role while LECs are seen to have an important role in injury resolution following myocardial infarction.

REFLECTING ON FUTURE DIRECTIONS

Models for Studying Lymphatic Vessel Regression

A comprehensive understanding of LV regression will require robust research tools, including appropriate animal models. Zhang et al. (2011), Shi et al. (2020) employed a murine cornea model to observe lymphatic regression. Zhang et al. (2011) proposed that the neovascular privilege of the cornea allows for a wide range of lymphatic growth and plasticity, while Shi et al. (2020) concluded that the cornea has strong potential for studying the effect of aqueous humor on lymphatic vessels (Zhang et al., 2011). The mouse tail has also been identified as a useful tool in lymphatic visualization (Weiler et al., 2019). Researchers have used this model in the context of lymphedema (Bramos et al., 2016; Zhou et al., 2020) and general lymphatic trafficking (Hassanein et al., 2021), but Weiler et al. (2019) were optimistic about its use in many other lymphatic conditions. In the context of Gorham Stout disease, Monroy et al. (2020) studied the extent of lymphatic growth due to pre-existing vessels in mouse bones. Like the cornea, bone is also devoid of lymphatic vessels in a healthy state, and using a model for lymphatic research similar to the cornea could lead to valuable insight into conditions such as Gorham Stout disease. Similarly, Yao et al. (2014) investigated VEGF-C overexpression mice to determine whether this model is useful to study LV development in the respiratory tract but found a condition resembling pulmonary lymphangiectasia, a serious condition in the newborn. Hence, models do not necessarily need to be devoid of LV originally, as this example demonstrates the lung as a valid option to better understand pulmonary lymphatic pathology. A valid model is needed also for future LV regression research in the context of cancer, and Frenkel et al. (2021) proposed the use of long-lived human LECs to better understand lymphangiogenesis and tumor–LV interactions. These cells represent a novel method for studying specifically human tumor lymphangiogenesis and can be further employed to study LV regression. In contrast, sentinel lymph node lymphangiogenesis is a well-documented research model that has been utilized in the study of cancer metastasis (Hirakawa et al., 2005). The lymph node lymphangiogenesis model also has been employed to study LV regression (Mumprecht et al., 2012). **Table 3** outlines research models that can facilitate increased understanding of LV regression. Most of these research models are *in vivo* tools that

TABLE 3 | Animal models for the study of LV regression.

Model	References	Utility and findings
Cornea (mouse)	Zhang et al., 2011; Shi et al., 2020	In tandem, these studies demonstrated the utility of the murine cornea for observing *de novo* lymphangiogenesis and LV regression. Due to the ordinarily avascular nature of the cornea, Prox-1 GFP transgenic mice can be utilized for live-imaging of LV progression and regression. The latter reference utilized this technology to demonstrate potentially therapeutic properties of aqueous humor in inducing LV regression.
Tail (mouse)	Bramos et al., 2016; Weiler et al., 2019; Zhou et al., 2020; Hassanein et al., 2021	The mouse tail lymphedema model involves 2-mm deep surgical circumferential excision of the portion of the tail 2 cm distal to the tail base, which disconnects the superficial and deep lymphatics of the tail, thereby locally mimicking lymphedema pathology. Visualization of lymphatic flow involves injection of a fluorescently labeled tracker, such as fluorescein isothiocyanate-dextran, into the mouse tail.
Bone (mouse)	Monroy et al., 2020	This work utilized several transgenic mouse models to visualize *de novo* lymphangiogenesis and LV regression in the context of generalized lymphatic anomaly, a pathology that may be caused by activating mutations of PIK3CA. Prox1-CreERT2;LSL-Pik3caH1047R transgenic mice offer a tamoxifen-inducible system for expression of PIK3CA in LECs. Osx-tTA-TetO-Cre;TetO-Vegfc;mT/mG transgenic mice offer a murine model of Gorham-Stout disease. This model utilizes the bone-specific Osterix promoter to drive a Tet-On system for VEGF-C overexpression in osteoblasts, osteocytes, and chondrocytes. Furthermore, the mT/mG reporter system causes all Cre-positive cells to express GFP. This work highlights the utility of designing transgenic mice to study LV progression and regression in a wide variety of disease contexts.
Lung (mouse)	Yao et al., 2014	CCSP-rtTA; tetO-VEGF-C transgenic mice can be used to study *de novo* lymphangiogenesis in the context of pulmonary lymphangiectasia. This construct allows for doxycycline-induced expression of VEGF-C in Clara cells and alveolar type II cells. These mice were crossed with Prox1-GFP mice to allow for live imaging of LVs, and the triple transgenic mouse allows for an analysis of the effects of VEGF-C to VEGFR-3 signaling in a pulmonary context. Utilization of this model revealed a critical period when VEGF-C expression and resultant lymphangiogenesis produce a pulmonary lymphangiectasia pathology. This model also enables the study of therapeutic modulation of LV regression to treat and prevent pulmonary lymphangiectasia.
Long-lived human LECs	Frenkel et al., 2021	A microfluidic LV model enables analysis of *de novo* lymphangiogenesis and tumor–LV interaction. Lentiviral delivery of human telomerase and BMI-1 expression cassettes was utilized to develop an immortalized human LEC line. This cell line was paired with a microfluidic chip consisting of a free-standing extracellular matrix to visualize the formation of LV-like structures. This model was next co-cultured with mouse colon cancer organoids, enabling live visualization of tumor-induced lymphatic vasculature changes. This microfluidic model can be utilized to mimic both native and tumoral contexts of lymphangiogenesis and LV regression. Application of exogenous therapeutics or molecules of interest to this model can be used to study methods for modulating LV regression and lymphangiogenesis.
Lymph Node	Hirakawa et al., 2005; Mumprecht et al., 2012; Truman et al., 2012	Transgenic mice overexpressing VEGF-A were seen to exhibit sentinel lymph node lymphangiogenesis in a cutaneous squamous cell carcinoma model. While this study by Hirakawa et al., 2005 identified VEGF-A as a tumor lymphangiogenesis inducer, it also demonstrated the utility of the lymph node as a model to study lymphatic vessel dynamics. A different study utilized radiolabeled antibodies against LYVE-1 in conjunction with positron emission tomography to visualize murine lymph node lymphangiogenesis in response to induced inflammation of the skin. Upon resolution of inflammation 3 months later, the authors observed LV regression, thereby demonstrating that inflammation-induced lymph node lymphangiogenesis is indeed reversible. With the progression of transgenic fluorescent reporter mice and robust visualization of LVs in lymph nodes, this remains a powerful tool for exploring lymphatic vessel dynamics.

allow for the perturbation and observation of LV dynamics in transgenic mice. The noted LEC microfluidic device represents an emerging area of research with microfluidics; in this example, the microfluidic device enables researchers to exert precise control over interactions between the tumor and LV.

Potential Therapeutic Applications of Lymphatic Vessel Regression

In Section "Pathologies Involving Lymphangiogenic Regression and Dysfunction," we explored pathologies with a component of LV regression. Accordingly, potential avenues exist for the therapeutic use of LV regression, further emphasizing the importance of characterizing LV regression. An understanding of the nuanced mechanisms by which LV regression occurs may facilitate methods to either therapeutically block these mechanisms in cases of pathological LV or therapeutically induce these mechanisms in cases of pathological lymphangiogenesis. **Table 4** lists anti-lymphangiogenic agents that have been

employed in pre-clinical studies, and **Table 5** lists anti-lymphangiogenic modulatory agents that have been tested in clinical trials for their therapeutic potential for a select few pathologies.

Nuanced Role of Lymphangiogenesis in Lymphedema

Lymphedema is a pathology characterized by deficient lymphatic transport, resulting in excessive regional lymphatic fluid accumulation (Rockson, 2001). Although lymphedema can be a primary disorder, this pathology is more commonly acquired as a secondary disruption of lymphatic vasculature caused by surgery, radiation, infection, or trauma (Rockson, 2001). In addition to disfigurement, chronic lymphedema also poses increased risk for cellulitis and lymphorrhea (Ogata et al., 2016). Transgenic mice models expressing soluble VEGFR-3 acquired a lymphedema-like phenotype due to LV regression and disrupted lymphangiogenesis (Mäkinen et al., 2001). As anti-lymphangiogenic agents are seen to precipitate

TABLE 4 | Anti-lymphangiogenic agents explored in pre-clinical studies.

Therapeutic agent	References	Context and mechanism of action
Atorvastatin	Ogata et al., 2016	In the context of an early lymphedema murine model, interactions between TH1/TH17 CD4 + T lymphocytes and macrophages result in increased macrophage VEGF-C expression. Daily oral atorvastatin for 1 month reduces the proportion of IFN-γ– and IL-17–secreting CD4 + T lymphocytes, thereby decreasing VEGF-C expression in lesional macrophages. This therapeutic intervention suppresses pathological lymphangiogenesis that exacerbates lymphedema pathology. The authors describe statins as inhibitors of isoprenoids synthesis, thereby resulting in decreased T cell proliferation and differentiation; however, they concede that the exact therapeutic mechanism of atorvastatin in lymphedema is likely still unknown.
Doxycycline	Han et al., 2014	The authors explored the effects of doxycycline on a corneal inflammation-induced lymphangiogenesis murine model. Topical doxycycline application over a 10-day period post corneal injury resulted in dramatically reduced lymphangiogenesis as compared to control mice. Doxycycline was determined to exert its anti-lymphangiogenic effects via overall inhibition of VEGF-C to VEGFR-3 signaling. Additionally, doxycycline application resulted in reduced VEGF-C–induced human dermal LEC proliferation as well as reduction of macrophage-produced lymphangiogenic factors. The authors deduced that the effects of doxycycline were mediated through the PI3k/Akt pathway and by inhibition of matrix metalloproteinases.
TH1 Cytokines	Shao and Liu, 2006; Kataru et al., 2011	Shao and Liu, 2006 utilized a porcine thoracic duct assay to demonstrate the anti-lymphangiogenic effects of interferon-α and interferon-γ in vitro. These cytokines, produced by TH1 CD4 + T lymphocytes, were deemed to induce LEC apoptosis. Kataru et al., 2011 demonstrated the anti-lymphangiogenic effects of TH1 signaling on lymph nodes through the transfer of T cells to athymic nude mice. Although interferon-γ signaling was identified as a likely mediator of the anti-lymphangiogenic effects of TH1 cells, the authors noted that other T-cell–derived factors may also exert anti-lymphangiogenic effects. Kataru et al., 2011 identified JAK1-STAT1 signaling as a key pathway in interferon-γ lymphangiogenesis inhibition.
TH2 Cytokines	Savetsky et al., 2015; Shin et al., 2015	TH2 CD4 + T lymphocyte-derived cytokines, namely IL-4 and IL-13, were seen to exert anti-lymphangiogenic effects. IL-4 and IL-13 resulted in the downregulation of essential LEC transcription factors. In an in vitro co-culture system of TH2 cells and LECs, TH2 cytokines were seen to inhibit lymphatic tube formation. Shin et al., 2015 demonstrated a therapeutic application of this finding in vivo by inhibiting IL-4 and IL-13 in a murine allergic asthma model; neutralizing antibodies against IL-4 and IL-13 resulted in increased lymphatic vessel density, enhanced functioning of lung lymphatic vessels, and subsequent improvement in antigen clearance.
IL-17A	Chen et al., 2010; Park et al., 2018	In the context of TH17-mediated immune responses, Park et al., 2018 described the anti-lymphangiogenic effects of IL-17A, a cytokine secreted by TH17 CD4 + T lymphocytes. The authors utilized a cholera toxin inflammation model and demonstrated that IL-17A suppresses lymphatic markers in LECs as well as inhibits lymphangiogenesis in the resolution phases of inflammation. The authors then utilized an IL-17A–neutralizing antibody to demonstrate increased lymphangiogenesis and lymphatic function. In a separate study pertaining to non-small cell lung cancer however, Chen et al., 2010 found that IL-17 upregulates VEGF-C expression in cancer cells and subsequently increases tumor lymphangiogenesis. The authors noted that the Lewis Lung carcinoma cells utilized express IL-17 receptor; therefore, it is possible that IL-17 may have context-dependent effects on lymphangiogenesis.
TGF- β	Clavin et al., 2008; Oka et al., 2008	In an acute lymphedema model of the murine tail by Clavin et al., 2008, TGF-β1 expression was modulated via the application of a topical collagen gel. Tail wound repair with collagen gel application resulted in decreased TGF-β1 expression, which in turn resulted in accelerated lymphatic vessel formation and improved healing. The authors found TGF-β1 to have dose-dependent effects on decreasing proliferation and tubule formation of LECs. A separate study by Oka et al., 2008 found that TGF-β reduced expression of LEC markers and lymph vessel development even in the presence of the pro-lymphangiogenic ligand VEGF-C. They also found that TGF-β1 plays important roles in negatively regulating lymphangiogenesis.
VEGFR-3 Blockade	He et al., 2002	As VEGF-C/VEGFR-3 signaling is the main driver of lymphangiogenesis, blockade of this interaction has long been utilized to exert anti-lymphangiogenic effects. He et al., 2002 transfected human lung cancer cell lines with a soluble fusion protein VEGFR-3-immunoglobulin and then implanted these tumor cells subcutaneously into severe combined immunodeficient mice. The soluble VEGFR-3 protein expressed by tumor cells inhibited VEGF-C/VEGFR-3 interaction. Through this experiment, the authors determined that inhibition of the VEGF-C/VEGFR-3 interaction can suppress tumor lymphangiogenesis and thereby prevent metastasis to regional lymph nodes; however, metastasis of tumor cells to the lungs still occurred via factors extraneous to VEGF-C signaling.

a lymphedema-like phenotype, the value of therapeutic lymphangiogenesis has been tested in animal models to treat lymphedema (Szuba et al., 2002; Saito et al., 2013). However, Ogata et al. (2016) demonstrated that lymphangiogenesis plays a more nuanced role in the progression of lymphedema; in fact, an initial phase of excessive lymphangiogenesis induced by inflammatory cell and LEC interaction exacerbates the development of lymphedema pathology (Ogata et al., 2016). In a murine lymphedema model, VEGF-C expression was found to be upregulated 4 days after lymphatic obstruction, resulting in the formation of immature LVs; inhibition of this prolymphangiogenic VEGF-C signaling reduced fibrosis and adipogenesis, phenotypic features of lymphedema (Ogata et al., 2016). This increased VEGF-C expression was largely attributed to an interaction between macrophages and CD4 + T lymphocytes. TH1 and TH17 CD4 + T lymphocytes release IFN-γ and IL-17, respectively, resulting in activation of macrophages to upregulate VEGF-C expression. To verify this finding, the authors utilized atorvastatin to reduce the proportion of IFN-γ– and IL-17–secreting CD4 + T lymphocytes. Subsequently,

TABLE 5 | Lymphangiogenic modulatory agents tested in clinical trials.

Agent name	Reference/identification number	Mechanism of action	Indication	Trial status
IMC-3C5	NCT01288989 Saif et al., 2016	Anti-VEGFR-3 mAb	Colorectal cancer and solid tumors	Phase 1
VGX-100	NCT01288989	Anti-VEGF-C mAb	Advanced solid tumors	Phase 1
Etrasimod	NCT02447302 Nagahashi et al., 2012; Sandborn et al., 2020	Sphingosine 1 phosphate receptor antagonist	IBD	Phase 2
Lymfactin	NCT03658967	Adenovirus gene therapy expressing human VEGF-C	Secondary Lymphedema	Phase 2
Doxycycline	NCT02929121	VEGF-C/VEGFR-3 modulation?	Lymphedema Filariasis	Phase 3
Pazopanib	NCT00827372	VEGFR-1,2,3 inhibitor	Secondary Lymphedema	Phase 2
Ubenimex	NCT02700529	Leukotriene A4 hydrolase inhibitor, biosynthetic enzyme for the anti-lymphangiogenic leukotriene B4	Lymphedema	Phase 2

macrophages were seen to secrete less VEGF-C and the phenotype of lymphedema was reduced (Ogata et al., 2016). These studies suggest that an interaction between inflammatory cells in early lymphedema results in lymphangiogenesis that exacerbates the acute lymphedema pathology. Although prior research in animal models has shown a role for therapeutic lymphangiogenesis in lymphedema, this example of aberrant lymphangiogenesis exacerbating early lymphedema pathology calls for caution when designing therapeutics that modulate lymphangiogenic processes (Kim et al., 2014; Ogata et al., 2016).

Inflammatory Bowel Disease

Inflammatory bowel disease (IBD), which includes Crohn's Disease (CD) and ulcerative colitis (UC), is a chronic inflammatory disorder of the gastrointestinal track with an increasing pediatric prevalence worldwide (Ye et al., 2015). Chronic IBD is accompanied by LV proliferation within the lamina propria and submucosa; a human study of UC found that the number of LVs in the lamina propria reflects the severity of disease (Fogt et al., 2004). Rahier et al. (2011) observed an increased density of LVs in both CD and UC, further attributing this process to lymphangiogenesis. Although Kim et al. (2014) reported that aberrant LV function is likely involved in IBD, it remains debated whether increased LV density exacerbates IBD pathology or serves a protective function through inflammation resolution (Kim et al., 2014). To determine if early lymphangiogenesis exacerbates IBD pathology, D'Alessiou et al. (2014) utilized adenoviral induction of VEGF-C in experimental murine models of IBD (D'Alessiou et al., 2014). Their results demonstrated that VEGF-C–induced lymphangiogenesis enhanced lymphatic flow and function, thereby improving intestinal inflammation in IBD. A supporting study utilized a VEGFR-3 blocking antibody in a murine model of IBD, demonstrating that inhibition of VEGF-C/VEGFR-3 signaling results in impaired lymphatic morphology that exacerbates the severity of inflammation (Jurisic et al., 2013). Taken together, these findings may suggest that therapeutic prolymphangiogenic signaling can improve the aberrant lymphatic morphology characteristic of IBD. Although lymphatic flow is essential in limiting the progression of inflammation, further studies are needed to characterize whether the increased LV density early in IBD pathology is pathological or protective (Rahier et al., 2011; Kim et al., 2014).

Lymphatic Preconditioning to Reduce Transplant Rejection

Despite the advent of human leukocyte antigen matching and the administration of immunosuppressants, allograft rejection remains the leading cause of graft failure beyond 1 year post-transplantation (Yamakawa et al., 2018; Wong, 2020). Lymphangiogenesis has been observed following transplantation of solid organs such as the heart, kidney, and lungs as well as the normally avascular cornea (Wong, 2020; Hou et al., 2021). This proliferation of novel LVs connects the transplanted organ to the systemic lymphatic circulation, thereby facilitating the arrival of antigen-presenting cells (APCs) to draining lymph nodes (Donnan et al., 2021). APC trafficking via LVs to nearby draining lymph nodes can orchestrate the pathological immune response of graft rejection (Donnan et al., 2021). A schematic illustrating the role of the vasculature in immune cell trafficking and corneal graft rejection is shown in **Figure 5**. Donnan et al. (2021) demonstrated that an increased degree of lymphangiogenesis is positively correlated with the degree of renal transplant rejection, further emphasizing the detrimental role that lymphangiogenesis may play in transplant rejection (Kerjaschki et al., 2004; Phillips et al., 2016; Donnan et al., 2021). Lymphangiogenesis post-transplantation is not always detrimental however, as it may have a protective role following lung transplantation (Wong, 2020).

Due to its immune privileged and avascular nature, the murine cornea also has been utilized as a research model of transplant rejection. Studies have repeatedly demonstrated that corneal neovascularization is correlated with corneal transplantation rejection risk (Bachmann et al., 2010; Le et al., 2018; Hou et al., 2021). Moreover, multiple studies from the Cursiefen group showed that promoting LV regression prior to corneal transplantation in high-risk eyes improves the likelihood of graft survival (Hou et al., 2017, 2018; Le et al., 2018). Hou et al. (2021) described this concept as "lymphangioregressive preconditioning," as promoting LV regression prior to corneal transplantation in high-risk
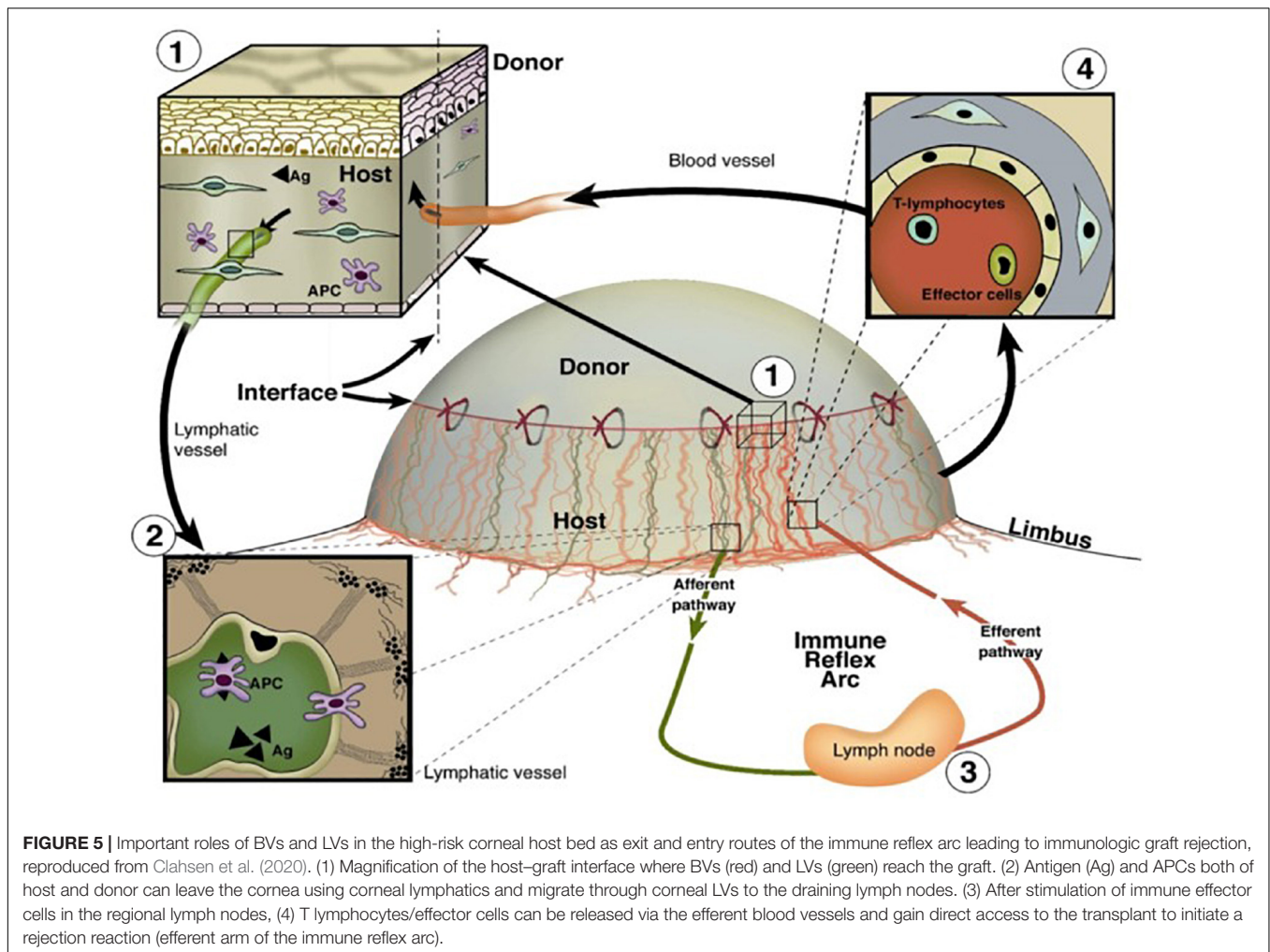
FIGURE 5 | Important roles of BVs and LVs in the high-risk corneal host bed as exit and entry routes of the immune reflex arc leading to immunologic graft rejection, reproduced from Clahsen et al. (2020). (1) Magnification of the host–graft interface where BVs (red) and LVs (green) reach the graft. (2) Antigen (Ag) and APCs both of host and donor can leave the cornea using corneal lymphatics and migrate through corneal LVs to the draining lymph nodes. (3) After stimulation of immune effector cells in the regional lymph nodes, (4) T lymphocytes/effector cells can be released via the efferent blood vessels and gain direct access to the transplant to initiate a rejection reaction (efferent arm of the immune reflex arc).

individuals improved transplantation outcomes. This notion of therapeutic LV regression to prevent graft rejection may also apply in other organ contexts, although further work is required to elucidate the precise roles of LVs in the transplantation of different organs (Hou et al., 2021).

Lymphatic Vessel Regression to Prevent Tumor Metastasis

Peritumoral lymphangiogenesis has been increasingly appreciated as a key driver in tumor metastasis and subsequent poor patient prognosis. The first step in metastasis of many cancers involves migration to regional lymph nodes (Detmar and Hirakawa, 2002). As described by Yamakawa et al. (2018), tumor cells can induce lymphangiogenesis from local lymph nodes through pro-lymphangiogenic signaling, effectively creating a highway for lymphatic metastasis. For an expert review on the pre-metastatic niche and tumor signaling in regional lymph nodes, readers are referred to the review by Gillot et al. (2021). Through the secretion of VEGF-C and VEGF-D, tumors of the breast, lung, colon, prostate, and cervix promote the formation of tumor lymphatic networks that serve as routes for metastasis (Detmar and Hirakawa, 2002; Kesler et al., 2013). Multiple

studies have confirmed the positive correlation between tumor-induced lymphangiogenesis and tumor metastasis (Wilting et al., 2005; Royston and Jackson, 2009; Nagahashi et al., 2010). Wilting et al. (2005) emphasized that approximately 80% of metastatic tumors coincide with tumor-induced lymphangiogenesis (Wilting et al., 2005).

Given this growing body of evidence that implicates peri-tumoral lymphangiogenesis in metastasis, a major indicator of poor prognosis in cancer, it is evident that therapeutics targeting this process may inhibit the progression of tumors (Khromova et al., 2012). In addition to the blockade of lymphangiogenic signaling, modulating non-overlapping mechanisms of LV regression may serve as another therapeutic avenue to prevent tumor metastasis. The objectives of this review were to summarize novel findings related to LV regression and pose questions for further characterization. Perhaps by inhibiting lymphangiogenesis and also employing novel methods for inducing LV regression, more effective methods for tumor therapy may be developed. Despite this theoretical basis in anti-lymphangiogenic tumor therapy, no anti-lymphangiogenic drugs have been approved for clinical use by the Food and Drug Administration to date (Raica et al., 2016; Okuda et al., 2018;

Yamakawa et al., 2018). The exact role of LVs in cancer biology seems to be more nuanced as induced-lymphangiogenesis has also been seen to increase immunosurveillance of a tumor (Vaahtomeri and Alitalo, 2020). Readers are referred herein for a review of the role of LVs in tumor metastasis and immunotherapy (Vaahtomeri and Alitalo, 2020).

CONCLUSION

Herein we have highlighted the importance of understanding LV regression in both physiological and pathological contexts and describe potential therapeutic applications for this knowledge. Despite its importance in pathologies such as neurodegenerative diseases, cardiovascular diseases, organ graft rejection, and tumor metastasis, the lymphatic system is largely understudied as compared to its blood vasculature counterpart. By summarizing principles of BV regression and possible extensions to the field of LV regression, we have described areas of study that warrant further exploration. We have summarized research tools that have been utilized to modulate and study LV

regression, so that future work can build upon this foundation. Although the lymphatic system and its roles in diverse pathologies have yet to be fully characterized, this review aims to accelerate the work required to better characterize LV regression so that this phenomenon may be modulated for therapeutic purposes.

AUTHOR CONTRIBUTIONS

FM, RB, MR, AK, J-HC, and DA contributed to the writing of the manuscript.

FUNDING

REFERENCES

Abouelkheir, G. R., Upchurch, B. D., and Rutkowski, J. M. (2017). Lymphangiogenesis: fuel, smoke, or extinguisher of inflammation's fire? *Exp. Biol. Med.* 242, 884–895. doi: 10.1177/1535370217697385

Adamczyk, L. A., Gordon, K., Kholová, I., Meijer-Jorna, L. B., Telinius, N., Gallagher, P. J., et al. (2016). Lymph vessels: the forgotten second circulation in health and disease. *Virch. Arch.* 469, 3–17. doi: 10.1007/s00428-016-1945-6

Adams, R. H., and Alitalo, K. (2007). Molecular regulation of angiogenesis and lymphangiogenesis. *Nat. Rev. Mol. Cell Biol.* 8, 464–478. doi: 10.1038/nrm2183

Alitalo, K. (2011). The lymphatic vasculature in disease. *Nat. Med.* 17, 1371–1380. doi: 10.1038/nm.2545

Alitalo, K., and Carmeliet, P. (2002). Molecular mechanisms of lymphangiogenesis in health and disease. *Cancer Cell* 1, 219–227. doi: 10.1016/S1535-6108(02)00051-X

Alitalo, K., Tammela, T., and Petrova, T. V. (2005). Lymphangiogenesis in development and human disease. *Nature* 438, 946–953. doi: 10.1038/nature04480

Antila, S., Karaman, S., Nurmi, H., Airavaara, M., Voutilainen, M. H., Mathivet, T., et al. (2017). Development and plasticity of meningeal lymphatic vessels. *J. Exp. Med.* 214, 3645–3667. doi: 10.1084/jem.20170391

Bachmann, B., Taylor, R. S., and Cursiefen, C. (2010). Corneal neovascularization as a risk factor for graft failure and rejection after keratoplasty: an evidence-based meta-analysis. *Ophthalmology* 117, 1300–1305.e7. doi: 10.1016/j.ophtha.2010.01.039

Barratt, S., and Millar, A. (2014). Vascular remodelling in the pathogenesis of idiopathic pulmonary fibrosis. *QJM* 107, 515–519. doi: 10.1093/qjmed/hcu012

Bergers, G., Song, S., Meyer-Morse, N., Bergsland, E., and Hanahan, D. (2003). Benefits of targeting both pericytes and endothelial cells in the tumor vasculature with kinase inhibitors. *J. Clin. Invest.* 111, 1287–1295. doi: 10.1172/JCI200317929

Bodnar, R. J., Yates, C. C., Rodgers, M. E., Du, X., and Wells, A. (2009). IP-10 induces dissociation of newly formed blood vessels. *J. Cell Sci.* 122, 2064–2077. doi: 10.1242/jcs.048793

Bramos, A., Perrault, D., Yang, S., Jung, E., Hong, Y. K., and Wong, A. K. (2016). Prevention of postsurgical lymphedema by 9-cis retinoic acid. *Ann. Surg.* 264, 353–361. doi: 10.1097/SLA.0000000000001525

Carmeliet, P., and Jain, R. K. (2011). Molecular mechanisms and clinical applications of angiogenesis. *Nature* 473, 298–307. doi: 10.1038/nature10144

Chade, A. R. (2013). Renal vascular structure and rarefaction. *Compr. Physiol.* 3, 817–831. doi: 10.1002/cphy.c120012

Chen, X., Xie, Q., Cheng, X., Diao, X., Cheng, Y., Liu, J., et al. (2010). Role of interleukin-17 in lymphangiogenesis in non-small-cell lung cancer: enhanced production of vascular endothelial growth factor C in non-small-cell lung carcinoma cells. *Cancer Sci.* 101, 2384–2390. doi: 10.1111/j.1349-7006.2010.01684.x

Clahsen, T., Büttner, C., Hatami, N., Reis, A., and Cursiefen, C. (2020). Role of endogenous regulators of Hem- And lymphangiogenesis in corneal transplantation. *J. Clin. Med.* 9:479. doi: 10.3390/jcm9020479

Clavin, N. W., Avraham, T., Fernandez, J., Daluvoy, S. V., Soares, M. A., Chaudhry, A., et al. (2008). TGF-beta1 is a negative regulator of lymphatic regeneration during wound repair. *Am. J. Physiol. Heart Circ. Physiol.* 295, H2113–H2127. doi: 10.1152/ajpheart.00879.2008

Claxton, S., and Fruttiger, M. (2003). Role of arteries in oxygen induced vaso-obliteration. *Exp. Eye Res.* 77, 305–311. doi: 10.1016/s0014-4835(03)00153-2

Cordeiro, I. R., Kabashima, K., Ochi, H., Munakata, K., Nishimori, C., Laslo, M., et al. (2019). Environmental oxygen exposure allows for the evolution of interdigital cell death in limb patterning. *Dev. Cell* 50, 155–166.e4. doi: 10.1016/j.devcel.2019.05.025

Csányi, G., and Singla, B. (2019). Arterial lymphatics in atherosclerosis: old questions, new insights, and remaining challenges. *J. Clin. Med.* 8:495. doi: 10.3390/jcm8040495

Cursiefen, C., Maruyama, K., Jackson, D. G., Streilein, J. W., and Kruse, F. E. (2006). Time course of angiogenesis and lymphangiogenesis after brief corneal inflammation. *Cornea* 25, 443–447. doi: 10.1097/01.ico.0000183485.85636.ff

Da Mesquita, S., Louveau, A., Vaccari, A., Smirnov, I., Cornelison, R. C., Kingsmore, K. M., et al. (2018). Functional aspects of meningeal lymphatics in ageing and Alzheimer's disease. *Nature* 560, 185–191. doi: 10.1038/s41586-018-0368-8

D'Alessio, S., Correale, C., Tacconi, C., Gandelli, A., Pietrogrande, G., Vetrano, S., et al. (2014). VEGF-C-dependent stimulation of lymphatic function ameliorates experimental inflammatory bowel disease. *J. Clin. Invest.* 124, 3863–3878. doi: 10.1172/JCI72189

Detmar, M., and Hirakawa, S. (2002). The formation of lymphatic vessels and its importance in the setting of malignancy. *J. Exp. Med.* 196, 713–718. doi: 10.1084/jem.20021346

Ding, X.-B., Wang, X.-X., Xia, D.-H., Liu, H., Tian, H.-Y., Fu, Y., et al. (2021). Impaired meningeal lymphatic drainage in patients with

idiopathic Parkinson's disease. *Nat. Med.* 27, 411–418. doi: 10.1038/s41591-020-01198-1

Donnan, M. D., Kenig-Kozlovsky, Y., and Quaggin, S. E. (2021). The lymphatics in kidney health and disease. *Nat. Rev. Nephrol.* 17, 655–675. doi: 10.1038/s41581-021-00438-y

Ebina, M., Shimizukawa, M., Shibata, N., Kimura, Y., Suzuki, T., Endo, M., et al. (2004). Heterogeneous increase in CD34-positive alveolar capillaries in idiopathic pulmonary fibrosis. *Am. J. Respir. Crit. Care Med.* 169, 1203–1208. doi: 10.1164/rccm.200308-1111OC

Elabi, O., Gaceb, A., Carlsson, R., Padel, T., Soylu-Kucharz, R., Cortijo, I., et al. (2021). Human alpha-synuclein overexpression in a mouse model of Parkinson's disease leads to vascular pathology, blood brain barrier leakage and pericyte activation. *Sci. Rep.* 11:1120. doi: 10.1038/s41598-020-80889-8

Eshkar-Oren, I., Krief, S., Ferrara, N., Elliott, A. M., and Zelzer, E. (2015). Vascular patterning regulates interdigital cell death by a ROS-mediated mechanism. *Development* 142, 672–680. doi: 10.1242/dev.120279

Esther, C. R., and Barker, P. M. (2004). Pulmonary lymphangiectasia: diagnosis and clinical course. *Pediatr. Pulmonol.* 38, 308–313. doi: 10.1002/ppul.20100

Fallah, J., and Rini, B. I. (2019). HIF inhibitors: status of current clinical development. *Curr. Oncol. Rep.* 21:6. doi: 10.1007/s11912-019-0752-z

Fan, J., Ponferrada, V. G., Sato, T., Vemaraju, S., Fruttiger, M., Gerhardt, H., et al. (2014). Crim1 maintains retinal vascular stability during development by regulating endothelial cell Vegfa autocrine signaling. *Development* 141, 448–459. doi: 10.1242/dev.097949

Fernández-Hernando, C. (2013). Lymphatic vessels clean up your arteries. *J. Clin. Invest.* 123, 1417–1419. doi: 10.1172/JCI68657

Filiberti, A., Gmyrek, G. B., Montgomery, M. L., Sallack, R., and Carr, D. J. J. (2020). Loss of osteopontin expression reduces HSV-1-induced corneal opacity. *Invest. Ophthalmol. Vis. Sci.* 61:24. doi: 10.1167/iovs.61.10.24

Fligny, C., and Duffield, J. S. (2013). Activation of pericytes: recent insights into kidney fibrosis and microvascular rarefaction. *Curr. Opin. Rheumatol.* 25, 78–86. doi: 10.1097/BOR.0b013e32835b656b

Fogt, F., Pascha, T. L., Zhang, P. J., Gausas, R. E., Rahemtulla, A., and Zimmerman, R. L. (2004). Proliferation of D2-40-expressing intestinal lymphatic vessels in the lamina propria in inflammatory bowel disease. *Int. J. Mol. Med.* 13, 211–214.

Folkman, J., Langer, R., Linhardt, R. J., Haudenschild, C., and Taylor, S. (1983). Angiogenesis inhibition and tumor regression caused by heparin or a heparin fragment in the presence of cortisone. *Science* 221, 719–725. doi: 10.1126/science.6192498

Franco, C. A., Jones, M. L., Bernabeu, M. O., Geudens, I., Mathivet, T., Rosa, A., et al. (2015). Dynamic endothelial cell rearrangements drive developmental vessel regression. *PLoS Biol.* 13:e1002125. doi: 10.1371/journal.pbio.1002125

Frenkel, N., Poghosyan, S., Alarcón, C. R., García, S. B., Queiroz, K., van den Bent, L., et al. (2021). Long-lived human lymphatic endothelial cells to study lymphatic biology and Lymphatic Vessel/Tumor Coculture in a 3D Microfluidic Model. *ACS Biomater. Sci. Eng.* 7, 3030–3042. doi: 10.1021/acsbiomaterials.0c01378

Gillot, L., Baudin, L., Rouaud, L., Kridelka, F., and Noël, A. (2021). The pre-metastatic niche in lymph nodes: formation and characteristics. *Cell. Mol. Life Sci.* 78, 5987–6002. doi: 10.1007/s00018-021-03873-z

Girling, J. E., and Rogers, P. A. W. (2005). Recent advances in endometrial angiogenesis research. *Angiogenesis* 8, 89–99. doi: 10.1007/s10456-005-9006-9

Goede, V., Schmidt, T., Kimmina, S., Kozian, D., and Augustin, H. G. (1998). Analysis of blood vessel maturation processes during cyclic ovarian angiogenesis. *Lab. Invest.* 78, 1385–1394.

Goligorsky, M. S. (2010). Microvascular rarefaction: the decline and fall of blood vessels. *Organogenesis* 6, 1–10. doi: 10.4161/org.6.1.10427

Gosain, A., Matthies, A. M., Dovi, J. V., Barbul, A., Gamelli, R. L., and DiPietro, L. A. (2006). Exogenous pro-angiogenic stimuli cannot prevent physiologic vessel regression. *J. Surg. Res.* 135, 218–225. doi: 10.1016/j.jss.2006.04.006

Gur-Cohen, S., Yang, H., Baksh, S. C., Miao, Y., Levorse, J., Kataru, R. P., et al. (2019). Stem cell–driven lymphatic remodeling coordinates tissue regeneration. *Science* 366, 1218–1225. doi: 10.1126/science.aay4509

Han, L., Su, W., Huang, J., Zhou, J., Qiu, S., and Liang, D. (2014). Doxycycline inhibits inflammation-induced lymphangiogenesis in mouse cornea by multiple mechanisms. *PLoS One* 9:e108931. doi: 10.1371/journal.pone.0108931

Hassanein, A. H., Sinha, M., Neumann, C. R., Mohan, G., Khan, I., and Sen, C. K. (2021). A murine tail lymphedema model. *J. Vis. Exp.* 168:10.3791/61848. doi: 10.3791/61848

He, Y., Kozaki, K., Karpanen, T., Koshikawa, K., Yla-Herttuala, S., Takahashi, T., et al. (2002). Suppression of tumor lymphangiogenesis and lymph node metastasis by blocking vascular endothelial growth factor receptor 3 signaling. *J. Natl. Cancer Inst.* 94, 819–825. doi: 10.1093/jnci/94.11.819

Hirakawa, S., Kodama, S., Kunstfeld, R., Kajiya, K., Brown, L. F., and Detmar, M. (2005). VEGF-A induces tumor and sentinel lymph node lymphangiogenesis and promotes lymphatic metastasis. *J. Exp. Med.* 201, 1089–1099. doi: 10.1084/jem.20041896

Holash, J., Maisonpierre, P. C., Compton, D., Boland, P., Alexander, C. R., Zagzag, D., et al. (1999). Vessel cooption, regression, and growth in tumors mediated by Angiopoietins and VEGF. *Science* 284, 1994–1998. doi: 10.1126/science.284.5422.1994

Hou, Y., Bock, F., Hos, D., and Cursiefen, C. (2021). Lymphatic trafficking in the eye: modulation of lymphatic trafficking to promote corneal transplant survival. *Cells* 10:1661. doi: 10.3390/cells10071661

Hou, Y., Le, V. N. H., Clahsen, T., Schneider, A.-C., Bock, F., and Cursiefen, C. (2017). Photodynamic therapy leads to time-dependent regression of pathologic corneal (Lymph) angiogenesis and promotes high-risk corneal allograft survival. *Invest. Ophthalmol. Visual Sci.* 58, 5862–5869. doi: 10.1167/iovs.17-22904

Hou, Y., Le, V. N. H., Tóth, G., Siebelmann, S., Horstmann, J., Gabriel, T., et al. (2018). UV light crosslinking regresses mature corneal blood and lymphatic vessels and promotes subsequent high-risk corneal transplant survival. *Am. J. Transpl.* 18, 2873–2884. doi: 10.1111/ajt.14874

Houssari, M., Dumesnil, A., Tardif, V., Kivela, R., Pizzinat, N., Boukhalfa, I., et al. (2020). Lymphatic and immune cell cross-talk regulates cardiac recovery after experimental myocardial infarction. *Arterioscler. Thromb. Vasc. Biol.* 40, 1722–1737. doi: 10.1161/ATVBAHA.120.314370

Huang, L.-H., Elvington, A., and Randolph, G. J. (2015). The role of the lymphatic system in cholesterol transport. *Front. Pharmacol.* 6:182. doi: 10.3389/fphar.2015.00182

Hurle, J. M., Colvee, E., and Fernandez-Teran, M. A. (1985). Vascular regression during the formation of the free digits in the avian limb bud: a comparative study in chick and duck embryos. *J. Embryol. Exp. Morphol.* 85, 239–250.

Irani, Y. D., Scotney, P. D., Klebe, S., Mortimer, L. A., Nash, A. D., and Williams, K. A. (2017). An Anti-VEGF-B antibody fragment induces regression of pre-existing blood vessels in the rat Cornea. *Invest. Ophthalmol. Vis. Sci.* 58, 3404–3413. doi: 10.1167/iovs.16-21343

Ito, M., and Yoshioka, M. (1999). Regression of the hyaloid vessels and pupillary membrane of the mouse. *Anat. Embryol.* 200, 403–411. doi: 10.1007/s004290050289

Iyer, D., Jannaway, M., Yang, Y., and Scallan, P. J. (2020). Lymphatic valves and lymph flow in cancer-related lymphedema. *Cancers* 12:2297. doi: 10.3390/cancers12082297

Ji, R.-C. (2014). Hypoxia and lymphangiogenesis in tumor microenvironment and metastasis. *Cancer Lett.* 346, 6–16. doi: 10.1016/j.canlet.2013.12.001

Johnson, A., and DiPietro, L. A. (2013). Apoptosis and angiogenesis: an evolving mechanism for fibrosis. *FASEB J.* 27, 3893–3901. doi: 10.1096/fj.12-214189

Johnson, L. A. (2021). In Sickness and in Health: the immunological roles of the lymphatic system. *Int. J. Mol. Sci.* 22:4458. doi: 10.3390/ijms22094458

Jurisic, G., Sundberg, J. P., and Detmar, M. (2013). Blockade of VEGF receptor-3 aggravates inflammatory bowel disease and lymphatic vessel enlargement. *Inflamm. Bowel Dis.* 19, 1983–1989. doi: 10.1097/MIB.0b013e31829292f7

Karpanen, T., Egeblad, M., Karkkainen, M. J., Kubo, H., Yla-Herttuala, S., Jaattela, M., et al. (2001). Vascular endothelial growth factor C promotes tumor lymphangiogenesis and intralymphatic tumor growth. *Cancer Res.* 61, 1786–1790.

Kataru, R. P., Kim, H., Jang, C., Choi, D. K., Koh, B. I., Kim, M., et al. (2011). T lymphocytes negatively regulate lymph node lymphatic vessel formation. *Immunity* 34, 96–107. doi: 10.1016/j.immuni.2010.12.016

Kelley, P. M., Steele, M. M., and Tempero, R. M. (2011). Regressed lymphatic vessels develop during corneal repair. *Lab. Invest.* 91, 1643–1651. doi: 10.1038/labinvest.2011.121

Kerjaschki, D., Regele, H. M., Moosberger, I., Nagy-Bojarski, K., Watschinger, B., Soleiman, A., et al. (2004). Lymphatic Neoangiogenesis in human kidney transplants is associated with immunologically active lymphocytic infiltrates. *J. Am. Soc. Nephrol.* 15, 603–612. doi: 10.1097/01.ASN.0000113316.52371.2E

Keshet, E. (2003). Preventing pathological regression of blood vessels. *J. Clin. Invest.* 112, 27–29. doi: 10.1172/JCI200319093

Kesler, C. T., Liao, S., Munn, L. L., and Padera, T. P. (2013). Lymphatic vessels in health and disease. *Wiley Interdiscip. Rev. Syst. Biol. Med.* 5, 111–124. doi: 10.1002/wsbm.1201

Khromova, N., Kopnin, P., Rybko, V., and Kopnin, B. P. (2012). Downregulation of VEGF-C expression in lung and colon cancer cells decelerates tumor growth and inhibits metastasis via multiple mechanisms. *Oncogene* 31, 1389–1397. doi: 10.1038/onc.2011.330

Kim, H., Kataru, R. P., and Koh, G. Y. (2014). Inflammation-associated lymphangiogenesis: a double-edged sword? *J. Clin. Invest.* 124, 936–942. doi: 10.1172/JCI71607

Kim, J. H., Kim, J. H., Yu, Y. S., Mun, J. Y., and Kim, K.-W. (2010). Autophagy-induced regression of hyaloid vessels in early ocular development. *Autophagy* 6, 922–928. doi: 10.4161/auto.6.8.13306

Kong, D. H., Kim, M. R., Jang, J. H., Na, H. J., and Lee, S. (2017). A review of anti-angiogenic targets for monoclonal antibody cancer therapy. *Int. J. Mol. Sci.* 18:1786. doi: 10.3390/ijms18081786

Korn, C., and Augustin, H. G. (2015). Mechanisms of vessel pruning and regression. *Dev. Cell* 34, 5–17. doi: 10.1016/j.devcel.2015.06.004

Korn, C., Scholz, B., Hu, J., Srivastava, K., Wojtarowicz, J., Arnsperger, T., et al. (2014). Endothelial cell-derived non-canonical Wnt ligands control vascular pruning in angiogenesis. *Development* 141, 1757–1766. doi: 10.1242/dev.104422

Kowanetz, M., and Ferrara, N. (2006). Vascular endothelial growth factor signaling pathways: therapeutic perspective. *Clin. Cancer Res.* 12, 5018–5022. doi: 10.1158/1078-0432.CCR-06-1520

Landau, S., Newman, A., Edri, S., Michael, I., Ben-Shaul, S., Shandalov, Y., et al. (2021). Investigating lymphangiogenesis in vitro and in vivo using engineered human lymphatic vessel networks. *Proc. Natl. Acad. Sci. U.S.A.* 118:e2101931118. doi: 10.1073/pnas.2101931118

Le, V. N. H., Schneider, A. C., Scholz, R., Bock, F., and Cursiefen, C. (2018). Fine Needle-Diathermy Regresses Pathological Corneal (Lymph)Angiogenesis and Promotes High-Risk Corneal Transplant Survival. *Sci. Rep.* 8:5707. doi: 10.1038/s41598-018-24037-3

Lee, S., Chen, T. T., Barber, C. L., Jordan, M. C., Murdock, J., Desai, S., et al. (2007). Autocrine VEGF signaling is required for vascular homeostasis. *Cell* 130, 691–703. doi: 10.1016/j.cell.2007.06.054

Liao, S., and von der Weid, P.-Y. (2014). Inflammation-induced lymphangiogenesis and lymphatic dysfunction. *Angiogenesis* 17, 325–334. doi: 10.1007/s10456-014-9416-7

Lingen, M. W., Polverini, P. J., and Bouck, N. P. (1996). Retinoic acid induces cells cultured from oral squamous cell carcinomas to become anti-angiogenic. *Am. J. Pathol.* 149, 247–258.

Liu, X., De la Cruz, E., Gu, X., Balint, L., Oxendine-Burns, M., Terrones, T., et al. (2020). Lymphoangiocrine signals promote cardiac growth and repair. *Nature* 588, 705–711. doi: 10.1038/s41586-020-2998-x

Lobov, I. B., Cheung, E., Wudali, R., Cao, J., Halasz, G., Wei, Y., et al. (2011). The Dll4/Notch pathway controls postangiogenic blood vessel remodeling and regression by modulating vasoconstriction and blood flow. *Blood* 117, 6728–6737. doi: 10.1182/blood-2010-08-302067

Logie, J. J., Ali, S., Marshall, K. M., Heck, M. M., Walker, B. R., and Hadoke, P. W. (2010). Glucocorticoid-mediated inhibition of angiogenic changes in human endothelial cells is not caused by reductions in cell proliferation or migration. *PLoS One* 5:e14476. doi: 10.1371/journal.pone.0014476

Lohela, M., Bry, M., Tammela, T., and Alitalo, K. (2009). VEGFs and receptors involved in angiogenesis versus lymphangiogenesis. *Curr. Opin. Cell Biol.* 21, 154–165. doi: 10.1016/j.ceb.2008.12.012

Louveau, A., Smirnov, I., Keyes, T. J., Eccles, J. D., Rouhani, S. J., Peske, J. D., et al. (2015). Structural and functional features of central nervous system lymphatics. *Nature* 523, 337–341. doi: 10.1038/nature14432

Ma, Q., Ineichen, B. V., Detmar, M., and Proulx, S. T. (2017). Outflow of cerebrospinal fluid is predominantly through lymphatic vessels and is reduced in aged mice. *Nat. Commun.* 8:1434. doi: 10.1038/s41467-017-01484-6

Mäkinen, T., Jussila, L., Veikkola, T., Karpanen, T., Kettunen, M. I., Pulkkanen, K. J., et al. (2001). Inhibition of lymphangiogenesis with resulting lymphedema in transgenic mice expressing soluble VEGF receptor-3. *Nat. Med.* 7, 199–205. doi: 10.1038/84651

Martínez-Corral, I., Olmeda, D., Diéguez-Hurtado, R., Tammela, T., Alitalo, K., and Ortega, S. (2012). In vivo imaging of lymphatic vessels in development, wound healing, inflammation, and tumor metastasis. *Proc. Natl. Acad. Sci. U.S.A.* 109, 6223–6228. doi: 10.1073/pnas.1115542109

Michaelson, I. C., and Schreiber, H. (1956). Influence of low-voltage X-radiation on regression of established corneal vessels. *AMA Arch. Ophthalmol.* 55, 48–51. doi: 10.1001/archopht.1956.00930030050010

Miele, L., and Osborne, B. (1999). Arbiter of differentiation and death: Notch signaling meets apoptosis. *J. Cell. Physiol.* 181, 393–409. doi: 10.1002/(SICI)1097-4652(199912)181:3<393::AID-JCP3>3.0.CO;2-6

Monroy, M., McCarter, A. L., Hominick, D., Cassidy, N., and Dellinger, M. T. (2020). Lymphatics in bone arise from pre-existing lymphatics. *Development* 147:dev184291. doi: 10.1242/dev.184291

Mumprecht, V., Roudnicky, F., and Detmar, M. (2012). Inflammation-induced lymph node lymphangiogenesis is reversible. *Am. J. Pathol.* 180, 874–879. doi: 10.1016/j.ajpath.2011.11.010

Murakami, M. (2012). Signaling required for blood vessel maintenance: molecular basis and pathological manifestations. *Int. J. Vasc. Med.* 2012:293641. doi: 10.1155/2012/293641

Nagahashi, M., Ramachandran, S., Kim, E. Y., Allegood, J. C., Rashid, O. M., Yamada, A., et al. (2012). Sphingosine-1-phosphate produced by sphingosine kinase 1 promotes breast cancer progression by stimulating angiogenesis and lymphangiogenesis. *Cancer Res.* 72, 726–735. doi: 10.1158/0008-5472.CAN-11-2167

Nagahashi, M., Ramachandran, S., Rashid, O. M., and Takabe, K. (2010). Lymphangiogenesis: a new player in cancer progression. *World J. Gastroenterol.* 16, 4003–4012. doi: 10.3748/wjg.v16.i32.4003

Ocansey, D. K. W., Pei, B., Xu, X., Zhang, L., Olovo, C. V., and Mao, F. (2021). Cellular and molecular mediators of lymphangiogenesis in inflammatory bowel disease. *J. Transl. Med.* 19:254. doi: 10.1186/s12967-021-02922-2

Ogata, F., Fujiu, K., Matsumoto, S., Nakayama, Y., Shibata, M., Oike, Y., et al. (2016). Excess lymphangiogenesis cooperatively induced by macrophages and CD4(+) T Cells Drives the Pathogenesis of Lymphedema. *J. Invest. Dermatol.* 136, 706–714. doi: 10.1016/j.jid.2015.12.001

Oka, M., Iwata, C., Suzuki, H. I., Kiyono, K., Morishita, Y., Watabe, T., et al. (2008). Inhibition of endogenous TGF-beta signaling enhances lymphangiogenesis. *Blood* 111, 4571–4579. doi: 10.1182/blood-2007-10-120337

Okuda, K., Ng, M. F., Samat, N., Ruslan, N. F., Tan, P. J., and Patel, V. (2018). Identification and development of novel anti-lymphangiogenic compounds as cancer therapeutics. *Front. Pharmacol.* 9:122. doi: 10.3389/conf.fphar.2018.63.00122

Oliver, G., Kipnis, J., Randolph, G. J., and Harvey, N. L. (2020). The Lymphatic Vasculature in the 21st century: novel functional roles in homeostasis and disease. *Cell* 182, 270–296. doi: 10.1016/j.cell.2020.06.039

Padera, T. P., Kadambi, A., di Tomaso, E., Carreira, C. M., Brown, E. B., Boucher, Y., et al. (2002). Lymphatic metastasis in the absence of functional intratumor lymphatics. *Science* 296, 1883–1886. doi: 10.1126/science.1071420

Park, H. J., Yuk, C. M., Shin, K., and Lee, S. H. (2018). Interleukin-17A negatively regulates lymphangiogenesis in T helper 17 cell-mediated inflammation. *Mucosal Immunol.* 11, 590–600. doi: 10.1038/mi.2017.76

Parra, E. R., David, Y. R., Costa, L. R. S. D., Ab'Saber, A., Sousa, R., Kairalla, R. A., et al. (2005). Heterogeneous remodeling of lung vessels in idiopathic pulmonary fibrosis. *Lung* 183, 291–300. doi: 10.1007/s00408-004-2542-z

Patan, S. (2004). Vasculogenesis and angiogenesis. *Cancer Treat. Res.* 117, 3–32. doi: 10.1007/978-1-4419-8871-3_1

Petrova, T. V., and Koh, G. Y. (2020). Biological functions of lymphatic vessels. *Science* 369:eaax4063. doi: 10.1126/science.aax4063

Phillips, S., Kapp, M., Crowe, D., Garces, J., Fogo, A. B., and Giannico, G. A. (2016). Endothelial activation, lymphangiogenesis, and humoral rejection of kidney transplants. *Hum. Pathol.* 51, 86–95. doi: 10.1016/j.humpath.2015.12.020

Polichnowski, A. J. (2018). Microvascular rarefaction and hypertension in the impaired recovery and progression of kidney disease following AKI in preexisting CKD states. *Am. J. Physiol. Renal Physiol.* 315, F1513–F1518. doi: 10.1152/ajprenal.00419.2018

Rahier, J. F., De Beauce, S., Dubuquoy, L., Erdual, E., Colombel, J. F., Jouret-Mourin, A., et al. (2011). Increased lymphatic vessel density and lymphangiogenesis in inflammatory bowel disease. *Aliment. Pharmacol. Ther.* 34, 533–543. doi: 10.1111/j.1365-2036.2011.04759.x

Raica, M., Jitariu, A.-A., and Cimpean, A. M. (2016). Lymphangiogenesis and anti-lymphangiogenesis in cutaneous melanoma. *Anticancer Res.* 36, 4427–4435. doi: 10.21873/anticanres.10986

Rockson, S. G. (2001). Lymphedema. *Am. J. Med.* 110, 288–295.

Rosenson, R. S., Brewer, H. B., Davidson, W. S., Fayad, Z. A., Fuster, V., Goldstein, J., et al. (2012). Cholesterol Efflux and Atheroprotection. *Circulation* 125, 1905–1919. doi: 10.1161/CIRCULATIONAHA.111.066589

Royston, D., and Jackson, D. G. (2009). Mechanisms of lymphatic metastasis in human colorectal adenocarcinoma. *J. Pathol.* 217, 608–619. doi: 10.1002/path.2517

Saif, M. W., Knost, J. A., Chiorean, E. G., Kambhampati, S. R., Yu, D., Pytowski, B., et al. (2016). Phase 1 study of the anti-vascular endothelial growth factor receptor 3 monoclonal antibody LY3022856/IMC-3C5 in patients with advanced and refractory solid tumors and advanced colorectal cancer. *Cancer Chemother. Pharmacol.* 78, 815–824. doi: 10.1007/s00280-016-3134-3

Saito, Y., Nakagami, H., Kaneda, Y., and Morishita, R. (2013). Lymphedema and therapeutic lymphangiogenesis. *Biomed Res. Int.* 2013:804675. doi: 10.1155/2013/804675

Sajib, S., Zahra, F. T., Lionakis, M. S., German, N. A., and Mikelis, C. M. (2018). Mechanisms of angiogenesis in microbe-regulated inflammatory and neoplastic conditions. *Angiogenesis* 21, 1–14. doi: 10.1007/s10456-017-9583-4

Sandborn, W. J., Peyrin-Biroulet, L., Zhang, J., Chiorean, M., Vermeire, S., Lee, S. D., et al. (2020). Efficacy and safety of etrasimod in a phase 2 randomized trial of patients with ulcerative colitis. *Gastroenterology* 158, 550–561. doi: 10.1053/j.gastro.2019.10.035

Sato, Y., and Sonoda, H. (2007). The vasohibin family: a negative regulatory system of angiogenesis genetically programmed in endothelial cells. *Arterioscler. Thromb. Vasc. Biol.* 27, 37–41. doi: 10.1161/01.ATV.0000252062.48280.61

Savetsky, I. L., Ghanta, S., Gardenier, J. C., Torrisi, J. S., Garcia Nores, G. D., Hespe, G. E., et al. (2015). Th2 cytokines inhibit lymphangiogenesis. *PLoS One* 10:e0126908. doi: 10.1371/journal.pone.0126908

Schafer, C. M., Gurley, J. M., Kurylowicz, K., Lin, P. K., Chen, W., Elliott, M. H., et al. (2020). An inhibitor of endothelial ETS transcription factors promotes physiologic and therapeutic vessel regression. *Proc. Natl. Acad. Sci. U.S.A.* 117, 26494–26502. doi: 10.1073/pnas.2015980117

Schito, L. (2019). Hypoxia-dependent angiogenesis and lymphangiogenesis in cancer. *Adv. Exp. Med. Biol.* 1136, 71–85. doi: 10.1007/978-3-030-12734-3_5

Shao, X., and Liu, C. (2006). Influence of IFN- alpha and IFN- gamma on lymphangiogenesis. *J. Interferon Cytokine Res.* 26, 568–574. doi: 10.1089/jir.2006.26.568

Shi, M., Zhang, L., Ye, E.-A., Wang, A., Li, G., and Chen, L. (2020). Aqueous humor induces lymphatic regression on the ocular surface. *Ocular Surf.* 18, 505–510. doi: 10.1016/j.jtos.2020.03.002

Shin, K., Kataru, R. P., Park, H. J., Kwon, B. I., Kim, T. W., Hong, Y. K., et al. (2015). TH2 cells and their cytokines regulate formation and function of lymphatic vessels. *Nat. Commun.* 6:6196. doi: 10.1038/ncomms7196

Shirasuna, K., Kobayashi, A., Nitta, A., Nibuno, S., Sasahara, K., Shimizu, T., et al. (2012). Possible action of vasohibin-1 as an inhibitor in the regulation of vascularization of the bovine corpus luteum. *Reproduction* 143, 491–500. doi: 10.1530/REP-11-0465

Skobe, M., Hawighorst, T., Jackson, D. G., Prevo, R., Janes, L., Velasco, P., et al. (2001). Induction of tumor lymphangiogenesis by VEGF-C promotes breast cancer metastasis. *Nat. Med.* 7, 192–198. doi: 10.1038/84643

Stacker, S. A., Achen, M. G., Jussila, L., Baldwin, M. E., and Alitalo, K. (2002). Lymphangiogenesis and cancer metastasis. *Nat. Rev. Cancer* 2, 573–583. doi: 10.1038/nrc863

Stacker, S. A., Williams, S. P., Karnezis, T., Shayan, R., Fox, S. B., and Achen, M. G. (2014). Lymphangiogenesis and lymphatic vessel remodelling in cancer. *Nat. Rev. Cancer* 14, 159–172. doi: 10.1038/nrc3677

Steele, M. M., Kelley, P. M., Schieler, A. M., and Tempero, R. M. (2011). Glucocorticoids suppress corneal lymphangiogenesis. *Cornea* 30, 1442–1447. doi: 10.1097/ICO.0b013e318213f39f

Stritt, S., Koltowska, K., and Makinen, T. (2021). Homeostatic maintenance of the lymphatic vasculature. *Trends Mol. Med.* 27, 955–970. doi: 10.1016/j.molmed.2021.07.003

Szuba, A., Skobe, M., Karkkainen, M. J., Shin, W. S., Beynet, D. P., Rockson, N. B., et al. (2002). Therapeutic lymphangiogenesis with human recombinant VEGF-C. *FASEB J.* 16, 1985–1987. doi: 10.1096/fj.02-0401fje

Taher, M., Nakao, S., Zandi, S., Melhorn, M. I., Hayes, K. C., and Hafezi-Moghadam, A. (2016). Phenotypic transformation of intimal and adventitial lymphatics in atherosclerosis: a regulatory role for soluble VEGF receptor 2. *FASEB J.* 30, 2490–2499. doi: 10.1096/fj.201500112

Tammela, T., and Alitalo, K. (2010). Lymphangiogenesis: molecular mechanisms and future promise. *Cell* 140, 460–476. doi: 10.1016/j.cell.2010.01.045

Tarasoff-Conway, J. M., Carare, R. O., Osorio, R. S., Glodzik, L., Butler, T., Fieremans, E., et al. (2015). Clearance systems in the brain-implications for Alzheimer disease. *Nat. Rev. Neurol.* 11, 457–470. doi: 10.1038/nrneurol.2015.119

Terry, T. L. (1942). Fibroblastic Overgrowth of Persistent Tunica Vasculosa Lentis in Infants Born Prematurely*: III. Studies in development and regression of hyaloid artery and tunica vasculosa lentis. *Am. J. Ophthalmol.* 25, 1409–1423. doi: 10.1016/s0002-9394(42)91858-0

Tomita, T., and Mah K. (2014). Cyclic changes of lymphatic vessels in human endometrium. *Open J. Pathol.* 04, 5–12. doi: 10.4236/ojpathology.2014.41002

Trivedi, A., Zhang, H., Ekeledo, A., Lee, S., Werb, Z., Plant, G. W., et al. (2016). Deficiency in matrix metalloproteinase-2 results in long-term vascular instability and regression in the injured mouse spinal cord. *Exp. Neurol.* 284(Pt A), 50–62. doi: 10.1016/j.expneurol.2016.07.018

Truman, L. A., Bentley, K. L., Smith, E. C., Massaro, S. A., Gonzalez, D. G., Haberman, A. M., et al. (2012). ProxTom lymphatic vessel reporter mice reveal Prox1 expression in the adrenal medulla, megakaryocytes, and platelets. *Am. J. Pathol.* 180, 1715–1725. doi: 10.1016/j.ajpath.2011.12.026

Vaahtomeri, K., and Alitalo, K. (2020). Lymphatic vessels in tumor dissemination versus immunotherapy. *Cancer Res.* 80, 3463–3465. doi: 10.1158/0008-5472.CAN-20-0156

Vourakis, M., Mayer, G., and Rousseau, G. (2021). The role of gut microbiota on cholesterol metabolism in atherosclerosis. *Int. J. Mol. Sci.* 22:8074. doi: 10.3390/ijms22158074

Wang, Z., Liu, C.-H., Huang, S., and Chen, J. (2019a). Assessment and characterization of hyaloid vessels in mice. *J. Vis. Exp.* 147:10.3791/59222. doi: 10.3791/59222

Wang, Z., Liu, C.-H., Huang, S., and Chen, J. (2019b). Wnt signaling in vascular eye diseases. *Prog. Retin. Eye Res.* 70, 110–133. doi: 10.1016/j.preteyeres.2018.11.008

Watanabe, K., Hasegawa, Y., Yamashita, H., Shimizu, K., Ding, Y., Abe, M., et al. (2004). Vasohibin as an endothelium-derived negative feedback regulator of angiogenesis. *J. Clin. Invest.* 114, 898–907. doi: 10.1172/JCI21152

Watson, E. C., Grant, Z. L., and Coultas, L. (2017). Endothelial cell apoptosis in angiogenesis and vessel regression. *Cell. Mol. Life Sci.* 74, 4387–4403. doi: 10.1007/s00018-017-2577-y

Weiler, M. J., Cribb, M. T., Nepiyushchikh, Z., Nelson, T. S., and Dixon, J. B. (2019). A novel mouse tail lymphedema model for observing lymphatic pump failure during lymphedema development. *Sci. Rep.* 9:10405. doi: 10.1038/s41598-019-46797-2

Welti, J., Loges, S., Dimmeler, S., and Carmeliet, P. (2013). Recent molecular discoveries in angiogenesis and antiangiogenic therapies in cancer. *J. Clin. Invest.* 123, 3190–3200. doi: 10.1172/JCI70212

Wietecha, M. S., Chen, L., Ranzer, M. J., Anderson, K., Ying, C., Patel, T. B., et al. (2011). Sprouty2 downregulates angiogenesis during mouse skin wound healing. *Am. J. Physiol. Heart Circ. Physiol.* 300, H459–H467. doi: 10.1152/ajpheart.00244.2010

Wilting, J., Hawighorst, T., Hecht, M., Christ, B., and Papoutsi, M. (2005). Development of lymphatic vessels: tumour lymphangiogenesis and lymphatic invasion. *Curr. Med. Chem.* 12, 3043–3053. doi: 10.2174/0929867057749 33407

Wong, B. W. (2020). Lymphatic vessels in solid organ transplantation and immunobiology. *Am. J. Transplant.* 20, 1992–2000. doi: 10.1111/ajt.15806

Yamakawa, M., Doh, S. J., Santosa, S. M., Montana, M., Qin, E. C., Kong, H., et al. (2018). Potential lymphangiogenesis therapies: learning from current anti-angiogenesis therapies - A review. *Med. Res. Rev.* 38, 1769–1798. doi: 10.1002/med.21496

Yao, L.-C., Testini, C., Tvorogov, D., Anisimov, A., Vargas, S. O., Baluk, P., et al. (2014). Pulmonary Lymphangiectasia resulting from vascular endothelial growth factor-C overexpression during a critical period. *Circ. Res.* 114, 806–822. doi: 10.1161/CIRCRESAHA.114.303119

Ye, Y., Pang, Z., Chen, W., Ju, S., and Zhou, C. (2015). The epidemiology and risk factors of inflammatory bowel disease. *Int. J. Clin. Exp. Med.* 8, 22529–22542.

Zhang, H., Hu, X., Tse, J., Tilahun, F., Qiu, M., and Chen, L. (2011). Spontaneous lymphatic vessel formation and regression in the Murine Cornea. *Invest. Ophthalmol. Vis. Sci.* 52, 334–338. doi: 10.1167/iovs. 10-5404

Zhang, L., Ocansey, D. K. W., Liu, L., Olovo, C. V., Zhang, X., Qian, H., et al. (2021). Implications of lymphatic alterations in the pathogenesis and treatment of inflammatory bowel disease. *Biomed. Pharmacother.* 140:111752. doi: 10. 1016/j.biopha.2021.111752

Zhong, W., Gao, X., Wang, S., Han, K., Ema, M., Adams, S., et al. (2017). Prox1-GFP/Flt1-DsRed transgenic mice: an animal model for simultaneous live imaging of angiogenesis and lymphangiogenesis. *Angiogenesis* 20, 581–598. doi: 10.1007/s10456-017-9572-7

Zhou, C., Su, W., Han, H., Li, N., Ma, G., and Cui, L. (2020). Mouse tail models of secondary lymphedema: fibrosis gradually worsens and is irreversible. *Int. J. Clin. Exp. Pathol.* 13, 54–64.

Zhu, M., Madigan, M. C., van Driel, D., Maslim, J., Billson, F. A., Provis, J. M., et al. (2000). The human hyaloid system: cell death and vascular regression. *Exp. Eye Res.* 70, 767–776. doi: 10.1006/exer.2000.0844

Zou, W., Pu, T., Feng, W., Lu, M., Zheng, Y., Du, R., et al. (2019). Blocking meningeal lymphatic drainage aggravates Parkinson's disease-like pathology in mice overexpressing mutated alpha-synuclein. *Transl. Neurodegener.* 8:7. doi: 10.1186/s40035-019-0147-y

GLOSSARY

AAV-VEGF-C, adeno-associated virus encoding VEGF-C; a-MSH, alpha-melanocyte-stimulating hormone; ANG2, angiopoietin-2; APCs, antigen-presenting cells; bFGF, basic fibroblast growth factor; BMI-1, B lymphoma Mo-MLV insertion region 1 homolog; BV, blood vessel; CCL21, chemokine (C-C motif) ligand 21; CCSP-rtTA; Clara cell secretory protein reverse tetracycline-controlled transactivator; CD31, cluster of differentiation 31; Celsr1, cadherin EGF LAG seven-pass G-type receptor 1; CRIM1, cysteine-rich transmembrane BMP regulator 1; CSF, cerebrospinal fluid; CXCL10, C-X-C motif chemokine ligand 10; CXCR3, C-X-C motif chemokine receptor 3; DLL4, Delta-like canonical Notch ligand 4; E15, embryonic day 15; ETS, transcription factor E26 transformation–specific sequence; Fas, Fas cell surface death receptor; Fat4, FAT tumor suppressor homolog 4; FGF2, fibroblast growth factor 2; Foxc2, Forkhead box C2; Gata2, transcription factor binds to the DNA sequence "GATA"; HDL, high-density lipoprotein; HEY, Hairy/enhancer-of-split related with YRPW motif protein; HIF-1, hypoxia-inducible factor 1; IA, intussusceptive angiogenesis; IL-13, interleukin 13; LEC, lymphatic endothelial cell; LV, lymphatic vessel; LYVE-1, lymphatic vessel endothelial hyaluronan receptor 1; Nrp1, neuropilin 1; PDGF, platelet-derived growth factor; PDGFR-α/β, platelet-derived growth factor receptor; PIK3CA, phosphatidylinositol-4,5-bisphosphate 3-kinase catalytic subunit alpha; Pkd1, polycystic kidney disease 1; Prox-1, prospero-related homeobox 1; ROP, retinopathy of prematurity; SA, sprouting angiogenesis; Sema3a, semaphoring 3a; TGF-β, transforming growth factor beta; TIE, tyrosine kinase with immunoglobulin-like and EGF-like domains; TLOs, tertiary lymphatic organs; TSP-1, thrombospondin-1; Vangl2, VANGL planar cell polarity protein2; VEC, vascular endothelial cell; VEGF-A, vascular endothelial growth factor A; VEGF-B, vascular endothelial growth factor B; VEGFR-1/2, vascular endothelial growth factor receptor 1/2; VEGFR-3, vascular endothelial growth factor receptor 3; VIP, vasoactive intestinal peptide; vWF, von Willebrand factor.

Check for
updates

Carotid Reservoir Pressure Decrease After Prolonged Head Down Tilt Bed Rest in Young Healthy Subjects Is Associated With Reduction in Left Ventricular Ejection Time and Diastolic Length

Carlo Palombo[1]*, Michaela Kozakova[2], Carmela Morizzo[1], Lorenzo Losso[3], Massimo Pagani[4], Paolo Salvi[5], Kim H. Parker[6] and Alun D. Hughes[7]

[1]Department of Surgical, Medical, Molecular Pathology and Critical Area Medicine, University of Pisa, Pisa, Italy, [2]Department of Clinical and Experimental Medicine, University of Pisa, Pisa, Italy, [3]Department of Medical Toxicology Unit and Poison Control Centre, Careggi University Hospital, Florence, Italy, [4]Department of Medicine, University of Milan, Milan, Italy, [5]Department of Cardiology, Istituto Auxologico Italiano, IRCCS, Milan, Italy, [6]Department of Bioengineering, Imperial College London, London, United Kingdom, [7]Department of Population Science and Experimental Medicine, University College of London, London, United Kingdom

Background: The arterial pressure waveform reflects the interaction between the heart and the arterial system and carries potentially relevant information about circulatory status. According to the commonly accepted 'wave transmission model', the net BP waveform results from the super-position of discrete forward and backward pressure waves, with the forward wave in systole determined mainly by the left ventricular (LV) ejection function and the backward by the wave reflection from the periphery, the timing and amplitude of which depend on arterial stiffness, the wave propagation speed and the extent of downstream admittance mismatching. However, this approach obscures the 'Windkessel function' of the elastic arteries. Recently, a 'reservoir-excess pressure' model has been proposed, which interprets the arterial BP waveform as a composite of a volume-related 'reservoir' pressure and a wave-related 'excess' pressure.

Methods: In this study we applied the reservoir-excess pressure approach to the analysis of carotid arterial pressure waveforms (applanation tonometry) in 10 young healthy volunteers before and after a 5-week head down tilt bed rest which induced a significant reduction in stroke volume (SV), end-diastolic LV volume and LV longitudinal function without significant changes in central blood pressure, cardiac output, total peripheral resistance and aortic stiffness. Forward and backward pressure components were also determined by wave separation analysis.

Results: Compared to the baseline state, bed rest induced a significant reduction in LV ejection time (LVET), diastolic time (DT), backward pressure amplitude (bP) and pressure reservoir integral (INTPR). INTPR correlated directly with LVET, DT, time to the peak of

backward wave (bT) and stroke volume, while excess pressure integral (INTXSP) correlated directly with central pressure. Furthermore, Δ.INTPR correlated directly with Δ.LVET, and Δ.DT, and in multivariate analysis INTPR was independently related to LVET and DT and INTXSP to central systolic BP.

Conclusion: This is an hypothesis generating paper which adds support to the idea that the reservoir-wave hypothesis applied to non-invasively obtained carotid pressure waveforms is of potential clinical usefulness.

Keywords: head-down tilt bed rest, arterial pressure waveform, reservoir pressure, excess pressure, forward pressure wave, backward pressure wave, Windkessel function, systemic haemodynamics

INTRODUCTION

The arterial blood pressure (BP) waveform reflects the complex interaction between the heart and the arterial system and carries potentially relevant information about circulatory status (Mynard et al., 2020). According to the commonly accepted 'wave transmission model', the net BP waveform results from the super-position of discrete forward (incident) and backward (reflected) traveling pressure waves, with the forward wave in systole determined mainly by the left ventricular (LV) ejection function and the backward wave by the wave reflection from the periphery, the timing and amplitude of which depend on arterial stiffness, the wave propagation speed and the extent of downstream admittance mismatching (Westerhof et al., 1972). This approach, however, obscures the cushioning effect of the elastic arteries, the reservoir function (commonly referred to as the 'Windkessel function'). It is also worth noting that variables derived from pressure waveform analysis based solely upon the wave transmission model, while predicting cardiovascular events, give little information about arterial function (Westerhof and Westerhof, 2013).

More recently Wang et al. described a mathematical model which includes the 'Windkessel' function in shaping the central arterial waveform, combining the wave-only theory (which explains the steep systolic pressure upstroke) with the arterial reservoir, which accounts for the diastolic decline (Wang et al., 2003).

This alternative model has been termed as 'reservoir-wave' or 'reservoir-excess pressure' (Davies et al., 2007) and interprets arterial BP waveform as a composite of a volume-related, 'reservoir' pressure, and a wave-related 'excess' pressure which, in turn, can be decomposed into incident and reflected waves (Hughes et al., 2012).

The model has been recently refined, highlighting the concept that both the reservoir and excess pressure are wave phenomena (Hughes and Parker, 2020).

Reservoir pressure has been shown to be highly correlated with changes in proximal aortic volume in the dog

---

(Wang et al., 2003) as well as in man (Schultz et al., 2014), confirming the hypothesis that it represents the cyclic volume increase and decrease during systole and diastole, i.e., of aortic distension and recoil. The aortic reservoir pressure is proportional to the volume of blood stored in the aorta, which in turns depends on the compliance of the aorta and the impedance to outflow (Davies et al., 2010). The 'excess' pressure is defined as the difference between the measured and the reservoir pressure and it is assumed to be the result of local waves (Parker et al., 2012). Consequently, the central BP during systole can be considered to be the result of forward wave propagation (as result of LV ejection) and the proximal aortic reservoir function (Davies et al., 2010), while the reservoir pressure will account for almost all the pressure recorded in diastole (Alastruey, 2010).

Despite a growing body of evidence indicating that the reservoir-excess pressure model may provide physiological and clinical insights above and beyond standard BP and pulse waveform analysis (Armstrong et al., 2021) and explain some unsolved issues of the simple wave propagation model, such as the presence of a definite diastolic component of the pressure waveform when net wave travel is close to zero (Parker, 2013), the clinical usefulness of the reservoir-wave paradigm is still debated (Segers et al., 2012).

Beyond some methodological reservations, recently overcome (Hughes and Parker, 2020), a main limitation of this approach for extended clinical use was that it initially required measurement of aortic flow to calculate reservoir pressure in systole. The development of an algorithm which enables reservoir pressure to be calculated from any pressure waveform alone (Michail et al., 2018) opens new horizons to the investigation of the reservoir-excess pressure model in the clinical setting.

In the present study, we applied the reservoir-excess pressure approach to the analysis of carotid arterial pressure waveforms in young healthy volunteers before and after prolonged bed rest which, as we have previously reported, induced a significant reduction in stroke volume (SV), end-diastolic LV volume and LV longitudinal function without significant changes in central blood pressure, cardiac output, total peripheral resistance and aortic stiffness (Kozàkovà et al., 2011; Palombo et al., 2015). In this model, we reassessed arterial pressure waveforms derived by applanation tonometry together with echocardiographic data in order to evaluate the haemodynamic

---

Abbreviations: BP, Blood pressure; cf-PWV, Carotid–femoral pulse wave velocity; AIx, Augmentation index; Pi, Pressure at the inflection point; LVET, Left ventricular ejection time; DT, Diastolic time; fP, Forward wave pressure amplitudes; bP, Backward wave pressure amplitudes; fT, Time to the forward wave; bT, Time to the backward pressure wave; TAC, Total arterial compliance.

determinants of the aortic reservoir and excess pressure components.

MATERIALS AND METHODS

Study Population

Ten healthy young volunteers, all men, mean age 23 ± 2 years, were enrolled in a bed rest study endorsed by the Italian Space Agency (ASI) and taking place at the Orthopedic Hospital Valdoltra, Ankaran, Slovenia. None of the volunteers was a smoker. Medical history, physical examination, laboratory examinations, resting and stress ECG and echocardiography have excluded any acute or chronic medical problem. The National Committee for Medical Ethics of the Slovene Ministry of Health (Ljubljana, Slovenia) approved the study. All participants were informed about the aim of the investigation, the procedures and the methods and signed a written informed consent form according to the Declaration of Helsinki.

Study Protocol

All participants underwent a 5-week period of bed rest in a 6°-head down tilt position (HDTBR). The study design and protocol were previously reported in detail (Kozàkovà et al., 2011; Palombo et al., 2015). Cardiac ultrasound, carotid applanation tonometry and carotid–femoral pulse wave velocity (cf-PWV) were performed the day before entering bed rest and within 24 h after its termination. All the examinations were performed by a single operator (CM) in a quiet room, 3 h after a light breakfast and, in case of post-bed rest examination, after an acclimatisation period of 30 min in a supine position.

Cardiac and Vascular Measurements

Cardiac ultrasound was performed as previously described (Kozàkovà et al., 2011). Stroke volume was measured as a product of aortic area and flow velocity integral in the aortic orifice (Lewis et al., 1984). Total arterial compliance (TAC) was estimated as the ratio of stroke volume to central pulse pressure (SV/cPP; Liu et al., 1986). Results on changes in LV volume mass, performance and loading conditions observed in the same study group were previously published in detail (Kozàkovà et al., 2011). Cf-PWV was measured according to current guidelines (Reference Values for Arterial Stiffness' Collaboration, 2010) using the Complior SP device (Alam Medical, Vincennes, France). Briefly, arterial waveforms were obtained transcutaneously over the right common carotid artery (CCA) and the femoral artery, and the time delay (t) was measured between the feet of the two waveforms. The distance (D) covered by the waves was established as the distance between the two recording sites. Cf-PWV was then calculated as D (meters)/t (seconds). The measurement was repeated three times and the mean value was used for statistical analysis.

Simultaneous BP measurement was performed at the left brachial artery (Omron, Kyoto, Japan).

Carotid applanation tonometry was performed on the right CCA using a PulsePen device (DiaTecne, San Donato Milanese, Italy; Salvi et al., 2004). Carotid pressure waveforms were calibrated according to brachial mean and diastolic pressure as previously described (Van Bortel et al., 2001). For each study, three consecutive acquisitions of 10 cardiac beats were performed, and the mean of three ensemble-averaged cycles was used for statistical analysis. The ensemble-averaged carotid pressure waveform was also decomposed into a forward and backward pressure wave (fP and bP, respectively), as previously described (Qasem and Avolio, 2008). From the carotid pressure waveform, the following parameters were measured, without the application of a generalised transfer function: local systolic BP, local pulse pressure, augmentation index (AIx), pressure at the inflection point (Pi), left ventricular ejection time (LVET), diastolic time (DT), R–R interval, forward and backward wave pressure amplitudes (fP and bP, respectively) and time to the forward and backward pressure wave peak (fT and bT, respectively).

Reservoir and Excess Pressure Analysis

Reservoir and excess pressure parameters were calculated based on a pressure-alone approach from the ensemble-averaged carotid pressure waveforms, which can be separated in a reservoir pressure component and an excess pressure component, represented by the difference between the measured pressure waveform and the reservoir pressure (Michail et al., 2018). For analysis in this study, we used the integrals of the reservoir pressure curves (INTPR) and excess pressure curves (INTXSP).

Statistical Analysis

Quantitative data are expressed as mean $\pm$ SD or number (%). Skewed data (AIx) are expressed as median [interquartile range] and were log-transformed for statistical analysis. A paired t-test was used to compare the measurements before and after bed rest. Linear correlation analysis was used to evaluate the associations of INTPR, INTXPR, fP, bP, cf-PWV and TAC with systemic haemodynamics parameters. A multivariate analysis was performed to evaluate the independent determinants of INTPR, INTXPR, fP, bP. All analyses were adjusted for study phase, age and anthropometric data. Statistical analysis was performed by JMP software, version 16.0.0 (SAS Institute Inc., Cary, North Carolina, United States), and statistical significance was set at a value of <0.05.

RESULTS

Impact of Bed Rest on Carotid Pressure Waveform, Systemic Haemodynamics, Regional and Systemic Stiffness

Data obtained by applanation tonometry, echocardiography and carotid–femoral pulse wave measurements are reported in **Table 1**. When compared to the baseline state, bed rest induced a significant reduction in R–R interval, LVET, DT, fT and bP,

TABLE 1 | Haemodynamic data obtained by applanation tonometry, echocardiography and carotid–femoral pulse wave velocity measurements before and after the bed rest.

	Before bed rest	After bed rest	p
BMI (kg/m^2)	23.3 ± 2.0	22.8 ± 1.6	<0.05
Central systolic BP (mmHg)	106 ± 12	101 ± 7	ns
Central pulse pressure (mmHg)	43 ± 11	36 ± 7	ns
Heart rate (bpm)	59 ± 8	71 ± 8	<0.0001
R–R (ms)	1,030 ± 171	851 ± 78	<0.01
LVET (ms)	305 ± 20	292 ± 11	<0.05
DT (ms)	723 ± 158	559 ± 75	<0.01
AIx (%)	2.0 [8.1]	2.1 [8.5]	ns
Pi (mmHg)	104 ± 13	100 ± 6	ns
fP (mmHg)	42.1 ± 12.3	35.1 ± 7.1	0.06
bP (mmHg)	13.0 ± 2.9	10.8 ± 2.3	0.05
fT (ms)	102 ± 25	90 ± 12	<0.05
bT (ms)	316 ± 86	268 ± 33	ns
INTPR (kPa*s)	10.6 ± 1.7	9.0 ± 1.3	<0.01
INTXSP (kPa*s)	0.77 ± 0.28	0.64 ± 0.25	ns
End-diastolic LV volume (ml)	144 ± 15	131 ± 18	<0.005
EF (%)	58 ± 3	57 ± 4	ns
Stroke volume (ml)	74 ± 10	62 ± 8	<0.01
Cardiac output (L/min)	4.6 ± 0.8	4.5 ± 0.6	ns
TAC (ml/mmHg)	1.85 ± 0.55	1.72 ± 0.32	ns
cf-PWV (m/ss)	6.9 ± 1.0	6.6 ± 0.8	ns

a non-significant decrease in fP as well in central BP and no changes in AIx, cf-PWV, TAC. Bed rest also significantly decreased INTPR, while the reduction of INTXSP was only mild and non-significant.

Figure 1 shows an example of net, reservoir and excess pressure before and after bed rest. Within the echocardiographic parameters, stroke volume decreased with bed rest, while cardiac output did not change due to the increase in heart rate.

Univariate Correlations

Table 2 shows correlation coefficients of the associations between INTPR, INTXSP, fP, bP, TAC, cf-PWV and the systemic haemodynamics, echocardiographic data, systolic and diastolic times. In analyses were included data obtained both before and after bed rest ($N = 20$). Values reported are after adjustment for study phase. INTPR correlated directly with R–R interval, LVET, DT, stroke volume and TAC. INTXSP correlated directly with central pressure, systolic and pulse, Pi and fP and inversely with TAC. Backward pressure amplitude correlated directly with R–R interval, DT, forward pressure amplitude and stroke volume. TAC correlated directly with time to the forward pressure peak, while direct correlations were found for cf-PWV with stroke volume and TAC.

The relationships between bed rest related changes (delta) in different parameters were also evaluated. Delta INTPR correlated directly with delta LVET ($r = 0.85$; $p < 0.005$) and delta DT ($r = 0.68$; $p < 0.05$). Delta fP correlated with delta bP ($r = 0.81$; $p < 0.005$) as well as with change in central pulse pressure ($r = 0.82$; $p < 0.005$).
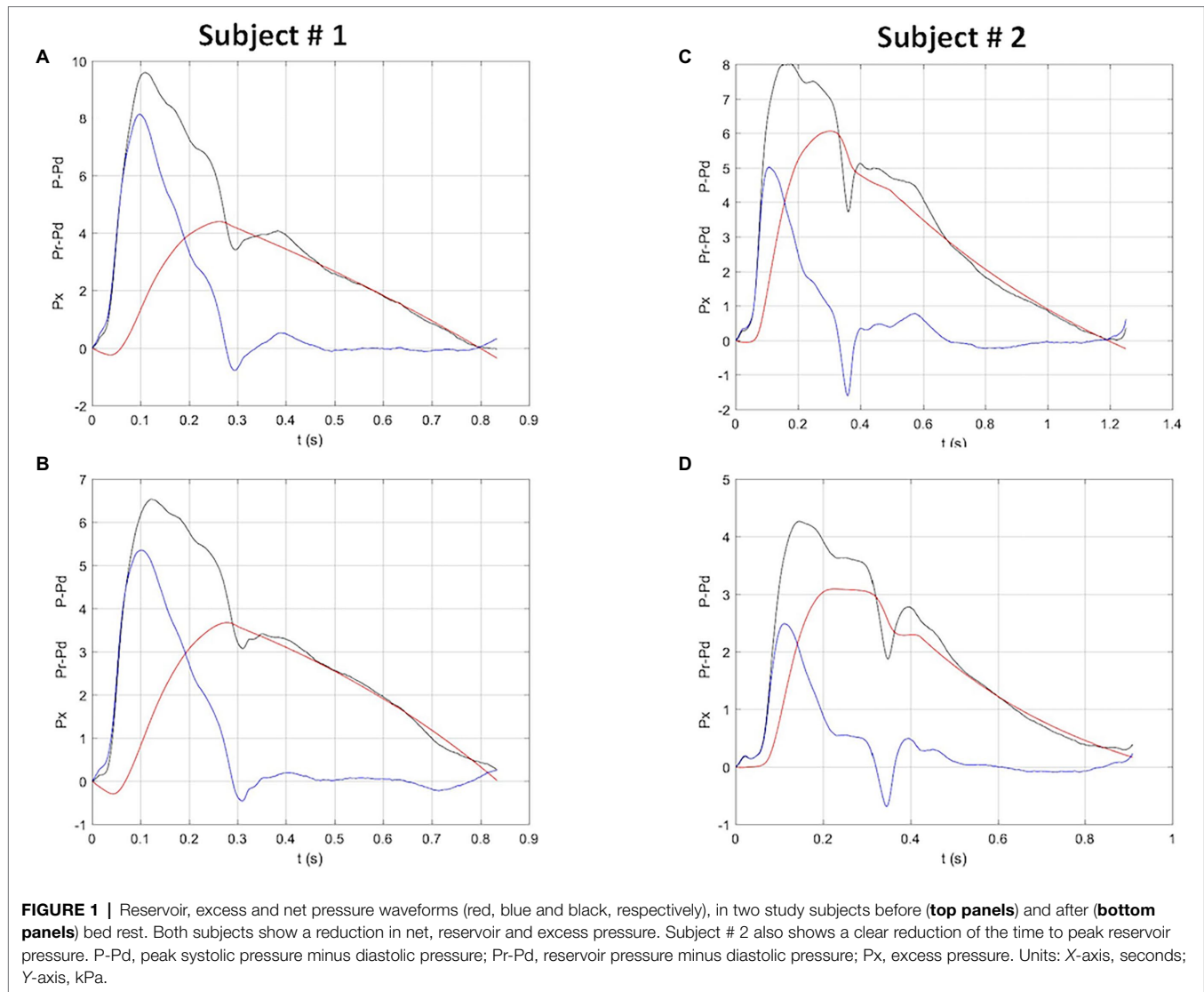
Multivariate Analysis

Table 3 demonstrates independent determinants of INTPR, INTXSP, wave pressure amplitudes and aortic stiffness. INTPR was independently related to LVET and DT and INTXSP to central systolic BP. The only independent predictor of fP was BMI, while bP was independently related to DT and fP.

DISCUSSION

The analysis of central arterial pressure waveform as a method providing relevant information about the interaction between LV and arterial function is gaining increasing clinical interest thanks to the availability of methods capable of capturing the signal in an accurate non-invasive way (Salvi et al., 2004). Although it is commonly assumed that arterial pressure waveforms are purely the result of forward and backward traveling waves, it has been pointed-out that arterial behaviour is difficult to explain using this assumption, particularly during the diastolic phase (Parker, 2013). Thus, a 'reservoir-wave' hypothesis has been introduced as a heuristic model, which gives emphasis to the role of aortic compliance ('reservoir' or 'Windkessel') and the change in arterial volume over the cardiac cycle, although preserving an important role for wave reflections and re-reflections in shaping the morphology of pressure (and flow) waveforms (Hughes et al., 2012; Hughes and Parker, 2020). This 'hybrid' reservoir-wave (or 'reservoir-excess pressure') model, is based upon the premise that not all changes in aortic pressure can be ascribed to forward and backward traveling waves and interprets the arterial BP waveform as a composite of a volume-related, 'reservoir' pressure, and a wave-related ('excess') pressure. It is thought to better describe the pressure waveform, providing physiological and clinical insights above and beyond the standard BP and pulse waveform analysis (Armstrong et al., 2021). Furthermore, reservoir and excess pressure analysis was recently shown to provide prognostically useful markers in various patients populations (Davies et al., 2014; Hametner et al., 2014; Narayan et al., 2015; Aizawa et al., 2021).

Nonetheless, doubts and reservations about the methodologic foundation and potential clinical usefulness of the 'reservoir-wave' approach still persist (Segers et al., 2012; Mynard and Smolich, 2014).

In this work, we aimed to verify the haemodynamic determinants of the aortic reservoir and excess pressure components, as well as their relations with forward and backward pressure waves, in a unique clinical model; the prolonged head down tilt bed rest (HDTBR). HDTBR mimics microgravity conditions and represents an established model of chronic circulatory unloading associated with a significant decrease in total body water and stroke volume, together with a parallel adaptive reduction in longitudinal LV myocardial function and a compensatory relative tachycardia, resulting in unchanged cardiac output (Kozàkovà et al., 2011).

FIGURE 1 | Reservoir, excess and net pressure waveforms (red, blue and black, respectively), in two study subjects before (**top panels**) and after (**bottom panels**) bed rest. Both subjects show a reduction in net, reservoir and excess pressure. Subject # 2 also shows a clear reduction of the time to peak reservoir pressure. P-Pd, peak systolic pressure minus diastolic pressure; Pr-Pd, reservoir pressure minus diastolic pressure; Px, excess pressure. Units: X-axis, seconds; Y-axis, kPa.

TABLE 2 | Correlation coefficients of reservoir pressure, excess pressure, separated backward and forward pressures, total arterial compliance and aortic stiffness with systemic haemodynamics parameters.

	INTPR (kPa*s)	INTXSP (kPa*s)	fP (mmHg)	bP (mmHg)	TAC (ml/mmHg)	cfPW-V (m/s)
cSBP (mmHg)	−0.01	0.66**	–	–	–	−0.06
cPP (mmHg)	−0.01	0.61**	–	–	–	−0.13
R–R (ms)	0.88**	−0.11	0.01	0.46*	0.33	0.13
LVET (ms)	0.74**	−0.34*	−0.29	0.05	0.41	−0.02
DT (ms)	0.86**	−0.08	0.03	0.49*	0.30	0.13
AIx (%)	0.21	−0.30	–	–	0.40	0.19
Pi (mmHg)	−0.03	0.68**	–	–	–	−0.09
fP (mmHg)	−0.15	0.62**	–	0.69**	–	−0.15
bP (mmHg)	0.40	0.40	0.69**	–	–	−0.07
fT (ms)	0.48	−0.27	−0.49**	−0.07	0.60**	0.44
bT (ms)	0.45	−0.17	−0.05	−0.2	0.13	0.07
EDV (ml)	0.45	−0.20	0.04	0.41	–	−0.15
SV (ml)	0.60*	0.11	0.28	0.45*	–	0.47*
TAC (ml/mmHg)	0.45*	−0.49*	–	–	–	0.48*

**p at least < 0.01; *p < 0.05.

TABLE 3 | Independent determinants of reservoir and excess pressure and separated pressure wave amplitudes.

	$b \pm SE$	p
INTPR (kPa*s)		
LVET (ms)	0.38 ± 0.12	<0.0001
DT (ms)	0.68 ± 0.14	<0.05
Cumulative R^2	0.83	<0.0001
INTXSP		
Central SBP (mmHg)	0.65 ± 0.18	0.001
Cumulative R^2	0.45	0.001
fP (mmHg)		
BMI (kg/m²)	0.60 ± 0.18	<0.005
Cumulative R^2	0.48	<0.005
bP (mmHg)		
DT (ms)	0.55 ± 0.17	<0.005
fP (mmHg)	0.73 ± 0.15	0.0001
Cumulative R^2	0.71	<0.0001

Impact of Prolonged HDTBR on Carotid Reservoir and Wave Pressure Components

In 10 young healthy volunteers, the reservoir pressure integral (INTPR) significantly decreased after prolonged bed rest, together with significant reductions in SV, R–R interval, left ventricular ejection time (LVET) and diastolic time (DT); the amplitude of backward pressure (bP) and the time to the peak of forward pressure (fT) were also significantly reduced. Reductions at the limits of statistical significance were found for central pulse pressure (cPP) and amplitude of forward pressure (fP), while no significant changes were observed for the excess pressure integral (INTXSP), augmentation index (AIx), aortic stiffness (cf-PWV) and total arterial compliance.

Reservoir and Excess Pressure Integrals and Their Physiologic Determinants

Pooling together individual data obtained before and after bed rest, we observed significant direct correlations between INTPR and SV, as well as between INTXSP and all systolic pressure components (cSBP, cPP, fP). Furthermore, INTPR was directly correlated also with LVET and DT. Taken together, these findings are substantially in keeping with the previous demonstrations by Schultz et al. (2014) that the reservoir pressure reflects the volume of blood transiently stored in the aorta soon after the ejection, by Hametner et al. (2014) of a direct relation between reservoir pressure and SV and heart rate, and the observation of Parker (2013) that the reservoir pressure will be primarily dependent upon heart rate and the global arterial properties. In our study, these conclusions are further supported by the finding of LVET and DT as independent predictors of the reservoir pressure integral and the observation of direct significant correlations between changes (Δ) in INTPR after bed rest compared to baseline and the corresponding changes in LV ejection time and diastolic time, in keeping with the hypothesis that reservoir pressure mainly depends on the LV ejection function during systole and on the aortic Windkessel during diastole (Armstrong et al., 2021). On the other hand, the correlations observed between excess pressure integral (INTXSP) and central BP (systolic and

pulse) and amplitude of forward pressure component, without any association with backward pressure amplitude or AIx, supports the hypothesis that it mainly reflects, at least in normal subjects, the early systolic LV pump function (Parker, 2013).

Separated Pressure Wave Analysis

Worth noting are the observations, in our study, of a robust direct association between the amplitude of forward and backward pressure waves, as well as between the reflected wave amplitude and R–R period and diastolic time. Thus, in conditions of normal arterial stiffness associated to young age, a main determinant of backward pressure amplitude seems to be the forward pressure amplitude, as previously reported by our group in different patients using a wave intensity approach (Rakebrandt et al., 2009).

Pulse Wave Velocity and Total Arterial Compliance

The direct association we observed between cf-PWV and stroke volume and time to the forward pressure peak (fT) is apparently counterintuitive and in contrast with the wave model, according to which cf-PWV represents aortic stiffness leading to an inverse relation between cf-PWV and fT. Actually, in young arteries with normal stiffness, even the speed of wave propagation seems to be related to haemodynamic variables, such as the volume flow (i.e., stroke volume).

Impact of Heart Rate in Shaping the Arterial Waveform

In our work, the R–R period and its systolic and diastolic segments were independent determinants of both reservoir pressure and the amplitude of the backward pressure wave. These findings are in agreement with those of Hametner et al. (2014), who showed highly significant relations of reservoir pressure with heart rate (inverse) and backward pressure amplitude (direct).

'Reservoir/Excess Pressure' and 'Wave-Alone' Model: Not Alternative but Complementary

Our data, together with those from the literature (Parker, 2013; Hametner et al., 2014; Hughes and Parker, 2020; Armstrong et al., 2021), tend to support the clinical usefulness of the reservoir-excess pressure model in interpreting physiological phenomenon and arterial pressure waveform features not completely explained by the wave-alone model. This is not alternative but complementary to the commonly accepted wave model, which considers the arterial waveform as the result of a super-position of a backward reflected wave. The forward wave is the result of the coupling between the activity of the left ventricle and the viscoelastic properties of the aorta (Windkessel phenomenon), while the backward waves are the result of the multiple reflections of the single waves, affected therefore by numerous factors (peripheral vascular resistance, distance of the reflection sites, heart rate). Both forward and backward waves are affected by arterial stiffening.

Integrating the Windkessel function into the model (Davies et al., 2007), the reservoir pressure will account for the systolic pressure associated with the blood inflow entering the aorta as well as for almost all the pressure recorded in diastole (Parker et al., 2012). For a given arterial stiffness, at least in young normal subjects, LV ejection time and diastolic time are key determinants of the pressure waveform features, and backward reflected wave occurring in the diastolic phase may contribute to support reservoir and diastolic pressure, instead of increasing LV systolic load as expected with an increased large artery stiffness.

Study Limitations

This study involves a small and selected population, represented by young healthy subjects, and thus, our findings cannot be extrapolated to older subjects with risk factors and increased arterial stiffness. Furthermore, correlation analyses were performed including individual data acquired both before and after bed rest. However, we accounted for the lack of independence in variables within an individual.

CONCLUSION

This is a confirmatory study, reproducing previous findings in an original 'clinical' model. However, according to Armstrong et al. (2021), 'the understanding of the reservoir-excess pressure model is still in its relative infancy, and more research is needed'. The paper provides a piece of evidence supporting the idea that the reservoir-wave hypothesis applied to non-invasively obtained carotid pressure waveforms is of potential clinical usefulness. Our results confirm the hypothesis that reservoir—excess pressure analysis complements the wave model adding a volume ('Windkessel') component, which may have variable impact and relevance according to age and health/disease status of the subject. In perspective, the pressure waveform analysis performed combining the two models with an assessment of the haemodynamic status by echocardiography

and an estimate of aortic stiffness would allow us to disentangle the role of various mechanisms in shaping the pressure waveform, with the aim of defining the informative content of the pressure waveform for clinical purposes in the individual subjects.

DATA AVAILABILITY STATEMENT

The raw data supporting the conclusions of this article will be made available by the authors, without undue reservation.

ETHICS STATEMENT

The studies involving human participants were reviewed and approved by The National Committee for Medical Ethics of the Slovene Ministry of Health (Ljubljana, Slovenia). The patients/participants provided their written informed consent to participate in this study.

AUTHOR CONTRIBUTIONS

CP contributed to the conceptualisation, data analysis, manuscript drafting and editing. AH, KP and PS developed the analytical methods and critically revised the manuscript. MK and MP contributed to the conceptualisation, manuscript editing, and project supervision. CM and LL contributed to the data acquisition and management. All authors contributed to the article and approved the submitted version.

FUNDING

REFERENCES

Aizawa, K., Casanova, F., Gates, P. E., Mawson, D. M., Gooding, K. M., Strain, W. D., et al. (2021). Reservoir-excess pressure parameters independently predict cardiovascular events in individuals with type 2 diabetes. *Hypertension* 78, 40–50. doi: 10.1161/HYPERTENSIONAHA.121.17001

Alastruey, J. (2010). On the mechanics underlying the reservoir-excess separation in systemic arteries and their implications for pulse wave analysis. *Cardiovasc. Eng.* 10, 176–189. doi: 10.1007/s10558-010-9109-9

Armstrong, M. K., Schultz, M. G., Hughes, A. D., Picone, D. S., and Sharman, J. E. (2021). Physiological and clinical insights from reservoir-excess pressure analysis. *J. Hum. Hypertens.* 35, 758–768. doi: 10.1038/s41371-021-00515-6

Davies, J. E., Baksi, J., Francis, D. P., Hadjiloizou, N., Whinnett, Z. I., Manisty, C. H., et al. (2010). The arterial reservoir pressure increases with aging and is the major determinant of the aortic augmentation index. *Am. J. Physiol. Heart Circ. Physiol.* 298, H580–H586. doi: 10.1152/ajpheart.00875.2009

Davies, J. E., Hadjiloizou, N., Leibovich, D., Malaweera, A., Alastruey-Arimon, J., Whinnett, Z. I., et al. (2007). Importance of the aortic reservoir in determining

the shape of the arterial pressure waveform – the forgotten lessons of frank. *Arthritis Res.* 1, 40–45. doi: 10.1016/j.artres.2007.08.001

Davies, J. E., Lacy, P., Tillin, T., Collier, D., Cruickshank, J. K., Francis, D. P., et al. (2014). Excess pressure integral predicts cardiovascular events independent of other risk factors in the conduit artery functional evaluation substudy of Anglo-Scandinavian cardiac outcomes trial. *Hypertension* 64, 60–68. doi: 10.1161/HYPERTENSIONAHA.113.02838

Hametner, B., Wassertheurer, S., Hughes, A. D., Parker, K. H., Weber, T., and Eber, B. (2014). Reservoir and excess pressures predict cardiovascular events in high-risk patients. *Int. J. Cardiol.* 171, 31–36. doi: 10.1016/j.ijcard.2013.11.039

Hughes, A. D., and Parker, K. H. (2020). The modified arterial reservoir: an update with consideration of asymptotic pressure ($P\omega$) and zero-flow pressure (Pzf). *Proc. Inst. Mech. Eng. H* 234, 1288–1299. doi: 10.1177/0954411920917557

Hughes, A., Wang, J. J., Bouwmeester, C., Davies, J., Shrive, N., Tyberg, J., et al. (2012). The reservoir- wave paradigm. *J. Hypertens.* 30, 1880–1881. doi: 10.1097/HJH.0b013e3283560960

Kozàkovà, M., Malshi, E., Morizzo, C., Pedri, S., Santini, F., Biolo, G., et al. (2011). Impact of prolonged cardiac unloading on left ventricular mass and

longitudinal myocardial performance: an experimental bed rest study in humans. *J. Hypertens.* 29, 137–143. doi: 10.1097/HJH.0b013e32833f5e01

Lewis, J. F., Kuo, L. C., Nelson, J. G., Limacher, M. C., and Quinones, M. A. (1984). Pulsed Doppler echocardiographic determination of stroke volume and cardiac output: clinical validation of two new methods using the apical window. *Circulation* 70, 425–431. doi: 10.1161/01.cir.70.3.425

Liu, Z., Brin, K. P., and Yin, F. C. P. (1986). Estimation of total arterial compliance: an improved method and evaluation of current methods. *Am. J. Physiol.* 251, H588–H600. doi: 10.1152/ajpheart.1986.251.3.H588

Michail, M., Narayan, O., Parker, K. H., and Cameron, J. D. (2018). Relationship of aortic excess pressure obtained using pressure-only reservoir pressure analysis to directly measured aortic flow in humans. *Physiol. Meas.* 39:064086. doi: 10.1088/1361-6579/aaca87

Mynard, J. P., Kondiboyina, A., Kowalski, R., Cheung, M. M. H., and Smolich, J. J. (2020). Measurement, analysis and interpretation of pressure/flow waves in blood vessels. *Front. Physiol.* 11:1085. doi: 10.3389/fphys.2020.01085

Mynard, J. P., and Smolich, J. J. (2014). The case against the reservoir-wave approach. Letter to the Editor. *Int. J. Cardiol.* 176, 1009–1012. doi: 10.1016/j.ijcard.2014.07.070

Narayan, O., Davies, J. E., Hughes, A. D., Dart, A. M., Parker, K. H., Reid, C., et al. (2015). Central aortic reservoir-wave analysis improves prediction of cardiovascular events in elderly hypertensives. *Hypertension* 65, 629–635. doi: 10.1161/HYPERTENSIONAHA.114.04824

Palombo, C., Morizzo, C., Baluci, M., Lucini, D., Ricci, S., Biolo, G., et al. (2015). Large artery remodeling and dynamics following simulated microgravity by prolonged head-down tilt bed rest in humans. *Biomed. Res. Int.* 2015:342565. doi: 10.1155/2015/342565

Parker, K. H. (2013). Arterial reservoir pressure, subservient to the McDonald lecture, artery 13. *Arthritis Res.* 7:171. doi: 10.1016/j.artres.2013.10.391

Parker, K. H., Alastruey, J., and Stan, G. B. (2012). Arterial reservoir-excess pressure and ventricular work. *Med. Biol. Eng. Comput.* 50, 419–424. doi: 10.1007/s11517-012-0872-1

Qasem, A., and Avolio, A. (2008). Determination of aortic pulse wave velocity from waveform decomposition of the central aortic pressure pulse. *Hypertension* 51, 188–195. doi: 10.1161/HYPERTENSIONAHA.107.092676

Rakebrandt, F., Palombo, C., Swampillai, J., Schön, F., Donald, A., Kozàkovà, M., et al. (2009). Arterial wave intensity and ventricular-arterial coupling by vascular ultrasound: rationale and methods for the automated analysis of forwards and backwards running waves. *Ultrasound Med. Biol.* 35, 266–277. doi: 10.1016/j.ultrasmedbio.2008.08.013

Reference Values for Arterial Stiffness' Collaboration (2010). Determinants of pulse wave velocity in healthy people and in the presence of cardiovascular risk factors: 'establishing normal and reference values.' *Eur. Heart J.* 31, 2338–2350. doi: 10.1093/eurheartj/ehq165

Salvi, P., Lio, G., Labat, C., Ricci, E., Pannier, B., and Benetos, A. (2004). Validation of a new non-invasive portable tonometer for determining arterial pressure wave and pulse wave velocity: the PulsePen device. *J. Hypertens.* 22, 2285–2293. doi: 10.1097/00004872-200412000-00010

Schultz, M. G., Davies, J. E., Hardikar, A., Pitt, S., Moraldo, M., Dhutia, N., et al. (2014). Aortic reservoir pressure corresponds to cyclic changes in aortic volume: physiological validation in humans. *Arterioscler. Thromb. Vasc. Biol.* 34, 1597–1603. doi: 10.1161/ATVBAHA.114.303573

Segers, P., Swillens, A., and Vermeersch, S. (2012). Reservations on the reservoir. Editorial comment. *J. Hypertens.* 30, 676–678. doi: 10.1097/HJH.0b013e32835077be

Van Bortel, L. M., Balkestein, E. J., van der Heijden-Spek, J. J., Vanmolkot, F. H., Staessen, J. A., Kragten, J. A., et al. (2001). Non-invasive assessment of local arterial pulse pressure: comparison of applanation tonometry and echo-tracking. *J. Hypertens.* 19, 1037–1044. doi: 10.1097/00004872-200106000-00007

Wang, J. J., O'Brien, A. B., Shrive, N. G., Parker, K. H., and Tyberg, J. V. (2003). Time-domain representation of ventricular-arterial coupling as a windkessel and wave system. *Am. J. Physiol. Heart Circ. Physiol.* 284, H1358–H1368. doi: 10.1152/ajpheart.00175.2002

Westerhof, N., Sipkema, P., Van Den Bos, G. C., and Elzinga, G. (1972). Forward and backward waves in the arterial system. *Cardiovasc. Res.* 6, 648–656. doi: 10.1093/cvr/6.6.648

Westerhof, N., and Westerhof, B. (2013). A review of methods to determine the functional arterial parameters stiffness and resistance. *J. Hypertens.* 31, 1769–1775. doi: 10.1097/HJH.0b013e3283633589

frontiers | Frontiers in Physiology

Check for updates

Corrigendum: Carotid reservoir pressure decrease after prolonged head down tilt bed rest in young healthy subjects is associated with reduction in left ventricular ejection time and diastolic length

Carlo Palombo[1]*, Michaela Kozakova[2], Carmela Morizzo[1], Lorenzo Losso[3], Massimo Pagani[4], Paolo Salvi[5], Kim H. Parker[6] and Alun D. Hughes[7]

[1]Department of Surgical, Medical, Molecular Pathology and Critical Area Medicine, University of Pisa, Pisa, Italy, [2]Department of Clinical and Experimental Medicine, University of Pisa, Pisa, Italy, [3]Department of Medical Toxicology Unit and Poison Control Centre, Careggi University Hospital, Florence, Italy, [4]Department of Medicine, University of Milan, Milan, Italy, [5]Department of Cardiology, Istituto Auxologico Italiano, IRCCS, Milan, Italy, [6]Department of Bioengineering, Imperial College London, London, United Kingdom, [7]Department of Population Science and Experimental Medicine, University College of London, London, United Kingdom

---

A Corrigendum on

Carotid reservoir pressure decrease after prolonged head down tilt bed rest in young healthy subjects is associated with reduction in left ventricular ejection time and diastolic length

by Palombo, C., Kozakova, M., Morizzo, C., Losso, L., Pagani, M., Salvi, P., Parker, K. H., and Hughes, A. D. (2022). Front. Physiol. 13:866045. doi: 10.3389/fphys.2022.866045

In the published article, there was an error in the **Funding** statement. The funding contribution of the Italian Ministry of Health was omitted. The corrected Funding statement appears below:

The authors apologize for this error and state that this does not change the scientific conclusions of the article in any way. The original article has been updated.

Publisher's note

All claims expressed in this article are solely those of the authors and do not necessarily represent those of their affiliated organizations, or those of the publisher, the editors and the reviewers. Any product that may be evaluated in this article, or claim that may be made by its manufacturer, is not guaranteed or endorsed by the publisher.

frontiers | Frontiers in Physiology

Application of a multicomponent model of convectional reaction-diffusion to description of glucose gradients in a neurovascular unit

Yaroslav R. Nartsissov*

Department of Mathematical Modeling and Statistical Analysis, Institute of Cytochemistry and Molecular Pharmacology, Moscow, Russia

A supply of glucose to a nervous tissue is fulfilled by a cerebrovascular network, and further diffusion is known to occur at both an arteriolar and a microvascular level. Despite a direct relation, a blood flow dynamic and reaction-diffusion of metabolites are usually considered separately in the mathematical models. In the present study they are coupled in a multiphysical approach which allows to evaluate the effects of capillary blood flow changes on near-vessels nutrient concentration gradients evidently. Cerebral blood flow (CBF) was described by the non-steady-state Navier-Stokes equations for a non-Newtonian fluid whose constitutive law is given by the Carreau model. A three-level organization of blood–brain barrier (BBB) is modelled by the flux dysconnectivity functions including densities and kinetic properties of glucose transporters. The velocity of a fluid flow in brain extracellular space (ECS) was estimated using Darcy's law. The equations of reaction-diffusion with convection based on a generated flow field for continues and porous media were used to describe spatial-time gradients of glucose in the capillary lumen and brain parenchyma of a neurovascular unit (NVU), respectively. Changes in CBF were directly simulated using smoothing step-like functions altering the difference of intracapillary pressure in time. The changes of CBF cover both the decrease (on 70%) and the increase (on 50%) in a capillary flow velocity. Analyzing the dynamics of glucose gradients, it was shown that a rapid decrease of a capillary blood flow yields an enhanced level of glucose in a near-capillary nervous tissue if the contacts between astrocytes end-feet are not tight. Under the increased CBF velocities the amplitude of glucose concentration gradients is always enhanced. The introduced approach can be used for estimation of blood flow changes influence not only on glucose but also on other nutrients concentration gradients and for the modelling of distributions of their concentrations near blood vessels in other tissues as well.

1 Introduction

It is well-known that a brain is the most nutrient sensitive organ in a human body. The adult human brain is generally limited to the use of glucose to fuel biochemical processes. It has an extremely high demand in metabolites especially in glucose and oxygen (Dwyer, 2002; Jespersen and Østergaard, 2012). The adult human brain consumes 20% of the total energy in the body while it comprises only 2% of the body weight (Ashrafi and Ryan, 2017). Indeed, the delivery of the compounds is fulfilled by a vasculature network which provide intensive cerebral blood flow (CBF) (Nartsissov, 2017).

Any kind of CBF impairment is the cause of sever neurodegenerative disorders like dementia and ischemic stroke (Gursoy-Ozdemir et al., 2012). Certainly, the nutrient supply is directly forming by a convectional reaction-diffusion in brain parenchyma. However, despite an obvious relation, theoretical modelling of a blood flow dynamic and metabolites reaction-diffusion are usually accomplished separately. Moreover, the type of the considered processes is often simplified advisedly. For example, under essential symmetrical properties of the system the general three-dimensional model can be reduced into a one-dimensional radial model by averaging over the vertical and angular variables in cylindrical coordinates and derive the one-dimensional reduced model similar to the lumped model (Calvetti et al., 2015). Sometimes such a way of modelling can be applied for analysis (Aubert and Costalat, 2005). Despite a complexity of the considering tissue, a remarkable success has been recently achieved in modeling of drug delivery systems for treatment of cancer. Numerical modeling of convectional diffusion yields a magnetically controlled intraperitoneal drug targeting system as a solution to improve the drug penetration into the tumor (Rezaeian et al., 2022). Moreover, the simulation results suggest that the thermosensitive liposomal doxorubicin delivery system in smaller tumors is far advantageous than larger ones (Rezaeian et al., 2019). Furthermore, it was shown that a multi-scale computational model in evaluating nano-sized drug-delivery systems can be used as a step forward towards optimization of patient-specific nanomedicine plans (Kashkooli et al., 2022). These findings clearly indicate an ability of combined multyphysical modeling to be a useful tool for pre-clinical and biomedical investigations.

Nevertheless, to get a right conclusion about the regulation properties of the system and explain or predict different effects, one needs to use the experimental or model approaches including an appropriate design of the complex phenomena. In the present study a theoretical approach to description of a spatial nutrient concentration distribution near a blood vessel has been established. It is based on a combination of a direct CBF modelling in a blood capillary with a convectional reaction-diffusion of the metabolite in a surrounding brain tissue. An essential feature of the introduced approach is explicit consideration of the metabolite transport systems in endothelia cells, and astrocyte end-feet. Moreover, the represented

design of the model makes it possible to distinguish the lumen- and tissue- orientated surfaces of the endothelial cells.

The represented design of the model adjusts to description of spatial-time gradients of glucose. The same scheme of a physical coupling with the transport systems on the surfaces may be implemented for other metabolites, like lactate, when the membrane transporters can provide a double-direction trans-membrane flow. For nutrients which have no especial transport systems, the approach also pertains, but the main difference will be in the absence of flux dysconnectivity functions on the internal boundaries. The examples of such nutrients are oxygen, nitric oxide, and some xenobiotic drugs. The advantage of the created approach with respect to estimation of the non-steady state metabolites gradients is the fundamental modification of boundary conditions. Indeed, when reaction-diffusion is modeled near a blood vessel the simplest way is to fix the concentration or fluxes on the boundaries corresponding to endothelium layer. However, in such a case the gradients will be unsensitive to the alterations of CBF. The introduced method helps to resolve this problem. Both hemodynamic and a convectional reaction-diffusion are explicitly coupled in a single project model. The introduced approach may examine alterations of metabolite concentrations gradients caused by time-scaled changes of CBF. The developed model is considered by the example of a neurovascular unit (NVU) with respect to diffusion of glucose.

2 A structural organization of neurovascular unit

Since turn of this century, it has been becoming clear that neurons, glia and microvessels are organized into well-structured anatomical formations which are involved in the regulation of CBF (Abbott et al., 2006). The brain is sheltered from the changing metabolite concentrations in blood by the obstacle which is called a blood–brain barrier (BBB). It surrounds the central nervous system (CNS) including the spinal cord (Hawkins et al., 2006). A selective 'physical barrier' is formed by the complex tight junctions between adjacent endothelial cells. They force most molecular traffic to take a transcellular route across blood/brain contact, rather than moving paracellularly through the junctions, as in most endothelia (Abbott et al., 2006). Moreover, pericytes, astrocytic end-feet and extracellular matrix (ECM) components are also included into the BBB as the structural components (Keaney and Campbell, 2015). These barriers will of course present challenges for delivery of nutrients, essential for normal brain growth, metabolism and function (Hladky and Barrand, 2018). While endothelial cells form the vessel walls, pericytes are embedded in the vascular basement membrane and astrocytic processes almost completely ensheath brain capillaries (Abbott et al., 2010). The endothelial layer is surrounded by a basement membrane and pericytes all closely enveloped by astrocyte (glial) end-feet (Hladky and Barrand, 2016). The pericytes have a contractile function as well as a role in inducing
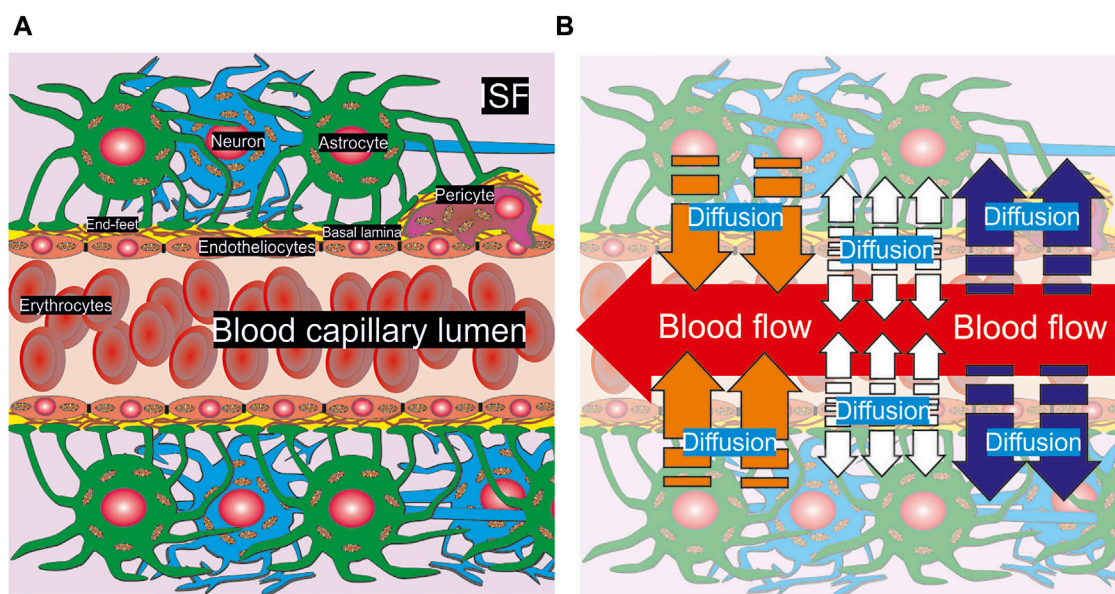
FIGURE 1
A scheme of anatomical composition of NVU. A part of a capillary pipe with erythrocytes included inside is surrounded by basal lamina, a pericyte, astrocytes and neurons **(A)**. The cells are pictured with the nucleus and mitochondria. End-feet are represented as the touch area near basal lamina and the pericyte. The physical processes of convection and diffusion are shown in appropriate areas of NVU **(B)**. A convectional CBF is represented as a red arrow in the capillary lumen. The diffusion of nutrients out/into the blood stream is indicated by blue and orange arrows respectively. The diffusion from the endothelium is marked by white arrows.

and maintaining barrier properties (Berthiaume et al., 2018). There are also nerve cells close by within the parenchyma. Finally, this whole assembly is called the neurovascular unit (NVU) (Hladky and Barrand, 2018). The role of glial cells is very essential, and it should be even reasonable to use a term "neuro-glial-vascular unit." However, during our further explanation a classic term NVU will be used because the sense of coupling in the model is to combine a convectional reaction-diffusion of metabolite (neuro including both neurons and glia cells) and hemodynamics (vascular).

At the present stage of a detailed geometry, there is no difference between glia cells and neurons in the medium of convectional reaction-diffusion of metabolites. The parameters are considered as the average values of consumption and diffusion. One should remark that the same structure appears under any level of vasculature bifurcation in brain but for large and medium arteries a smooth muscle wall must be considered as an external cover of endothelial cells. However, due to a relatively high CBF rate and the multilevel boundary structure there is no real diffusion of glucose and other nutrients form the vessels with diameter more than approximately 60 μm. Thus, for description of CBF and metabolites convectional reaction-diffusion coupling a structure of capillary type NVU can be properly used. A summarized scheme of NVU is represented in Figure 1A.

It is very essential that the processes in a brain parenchyma near a capillary are clearly structured. On the one hand, blood is coming inside a capillary lumen supplying different chemical compounds.

This process is described in terms of the fluid flow dynamics (Pontrelli, 1998) and it is a subject of experimental and theoretical studying of microvascular perfusion (Davis et al., 2008; Jensen and Chernyavsky, 2019). On the other hand, the nutrients can penetrate out or into a blood stream. For small arterioles, pre-capillaries, and capillaries the diffusion will be directed out of lumen (blue arrows, Figure 1B). On the contrary, for veins the opposite direction of metabolites transport dominates (orange arrows, Figure 1B). Some chemical compounds can be synthesized in endothelium cells and then they will spread out in both directions into capillary lumen and brain parenchyma (white arrows, Figure 1B). The example of such a compound is nitric oxide. The introduced approach yields evaluation of nutrients gradients for all possible considered conditions, because CBF and convectional reaction-diffusion are considered explicitly. Nevertheless, the calculations are fulfilled for the example of glucose diffusion.

3 A mathematical description of convectional reaction-diffusion in neurovascular unit

According to consideration of a complex biological structure mentioned in the previous Section A combined multiphysics approach needs to be used for description of the spatial non-steady state gradients of glucose in NVU. For successful
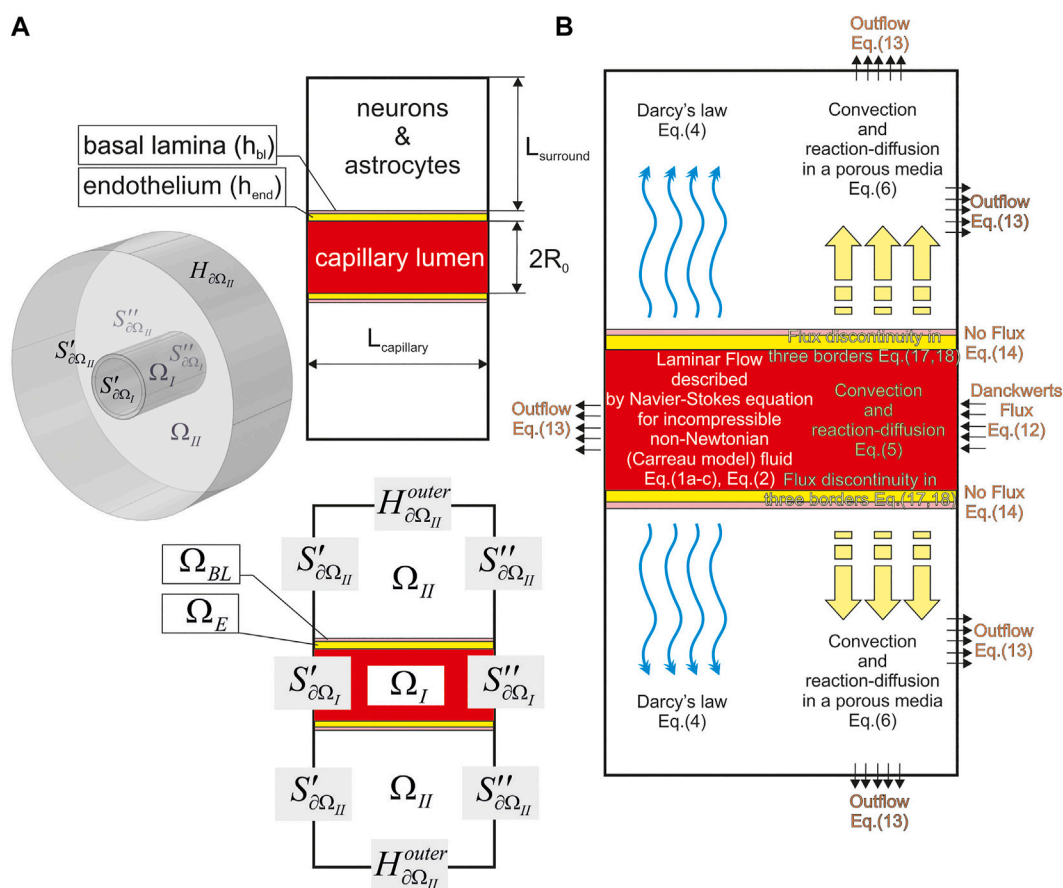
FIGURE 2

A geometry of the used digital NVU phantom. The main parameters are indicated on the plane projection **(A)** and the indication of the phantom parts and surfaces are shown both in an isometric drawing [The left part of **(A)**] and the plain view [The bottom part of **(A)**]. It is assumed that $H_{\partial\Omega_I} = H_{\partial\Omega_E}^{inner}$; $H_{\partial\Omega_E}^{outer} = H_{\partial\Omega_{BL}}^{inner}$; $H_{\partial\Omega_{BL}}^{outer} = H_{\partial\Omega_{II}}^{inner}$. The distribution of physical processes with referenced number of the equations is represented in all parts of Ω **(B)** (see the text).

modeling one has to consider different processes which provide evident influence on a glucose level in brain parenchyma. There is a successful example where a combined model has been applied to description of a novel drug delivery system based on the use of acoustic waves and temperature-sensitive liposomes. Herein, using an acoustics-thermal-fluid-mass transport coupling model, it was shown that the effective drug penetration into the tissue increased by 56% compared to conventional drug delivery (Sedaghatkish et al., 2020). In the present study, a mathematical model which describes physical phenomena near the inside/outside space of a blood vessel will be a combination of the fluids flow dynamics, diffusion, and kinetic consumption/production. In fact, the last ones are merged into reaction-diffusion and under a wide range of conditions the first process is included into the governing equation as an appropriate term.

Moreover, one should note that convection is also present in brain parenchyma. Despite a relatively low velocity as compared to CBF, it must be also regarded. Furthermore, a physiologically important role for local parenchymal convective flow in solute transport through brain extracellular space (ECS) is matched against diffusion even though it is not finally approved (Jin et al., 2016). Thus, the model of NVU is proposed as combined consideration of a blood flow and convectional reaction-diffusion for a metabolite both inside the capillary and in a surrounding tissue.

3.1 The geometry of the considered area of neurovascular unit

Initially, the geometrical shape of the modelled area must be determined. For this purpose, one needs to create a virtual (digital) phantom (Ω) which is in fact represent a combination of digital areas corresponding to biological prototype. A term "phantom" is used here as a description of

TABLE 1 The geometrical parameters of a NVU virtual phantom used for the modelling.

Symbol	Parameter	Value	Source
$L_{capillary}$	The length of the considered capillary part	25 μm	According to the experimental limitations (Abbott et al., 2010)
R_0	A capillary lumen radius	7 μm	Based on a possible upper range (Fleischer et al., 2020)
h_{end}	The fixed thickness of the endothelial cells layer	1 μm	(Payne, 2004; Yazdani et al., 2019)
h_{bl}	The thickness of a basal lamina layer	100 nm	(Arifin et al., 2009; Krüger-Genge et al., 2019)
$L_{surround}$	A radial distance from $H_{\partial\Omega_{II}}^{inner}$ to $H_{\partial\Omega_{II}}^{outer}$	25 μm	According to the experimental limitations (Gould et al., 2017)

the object where further numerical calculations will be fulfilled. It has a direct similarity with a physical imitation of the object during ionizing irradiation research. According to biological features of NVU described above (see Section 2.), all structures have been placed one after another (Figure 2A). A capillary lumen is represented as a short tube (Ω_I) with a circular section and the length of $L_{capillary}$. Endothelial cells line the vessel intima, and they are regarded as a cylinder (Ω_E) with the fixed thickness of h_{end}. The next cover is basal lamina which is also formalized as a thin cylinder (Ω_{BL}) with the width of h_{bl}. For simplification, the line segment of a capillary without pericytes is used for modelling.

The rest part of NVU is approximated as a cylinder (Ω_{II}) surrounding all structures described above. This cylinder is supposed to consist of different cells. Astrocytes inhere in the first layer forming the end-feet contacting with basal lamina. In the further space neurons and astrocytes compose a heterogenic structure containing cells and interstitial fluid organized in sheets and tunnels. It was anatomical proved that diffusion distances to neurons and glial cell bodies for solutes and drugs are short because no brain cell is further than about 25 μm from a capillary (Abbott et al., 2010; Gould et al., 2017). Based on the indicated observation, the thickness of tissue-cylinder Ω_{II} is fixed on this value ($L_{surround}$). For each type of the considered area the whole surface will be indicated as $\partial\Omega$ and the transverse and longitudinal surfaces as $S_{\partial\Omega}$ and $H_{\partial\Omega}$ respectively. The distances between neighbor end-feet are modelled by a division of $H_{\partial\Omega_{II}}^{inner}$ on two parts. One of them corresponds to the astrocytes processes with area $S_{end-feet}$. Another one represents a cleft-area where a free diffusion occurs. Due to the system has a cylindrical symmetry the division of $H_{\partial\Omega_{II}}^{inner}$ should be made by intermittent circular stripes. The set of gemetrical parameters of the virtual phantom is represented in Table 1.

3.2 Modeling of the capillary blood flow

For many cases, the governing equation for the fluid flow is the non-steady-state Navier-Stokes equation for an incompressible flow without buoyancy effects (Huang et al., 2013; Iasiello et al., 2016)

$$\rho \frac{\partial \vec{u}}{\partial t} + \rho \left(\vec{u} \cdot \nabla \right) \vec{u} = -\nabla p + \nabla \left(\mu \left(|\dot{\gamma}| \right) \left(\nabla \vec{u} + \left(\nabla \vec{u} \right)^{\mathrm{T}} \right) \right); \quad (1a)$$

$$\dot{\gamma} = 2\varepsilon = \nabla \vec{u} + \left(\nabla \vec{u} \right)^{\mathrm{T}}, |\dot{\gamma}| = \sqrt{2 \left(\varepsilon : \varepsilon \right)}; \quad (1b)$$

$$\nabla \vec{u} = 0; \quad (1c)$$

where $\vec{u}$ is the velocity vector along the coordinate system; ε denotes strain rate tensor; p, t and ρ are pressure, time, and the fluid density respectively. There is no slip on the boundary of the capillary lumen. The specific feature of this Eq. 1a for the non-Newtonian fluid flow is the dependence of the dynamics viscosity μ on shear rate $|\dot{\gamma}|$.

There are a lot of time-dependent models proposed to describe thixotropic and viscoelastic behavior of blood (Yilmaz and Yaar Gundogdu, 2008). They designate the dependence of $\mu \left(|\dot{\gamma}| \right)$ directly. It was previously shown that the non-Newtonian nature of blood acts as a regulating factor to reduce the flow resistance and wall shear stress thereby considering shear thinning to have the most significant role in facilitating blood flow through stenotic vessels (Shukla et al., 1980). Moreover, blood is usually considered as a predominantly shear thinning fluid, especially under steady flow conditions (Fatahian et al., 2018). Thus, this property seems to have the most important non-Newtonian impact (Sochi, 2013). Having quickly considered a competitive analysis of the obtained modelled values in the literature, one is able to conclude that shear thinning is evaluated using the Carreau-Yasuda model, and yield stress is usually described by the Casson model (Yilmaz and Yaar Gundogdu, 2008; Sochi, 2013). As it was mentioned above shear thinning is the most important property in the description of hemorheology and hemodynamics.

Therefore, the Carreau model has been used for Eq. 1a in the present study. According to the Carreau model the dynamics viscosity is described by the following expression:

$$\mu \left(|\dot{\gamma}| \right) = \mu_\infty + \left(\mu_0 - \mu_\infty \right) \left[1 + \left(\lambda \dot{\gamma} \right)^2 \right]^{(n-1)/2} \quad (2)$$

where μ_∞ connotes a constant limit value when blood is treated as a Newtonian fluid, μ_0 is the blood viscosity at a zero shear rate, λ is the time constant associated with the viscosity that changes with the shear rate, and n is an index parameter (Molla and Paul, 2012).
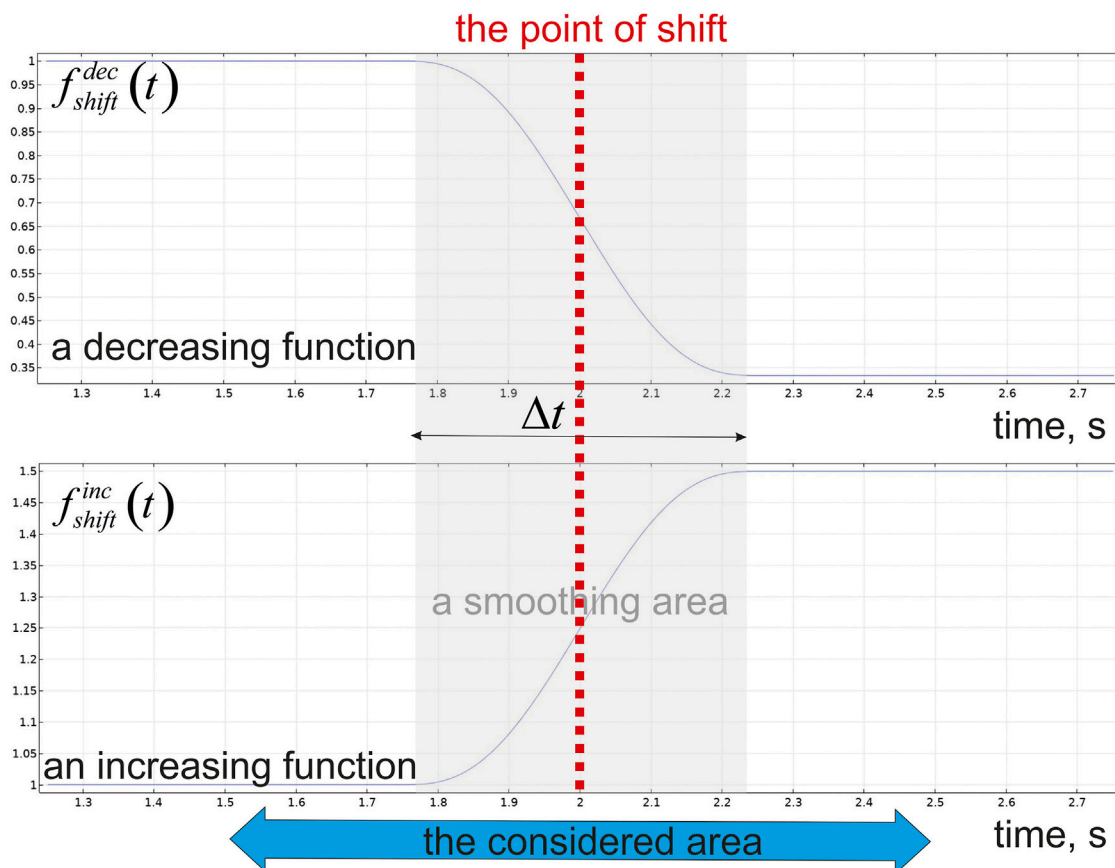
FIGURE 3
The step-like function governing inlet/outlet pressure in a capillary blood flow.

3.3 Numerical simulation of capillary blood flow changes

Although the exact value of p under a microcirculation level is controversial, the initial pressure in the capillary has been fixed at $p_0 = 18.5$ mmHg, and the difference of pressure Δp between inlet and outlet surfaces assigns CBF. The alteration in CBF is modelled by an application of a step-like function $f_{shift}^{dec/inc}(t)$, which shifts both p_0 and Δp to the modified values. If one needs to consider a decrease of CBF, $f_{shift}^{dec}(t)$ will fall down to the fixed value which is lower than 0.5. For the example of an increased CBF the same function $(f_{shift}^{inc}(t))$ raises up to the value 1.5.

$$p_{inlet} = (p_0 + \Delta p) f_{shift}^{dec/inc}(t); p_{outlet} = (p_0 - \Delta p) f_{shift}^{dec/inc}(t);$$

$$f_{shift}^{dec}(t) = \begin{cases} 1, t < t_0; \\ 1 - \delta(t), t \geq t_0; \end{cases}$$

$$f_{shift}^{inc}(t) = \begin{cases} 1, t < t_0; \\ 1 + \delta(t), t \geq t_0; \end{cases} \forall t: \delta(t) \in [0, a]; 0.5 \leq a < 1; \quad (3)$$

The view of $f_{shift}^{dec/inc}(t)$ is represented in Figure 3. The considered time is in a second's range with the time-point of shift $t_0 = 2 s$. Indeed, the changes in a blood flow are always

appeared with a continues lag phase, and a shift time-point is only a mid-point of the transition time area. This effect is modelled by a time dependent function ($\delta(t)$) which helps to evaluate alteration of the pressure in the capillary fluently. The range of a smoothed area near the time-point of shift is characterized by Δt. It is taken as high as 50% of the considered area because the values are shifted smoothly from initial levels to final ones.

3.4 Modeling of a fluid flow in parenchymal extracellular space

Forming of metabolic gradients near a capillary surface obviously composes of diffusion and advection in the interstitial space which is facilitated by convection of interstitial fluid (ISF) in the paravascular space (Jin et al., 2016). To describe these processes the form of tissue structure geometry should be set explicitly. In some case it has been done on the base of 3D reconstructions of neuropil from electron microscopy images (Kinney, 2009; Mishchenko et al.,

TABLE 2 The main properties of theneeds to consider the diffusion of parenchyma medium and the characteristics of capillary blood flow. It should be stressed that there are a lot of measured values of ρ which are reported to blood. However, the most of them belong to the range from 1,029 kg/m³ (Gijsen et al., 1999; Kim et al., 2008), to 1,087 kg/m³ (Fan et al., 2009). Nevertheless, both a low (1,000 kg/m³), and a high density (1,410 kg/m³) are also described (Chen et al., 2006; Vimmr and Jonasova, 2008).

Symbol	Parameter	Value	Source
ρ_{blood}	Density of blood	1,070 kg/m³	Huang et al. (2013)
ρ_{ISF}	Density of an interstitial fluid	1,000 kg/m³	Zhan et al. (2017)
μ_{ISF}	Viscosity of an interstitial fluid	7×10^{-4} kg/m/s	Zhan et al. (2017)
κ	Darcy's permeability	6.5×10^{-15} m²	Arifin et al. (2009)
μ_{∞}	Limit viscosity of a Newtonian fluid	3.45×10^{-3} Pa × s	Molla and Paul. (2012)
λ	Time constant in the Carreau model	3.131 s	Molla and Paul. (2012)
μ_0	Viscosity at a zero-shear rate	5.6×10^{-2} Pa × s	Molla and Paul. (2012)
n	Index constant in the Carreau model	0.3568	Molla and Paul. (2012)

2010; Kinney et al., 2013). However, a digital form of the phantom is sometimes created based on the anatomical information. For example, to consider the glymphatic mechanism by modeling diffusive and convective transport in brain ECS, the geometry of the microvascular lobule can be idealized as a hexagonal lattice with a venule at the center, surrounded by six arterioles (Jin et al., 2016).

If the parenchymal structure is not assigned plainly the velocity of fluid flow in brain ECS can be estimated using Darcy's law,

$$\vec{u} = -\frac{\kappa}{\mu_{ISF}}\nabla p \qquad (4)$$

where κ and μ_{ISF} are permeability and dynamic viscosity of the interstitial fluid, respectively. The Eq. 4 is appropriate for description of convectional processes in Ω_{II} because it describes a flow in a porous media. This media includes conditions where ISF is incompressible fluid which is placed around the rigid bodies depicting neurons and glia cells. The set of the physical parameters used in the modelling of CBF and ECF is represented in Table 2.

3.5 Convectional reaction-diffusion of glucose in capillary and surrounding tissue

Having obtained the velocity field $\vec{u}$ using Eqs 1a, 4, one needs to consider the diffusion of glucose in the model. The equation governing the system describes several processes. They are diffusion, convection, and glucose consumption. The type of the equation depends on the considered area. For a blood stream, endothelium and the basal lamina large stain objects forming the obstacles are supposed to be insufficient. On the contrary, for parenchyma the most essential contribution is given by spatial heterogeneity of neurons and glia cells forming a typical porous media. Thus, the gradient of metabolites will be formed in the

capillary lumen and two surrounding structures on the base of the following equation:

$$\frac{\partial c(\vec{r},t)}{\partial t} = \nabla \cdot \left(\mathbf{D} \cdot \nabla c(\vec{r},t) \right) - \vec{u} \cdot \nabla c(\vec{r},t) + f_{con}\left(c(\vec{r},t), \vec{r} \right); \qquad (5)$$

where c is the volume concentration of glucose, $\mathbf{D}$ is a diffusion tensor and $f_{con}(c(\vec{r},t),\vec{r})$ is the function describing the rate of metabolic reactions which consume the diffusing molecules. There is no convection in $\Omega_{E,BL}$. Thus, Eq. 5 will be applied in these areas with the zero second summand in the second member of equation. In the outside space diffusion is supplied by percolation of ISF into shears and tunnels of the parenchyma. It transforms Eq. 5 into the following form:

$$\frac{\partial}{\partial t}\left[\alpha_{ICF} c(\vec{r},t) \right] = \nabla \cdot \left(\left(\mathbf{D}_d + \frac{\alpha_{ICF}}{\tau}\mathbf{D} \right) \cdot \nabla c(\vec{r},t) \right) - \vec{u} \cdot \nabla c(\vec{r},t)$$
$$+ f_{con}\left(c(\vec{r},t), \vec{r} \right); \qquad (6)$$

where α_{ICF} is porosity and it is also called volume fraction of ISF and τ is interstitial tortuosity. Additionally, the dispersion tensor $\mathbf{D}_d$ for ISF has been included. It depends also on the fluid's average velocity $\vec{u}$ in the void space,

$$D_{(d)ij} = \frac{1}{u}\sum_{k,l=1}^{3} a_{ijkl}u_k u_l; \; u = \sqrt{\sum_{k=1}^{3} u_k^2}; \qquad (7)$$

where a_{ijkl} is a property, called dispersivity, of the porous medium only, and u_k is the kth component of the fluid's average velocity vector $\vec{u}$ (Bear, 1961). Since the early 60 s, almost all research on (solute) dispersion has been limited to isotropic porous media. For such media, the components of the dispersivity tensor have been shown to depend only on two material moduli, referred to as longitudinal $(D_{(d)L})$ and transversal $(D_{(d)T})$ dispersivities (Fel and Bear, 2010). In a

common case the coefficients of transverse and longitudinal dispersion are non-linear functions of velocity:

$$D_{(d)L} = \frac{D_c}{\tau} + \alpha_L u^n; \quad D_{(d)T} = \frac{D_c}{\tau} + \alpha_T u^n; \quad n \in [1, 2] \quad (8)$$

where the coefficients α_L and α_T are the longitudinal and transverse dispersivities, respectively, of the porous medium in the direction of transport, D_c is a diffusion coefficient of substance c in the solvent and n is an empirically constant (Delgado, 2007).

Having assumed longitudinal dispersivity is proportional to a linear size of the system ($L_{surround}$) (Pickens and Grisak, 1981) and taking into account the medium value of ISF in approximately 5×10^{-7} m/s (Zhan et al., 2017), one can neglect the second summand in a right part of Eq. 7. Thus, the dispersion transforms into:

$$D_{(d)L} = D_{(d)T} = \frac{D_c}{\tau}; \quad (9)$$

Indeed, tensors in Eqs 5, 6 are the subject for experimental measurements. Despite the attempts to depict the true diffusion process, it was generally accepted that the gradients in a biological tissue be portrayed on a voxel scale of obtained images (Basser and Jones, 2002). In that case the physical diffusion coefficient has been replaced with a global, statistical parameter, the apparent diffusion coefficient (ADC) (Chanraud et al., 2010). The non-invasive observation of the water diffusion driven displacement distributions *in vivo* provides unique clues to the fine structural features and geometric organization of neural tissues, and the technique of brain tissue anisotropy measurement is actually based on a water diffusion magnetic resonance imaging (Le Bihan, 2003).

Taking together the mentioned above, the elements of diffusion tensors can be represented as production of the mean diffusion coefficient and anisotropy matrix.

$$\mathbf{D} = D_c \cdot \begin{pmatrix} \sigma_{xx} & \sigma_{xy} & \sigma_{xz} \\ \sigma_{yx} & \sigma_{yy} & \sigma_{yz} \\ \sigma_{zx} & \sigma_{zy} & \sigma_{zz} \end{pmatrix}; \quad (10)$$

Certainly, in a common case it is difficult to indicate the sharp orientation of a short capillary part to parenchyma anisotropy. Nevertheless, without loss of generality one can suppose that $\sigma_{ij} = \delta_{ij} \cdot \xi_{ij}$ where δ_{ij} is Kronecker delta and ξ_{ij} is a dimensionless value indicating the relative ratio between the directions. The physical parameters of diffusion in distinct parts of the considered virtual phantom (Ω) is represented in Table 3.

The third summand in the second member of Eqs 5, 6 is corresponds to consumption of glucose in the medium. As for many metabolites this process is mediated by an activity of enzymes transforming an initial substrate to the products of reaction. It should be noticed that the first step of the metabolic pathway for glucose oxidation is considered to be a unique reaction forming $f_{con}(c(\vec{r}, t), \vec{r})$. Upon glucose has

come to the cells, it is transformed into glucose-6-phosphate by hexokinase. It is generally considered that this first step of glycolysis has more flux control than its transmembrane transport. The activity of hexokinase is observed both in blood stream, endothelial cells and nervous parenchyma. Although the kinetic properties of such an enzyme is known well, the activity of the whole metabolic pathway should be taken into account. The rate equation of the hexokinase–phosphofructokinase system was proposed by Heinrich and Schuster (1996), but it should be extended by a term that accounts for the glucose effect according to classical Michaelis–Menten kinetics (Aubert and Costalat, 2005). The parameters

$$f_{con}\left(c(\vec{r}, t), \vec{r}\right) = -\frac{\varepsilon_{Glc/ATP}^{\Omega_{I/E/II}} c(\vec{r}, t)}{c(\vec{r}, t) + K_{Glc}}; \quad \varepsilon_{Glc/ATP}^{\Omega_{I/E/II}}$$

$$= k_{Glc}^{\Omega_{I/E/II}} c_{ATP}^{\Omega_{I/E/II}} \left[1 + \left(\frac{c_{ATP}^{\Omega_{I/E/II}}}{K_{I,ATP}}\right)^{nH}\right]^{-1} \quad \vec{r} \in \Omega_{I/E/II}$$

$$(11)$$

The Eq. 11 includes not only glucose concentration but also concentration of adenosine triphosphate (ATP) - $c_{ATP}^{\Omega_{I/E/II}}$. The kinetic equation of steady-state hexokinase reaction depends on ATP concentration explicitly. However, due to the level of such a metabolite is essentially regulated in the living cells, it remains stable in a wide range of other parameters (Ainscow et al., 2002; Nartsissov and Mashkovtseva, 2006). Thereby, in the present study ATP concentration is considered as a constant and Eq. 11 is transformed to the classical simplified hyperbolic dependence. It is also supposed that endothelial cells and neuronal parenchyma have similar kinetic properties with respect to glucose consumption, but the level of hexokinase in blood cells is lower $\varepsilon_{Glc/ATP}^{\Omega_I} \ll \varepsilon_{Glc/ATP}^{\Omega_E} \approx \varepsilon_{Glc/ATP}^{\Omega_{II}}$.

3.6 Boundary conditions and initial values

For any kind of partial differential equation problem, the boundary conditions are the most essential part which determines, in fact, quantitative characteristics of the solution. Moreover, the type of condition is related to the physical properties of the system. It is supposed that the capillary is essentially isolated from the external influence, and the main part of metabolites is coming with CBF. It means that on the end transverse surface of Ω_I Danckwerts condition has been set up:

$$\vec{n} \cdot \left(\vec{J} + \vec{u} \cdot c(\vec{r}, t)\right) = \vec{n} \cdot \left(\vec{u} \cdot \tilde{c}(t)\right); \quad \vec{r} \in S''_{\partial\Omega_I} \quad (12)$$

Another end transverse surface was validated with outflow condition:

TABLE 3 The diffusion property of the medium. Diffusion coefficients for glucose considered as mean physical values which will be used as D_c in Eq. 10 (Simpson et al., 2007).

Symbol	Parameter	Value	Source
$D_{Glc\,CBF}$	Glucose diffusion coefficient in CBF	3.1×10^{-10} m²/s	Kreft et al. (2013)
$D_{Glc\,BL}$	Glucose diffusion coefficient in basal lamina	1.6×10^{-10} m²/s	Bashkatov et al. (2003)
D_{Glc}	Glucose diffusion coefficient in astrocytes and neurons at 37°C	8.7×10^{-10} m²/s	Kreft et al. (2013)
σ_{xx}	Coefficient in diffusion/dispersion tensor	1	Le Bihan, (2003)
$\sigma_{yy} = \sigma_{zz}$	Coefficient in diffusion/dispersion tensor	0.33	Le Bihan, (2003)
α_{ISF}	Porosity (volume fraction of ISF)	0.36	Vendel et al. (2019)
τ	Interstitial tortuosity	1.635	Sykova and Nicholson. (2008)

$$\vec{n} \cdot \left(\mathbf{D} \cdot \nabla c\left(\vec{r}, t \right) \right) = 0; \; \vec{r} \in S'_{\partial \Omega_I} \qquad (13)$$

Considering a convection field in ISF, the concentrations on $H^{outer}_{\partial \Omega_{II}}$ will be governed by Eq. 13 as well. Furthermore, appropriate end transverse surfaces of Ω_E and Ω_{BL} should be considered with an no flux condition:

$$-\vec{n} \cdot \vec{J} = 0 ; \qquad \vec{r} \in S'_{\partial \Omega_{E/BL}}; \; \vec{r} \in S''_{\partial \Omega_{E/BL}} \qquad (14)$$

If the virtual phantom length is long i.e., $L_{capillary} \gg L_{surround}$ and $c^0(t) \sim \langle c \rangle$ then Eq. 14 can be replaced on the fixed boundary concentration.

$$c\left(\vec{r}, t \right) = c^0(t); \; \vec{r} \in S'_{\partial \Omega_{E/BL}}; \; \vec{r} \in S''_{\partial \Omega_{E/BL}} \qquad (15)$$

It should be stressed that a peculiarity of the brain tissue causes an evident effect of ISF on medium convection properties. Under considered conditions, a flow takes the metabolites away from the blood vessel boundary and it turns mathematical expression of Eq. 14 equal to Eq. 13 for $\vec{r} \in (\partial \Omega_{II} \backslash H^{inner}_{\partial \Omega_{II}})$. The difference between 13) and 14) will appear when the external flow of interstitial liquid is directed inside the virtual phantom. This case corresponds to veins type of a blood vessel, and it causes the substitution of Eq. 13 with Eq. 12 including an appropriate value of $\tilde{c}(t)$.

The gradients of glucose will be always formed under circumstances of non-zero initial values of the metabolite. This essential feature of native compounds has a substantial difference with the same one to the toxic chemicals. Indeed, usual concentration of some mediator or a drug can be awfully close to zero because a high regulatory effect of the molecules needs to be appeared shortly. On the contrary, common participants in the metabolic pathways must be present in an essential amount in tissues all the time. It means that the initial concentrations of each metabolite are reasonably fixed at an average tissue level.

$$c\left(\vec{r}, t \right)\big|_{t=0} = \langle c \rangle\big|_{I/E/BL/II}; \; \vec{r} \in \Omega_{I/E/BL/II} \qquad (16)$$

In a common case the sharp values of initial concentrations are varied for different areas. However, the most diversity is observed between CBF and parenchyma.

3.7 Internal boundary discontinuities forming the flux dysconnectivity functions

The essential processes forming the gradients of metabolites near a capillary are the transport across the membranes. The transport of glucose is mediated by a well-known family of sodium-independent bi-directional facilitative transporters from the solute carrier 2 (SLC2) family of which 14 isoforms (GLUTs 1–14) are widely represented in endothelial cells, glia and neurons (Lizák et al., 2019). Despite variety of identified membrane carriers, GLUT1 and GLUT3 are the major glucose transporters in NVU (Patching, 2017). It is described by the usual equation of a passive transport. Under normal circumstances, as it was mentioned above brain glycolysis is not limited by glucose transport, but by phosphorylation of glucose to glucose-6-phosphate. Quantitative measurements suggest an asymmetric distribution of GLUT1 at the luminal and abluminal membranes and up to 40% of the GLUT1 protein may be sequestered within the cell cytoplasm at any given time (Patching, 2017). A number of other studies have quantified the relative amounts of GLUT1 in luminal and abluminal membranes and cytoplasm from humans and from other mammals with variable results (Deng and Yan, 2016).

The existence of the transmembrane transporters in endothelial cells and astrocytes end-feet forms an irregularity in a diffusion process. Indeed, having reached the surfaces of different areas, the molecules of glucose collide with an obstacle. There is no free diffusion available when they pass through $H^{inner}_{\partial \Omega_E}$ and $H^{outer}_{\partial \Omega_E}$. For $H^{inner}_{\partial \Omega_{II}}$ there is a combination of the space with a free diffusion—the cleft between end-feet, and the membrane of astrocytes where the process of glucose entrance into the cell is the same as in endothelium. The phenomena described above form the internal flux irregularities in Ω which are introduced by the dysconnectivity functions.

These functions includes both kinetic properties of membrane transporters and their capacity on the surfaces $H_{\partial\Omega_E}^{inner}$, $H_{\partial\Omega_E}^{outer}$ and $H_{\partial\Omega_{II}}^{inner}$. It should be remarked that even though only one type of the transporter is considered but the formed fluxes are variated. Since the affinity of the protein to glucose is unchangeable under fixed conditions an obvious reason for such a diversity is the amount of GLUT incorporated into the membrane. A fluctuation of the typical value of GLUT content causes the quantitative multiplicity of the glucose transport in endothelium and end-feet. The combination of different GLUT yields the transmembrane flux of the metabolite. For each transporter, the rate equation is a typical hyperbolic function with maximal rate (V_{max}^k) and affinity (K_m^k).

A superposition of the transport activity is defined as the following expression:

$$-\vec{n} \cdot \left(\vec{J} + \vec{u} \cdot c\left(\vec{r}, t\right) \right)_{H_{\partial\Omega_E}^{inner} / H_{\partial\Omega_E}^{outer} / H_{\partial\Omega_{II}}^{inner}}$$

$$= \sum_k \frac{f_{GLUT(k)}\left(\vec{r}\right) \cdot V_{max}^k \cdot c\left(\vec{r}, t\right)}{K_m^k + c\left(\vec{r}, t\right)}; |_{\vec{r}\in S_{end-feet}}$$

$$-\vec{n} \cdot \left[\left(\vec{J} + \vec{u} \cdot c\left(\vec{r}, t\right)\right)_{H_{\partial\Omega_{II}}^{inner}} - \left(\vec{J} + \vec{u} \cdot c\left(\vec{r}, t\right)\right)_{H_{\partial\Omega_{BL}}^{outer}} \right]$$

$$= 0; \quad \vec{r} \in H_{\partial\Omega_{II}}^{inner} \backslash S_{end-feet} \qquad (17)$$

The function $f_{GLUT(k)}\left(\vec{r}\right)$ in Eq. 17 describes a spatial distribution of GLUTs in the compartment's membranes. It is validated in $H_{\partial\Omega_E}^{inner}$, $H_{\partial\Omega_E}^{outer}$ and $H_{\partial\Omega_{II}}^{inner}$. The first and the second surfaces contain the transporters in the endothelium cells and the last one comprises the GLUTs in end-feet of astrocytes. Generally, it is supposed that glucose transport in both barriers before parenchyma is mediated by GLUT1 isoenzymes (Weiler et al., 2017). According to this assumption the right part of Eq. 17 is transformed to

$$\sum_k \frac{f_{GLUT(k)}\left(\vec{r}\right) \cdot V_{max}^k \cdot c\left(\vec{r}, t\right)}{K_m^k + c\left(\vec{r}, t\right)} = \frac{N_{GLUT1}^{H_{\Omega_E}^{inner}/H_{\Omega_E}^{outer}/H_{\Omega_{II}}^{inner}} \cdot k_{cat}^1 \cdot c\left(\vec{r}, t\right)}{N_A \cdot \left(K_m^1 + c\left(\vec{r}, t\right)\right)}$$

$$(18)$$

where $N_{GLUT1}^{H_{\Omega_E}^{inner}/H_{\Omega_E}^{outer}/H_{\Omega_{II}}^{inner}}$ is the number of carriers per μm^2; k_{cat}^1 is the number of GLUT1 turnovers and N_A is the Avogadro constant.

Finally, the kinetic constants and the parameters of transporters densities can be found in Table 4.

3.8 Computation and model evaluation

The model is created on the base of COMSOL Multiphysics ver. 5.5. All physical processes described above are included into structural geometry of NVU in appropriate way (Figure 2B). As it was mentioned above, the size of the blood vessel is taken as

R_0 = 7 μm. The set of concentration values is the following $\tilde{c}(t) = 5\,mM$, $\langle c\rangle|_{E/BL/II} = 1\,mM$, $\langle c\rangle|_I = 5\,mM$. The calculations have been evaluated using Intel® Core ™ i9-7960X CPU 4.40 GHz and AMD Ryzen Threadripper 3990 × 64-Core Processor 4.3 GHz. The velocities fields and concentration gradients were obtained using the finite element method (FEM) applying User-Controlled Extra-Fine Meshes with minimum angle between boundaries in 240° and elemental size scaling factor 0.1. The governing equations of ISF (Eq. 4) and CBF (Eq. 1a) are solved to generate a flow field, and the velocities of both ISF and CBF are implemented into the reaction-diffusion equation with convection for transient simulations of the glucose gradients in blood flow (Eq. 5) and surrounding nervous tissue (Eq. 6), respectively. A mean calculation time was approximately 2.25 h for glucose estimations. The changes of CBF were simulated by a step-like function with a jump of pressures at t_0 = 2 s (Figure 3).

The calculations have been made for the time range from t = 0 to t = 4 s. The considered area in a time scale is chosen as $1.5\,s \le t \le 2.5\,s$ because the calculated values of blood flow velocities and glucose concentrations are changed in the smoothing area $1.75\,s \le t \le 2.25\,s$ only. They eighter decrease or increase the base value p_0 and Δp with smoothing size of transitional zone in Δt = 0.5 s. The structure of NVU will be characterized by the ratio which describes the density of end-feet covering basal lamina. The parameter is calculated on the base of $H_{\partial\Omega_{II}}^{inner}$ division and it can be written as the following expression:

$$\delta_{end-feet} = \frac{S_{end-feet}}{S_{total}} \cdot 100\%. \qquad (19)$$

The results of the modelling are both the velocity field in $\Omega_{I,II}$ and spatial-time distribution of the glucose concentration in all parts of the virtual phantom. If one needs to compare the results of modelling to the experimental data, the values are represented as a mean ± SD.
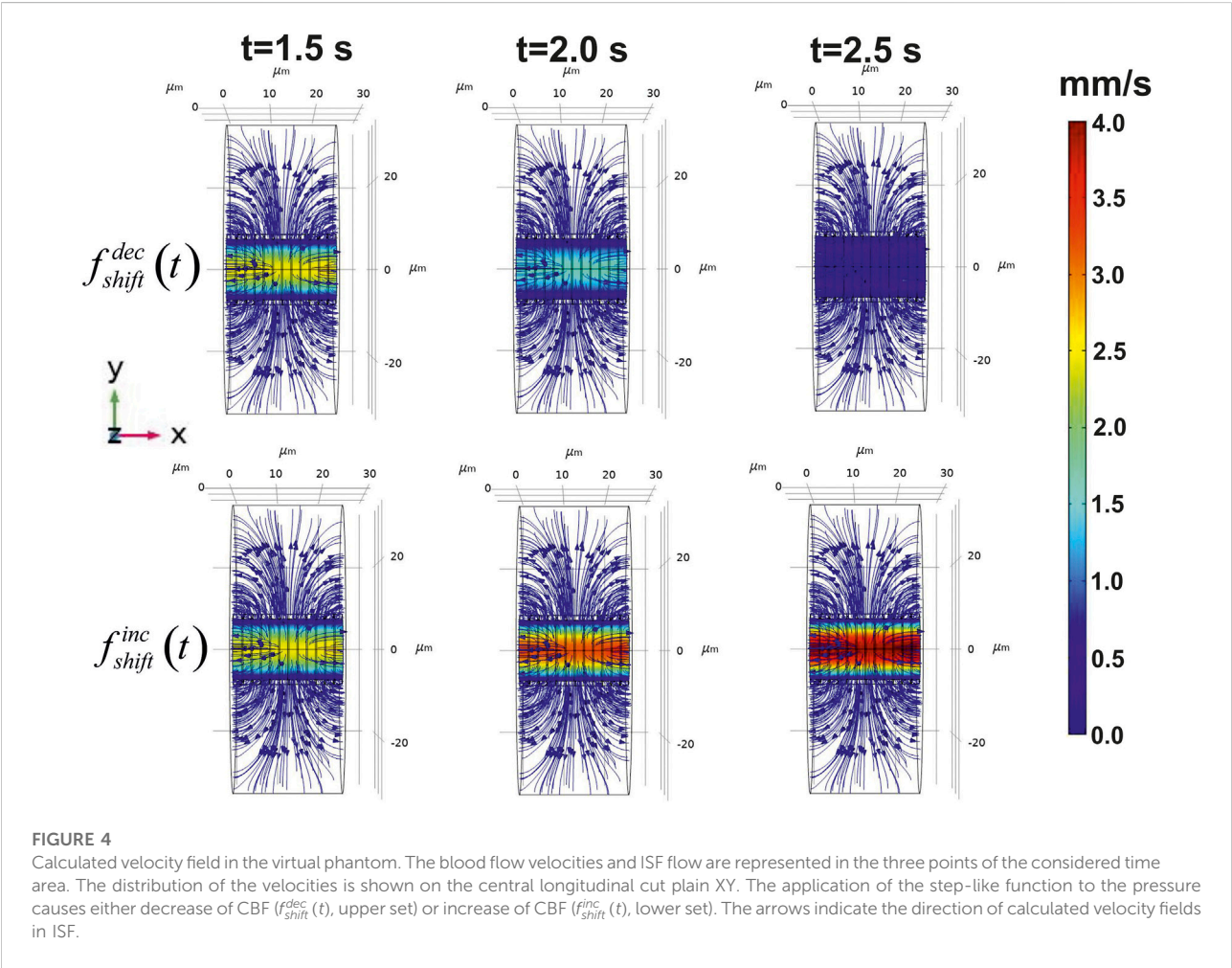
4 Results

The introduced approach makes it possible to evaluate both a velocity field in a blood stream/ISF convection and reaction diffusion of glucose in distinct parts of the considered phantom. Initially, the velocity field for CBF and convection in a nervous parenchyma part was obtained. The diagrams of this field are represented in Figure 4.

The chosen parameters of the pressure in a considered blood vessel yield the appropriate modeled values of velocity magnitude $\langle\vec{u}\rangle$ (1.28 ± 0.06 mm/s) in compare to the experimental results (1.60 ± 0.70 mm/s (Hudetz et al., 1996); 2.03 ± 1.42 mm/s (Unekawa et al., 2010); 0.99 ± 0.17 mm/s (Lyons et al., 2016)); Simultaneously, the velocities calculated with governing Eq. 4 (4.1 ± 0.5 × 10^{-7} m/s) are also in a good relation to the measured values of ISF in approximately 5 × 10^{-7} m/s (Zhan et al., 2017). It
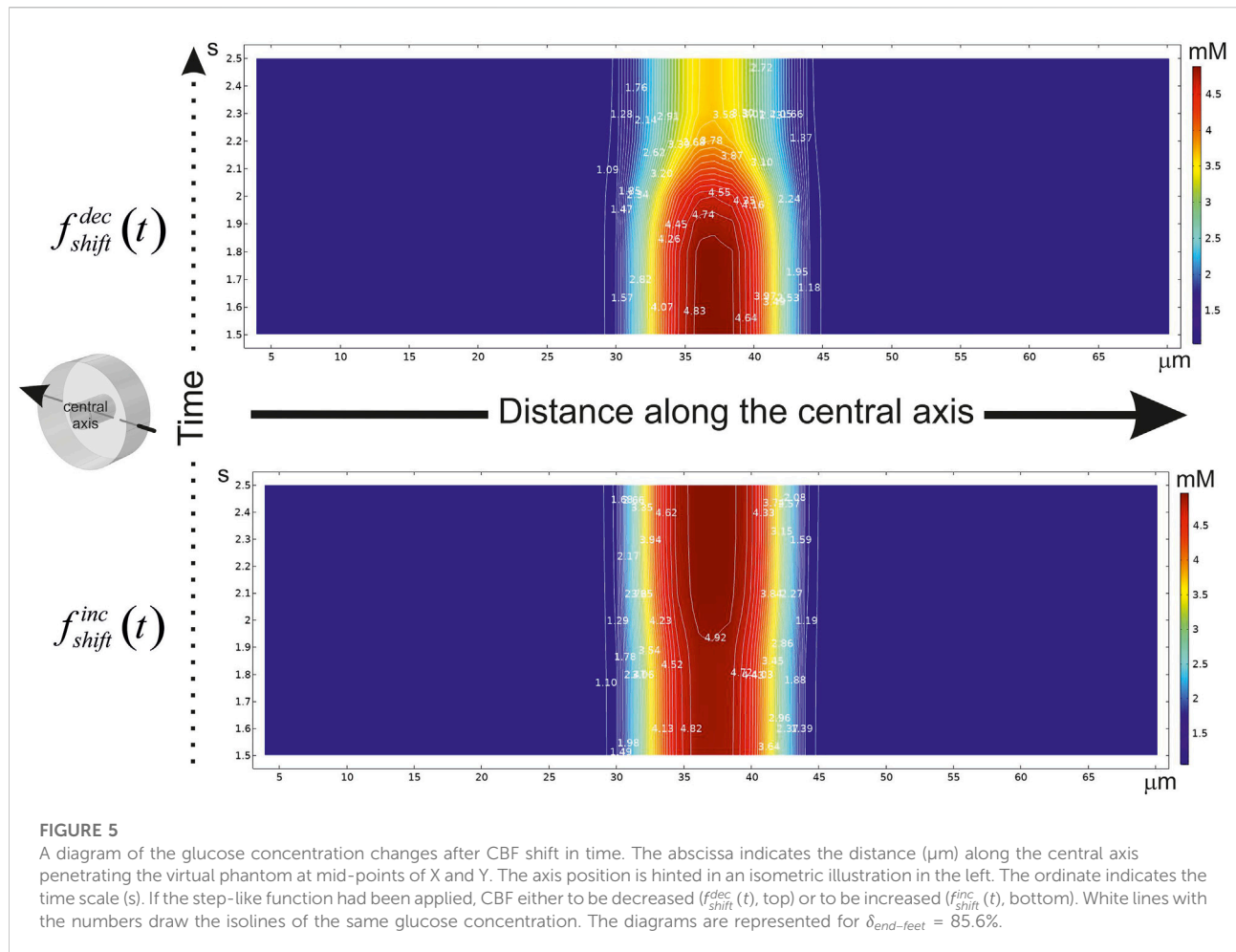
TABLE 4 The parameters of transmembrane glucose transport and the constants of consumption rates for glucose.

Symbol	Parameter	Value	Source
K_m^1	Glucose affinity constant of GLUT1	8 mmol/L	Simpson et al. (2007)
$N_{GLUT1}^{H_{\partial\Omega_E}^{inner}/H_{\partial\Omega_E}^{outer}}$	Number of GLUT1 in the endothelial membrane	1.0×10^3 1/μm²	Simpson et al. (2007)
$N_{GLUT1}^{H_{\partial\Omega_{II}}^{inner}}$	Number of GLUT1 in the end-feet membrane	0.018×10^3 1/μm²	Simpson et al. (2007)
k_{cat}^1	The number of GLUT1 turnover at 37°C	1.166×10^3 1/s	Lowe and Walmsley. (1986)
$k_{Glc}^{\Omega_{E/II}}$	Kinetic constant of hexokinase–phosphofructokinase system	120×10^{-3} 1/s	Aubert et al. (2001)
$K_{I,ATP}$	ATP inhibition constant on hexokinase–phosphofructokinase system	1 mM	Aubert et al. (2001)
K_{Glc}	Affinity constant to glucose	0.05 mM	Aubert and Costalat. (2005)
nH	Degree parameter of hexokinase–phosphofructokinase system	4	Aubert and Costalat. (2005)
$c_{ATP}^{\Omega_{I/E/II}}$	Concentration of ATP in distinct parts of the virtual phantom	1 mM	Köhler et al. (2020)

FIGURE 4
Calculated velocity field in the virtual phantom. The blood flow velocities and ISF flow are represented in the three points of the considered time area. The distribution of the velocities is shown on the central longitudinal cut plain XY. The application of the step-like function to the pressure causes either decrease of CBF ($f_{shift}^{dec}(t)$, upper set) or increase of CBF ($f_{shift}^{inc}(t)$, lower set). The arrows indicate the direction of calculated velocity fields in ISF.

should be noticed that the velocity field has been formed as a gradient in both Ω_I and Ω_{II}. The introduced approach makes it possible to evaluate not only a mean value of $\vec{u}$, but a distribution of this variable can be also represented for analysis. An application of $f_{shift}^{dec/inc}(t)$ to the pressure on the end transverse surfaces $S'_{\partial\Omega_I}$ and $S''_{\partial\Omega_I}$ modifies a blood flow forming a

FIGURE 5
A diagram of the glucose concentration changes after CBF shift in time. The abscissa indicates the distance (μm) along the central axis penetrating the virtual phantom at mid-points of X and Y. The axis position is hinted in an isometric illustration in the left. The ordinate indicates the time scale (s). If the step-like function had been applied, CBF either to be decreased ($f_{shift}^{dec}(t)$, top) or to be increased ($f_{shift}^{inc}(t)$, bottom). White lines with the numbers draw the isolines of the same glucose concentration. The diagrams are represented for $\delta_{end-feet}$ = 85.6%.

decreased or an increased CBF. These changes cause an essential alteration of a spatial-time distribution of glucose concentration in a capillary lumen. The example of such a gradient is shown in Figure 5.

The essential variance is localized in a smoothing area near the point of shift. Indeed, the main influence on the gradient in Ω_I is accomplished by velocity field changes comparing to reaction-diffusion. It is remarkable that a blood flow velocity has a considerable impact on glucose gradients in a tissue part of the phantom, but the changes of this metabolite level in brain parenchyma crucially depend on the value of $\delta_{end-feet}$. If the end-feet cover the basal lamina continuously with a small free diffusion area on $H_{\partial\Omega_{II}}^{inner}$ ($\delta_{end-feet}$ is high) than the changes in glucose gradients in Ω_{II} seems to be simply predictable.

Decrease of an incoming glucose causes a lowered level of this metabolite in the tissue part (Figure 6, top). However, if the area of a free diffusion from the basal lamina is high ($\delta_{end-feet}$ is low), a slow-down velocity of CBF breeds an increased amount of glucose in Ω_{II} (Figure 6, medium and bottom).

On the contrary, there is no such a difference between $\delta_{end-feet}$ in the case of $f_{shift}^{inc}(t)$. An increased CBF always cause an enhanced level of glucose in Ω_{II} (Figure 7). The structure of $H_{\partial\Omega_{II}}^{inner}$ also influence the amplitude of a glucose gradient in Ω_{II}. An average value of glucose level in a nervous parenchyma part of the phantom is variated from 1.03 ± 0.02 mM ($\delta_{end-feet}$ =85.6%) to 2.2 ± 0.3 mM ($\delta_{end-feet}$ =20.8%) which is in a good relation to the experimentally measured value of 1.7 ± 0.9 mM (Choi et al., 2001).

5 Discussion

The results of the introduced multyphysical approach reveal an especial physiological feature of BBB. In a classic view BBB is created by a tight junction between endothelial cells that form the walls of the capillaries (Abbott et al., 2010). Nevertheless, astrocytes also sealed the area around a blood vessel by the end-feet network. Certainly, there is a complex structure of the
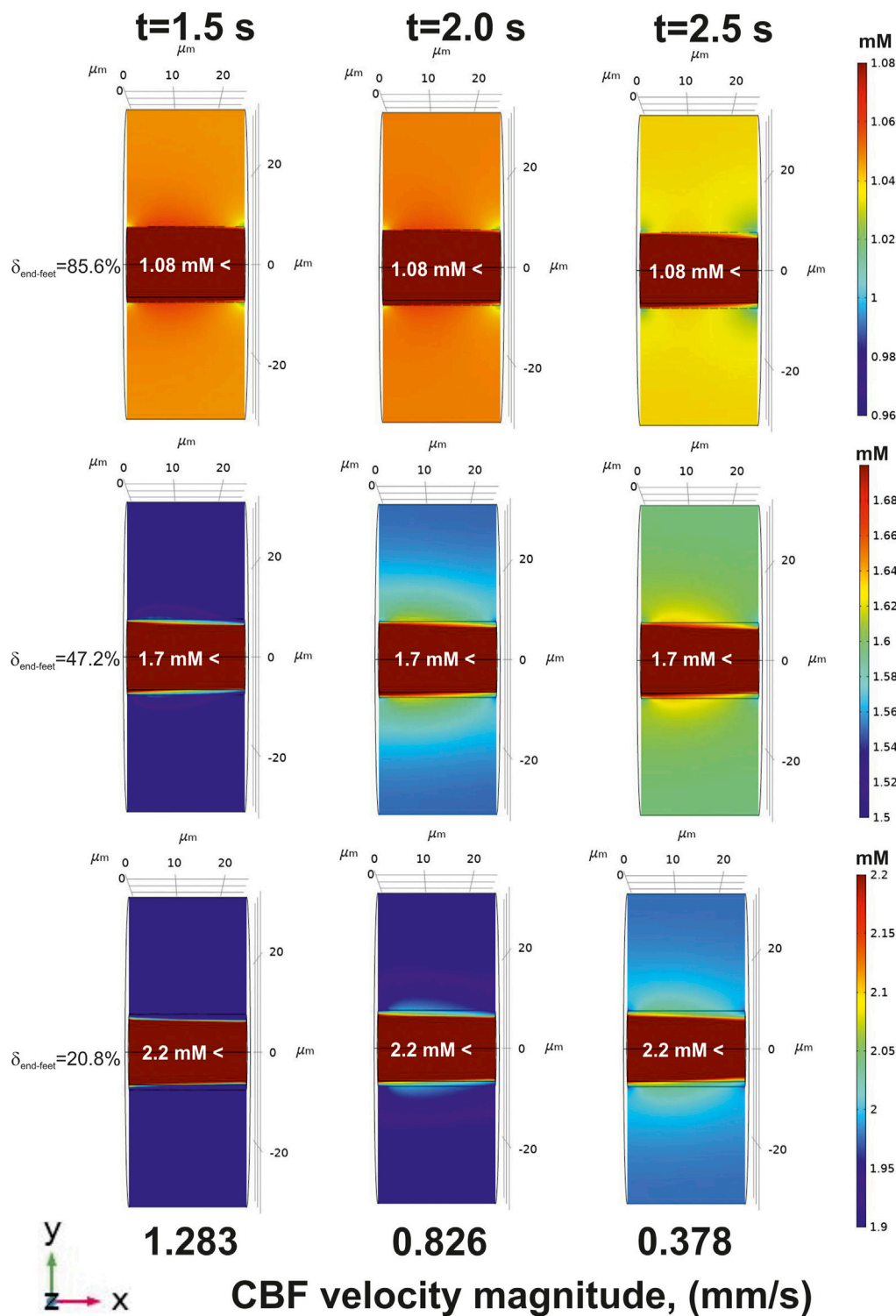
FIGURE 6
The glucose gradients near a blood capillary surface after CBF decrease (an application of $f^{dec}_{shift}(t)$ to the pressure on the end transverse surfaces $S'_{\partial\Omega_l}$ and $S''_{\partial\Omega_l}$). The concentrations are represented in the central longitudinal cut plain XY at the three moments of time (indicated in the top). The corresponding CBF velocity magnitudes are specified in the bottom. For clear visualization the different glucose concentration scales are chosen in each case. The lumen of blood capillary (Ω_l) has a separate distribution of glucose formed by reaction-diffusion and convection. Due to a narrow range of scale, it is filled with a single color and a numerical indication. The glucose gradients represented for 85.6%, 47.2%, and 20.8% of $\delta_{end-feet}$ respectively.
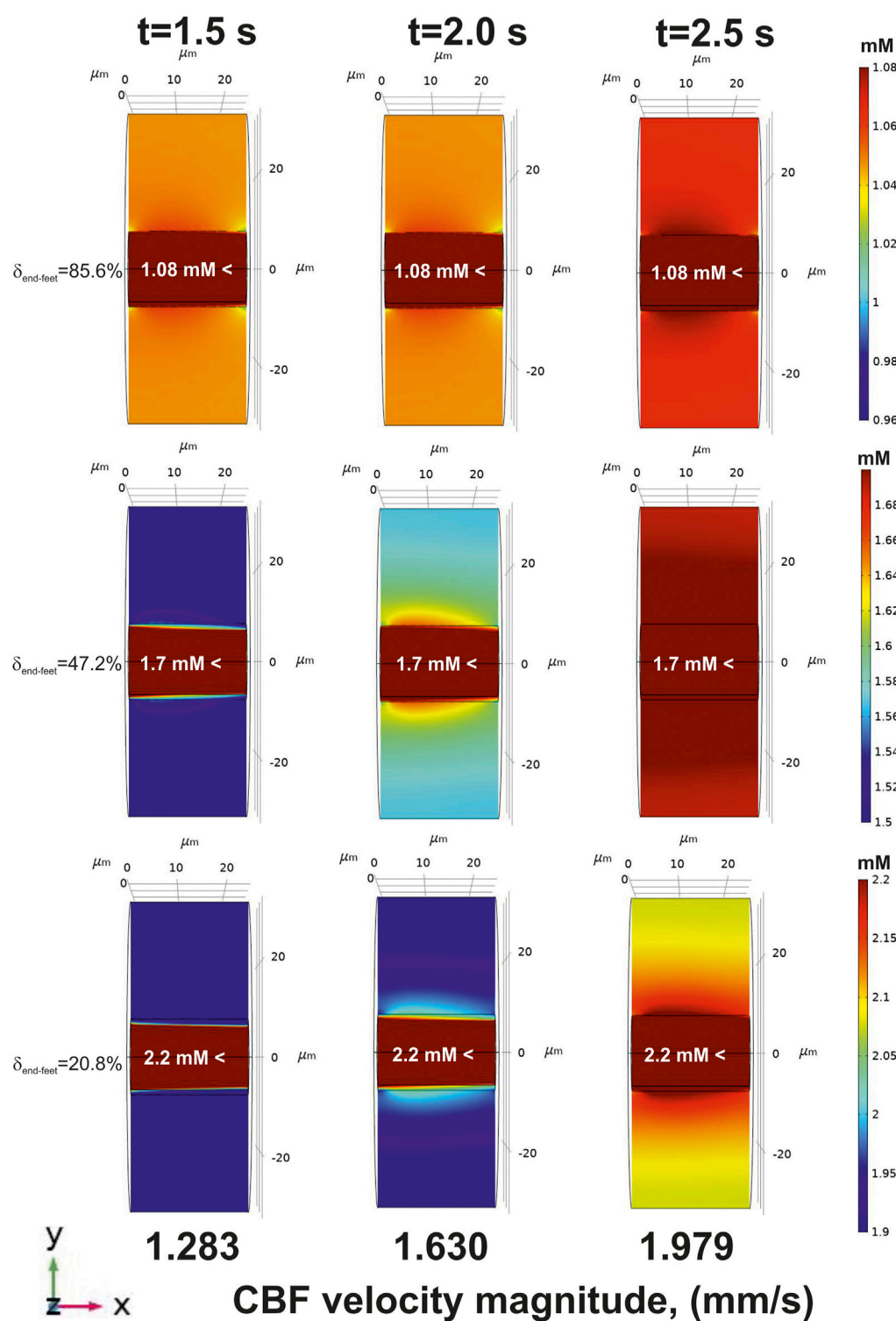
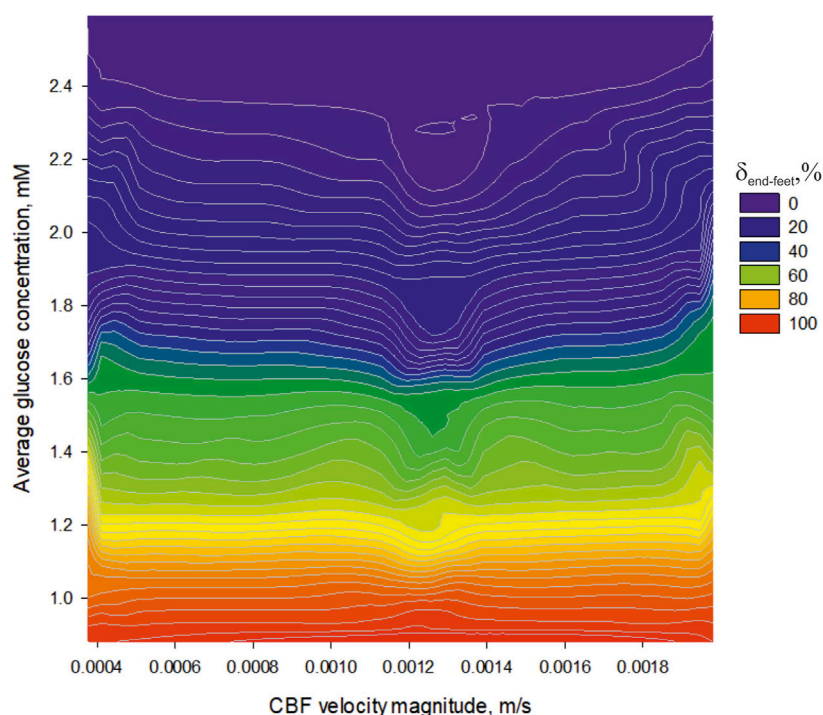**FIGURE 7**
The glucose gradients near a blood capillary surface after CBF increase [application of $f_{shift}^{inc}(t)$]. All designations are the same as in Figure 5.

FIGURE 8
The dependence of an average glucose concentration in nervous parenchyma (Ω_{II}) near a capillary surface on CBF velocity magnitude (Ω_I) under different percent of the end-feet cover.

clefts between the astrocytes where nutrients can penetrate fluently. According to the methodology of the present study it means in that area glucose incomes by a simple diffusion. The existence of a free diffusion area intermitting end-feet was experimentally observed (Hawkins et al., 2006). Moreover, the simulations predicted a very close correspondence between theory and data obtained in rats and humans (Gruetter et al., 1998; Choi et al., 2001) only under conditions when $\delta_{end-feet}$ <100% (Simpson et al., 2007). Indeed, the proportion of GLUTi/free diffusion areas can be a subject of discussion, however, an enhanced level of glucose due to CBF reduction is already observed under the condition of $\delta_{end-feet} \leq 85\%$ (Figure 8). Thus, the part of the third internal obstacle for a free diffusion can be relatively high to make the effect visible.

A physical background of this phenomenon has previously been explained (Nartsissov, 2021a). The increased CBF always causes an enhanced amplitude of the glucose gradient in Ω_{II} because the level of this metabolite will continuously raise up with an incoming flow according to Eq. 12. The extremum values of CBF velocity magnitude in Figure 8 can be explained by the optimum relation between GLUT density, $H_{\partial\Omega_{II}}^{outer}$ area and $c(\vec{r},t)|_{\Omega_I}$. Indeed, the relation depends on a blood vessel dimeter, but the general effect will be the same.

The introduced model has different physiological applications which help clinicians to investigate the aspects of neuropathology. First, the geometry of the phantom Ω can be easily reshaped. The structural principles of NVU organization will be the same for a long-type capillary and even for a vessel network. Furthermore, the diameter of a capilllary is also among the parameters to be modified. The small blood capillary vessels are usually ranged from 5 to 10 μm in diameter (Vendel et al., 2019; Xing et al., 2020). However, a distinction of caliber between arterioles, pre-capillaries and capillary is blur, and the range of a capillary network with the diameter up to 15 μm is also reported (Fleischer et al., 2020). During experimental studying of a cerebral capillaries functional reactivity, the vessels with diameter above 10 μm and below 30 μm are classified as the medium-size vessels (Stefanovic et al., 2008). Due to a normal human red blood cell has the shape of a biconcave disk with a diameter of approximately 8 μm and a thickness of approximately 2 μm (Secomb, 2017), a short length of a small capillary can get some especial properties resulting from a vessel wall friction. That is why in the present study the geometry of the considered system is designed to the upper range of a capillary diameter (R_0, see Table 1). Due to the surrounding capillaries get pronounceable effects on glucose gradients near the external boundary of the virtual phantom ($H_{\partial\Omega_{II}}^{outer}$), an extension of the

phantom by inclusion of a vasculature network is preferable. It is remarkable that arterioles and capillaries can be included in the model all together. The modification of the general phantom structure should be made by an addition of a smooth muscle wall for arterioles which is represent as Ω_{SMW} placed between Ω_E and Ω_{BL}. The reconstruction of a vascular network can be fulfilled by either digital proceedings of experimental images or especially created blood vessels tree phantoms. The principles of digital arterial network creation has recently been discussed elsewhere (Kopylova et al., 2017). An application of the step-like functions $f_{shift}^{dec/inc}(t)$ to the pressure on the end transverse surfaces of the network can simulate a brain circulation disorder with further alteration of the glucose levels inside nervous parenchyma.

Moreover, the developed approach can be used for estimation of CBF alteration influence on several types of metabolites. For oxygen and nitric oxide, the model will be simplified by the omitting of the flux discontinuity on the internal borders, but the other principles remain the same. For the drugs, the structure of the flux dysconnectivity functions in Eq. 15 should be modified. Additionally, the third summand in the second member of Eqs 5, 6 can be simplified to a linear dependence. However, as in the case of oxygen, the main described algorithm will persist the same.

Another advantage of the model is to evaluate a wide set of physical parameters which are useful for medical purposes. The considered CBF velocities can be transformed into the standard unit of measurement for CBF which is milliliters of blood per 100 g of tissue per minute (Liu, 2015). The considered time area in $f_{shift}^{dec/inc}(t)$ connecting with short-term (>0.20 Hz) fluctuations in CBF velocity. They closely match those observed in arterial pressure and likely reflect mechanical/biophysical properties of the cerebrovascular bed in response to changes in arterial pressure (Zhang et al., 2000). However, Δt can be extended to several seconds, and this time range is associated with cerebral autoregulation which does not depend on changes in arterial pressure.

Nevertheless, impaired cerebral autoregulation leads to dependence of blood flow on blood pressure, which may affect blood supply to brain when peripheral blood pressure is reduced under physiological and pathological conditions (Hu et al., 2008). This phenomenon is also the subject of consideration in the introduced model.

Another aspect of the introduced approach is a detailed consideration of brain parenchyma—the area Ω_{II}. For general purpose it can be approximated by a porous media. This description is commonly used in the most spatial-time models (Syková and Nicholson, 2008). Nevertheless, there are several metabolites which have an essential difference in diffusion inside astrocyte/neurons area and ISF. A well-known example of such metabolites is glutamate (Nartsissov, 2022). This neuromediator has a strong regulated level in the inter-cell space and the most part of its concentration is stored into astrocytes (Selivanov et al.,

2021). For modeling of spatial-time gradients of such neurotransmitters the explicit form of cell-to-cell position in parenchyma should be designed. It can be done using an algorithm based on 3D Voronoi diagram application (Nartsissov, 2021b). The obtained structure will have a drawn area for diffusion and convection. It causes spatial complication of Ω_{II} but more precise effects become accessible.

Thus, the introduced method is an adaptive tool for analysis of CBF changes influence on spatial-time gradients of glucose. It can be also used for evaluation of non-steady state spatial distribution of different chemical compounds. Certainly, the supposed model can be applied not only to modeling of brain parenchyma but also for estimation of the gradients near blood vessels in other tissues as well.

Data availability statement

The original contributions presented in the study are included in the article/Supplementary Material, further inquiries can be directed to the corresponding author.

Author contributions

YN developed algorithms, created the model in COMSOL Multiphysics Software, fulfilled all calculations, designed the work, analysed the data, wrote, and edited the text.

Acknowledgments

Conflict of interest

The authors declare that the research was conducted in the absence of any commercial or financial relationships that could be construed as a potential conflict of interest.

Publisher's note

All claims expressed in this article are solely those of the authors and do not necessarily represent those of their affiliated organizations, or those of the publisher, the editors and the reviewers. Any product that may be evaluated in this article, or claim that may be made by its manufacturer, is not guaranteed or endorsed by the publisher.

References

Abbott, N. J., Patabendige, A. A. K., Dolman, D. E. M., Yusof, S. R., and Begley, D. J. (2010). Structure and Function of the Blood-Brain Barrier. *Neurobiol. Dis.* 37 (1), 13–25. doi:10.1016/j.nbd.2009.07.030

Abbott, N. J., Rönnbäck, L., and Hansson, E. (2006). Astrocyte-endothelial Interactions at the Blood-Brain barrier.Review DB - Scopus. *Nat. Rev. Neurosci.* 7 (1), 41–53. doi:10.1038/nrn1824

Ainscow, E. K., Mirshamsi, S., Tang, T., Ashford, M. L. J., and Rutter, G. A. (2002). Dynamic Imaging of Free Cytosolic ATP Concentration during Fuel Sensing by Rat Hypothalamic Neurones: Evidence for ATP-independent Control of ATP-Sensitive K+ Channels. *J. Physiol.* 544 (2), 429–445. doi:10.1113/jphysiol.2002.022434

Arifin, D. Y., Lee, K. Y. T., and Wang, C. H. (2009). Chemotherapeutic Drug Transport to Brain Tumor. *J. Control. Release* 137 (3), 203–210. doi:10.1016/j.jconrel.2009.04.013

Ashrafi, G., and Ryan, T. A. (2017). Glucose Metabolism in Nerve Terminals. *Curr. Opin. Neurobiol.* 45, 156–161. doi:10.1016/j.conb.2017.03.007

Aubert, A., and Costalat, R. (2005). Interaction between Astrocytes and Neurons Studied Using a Mathematical Model of Compartmentalized Energy Metabolism. *J. Cereb. Blood Flow. Metab.* 25 (11), 1476–1490. doi:10.1038/sj.jcbfm.9600144

Aubert, A., Costalat, R., and Valabrègue, R. (2001). Modelling of the Coupling between Brain Electrical Activity and Metabolism. *Acta Biotheor.* 49 (4), 301–326. doi:10.1023/A:1014286728421

Bashkatov, A. N., Genina, E. A., Sinichkin, Y. P., Kochubey, V. I., Lakodina, N. A., and Tuchin, V. V. (2003). Glucose and Mannitol Diffusion in Human Dura Mater. *Biophys. J.* 85 (5), 3310–3318. doi:10.1016/S0006-3495(03)74750-X

Basser, P. J., and Jones, D. K. (2002). Diffusion-tensor MRI: Theory, Experimental Design and Data Analysis - A Technical Review. *NMR Biomed.* 15 (7-8), 456–467. doi:10.1002/nbm.783

Bear, J. (1961). On the Tensor Form of Dispersion in Porous Media. *J. Geophys. Res.* 66 (4), 1185–1197. doi:10.1029/jz066i004p01185

Berthiaume, A. A., Hartmann, D. A., Majesky, M. W., Bhat, N. R., and Shih, A. Y. (2018). Pericyte Structural Remodeling in Cerebrovascular Health and Homeostasis. *Front. Aging Neurosci.* 10, 210. doi:10.3389/fnagi.2018.00210

Calvetti, D., Cheng, Y., and Somersalo, E. (2015). A Spatially Distributed Computational Model of Brain Cellular Metabolism. *J. Theor. Biol.* 376, 48–65. doi:10.1016/j.jtbi.2015.03.037

Chanraud, S., Zahr, N., Sullivan, E. V., and Pfefferbaum, A. (2010). MR Diffusion Tensor Imaging: A Window into White Matter Integrity of the Working Brain. *Neuropsychol. Rev.* 20 (2), 209–225. doi:10.1007/s11065-010-9129-7

Chen, J., Lu, X. Y., and Wang, W. (2006). Non-Newtonian Effects of Blood Flow on Hemodynamics in Distal Vascular Graft Anastomoses. *J. Biomech.* 39 (11), 1983–1995. doi:10.1016/j.jbiomech.2005.06.012

Choi, I. Y., Lee, S. P., Kim, S. G., and Gruetter, R. (2001). *In Vivo* measurements of Brain Glucose Transport Using the Reversible Michaelis-Menten Model and Simultaneous Measurements of Cerebral Blood Flow Changes during Hypoglycemia. *J. Cereb. Blood Flow. Metab.* 21 (6), 653–663. doi:10.1097/00004647-200106000-00003

Davis, M. J., Hill, M. A., and Kuo, L. (2008). "Chapter 6. Local Regulation of Microvascular Perfusion," in *Microcirculation.* Second Edition (Academic Press), 161–284.

Delgado, J. M. P. Q. (2007). Longitudinal and Transverse Dispersion in Porous Media. *Chem. Eng. Res. Des.* 85 (9), 1245–1252. doi:10.1205/cherd07017

Deng, D., and Yan, N. (2016). GLUT, SGLT, and SWEET: Structural and Mechanistic Investigations of the Glucose Transporters. *Protein Sci.* 25 (3), 546–558. doi:10.1002/pro.2858

Dwyer, D. e. (2002). Glucose Metabolism in the Brain. *Int. Rev. Neurobiol.* 51, 1–535.

Fan, Y., Jiang, W., Zou, Y., Li, J., Chen, J., and Deng, X. (2009). Numerical Simulation of Pulsatile Non-newtonian Flow in the Carotid Artery Bifurcation. *Acta Mech. Sin.* 25 (2), 249–255. doi:10.1007/s10409-009-0227-9

Fatahian, E., Kordani, N., and Fatahian, H. (2018). A Review on Rheology of Non-newtonian Properties of Blood. *IIUM Eng. J.* 19 (1), 237–250. doi:10.31436/iiumej.v19i1.826

Fel, L., and Bear, J. (2010). Dispersion and Dispersivity Tensors in Saturated Porous Media with Uniaxial Symmetry. *Transp. Porous Media* 85 (1), 259–268. doi:10.1007/s11242-010-9558-z

Fleischer, S., Tavakol, D. N., and Vunjak-Novakovic, G. (2020). From Arteries to Capillaries: Approaches to Engineering Human Vasculature. *Adv. Funct. Mat.* 30 (37), 1910811. doi:10.1002/adfm.201910811

Gijsen, F. J. H., Allanic, E., Van De Vosse, F. N., and Janssen, J. D. (1999). The Influence of the Non-Newtonian Properties of Blood on the Flow in Large Arteries: Unsteady Flow in a 90 Degrees Curved Tube. *J. Biomech.* 32 (7), 705–713. doi:10.1016/S0021-9290(99)00014-7

Gould, I. G., Tsai, P., Kleinfeld, D., and Linninger, A. (2017). The Capillary Bed Offers the Largest Hemodynamic Resistance to the Cortical Blood Supply. *J. Cereb. Blood Flow. Metab.* 37 (1), 52–68. doi:10.1177/0271678X16671146

Gruetter, R., Ugurbil, K., and Seaquist, E. R. (1998). Steady-state Cerebral Glucose Concentrations and Transport in the Human Brain. *J. Neurochem.* 70 (1), 397–408. doi:10.1046/j.1471-4159.1998.70010397.x

Gursoy-Ozdemir, Y., Yemisci, M., and Dalkara, T. (2012). Microvascular Protection Is Essential for Successful Neuroprotection in Stroke. *J. Neurochem.* 123 (Suppl. 2), 2–11. doi:10.1111/j.1471-4159.2012.07938.x

Hawkins, R. A., O'Kane, R. L., Simpson, I. A., and Viña, J. R. (2006). Structure of the Blood-Brain Barrier and its Role in the Transport of Amino acidsConference Paper DB - Scopus. *J. Nutr.* 136 (1), 218S–226S.

Heinrich, R., and Schuster, S. (1996). *The Regulation of Cellular Systems.* New York: Springer New York, NY. doi:10.1007/978-1-4613-1161-4

Hladky, S. B., and Barrand, M. A. (2018). Elimination of Substances from the Brain Parenchyma: Efflux via Perivascular Pathways and via the Blood-Brain Barrier. *Fluids Barriers CNS* 15 (1), 30. doi:10.1186/s12987-018-0113-6

Hladky, S. B., and Barrand, M. A. (2016). Fluid and Ion Transfer across the Blood-Brain and Blood-Cerebrospinal Fluid Barriers; a Comparative Account of Mechanisms and Roles. *Fluids Barriers CNS* 13 (1), 19. doi:10.1186/s12987-016-0040-3

Hu, K., Peng, C. K., Huang, N. E., Wu, Z., Lipsitz, L. A., Cavallerano, J., et al. (2008). Altered Phase Interactions between Spontaneous Blood Pressure and Flow Fluctuations in Type 2 Diabetes Mellitus: Nonlinear Assessment of Cerebral Autoregulation. *Phys. A* 387 (10), 2279–2292. doi:10.1016/j.physa.2007.11.052

Huang, C., Chai, Z., and Shi, B. (2013). Non-newtonian Effect on Hemodynamic Characteristics of Blood Flow in Stented Cerebral Aneurysm. *Commun. Comput. Phys.* 13 (3), 916–928. doi:10.4208/cicp.281011.020212s

Hudetz, A. G., Fehér, G., and Kampine, J. P. (1996). Heterogeneous Autoregulation of Cerebrocortical Capillary Flow: Evidence for Functional Thoroughfare Channels? *Microvasc. Res.* 51 (1), 131–136. doi:10.1006/mvre.1996.0015

Iasiello, M., Vafai, K., Andreozzi, A., and Bianco, N. (2016). Analysis of Non-newtonian Effects on Low-Density Lipoprotein Accumulation in an Artery. *J. Biomech.* 49 (9), 1437–1446. doi:10.1016/j.jbiomech.2016.03.017

Jensen, O. E., and Chernyavsky, I. L. (2019). Blood Flow and Transport in the Human Placenta *Ann. Rev. Fluid Mech.* 51 (1), 25–47. doi:10.1146/annurev-fluid-010518-040219

Jespersen, S. N., and Østergaard, L. (2012). The Roles of Cerebral Blood Flow, Capillary Transit Time Heterogeneity, and Oxygen Tension in Brain Oxygenation and Metabolism. *J. Cereb. Blood Flow. Metab.* 32 (2), 264–277. doi:10.1038/jcbfm.2011.153

Jin, B. J., Smith, A. J., and Verkman, A. S. (2016). Spatial Model of Convective Solute Transport in Brain Extracellular Space Does Not Support a "glymphatic" Mechanism. *J. Gen. Physiol.* 148 (6), 489–501. doi:10.1085/jgp.201611684

Kashkooli, F. M., Rezaeian, M., and Soltani, M. (2022). Drug Delivery through Nanoparticles in Solid Tumors: a Mechanistic Understanding. *Nanomedicine* 17, 695–716. doi:10.2217/nnm-2021-0126

Keaney, J., and Campbell, M. (2015). The Dynamic Blood-Brain Barrier. *FEBS J.* 282 (21), 4067–4079. doi:10.1111/febs.13412

Kim, Y. H., VandeVord, P. J., and Lee, J. S. (2008). Multiphase Non-Newtonian Effects on Pulsatile Hemodynamics in a Coronary Artery. *Internat. J. Numerical Methods Fluids* 58 (7), 803–825. doi:10.1002/fld.1768

Kinney, J. P. (2009). *Investigation of Neurotransmitter Diffusion in Three-Dimensional Reconstructions of Hippocampal Neuropil.* PhD, University of California.

Kinney, J. P., Spacek, J., Bartol, T. M., Bajaj, C. L., Harris, K. M., and Sejnowski, T. J. (2013). Extracellular Sheets and Tunnels Modulate Glutamate Diffusion in Hippocampal Neuropil. *J. Comp. Neurol.* 521 (2), 448–464. doi:10.1002/cne.23181

Köhler, S., Schmidt, H., Fülle, P., Hirrlinger, J., and Winkler, U. (2020). A Dual Nanosensor Approach to Determine the Cytosolic Concentration of ATP in Astrocytes. *Front. Cell. Neurosci.* 14, 565921. doi:10.3389/fncel.2020.565921

Kopylova, V. S., Boronovskiy, S. E., and Nartsissov, Y. R. (2017). Fundamental Principles of Vascular Network Topology. *Biochem. Soc. Trans.* 45 (3), 839–844. doi:10.1042/BST20160409

Kreft, M., Lukšič, M., Zorec, T. M., Prebil, M., and Zorec, R. (2013). Diffusion of D-Glucose Measured in the Cytosol of a Single Astrocyte. *Cell. Mol. Life Sci.* 70 (8), 1483–1492. doi:10.1007/s00018-012-1219-7

Krüger-Genge, A., Blocki, A., Franke, R. P., and Jung, F. (2019). Vascular Endothelial Cell Biology: An Update. *Int. J. Mol. Sci.* 20 (18), E4411. doi:10.3390/ijms20184411

Le Bihan, D. (2003). Looking into the Functional Architecture of the Brain with Diffusion MRI. *Nat. Rev. Neurosci.* 4 (6), 469–480. doi:10.1038/nrn1119

Liu, T. T. (2015). "Perfusion Imaging with Arterial Spin Labeling MRI," in *Brain Mapping*. Editor A. W. Toga (Waltham: Academic Press), 149–154.

Lizák, B., Szarka, A., Kim, Y., Choi, K. S., Németh, C. E., Marcolongo, P., et al. (2019). Glucose Transport and Transporters in the Endomembranes. *Int. J. Mol. Sci.* 20 (23), E5898. doi:10.3390/ijms20235898

Lowe, A. G., and Walmsley, A. R. (1986). The Kinetics of Glucose Transport in Human Red Blood Cells. *Biochim. Biophys. Acta* 857 (2), 146–154. doi:10.1016/0005-2736(86)90342-1

Lyons, D. G., Parpaleix, A., Roche, M., and Charpak, S. (2016). Mapping Oxygen Concentration in the Awake Mouse Brain. *eLife* 5 (FEBRUARY2016), e12024. doi:10.7554/eLife.12024

Mishchenko, Y., Hu, T., Spacek, J., Mendenhall, J., Harris, K. M., and Chklovskii, D. B. (2010). Ultrastructural Analysis of Hippocampal Neuropil from the Connectomics Perspective. *Neuron* 67 (6), 1009–1020. doi:10.1016/j.neuron.2010.08.014

Molla, M. M., and Paul, M. C. (2012). LES of Non-newtonian Physiological Blood Flow in a Model of Arterial Stenosis. *Med. Eng. Phys.* 34 (8), 1079–1087. doi:10.1016/j.medengphy.2011.11.013

Nartsissov, Y. R. (2021b). A Novel Algorithm of the Digital Nervous Tissue Phantom Creation Based on 3D Voronoi Diagram Application. *J. Phys. Conf. Ser.* 2090 (1), 012009. doi:10.1088/1742-6596/2090/1/012009

Nartsissov, Y. R. (2022). "Amino Acids as Neurotransmitters. The Balance between Excitation and Inhibition as a Background for Future Clinical Applications," in *Recent Advances in Neurochemistry*. Editor D. T. Heinbockel.

Nartsissov, Y. R. (2017). Geometries of Vasculature Bifurcation Can Affect the Level of Trophic Damage during Formation of a Brain Ischemic Lesion. *Biochem. Soc. Trans.* 45 (5), 1097–1103. doi:10.1042/BST20160418

Nartsissov, Y. R., and Mashkovtseva, E. V. (2006). Application of Rigid Body Mechanics to Theoretical Description of Rotation within F0F1-ATP Synthase. *J. Theor. Biol.* 242 (2), 300–308. doi:10.1016/j.jtbi.2006.02.018

Nartsissov, Y. R. (2021a). The Effect of Flux Dysconnectivity Functions on Concentration Gradients Changes in a Multicomponent Model of Convectional Reaction-Diffusion by the Example of a Neurovascular Unit. *Defect Diffusion Forum* 413, 19–28. doi:10.4028/www.scientific.net/ddf.413.19

Patching, S. G. (2017). Glucose Transporters at the Blood-Brain Barrier: Function, Regulation and Gateways for Drug Delivery. *Mol. Neurobiol.* 54 (2), 1046–1077. doi:10.1007/s12035-015-9672-6

Payne, S. J. (2004). Analysis of the Effects of Gravity and Wall Thickness in a Model of Blood Flow through Axisymmetric Vessels. *Med. Biol. Eng. Comput.* 42 (6), 799–806. doi:10.1007/BF02345213

Pickens, J. F., and Grisak, G. E. (1981). Scale-dependent Dispersion in a Stratified Granular Aquifer. *Water Resour. Res.* 17 (4), 1191–1211. doi:10.1029/WR017i004p01191

Pontrelli, G. (1998). Pulsatile Blood Flow in a Pipe. *Comput. Fluids* 27 (3), 367–380. doi:10.1016/S0045-7930(97)00041-8

Rezaeian, M., Sedaghatkish, A., and Soltani, M. (2019). Numerical Modeling of High-Intensity Focused Ultrasound-Mediated Intraperitoneal Delivery of Thermosensitive Liposomal Doxorubicin for Cancer Chemotherapy. *Drug Deliv.* 26 (1), 898–917. doi:10.1080/10717544.2019.1660435

Rezaeian, M., Soltani, M., Karimvand, A. N., and Raahemifar, K. (2022). Mathematical Modeling of Targeted Drug Delivery Using Magnetic Nanoparticles during Intraperitoneal Chemotherapy. *Pharmaceutics* 14 (2), 324. doi:10.3390/pharmaceutics14020324

Secomb, T. W. (2017). Blood Flow in the Microcirculation. *Annu. Rev. Fluid Mech.* 49, 443–461. doi:10.1146/annurev-fluid-010816-060302

Sedaghatkish, A., Rezaeian, M., Heydari, H., Ranjbar, A. M., and Soltani, M. (2020). Acoustic Streaming and Thermosensitive Liposomes for Drug Delivery into Hepatocellular Carcinoma Tumor Adjacent to Major Hepatic Veins; an Acoustics–Thermal–Fluid-Mass Transport Coupling Model. *Int. J. Therm. Sci.* 158, 106540. doi:10.1016/j.ijthermalsci.2020.106540

Selivanov, V. A., Zagubnaya, O. A., Nartsissov, Y. R., and Cascante, M. (2021). Unveiling a Key Role of Oxaloacetate-Glutamate Interaction in Regulation of Respiration and ROS Generation in Nonsynaptic Brain Mitochondria Using a Kinetic Model. *PLoS ONE* 16 (8), e0255164. doi:10.1371/journal.pone.0255164

Shukla, J. B., Parihar, R. S., and Rao, B. R. P. (1980). Effects of Stenosis on Non-newtonian Flow of the Blood in an Artery. *Bull. Math. Biol.* 42 (3), 283–294. doi:10.1007/BF02460787

Simpson, I. A., Carruthers, A., and Vannucci, S. J. (2007). Supply and Demand in Cerebral Energy Metabolism: The Role of Nutrient Transporters. *J. Cereb. Blood Flow. Metab.* 27 (11), 1766–1791. doi:10.1038/sj.jcbfm.9600521

Sochi, T. (2013). *Non-Newtonian Rheology in Blood Circulation*. arXiv:1306.2067.

Stefanovic, B., Hutchinson, E., Yakovleva, V., Schram, V., Russell, J. T., Belluscio, L., et al. (2008). Functional Reactivity of Cerebral Capillaries. *J. Cereb. Blood Flow. Metab.* 28 (5), 961–972. doi:10.1038/sj.jcbfm.9600590

Syková, E., and Nicholson, C. (2008). Diffusion in Brain Extracellular Space. *Physiol. Rev.* 88 (4), 1277–1340. doi:10.1152/physrev.00027.2007

Unekawa, M., Tomita, M., Tomita, Y., Toriumi, H., Miyaki, K., and Suzuki, N. (2010). RBC Velocities in Single Capillaries of Mouse and Rat Brains Are the Same, Despite 10-fold Difference in Body Size. *Brain Res.* 1320, 69–73. doi:10.1016/j.brainres.2010.01.032

Vendel, E., Rottschäfer, V., and De Lange, E. C. M. (2019). The Need for Mathematical Modelling of Spatial Drug Distribution within the Brain. *Fluids Barriers CNS* 16 (1), 12. doi:10.1186/s12987-019-0133-x

Vimmr, J., and Jonasova, A. (2008). On the Modelling of Steady Generalized Newtonian Flows in a 3D Coronary Bypass. *Eng. Mech.* 15 (3), 193–203.

Weiler, A., Volkenhoff, A., Hertenstein, H., and Schirmeier, S. (2017). Metabolite Transport across the Mammalian and Insect Brain Diffusion Barriers. *Neurobiol. Dis.* 107, 15–31.

Xing, F., Lee, J. H., Polucha, C., and Lee, J. (2020). Three-dimensional Imaging of Spatio-Temporal Dynamics of Small Blood Capillary Network in the Cortex Based on Optical Coherence Tomography: A Review. *J. Innov. Opt. Health Sci.* 13 (1), 2030002. doi:10.1142/S1793545820300025

Yazdani, S., Jaldin-Fincati, J. R., Pereira, R. V. S., and Klip, A. (2019). Endothelial Cell Barriers: Transport of Molecules between Blood and tissues.Review DB - Scopus. *Traffic* 20 (6), 390–403. doi:10.1111/tra.12645

Yilmaz, F., and Yaar Gundogdu, M. (2008). A Critical Review on Blood Flow in Large Arteries; Relevance to Blood Rheology, Viscosity Models, and Physiologic Conditions. *Korea-Australia Rheology J.* 20 (4), 197–211.

Zhan, W., Arifin, D. Y., Lee, T. K., and Wang, C. H. (2017). Mathematical Modelling of Convection Enhanced Delivery of Carmustine and Paclitaxel for Brain Tumour Therapy. *Pharm. Res.* 34 (4), 860–873. doi:10.1007/s11095-017-2114-6

Zhang, R., Zuckerman, J. H., and Levine, B. D. (2000). Spontaneous Fluctuations in Cerebral Blood Flow: Insights from Extended- Duration Recordings in Humans. *Am. J. Physiol. Heart Circ. Physiol.* 278 (6 47-6), H1848–H1855. doi:10.1152/ajpheart.2000.278.6.h1848

Frontiers in
Physiology

Understanding how an organism's components work together to maintain a healthy state

The second most-cited physiology journal, promoting a multidisciplinary approach to the physiology of living systems - from the subcellular and molecular domains to the intact organism and its interaction with the environment.

Discover the latest Research Topics

See more →

frontiers in
Physiology

frontiers | Research Topics